UNIVERSITÀ DEGLI STUDI DI
CASSINO E DEL LAZIO MERIDIONALE

Corso di Dottorato in

Metodi, modelli e tecnologie per l'ingegneria

Ciclo XXXIII

curriculum Ingegneria Civile

Ciclo XXXIII

MULTILEVEL PROBABILISTIC RISK ASSESSMENT OF SEISMIC LIQUEFACTION ON URBAN SYSTEMS

SSD: ICAR - 07

Coordinatore del Corso
Chiar.ma Prof. Wilma Polini

Dottorando
Luca Paolella

Supervisori
Chiar.mo Prof. Giuseppe Modoni
Chiar.mo Prof. Gabriele Chiaro
(U.C. University of Canterbury, N.Z.)

To my family.

ACKNOWLEDGEMENTS

The author wishes to acknowledge the contribution by the EU funded project LIQUEFACT “Assessment and mitigation of liquefaction potential across Europe: a holistic approach to protect structures/infrastructures for improved resilience to earthquake-induced liquefaction disasters”, project ID 700748 funded under the H2020-DRS-2015.

ABSTRACT

Proven that risk management embraces a series of subsequent steps, including communication strategies and political decisions, which are not explicitly discussed in this work, the study's general scope aims to develop an operative procedure to quantify and mitigate the liquefaction risk on urban aggregate. Bearing this goal in mind, the action has been focused on two complementary targets, i.e., evaluating the liquefaction risk of a generic system and standardizing the use of ground improvement technologies to mitigate the liquefaction risk. The former goal has been achieved by customizing the well-consolidated performance-based earthquake engineering approach to the liquefaction-induced damage on buildings. The latter plan involves a first classification and a global technical comparison of the most widely adopted countermeasures. Besides, the performance of benefit/costs analyses allows to estimate on an annual basis the economic convenience of mitigating. In the context of liquefaction, the proposed framework represents a primary component of a holistic seismic risk assessment and management, capable of evaluating the potential consequences of earthquakes and secondary seismic hazards (like Landslides, Etc.).

From a historical viewpoint, some of the most spectacular examples of earthquake-induced damage occurred because of the reduction of cohesionless soils' strength until, in extreme cases, they appeared to flow like a fluid. Thus, the above behavior of saturated coarse soils is known as seismic liquefaction. The word liquefaction is commonly used to encompass several liquefaction-related phenomena that Kramer (1996) grouped in two categories: flow liquefaction (less frequent but responsible for the most dramatic instabilities, i.e., flow failures) and cyclic mobility, the latter including level ground liquefaction. Only in a few cases liquefaction affected the territory massively, like in the flow failure examples occurred in 1964 in Alaska, which caused 32 casualties, or in the more recent 2018 earthquake occurred in Palu (Indonesia). This mechanism occurs in particular conditions, namely when the static shear stresses on sloping ground exceed the soil's frictional shear strength deteriorated by the pore pressure build-up. In this case, displacement can be very large, in the order of tens of meters or even more, and may disrupt buildings and infrastructure over vast areas.

Apart from this extreme case, cyclic mobility-related phenomena include a more heterogeneous range of effects (e.g., level ground liquefaction, lateral spreading, etc.) that frequently regard the foundation of buildings and infrastructures affecting their performance. Even when such massive disruption does not occur, the effects of liquefaction are harmful to the communities in terms of economic losses and social consequences. Several worldwide earthquakes (Turkey, Greece, Taiwan, India, Japan, New Zealand, Italy) have highlighted the complex behavior of the structure-foundation system subjected to earthquake vibrations. For example, after the 1999 Kocaeli Earthquake, the Adapazari area (Turkey) suffered extensive liquefaction with buildings that rotated significantly, and others that underwent relatively uniform settlements of several dozen centimeters. In other cases, ununiform settlement caused the deformation of the superstructures up to intolerable levels. Other effects can be seen on horizontal infrastructures like breakage or disconnection of pipelines or uplift of sewer manholes. These examples highlight the importance of understanding the mechanism triggering liquefaction, predicting soil response subjected to ground shaking and the interaction with the overlying or embedded structures, and transferring this knowledge into robust operative procedures for risk assessment. The applicability of individual tools and the complete procedures needs to be examined with real situations facing the complexity of using data of different nature, origin, and quality standards and merging them into a unified framework. Thus, it is fundamental to observe the performance of real structures and infrastructures, reconstructing in the best possible way the subsoil and structural characteristics to interpret the occurred phenomena.

The challenge for risk assessment comes from investigating different concurrent factors: the seismicity and the liquefaction susceptibility of a soil, i.e. the ability of a soil to liquefy irrespective of the level of earthquake shaking (Youd and Perkins, 1978). The former affects the territory in the radius of dozens of kilometers from the epicenter; the latter, i.e. the set of geological conditions by which recent deposits of saturated granular soils tend to compact and develop excess pore pressures upon cyclic shearing, is variable in the scale of dozens of meters. A combination of different studies must thus be conceived conjugating information at different geographical scales: seismic hazard dictated by macrophenomena producing effects at the regional scale; lithological, stratigraphic, geotechnical, and hydrogeological conditions.

The question becomes more complicated when considering that risk assessment involves buildings and infrastructures whose vulnerability must be assessed firstly at

the physical level, considering their structural characteristics, then at the serviceability level, implying to estimate their weight on the life of the community.

Proven that the most sophisticated tools are nowadays able to reproduce phenomena with reasonable accuracy, but also ascertained that results depend very much on the quality of the available information used as input, primarily the geometrical and mechanical properties of soil and structures, the efficacy of risk assessment is a matter of how precisely the predictive model is built. This need imposes the maximum precision in conjunction with the coverage of the studied area, optimizing the investigation strategy. Investigations should be preferably performed where the presence of elements at risk is significant, and information should be interpreted altogether, taking advantage of their spatial distribution.

Methodologies and approaches of assessing of liquefaction potential are the subjects of significant and ongoing research. this document tries to summarize part of the extensive body of technical literature in this area to define a methodology for risk assessment. Considering the variability of possible situations, given by different scopes of the analysis (e.g., loss estimates, urban planning, emergency management, Etc.), different typology of the system exposed (building assets, horizontal infrastructures etc.), different extension (region, municipality, district or even single building) the methodology has been purposely defined in the general terms, leaving a variety of options.

Besides, the extensive physical damage produced on buildings and lifelines is only a part of the impact of liquefaction, as injuries are aggravated by the prolonged reduced serviceability of the critical infrastructures, i.e., those systems and organizations that deliver goods and services fundamental for the functioning of society and economy (Macaulay et al., 2009). This distinction requires introducing the concept of direct and indirect disaster losses. The former refers to directly quantifiable losses (such as the number of people killed and the damage to buildings, infrastructure, and natural resources); the latter include declines in output or revenue, and impact on the wellbeing of people, and generally arise from disruptions to the flow of goods and services because of a disaster (UNDRR, 2015). Population, structures, utilities, and socio-economic activities form together an integrated system of interdependent entities. Therefore, damages affecting the building asset or the facilities (roads, waterways, electric and communication lines) impact, directly or indirectly, onto the whole system, undermine its productive capacity and the whole social organization in a way that quality of life is jeopardized. The long time necessary to restore original conditions

plays the final negative role because the population may be discouraged to undertake reclamation and persuaded to abandon the place.

Earthquake-specific studies quantified the role of direct damages together with the reduction in production (business interruption) on economic growth. An analysis by Standard & Poor's (2015) (using Swiss Re data on expected losses) found that GDP per capita would be lower in all but one of the examined countries five years after a 1-in-250-year earthquake event. In some countries, including Chile, Costa Rica, Japan, Panama, Peru, the Philippines, Chinese Taipei, and Turkey, the decline in GDP per capita is estimated at more than 5%. Other studies of actual events (see Loayza et al., 2009) tend to balance the negative impacts of direct damages and production losses in many sectors with the increased activity in other sectors of the economy that may benefit due to reconstruction activities (e.g., construction sector). The significant capital investment to replace damaged equipment and machinery with new (potentially more productive) equipment and machinery could support future economic growth. Figure I illustrate the impact of recent earthquakes on economic growth by comparing pre-event economic projections with actual post-event economic outcomes. As it is obvious to expect, Figure I demonstrate that the considered recent events have impacted the national economic growth in a way proportional to the magnitude of the event and the exposure of the hit areas and inversely proportional to the economic system’s robustness. These evaluations do not consider the implications for public finances. There will likely be a need for a (potentially unexpected or unfunded) fiscal outlay to address emergency response, recovery, and reconstruction, as well as a decline in tax revenues. For example, to support recovery and reconstruction after the Great East Japan Earthquake, the Japanese government approved three supplementary budgets in 2011, totaling JPY 15 trillion (Ranghieri and Ishiwatari, 2014).

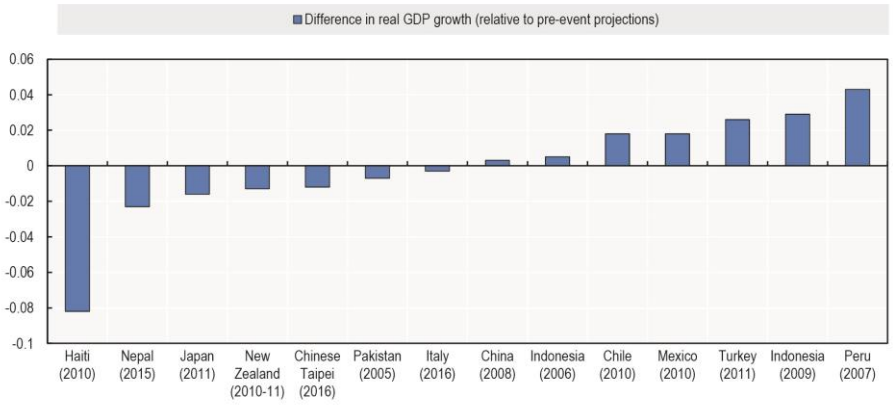

Source: IMF World Economic Outlook (various years).

Figure I - The economic impact of recent earthquakes (OECD, 2018).

All the above concerns raise the need for improving the recovery capacity and resilience of the community, involving stakeholders (boards, governments, regulators, suppliers of services) in unified strategies aimed at increasing security, preparedness and survivability. The international community has become progressively aware that resilience is the key to describe earthquake engineering performance and that technological units and social systems cannot be decoupled (e.g., Bruneau et al., 2003). The focus on technological aspects applied to critical infrastructure must be broadened to include the interplay of multiple systems – human, environmental, and others – which together add up to ensure the society's functioning.

The present work consists of 6 chapters, whose content is summarized as follows.

In the first chapter, the most hazardous natural phenomena are presented, highlighting the different impacts they produce on a community. Then, the basic principles of risk assessment and its historical evolution are briefly described.

In chapter 2, the main concepts forming the seismic risk assessment are reported to provide an overview of the methodology, the most known existing tools, and to underline the role of stakeholders.

In chapter 3, the mechanical characterization of seismic-induced liquefaction is introduced, focusing on the most popular procedures to predict the triggering and the severity of liquefaction in free field conditions and in the presence of buildings.

In chapter 4, firstly, the main principles of multilevel liquefaction risk are introduced, emphasizing the possibility of defining for each element the hazard factor (i.e., the demand), the vulnerability to such hazard, and evaluating the corresponding risk. A procedure to assess the liquefaction risk on buildings is defined, highlighting the non-negligible role of uncertainty, which propagates from the definition of representative variables to the obtained results. To quantify uncertainty, when risk assessments are carried out over large areas (e.g., urban areas), the combination of geostatistics with the error propagation theory represents a powerful analytical tool.

In chapter 5, the liquefaction risk assessment is first tested and validated by comparing predictions with liquefaction-induced effects observed in Christchurch (New Zealand) after the 22nd February 2011 Mw 6.2 earthquake. Then, the physical/economic impact on RC-F residential buildings is calculated accounting to the seismic hazard of the area; this analysis allows to evaluate the economic convenience of different mitigation options.

Chapter 6 relates about liquefaction-induced land and buildings damage following the 20 May 2012 Emilia (Italy) Mw 6.1 Earthquake, focusing on the municipalities of

S. Agostino and Mirabello. Additionally, a probabilistic liquefaction risk analysis is carried out on residential and industrial buildings. In this case, an appropriate economic model must be introduced to link the expected physical impact to the annualized economic loss resulting from the considered seismic scenarios. Finally, a benefit/cost analysis is performed for each building to assess the convenience of any mitigation treatment on an annual basis.

TABLE OF CONTENTS

LIST OF FIGURES

LIST OF TABLES

LIST OF SYMBOLS, ABBREVIATIONS AND ACRONYMS

Acronym	Description
AEL	Annualized Earthquake Loss
AFE	Annual Frequency of Exceedance
ALARP	As Low As Reasonably Practicable
ASTM	American Society for Testing and Materials International
AUC	Area Under Curve
BRT_i	Building Recovery Time (for the generic activity)
CAV	Cumulative Absolute Velocity
CBD	Central Business District
CEBA	Canterbury Earthquake Building Assessment
CEN	European Committee for Standardization
CERA	Canterbury Earthquake Recovery
C.E.S.	Christchurch Earthquake Sequence

CGD	Canterbury Geotechnical Database
CPT	Cone Penetration Test
CPTe	Electrical Cone Penetration Test
CPTm	Mechanical Cone Penetration Test
CPTu	Cone Penetration Test with Piezocone
CRR	Cyclic Resistance Ratio
CSR	Cyclic Stress Ratio
CT	Crust Thickness
CTL	Cumulative Thickness of Liquefiable Layers
CTMS	Commissione Tecnica per la Microzonazione Sismica
DEM	Digital Elevation Model
DPC	Department of Civil Protection
DTM	Digitail Terrain Model
EDP	Engineering Demand Parameter
EERI	Earthquake Engineering Research Institute
EMS	European Macroseismic Scale
EN	European Norm
EILD	Earthquake Induced Liquefaction Disaster
EQC	Earthquake Commission
ESP	Equivalent Soil Profile
FEMA	Federal Emergency Management Agency
F_L, FS_L	Factor of safety against Liquefaction

FLT	Functionality Loss Time
FN	False Negative
FORM	First Order Reliability Method
FP	False Positive
FPR	False Positive Ratio
GDP	Gross Domestic Product
GIS	Geographical Information System
GMPE	Ground Motion Prediction Equation
H_c, H_{crust}	Non-liquefiable crust thickness
H_{liq}	Thickness of Liquefiable Layer
ICMS	Indirizzi e criteri per la microzonazione sismica
IM	Earthquake Intensity Measure
INGV	Istituto Nazionale Geofisica e Vulcanologia
INV_DAM_i	Inventory losses for the business activity i
ISTAT	Istituto Nazionale di Statistica
JGS	Japan Geotechnical Society
KS	Kolmogorov Smirnov
LDI	Lateral Displacement Index
LDP	Liquefaction Demand Parameter
Li	Loss of Income
LPI	Liquefaction Potential Index
LPI_{ISH}	Ishihara-inspired Liquefaction Potential Index

LSs	Limit State
LSN	Liquefaction Severity Number
MASW	Multichannel Analysis of Surface Waves
MBIE	Ministry of Business, Innovation and Employment (N. Z.)
MCC	Matthews Correlation Coefficient
MDR	Mean Damage Rate
MUDE	Modello Unico Digitale per l'Edilizia
Mw	Moment Magnitude
NCEER	National Center for Earthquake Engineering Research
NEHRP	National Earthquake Hazard Reduction Program
NTC	Italian National Building Code
NZGS	New Zealand Geotechnical Society
OFR	Overall Failure Rate
OPCM	Ordinanza del Presidente del Consiglio dei Ministri
OSR	Overall Success Rate
PBD	Performance Based Design
PBEE	Performance Based Earthquake Engineering
PEER	Pacific Earthquake Engineering Research
PESH	Potential Earth Science Hazards
PGA	Peak Ground Acceleration
PGD	Peak Ground Displacement
PGDf	Permanent Ground Deformation

PGV	Peak Ground Velocity
PL	Probability of Liquefaction
P_{LS}	Probability of exceedance of designated limit states
PSHA	Probabilistic Seismic Hazard Analysis
RAIF	Resilience Assessment and Improvement Framework
RAN	Rete Accelerometrica Nazionale
RC-F	Reinforced Concrete Framed
Rc	Repair cost
RER	Regione Emilia Romagna
ROC	Receiver Operative Characteristic
$w_{v,1D}$	One-dimensional volumetric reconsolidation settlement
Sa	Spectral Acceleration
SBT	Soil Behavior Type
SCPT	Seismic Cone Penetration Test
SLM_i	Service Interruption Multiplier (for the generic activity)
SLS	Serviceability Limit State
SM	Seismic Microzonation
SORM	Second Order Reliability Method
SPT	Standard Penetration Test
SS	Stratigraphic Amplification Coefficient
TF	Topographic Factor
TN	True Negative

TP	True Positive
TPR	True Positive Ratio
UL	Utility Loss
ULS	Ultimate Limit State
USGS	United States Geological Survey
Symbols	
A_{d0}	Dilatancy calibration coefficient
a_{max}	Maximum horizontal acceleration
c	Cohesion
CN	Overburden correction factor
Dw	Groundwater depth
Dr	Soil Relative Density
FC	Fine content
fs	Sleeve friction
G	Shear modulus
G_0	Small-strain shear stiffness
h_{po}	Plastic modulus calibration parameter
Ic	Soil Behaviour Type Index
K	Bulk modulus
k	Soil permeability
$K\alpha$	Corrected term for influence of static shear stress
$K\sigma$	Corrected term for overburden pressure

L_1, L_2	Soil damping parameters
MSF	Magnitude Scaling Factor
n	Porosity
n^b	Bounding surface calibration coefficient
n^d	Dilatation surface calibration coefficient
$N1_{60}$	SPT number of blows.
$(N1_{60})_{cs}$	Equivalent clean sand normalized number of blows
Pa	Atmospheric pressure
qc	Tip resistance in cone penetration test
$(qc_{1N})_{cs}$	Equivalent clean sand normalized cone tip resistance
rd	Depth-dependent shear stress reduction coefficient
ru	Pore Pressure Ratio
$Sa(T)$	Acceleration response spectrum
SSI	Soil Structure Interaction
T	Fundamental Period
Tr	Return Period
U	Pore pressure
Uc	Coefficient of uniformity
VR	Reference Period
Vs	Shear wave velocity
$Vs1$	Normalized shear wave velocity
w_s	Shear-induced building settlement

w_v , $w_{v,1D}$	One-dimensional volumetric reconsolidation settlement
Z	Depth
Greek Symbols	
βk	Damage standard deviation value
Δu	Excess pore pressure
ε_v	Volumetric consolidation strains
ε_h	Horizontal strain
σv	Total vertical stress
$\sigma v'$	Effective vertical stress
σ	Normal stress
$\tau soil$	Shear stress of soil column mass
ϕ	Friction angle
ϕdeg	Equivalent degraded friction angle of the liquefiable layer
ψ	State parameter
χ^2	Chi-squared test
γ	Shear strain
ρ	Mass density of the soil
ρ_{dyn}	Shaking-induced the settlement

Chapter 1. INTRODUCTION TO NATURAL DISASTERS AND RISK

1.1 Abstract

Every day the natural and built environment deal with natural hazardous phenomena potentially able to affect any place with probability dictated sometimes by the geological/geomorphological conditions (earthquakes, volcanic eruptions), sometimes by climate implications (drought, wildfires, and extreme weather events), sometimes by a combination of both factors. All these phenomena may be conceptualized as natural hazards, i.e., necessary but not sufficient for a disaster to occur. They only become disasters through their match with human vulnerability (UNISDR, 2019). Despite human life loss occurs differently from one case to the other, hazardous phenomena are often responsible for significant short and long-term impacts on the existing communities (physical damage, economic losses, and loss of functionality). Therefore, the reduction of such impacts involves the entire risk management process. In this chapter, some of the recent case histories about natural phenomena that differently affected the community are briefly introduced and compared in terms of impact. Then, the concepts of risk assessment and its historical evolution are described.

1.2 Natural Hazards

From 1900, more than 15000 natural disasters have been collected and reported in the EM-DAT International Disaster Database maintained by the Centre for Research on the Epidemiology of Disasters (CRED) at the Catholic University in Louvain, Belgium. The Center for Research on the Epidemiology of Disasters (CRED) defines a disaster as the situation or event that overwhelms local capacity, necessitating a request at the national or international level for external assistance; an unforeseen and often sudden event that causes significant damage, destruction and human suffering". From a technical viewpoint, a phenomenon is assessed as a disaster, and thus incorporated in the EM-DAT, if at least one of the following criteria is satisfied: 10 or more reported killed people; 100 or more reported affected people; declaration of a state of emergency; call for international assistance.

For the last decade, the EM-DAT reports an average of 60 000 people globally died from natural disasters each year, corresponding to 0.1% of the global deaths rate. However, this rate dramatically increased in the past following catastrophic events like the 1983-85 famine and drought in Ethiopia, the 2004 Indian Ocean earthquake and tsunami, Cyclone Nargis that struck Myanmar in 2008, 2010 Port-au-Prince earthquake in Haiti. These phenomena pushed global disaster deaths over 200,000, representing 0.4% of the global annual deaths in these years.

Data summarized in Figure 1-1 attributes to drought and floods the highest number of victims since 1900; they appear the most severe and huge among the weather-related natural hazards, affecting respectively 2.0 and 1.5 billion people globally. Drought is probably the most complex due to its intrinsic nature, which connotates it as a hidden hazard and also to its wide-ranging and cascading impacts: it directly/indirectly affects agricultural production, water supply, energy production, transportation, tourism, human health, biodiversity and natural ecosystems in many areas of the globe.

Despite the size of circles showing the number of victims in Figure 1-1 may appear significantly low if compared to Floods and Drought, Earthquakes come immediately after human life lost, capable of few seconds of producing enormous damage over large areas. Around 4 000 Earthquakes per day (1.4 million per year) happen all around the world (https://earthquake.usgs.gov/): among them, an average of 21-30 strong earthquakes per year has been experienced in highly densely populated regions of the world since the 1970s, highlighting China and Indonesia as the most severely affected areas in the world, experiencing respectively 99 and 80 destructive events,

with Italy and Greece respectively ninth and 10th on the global scale (Guha-Sapir and Vos, 2011).

Between 1998-2017, Earthquakes caused approximately 750 000 deaths globally (CRED & UNISDR, 2018), being responsible for more than half of all deaths related to natural disasters (around 1.3 million), and affected more than 125 million people if considering injured, homeless, displaced or evacuated during the emergency phase of the disaster. The considerable number of deaths over the last two decades is strongly influenced by some extreme events like the 2004 Indian Ocean Tsunami, the 2008 Wenchuan (China) Earthquake, the 2010 Haiti Earthquake, and the 2011 Tohoku (Japan) Earthquake followed by a tsunami, which features are summarized in Table 1-1. By contrast, a similar magnitude earthquake to Haiti hit the New Zealand South Island, affecting 400 000 people, but without deaths due to the New Zealand building codes and to the preparedness of such community.

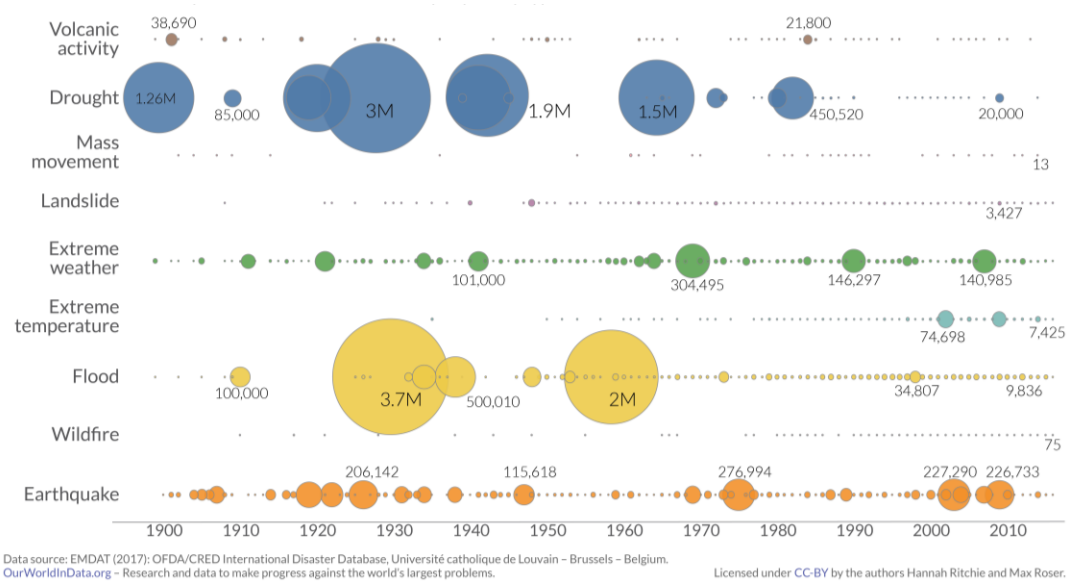

Figure 1-1 Global deaths caused by natural disasters between 1900-2016 (EM-DAT).

Table 1-1 Largest worldwide earthquake-induced disasters since 2004.

Date	Primary Hazard	Secondary Hazards	Affected People
December 26th, 2004	M9.1 Sumatra-Andaman earthquake (the third strongest since 1900) which occurred off the coast of Indonesia's Sumatra island, along a tectonic subduction zone in which the India Plate	After the Earthquake, the seafloor overlying the thrust fault was uplifted by several meters causing the Indian Ocean Tsunami; up to 20 meters height waves hit land, in Indonesia's Aceh region.	230 000 deaths distributed among 14 countries of the Indian area, 170 000 deaths in the only Indonesia Aceh region where the total economic loss reached 97% of the regional GDP. 1.7 million people displaced.
May 12th, 2008	Wenchuan (China) Earthquake M8.0	The Sichuan (central China) earthquake originated at the 'Longmenshan Fault' zone that follows the southern flanks of the Tibetan Massif; it induced more than 56 000 landslides in steep mountainous areas that additionally caused more than 2000 fatalities. Additionally, the earthquake-induced landslides produced extensive damage to housing settlements, irrigation channels, and rivers. Highways and bridges were blocked or destroyed, and the city of Wenchuan and many other towns became isolated.	70 000 fatalities, 350 000 persons injured and 20 000 missings; 20 million houses damaged, and more than 5million people homeless
January 12nd, 2010	Port-au-Prince, (Haiti) Earthquake M7.0	The 2010 Earthquake destroyed 300.00 dwellings, i.e. the 90% of the building stock in the epicentral area. Additionally, 60% of the nation's administrative and economic infrastructure was lost; 80% of the schools and more than 50% of the hospitals were destroyed or seriously damaged, 180 government buildings and the Parliament collapsed (GOH, 2010). Extensive liquefaction was triggered: lateral spreading-induced damage on the main port of Port-au-Prince and the blockage of lifelines from debris further hampered the emergency management and the post-earthquake recovery for many months after the earthquake.	316 000 deaths, 300 000 injured and over 1.3 million homeless (reported by the Haiti Government in 2011).
March 11th, 2011	Tohoku (Japan) Earthquake	The event triggered a tsunami which destroyed most of the infrastructure	16 000 deaths; 4 500 people missing.

	M9.0	of the Fukushima-Daiichi nuclear power plant causing the failure of the emergency cooling system and a series of hydrogen explosions was triggered inside the reactor until four of the five power-generating blocks were destroyed and a massive radioactive fallout and extremely contaminated fluids were released into the Pacific Ocean. Additionally, extensive liquefaction was experienced in the Kanto Region and especially in the city of Urayasu, in Tokyo Bay (up to 400km far from the hypocenter location). Hundreds of buildings suffered differential and absolute settlements, and most of the networks were heavily interested by liquefaction phenomena like ground cracks, settlement and dislocation of pipes and uplift of manholes with ejecta material (Bhattacharya S. et al., 2011).	400 000 people originally living in the area of Fukushima were sheltered in provisional camps

The few but exhaustive examples of earthquake-induced disasters showed in Table 1-1, together with other recent earthquake-induced disasters and the improvement in media communication and data quality in the last decades increased in people and Governments the awareness that a so considerable number of victims is unacceptable for a modern society. Especially in case of phenomena like earthquakes, which causes, effects and spatial distribution over the globe are almost completely understood.

Despite differences among each other, all the recent events demonstrated that physical damage, deaths, and injuries are not the only consequences of Earthquakes. Long term impact on the communities and societal aspects connected to the reconstruction and the restoration of the functionality of damaged structures and infrastructures/critical infrastructures should not be neglected since this process may take years until the pre-disaster conditions are restored.

For a given Earthquake the total extent of destruction and harm depends not only on the magnitude, intensity, and duration but also on the structural design and material, the time of day that it occurs, the existence of management policies aimed at increasing the preparedness of a community to any potentially harmful consequences. Finally, the local geological and geotechnical conditions play a non-negligible role in the seismic response of a given site since they are responsible for seismic amplification and capable of triggering seismic secondary hazards. In the different possible scenarios, a non-negligible role is often played by liquefaction. An estimate on the

economic impact of around 7000 global earthquakes from 1900 to 2012 has been carried out by Daniell et al. (2012). The authors disaggregate primary (shaking) and secondary causes (tsunami, fire, landslides, liquefaction, fault rupture, and other type losses), attributing to liquefaction about 2.2% of the direct economic losses, globally estimated in 2.24 trillion US dollars, and 3.6 % when considering total losses, i.e., direct plus indirect. This relatively small fraction might wrongly diminish the relevance of this phenomenon if not considering that, when liquefaction occurs in an urbanized system like a city or an industrial district, the physical damage and prolonged impracticability of buildings and infrastructures can be devastating and undermine the recovery of normal living conditions (Macaulay et al., 2009; CSAPEISLA, 2016). During the 1906 earthquake in San Francisco, failures attributed to liquefaction occurred in many locations within a 560 km long zone along the coast, inland as far as 64 km (Youd and Hoose, 1976); the city of Kobe, Japan, underwent a prolonged economic recovery process from liquefaction-related damage at its port caused by the 1995 Hyogo-ken Nanbu earthquake; liquefaction generated a relatively modest magnitude event (Mw=6.2) in Christchurch, New Zealand, led to the loss of 15,000 single-family homes and hundreds of buildings in the Central Business District – CBD (Cubrinovski et al., 2011 b and c).

Knowing in advance the zones that could potentially be affected by liquefaction and predicting the effects on the most relevant territorial assets helps to minimize impact enabling stakeholders (urban planners, public administrators, private investors, managers of services and lifelines, emergency departments, insurance companies etc.) to undertake mitigation actions, inform the population and make communities more seismic resilient. These studies' importance is confirmed by the trend undertaken in nations more sensitive to seismic activity, where the territorial planning is subordinated to risk assessment (e.g., NZGS, 2016; DPC, 2008 and 2017).

1.3 **Risk**

The United Nations International Strategy for Disaster Reduction "*UNISDR"* (UN, 2009) defines risk as to the combination of the probability of an event and its negative consequences, in a way that emphasizes both the concept of chance, possibility (e.g., the risk of an accident) as well the potential losses, for a given cause, location and period. In its simplest way, risk can be expressed with the product of three factors that encompass the concepts:

$$Risk = Hazard \times Consequences \quad \textit{Eq. 1.1}$$

$$Risk = Hazard \times Vulnerability \times Exposure \quad \textit{Eq. 1.2}$$

Where:

- Hazard "H" quantifies the probability that an event occurs in the considered time length;
- Vulnerability "V": is the characteristic of a system to undergo damage as a consequence of the hazard;
- Exposure "E" indicates the value of the elements at risk, i.e. of all the system components that are subject to potential loss.

By looking separately at each term from which risk results, the units of risk can be determined. Hazard is defined as a probability for a given period, e.g., the annual probability of exceeding; since vulnerability represents a fraction value, it has no units and E depends on the scale of the analysis, i.e., on the nature of the considered element at risk (number of lives, monetary value..).

$$R = H \cdot V \cdot E = [P \cdot time^{-1}] \cdot [Value] = [P \cdot time^{-1} \cdot Value] \quad \textit{Eq. 1.3}$$

In the UNISDR definition, the term risk extends beyond a single measure of the impact of an event to encompass a range of "… potential disaster losses, in lives, health status, livelihoods, assets, and services, which could occur to a particular community or a society over some specified future time period". It includes indicators and metrics required to measure vulnerability and exposure as much as the need to reflect the inter-relationships between the system characteristics (or between systems) and multiple potential losses. Thus, establishing a risk measure is further complicated since it could not be meaningful in a disaster risk context. In a simple way, Risk may be related to the total economic loss induced by a given event, even if an exact characterization should also account for indirect losses and the impact on the social and cultural aspects often difficult to quantify for a community.

Despite the analytical form of Eqn. 1.2 quantifies risk from a technical viewpoint, the risk concept encompasses fundamental aspects constantly dealt by people, including an ancestral concept that has always influenced human choices. In fact, Mankind always established its settlements in places assessed strategic for the economic and political development of that society in each historical context, even

when this implied to experience severe or extreme natural phenomena (floods, earthquakes, tsunami, landslides, volcanic eruptions) capable of compromising the safety of the community. In other words, they were implicitly accepting a "risk". In the year 79 A.D., it is noticeable, one of the most famous volcanic eruptions of Mount Vesuvius, which destroyed the ancient Roman cities of Pompeii, Herculaneum and Stabiae, in the Bay of Naples (Italy). As reported by Plinius the Young, the eruption began with a high eruptive column depositing a thick air fall pumice deposit to the South East of the volcano, and the emplacement of destructive glowing avalanches followed it. Two thousand people died in Pompei's municipality, which was completely buried by ashes and discovered in 1748 by a group of explorers. At the present, more than three million people live within 20 km from a possible eruptive event (De Natale et al., INGV, 2020) due to the climate conditions and the strategic position that have encouraged the development of activities, especially agriculture, industry, commerce and tourism. The presence of three volcanoes and such a great concentration of people closely exposed to any possible eruptions makes the Neapolitan area the largest volcanic risk example in the world. This induced the Italian Government to prepare emergency plans, issued by the National Department of Civil Protection (whose first version was released in 1995), and support a constant monitoring activity through the INGV Observatory.

1.4 Background of Risk Management: the 1979 UNDRO Conference

The first need for a coded risk assessment strategy appeared in the 1970s when the International Community realized that natural phenomena were becoming so serious and impacting obstacles to the development of urban areas that much greater emphasis had to be given to pre-disaster planning and prevention. This induced many Governments to adopt pre-disaster urban planning as part of national development policies. The basic idea behind this is that the effects of natural disasters must be considered in humanitarian and social terms and economic and development, especially for those countries where rapid urbanization involves areas prone to earthquakes, floods, tsunami, fires and any other possible natural phenomena. In 1979, after years of research about the major natural hazards (phenomena) of meteorological, geological, and geophysical origins, the United Nations Disaster Relief Office

(UNDRO) conference defined risk as the expected number of lives lost, persons injured, damage to property and disruption of economic activity due to a particular natural phenomenon. Besides, the following definitions were introduced after the homogenization of the existing terminology:

- *Hazard:* is the probability of occurrence, within a specific period in a given area, of a potentially damaging natural phenomenon.
- *Vulnerability:* represents the degree of loss to a given element at risk or set of such elements resulting from the occurrence of a natural phenomenon having a given magnitude. Vulnerability is expressed on a scale from 0 (no damage) to 1 (complete damage).
- *Element at Risk:* meaning the population, buildings, and civil engineering constructions, economic activities, public services, utilities, and infrastructure present over a given area.

The UNDRO conference expressed risk associated with a given hazard as the product of specific risk (i.e., the expected degree of loss due to a natural phenomenon, a function of both hazard and vulnerability) and elements at risk. This means that in every risk assessment, i.e., independently from the hazard, two are the key parameters to be firstly declared: the former is the identification of the element or system under assessment (a building, a road or a road network, an entire city or a community..); the latter is the time horizon, which the analysis is referred. This results from the definition of hazard which is commonly referred to as a return period.

1.5 Theoretical basis of Risk Assessment

The UNDRO Committee defined steps to evaluate most thoroughly the potential loss due to a given natural hazard, emphasizing the following aspects:

- The spatial/temporal variability of natural hazards at a given site;
- The role of existing structures, whose vulnerability to a given hazard is dictated by the magnitude of that phenomenon;
- The importance of the elements (human population, dwellings, economic activities..) possibly affected which are commonly referred to as “elements at risk”;
- The estimation of the expected risk over a period of time.

The effects of natural phenomena on-site are quantified through its magnitude *(x)*, which is a variable or a set of variables. Generally, the distribution of *x* is known, being expressed through the function $\phi(x)$ which represents the joint probability of exceedance of each value of $x = (x_1, x_2, \ldots, x_n)$ within the reference period. Conversely, the functions $F(x) = 1 - \phi(x)$ or $p(x) = dF/dx$ representing respectively the probability of x_i not being exceeded or the probability density function, can be considered. On the other hand, vulnerability represents the expected degree of loss/damage on a structure, or a population induced by a given magnitude phenomenon. Formally, it can be written as $\alpha = \alpha(x)$. Thinking on a structure potentially exposed to a given natural phenomenon, the evaluation of the risk should proceed through the following steps from a theoretical viewpoint. Known the distribution of the hazard through the probability density function $p_H(x)$ or the probability of exceedance $\phi_H(x)$ and known the distribution of the mechanical properties of the structure, e.g., its strength *(S)* in terms of density function $p_S(x)$ or probability of non-exceedance $F_S(x)$, the probability of failure associated with the probability of the hazard x ranging between *x* and $x + dx$ can be written as (Figure 1-2.a):

$$df = p_H F_S dx \qquad \textit{Eq. 1.4}$$

Similarly, from Figure 1-2b the probability of failure associated with the probability of the strength x ranging between *x* and $x + dx$ is:

$$df = p_S \phi_H dx \qquad \textit{Eq. 1.5}$$

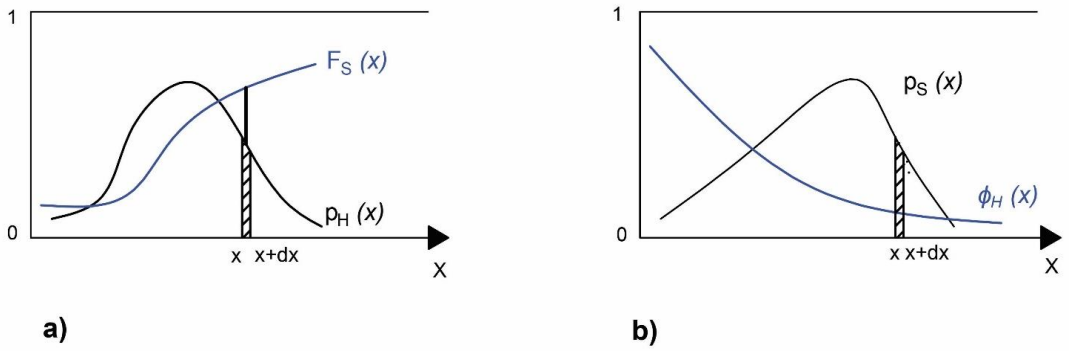

Figure 1-2 Functional forms of the hazard and structural strength probabilities: a) probability density function $p_h(x)$ and probability of non-exceedance a level of structural strength $F_S(x)$ for a given value of the magnitude x; b) probability of exceedance $\phi_H(x)$ and probability density function of a structural strength $p_s(x)$ for a given value of the magnitude x (modified after UNDRO, 1979).

Thus, the probability of failure associated to the whole distribution of x can be equivalently defined as:

$$f = \int_0^\infty p_H F_S dx = \int_0^\infty p_S \phi_H dx \qquad \textit{Eq.1.6}$$

The elementary specific risk associated with the probability of the magnitude of the event between x and $x + ds$ is:

$$\frac{dr}{(E)} = \alpha(x) F_S p_H dx = \alpha(x) \phi_H p_S dx \qquad \textit{Eq.1.7}$$

where (E) are the elements at risk. As before done, considering the whole distribution of x, the specific risk is:

$$\frac{r}{E} = \int_0^\infty \alpha(x) F_S(x) p_H(x) dx = \int_0^\infty \alpha(x) p_S(x) \phi_H(x) dx \qquad \textit{Eq.1.8}$$

In both expressions of Eqn. 1.8, the first two terms under the sign of integration depend only upon the structures, and the third one only upon the natural phenomenon. The first two terms thus define the vulnerability when considering the randomness of the properties of structures. It may be seen that this definition changes depending upon whether the hazard is introduced through its probability of exceedance or its density of probability. Although a complete solution of the problem should involve the randomness of the structures' mechanical properties and their vulnerability, the original procedure outlined by UNDRO necessitates introducing some simplifications. The first is to consider that the randomness of the strength of structures and their vulnerability is negligible concerning the variability of the hazard. This implies that the vulnerability function α (x) assumes a profile qualitatively like the one represented in Figure 1-3a.

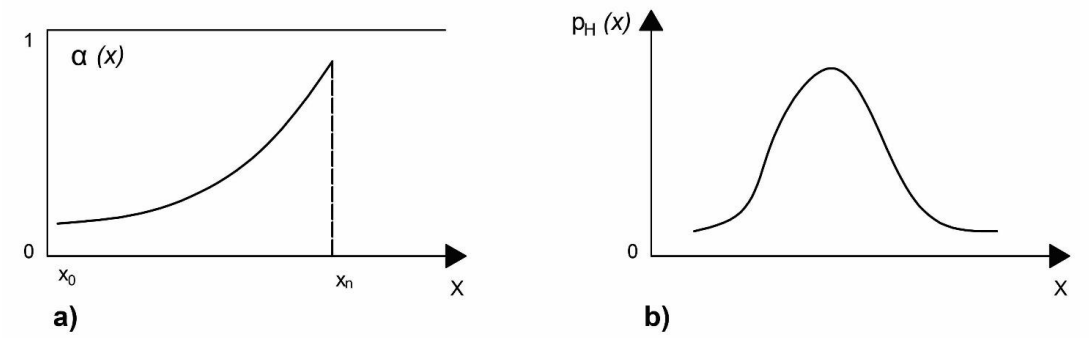

Figure 1-3 – a) Sample vulnerability function α(x) in the hypothesis of structural strength as hazard-independent variable; b) probability density function of the magnitude x $p_h(x)$ (modified after UNDRO, 1979)

From the combination of the hazard probability function and vulnerability profile, the elementary specific risk respectively due to the probability of the magnitude x lying between x and x + dx and for the whole range of magnitudes are:

$$\frac{dr}{(E)} = \alpha(x) p_H dx \qquad \textit{Eq.1.9}$$

$$\frac{r}{E} = \int_0^\infty \alpha(x) p_H(x) dx \qquad \textit{Eq.1.10}$$

Accounting to the particular values of α for $x < x_0$ or $x > x_1$

$$\frac{r}{E} = \int_0^\infty \alpha(x) p_H(x) dx = \int_{x_0}^{x_n} \alpha(x) p_H(x) dx + \phi_H(x_1) \qquad \textit{Eq.1.11}$$

A further simplification is to replace the curve α(x) by a step function (Figure 1-4). It may be seen that in this case the expression of the specific risk takes the form:

$$\frac{r}{E} = \sum_j \Delta_j \alpha \cdot \phi_j \qquad \textit{Eq.1.12}$$

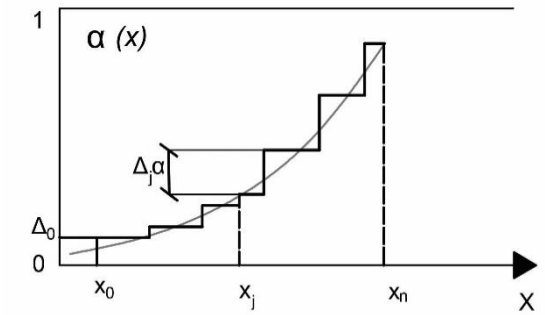

Figure 1-4 – Simplification of vulnerability curve through step function (modified after UNDRO, 1979).

For a selected hazard, the probability of exceedance ϕj is generally tabulated, or it is supposed to be preliminarily characterized. This led that designers could take advantage of this framework since they had only to compute the $\Delta \alpha j$ from the table of the values of α like the one displayed in Figure 1-4 and perform the summation above.

1.6 Development of Risk Framework and Change in Paradigm: from the UNDRO Program to the Global Risk Assessment Framework

The UNDRO Conference work laid the foundations for the development of the International Framework of Action for the International Decade for Natural Disaster Reduction (IDNDR), beginning on 1 January 1990, whose main goal was to reduce life loss, property damage, social and economic disruption caused by "natural disasters", especially in developing countries. As part of the IDNDR decade, the 1994 Yokohama Strategy for a Safer World marked a shift in the political and analytical context within which disaster reduction was being considered, since great importance was attributed to socioeconomic vulnerability, emphasizing the crucial role of human actions in reducing the vulnerability of societies to natural hazards. Furthermore, the Yokohama Strategy identified challenges and gaps in five main areas: governance; risk identification, assessment, monitoring and early warning; knowledge management and education; reducing underlying risk factors; preparedness for effective response and recovery. These shreds of evidence formed the basis to the institution of the Hyogo Framework for Action 2005–2015 aimed at Building the Resilience of Nations and Communities to Disasters, encouraging International cooperation and development of

regional strategies, and the creation of global and regional platforms for disaster risk reduction (DRR). In general, being resilient for a community means assuming proactive behavior, ready to survive disasters, and maintain economic competitiveness. In other words, the question is to move beyond a just protective posture to an attitude that withstands crisis and deflect attacks. This behavior implies for the community to be aware of risks, vulnerabilities, and the current capabilities to deal with them, to make informed tactical and strategic decisions promptly. A comprehensive assessment of risks that correctly estimate losses addressing the distribution over the territory of hazard, vulnerability, and exposure becomes fundamental. It assists the stakeholders' decision-making (city planners, governmental institutions, emergency agencies, insurance companies, private investors, and citizens) who need to control their "portfolio" of properties, undertake appropriate mitigation actions, and optimize the budget allocation.

Member States adopted a series of principles to support the Hyogo Framework program: they became aware of their primary role in preventing and reduce disaster risk and therefore empowered local authorities and facilitated the cooperation among private and public sectors, but no effective holistic strategies were enterprise to face disaster risk. Consequently, hazard exposure in both low- and high-income countries increased faster than vulnerability decreased, meaning that new risks were being generated faster than existing reduced. Despite at the end of the period Member States realized that efforts had not led to reduced physical losses and economic impacts, the Hyogo Framework is considered a milestone in disaster risk reduction because it catalyzed national and local attention to the pursuit of disaster risk reduction by introducing a change in the strategies. In fact, the new paradigm shifted from protecting social and economic development against external shocks to plan growth and development to manage risks in a holistic manner meaning the establishment of multidisciplinary approaches to promote sustainable economic and social growth, protecting health environmental conditions, and strengthening resilience and stability. This conclusion formed the basis for the development of the 2015-2030 Sendai Framework and the subsequently increased emphasis on addressing the underlying drivers of risk, preventing the creation of new risk, reducing the existing stock of risk, and strengthening the resilience of nations and communities through integrated and inclusive economic, structural, legal, social, health, cultural, educational, environmental, technological, political and institutional measures that prevent and reduce hazard exposure and vulnerability to disaster, increase preparedness for response and recovery, and thus strengthen resilience.

The Sendai Framework promotes a strengthening in community resilience, through multi-risk disaster management. Such a goal has become a priority for the 180 member States which joined this challenge promoting new policies supported by financial plans with guided investments. In fact, the strengthening of disaster risk governance is a necessary element for the development of prevention, mitigation, and risk management activities and international cooperation to contribute to the development of knowledge at all levels, particularly for developing countries. Starting with the Hyogo Action Framework, the Sendai Disaster Risk Reduction goal is also recognized as a prevention tool for containing future losses and an effective investment in sustainable development. Looking forward, reduction, management, and knowledge of risks represent ten of the seventeen objectives among the 2030 Agenda for Sustainable Development that adopts an integrated vision of the social, economic, and environmental dimension. The substantial reduction of disaster risk and losses in lives, livelihoods, and health and the economic, physical, social, cultural and environmental assets of persons, businesses, communities, and countries is designated as the outcome of the framework (Figure 1-5).

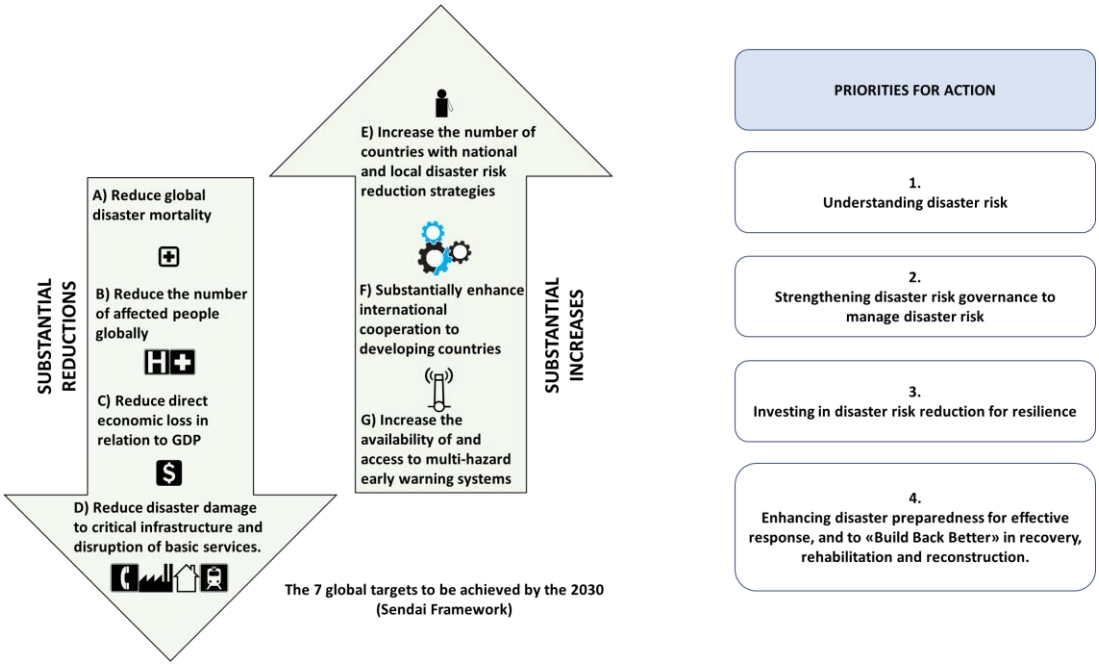

Figure 1-5 – Objective of the SENDAI Framework and priorities for action (UNISDR, 2015).

1.7 Systemic risk and primary risk

In the first decade of the 21st century, our society realized that the Earth is one system, a system of systems. Conversely to the complicated system that can be disassembled and seen as the sum of its parts (e.g., a car), a complex system shows properties arising from the interaction among its constituent elements (like a road/pipe network or a traffic jam). This dualism is also reflected in the definition of risk. Thinking on complex systems, the introduction of the systemic risk concept is required: it refers to the risk of an entire system rather than individual parts' failure. On a large scale, systemic risks can induce great instability and uncontrollability that highlighted a growing need to understand better and manage uncertainties and mobilize people, innovation and finance. The concept of systemic risk captures the risk of a cascading failure in the financial sector. Because of the interlinkages in the financial system, the default of a Bank may result in a severe economic downturn involving other companies and investors. Similarly, this example can be referred to many natural disasters that are cascade effects of others. For example, extreme rainfalls or earthquakes can cause floods or landslides, respectively. In those cases, the risk assessment begins by estimating the primary hazards, such as extreme rainfalls or earthquakes, identifying the exposure, and assessing their vulnerability, i.e., hydrological floodplain vulnerability or slope stability. These elements calculate the primary risk, which becomes the secondary hazard by looking at the built environment risk perspective. In fact, these phenomena cause damages to buildings and infrastructures, which are the exposure of the secondary hazard. The vulnerability of buildings and infrastructures is the measure of potential physical damage caused by a specific hazard with a given intensity. The risk of physical damage to built assets is a secondary or cascade risk. Buildings and infrastructures are not the last rings of the chain, including service delivery and end with the community. It is possible to state that the assessment of hazard, vulnerability, exposure, and risk varies on a case-by-case basis depending on the system's definition: what is risk in a case becomes hazard at a higher level. At the highest analysis levels, elements at risk are interdependent and form a complex system. Risk assessment with quantitative methods is inefficient and different metrics to estimate each element's vulnerability must be used. The potential impacts caused by a hazard to a complex system are economic, social, environmental, and cultural: they produce both direct (immediate effect) and indirect (medium-long

term effect, as a consequence of the direct impacts) losses, assessed in monetary or non-monetary terms (Mechler, 2005).

1.8 Looking Forward

The evolution in the conceptual and practical framework of risk assessment observed over the years is depicted in Figure 1-6. It shifted from the traditional hazard-based approach delineated by the UNDRO activities to an integrated one culminated with the development of the Global Risk Assessment Framework. To fully achieve the Sendai Framework's challenge and its multi-hazard management in disaster risks and development at all levels strategies through cooperation among all sectors, major renovations of risk assessment approaches and analysis are needed. This became more marked in the last two decades when many other types of risks of the greatest consequences for humankind have been created and recognized (e.g., the 2008 financial crisis highlighted the dramatic consequences of bank risk, or the cyber risks, etc.). Understanding the systemic nature of risks, instead of treating only the most largely experienced without an explicit account of the interdependencies between risks, will be the first half of the twenty-first century's central challenge. As a part of this challenge, the United Nations Office for Disaster Risk Reduction (UNDRR) and experts established a process to co-design and developed a Global Risk Assessment Framework (GRAF) to inform stakeholders and decision making, and to change the people approach specifically concerning systemic risks. One of the main outcomes will be to support national and subnational governments in recognizing new patterns of vulnerability and risk, monitoring the progress in risk reduction, for to the UN Plans for Prevention and Resilience Framework, and the Sendai, 2015 and the more general 2030 Agenda.

The Global Risk Assessment Framework encompasses multiple issues concerning systemic vulnerabilities of agricultural systems or the resilience of electricity generation and distribution systems in hurricane-prone locations, or business continuity planning for public and private sector actors for basic service delivery in rapidly growing metropolitan areas. GRAF's goal is to improve the understanding and management of current and future risks at all spatial and temporal scales. It aims to manage uncertainties better and mobilize people, innovation, and finance by fostering interdisciplinary systems thinking and identifying anomalies and precursor signals. It

seeks to reveal the interlinkages, relationships, correlations, and dependencies of multiple risks and actors across systems to build a shared understanding and enable decision-makers to act. Further topics covered in the GRAF concern critical systems such as human health, the balance of natural ecosystems, and economic development.

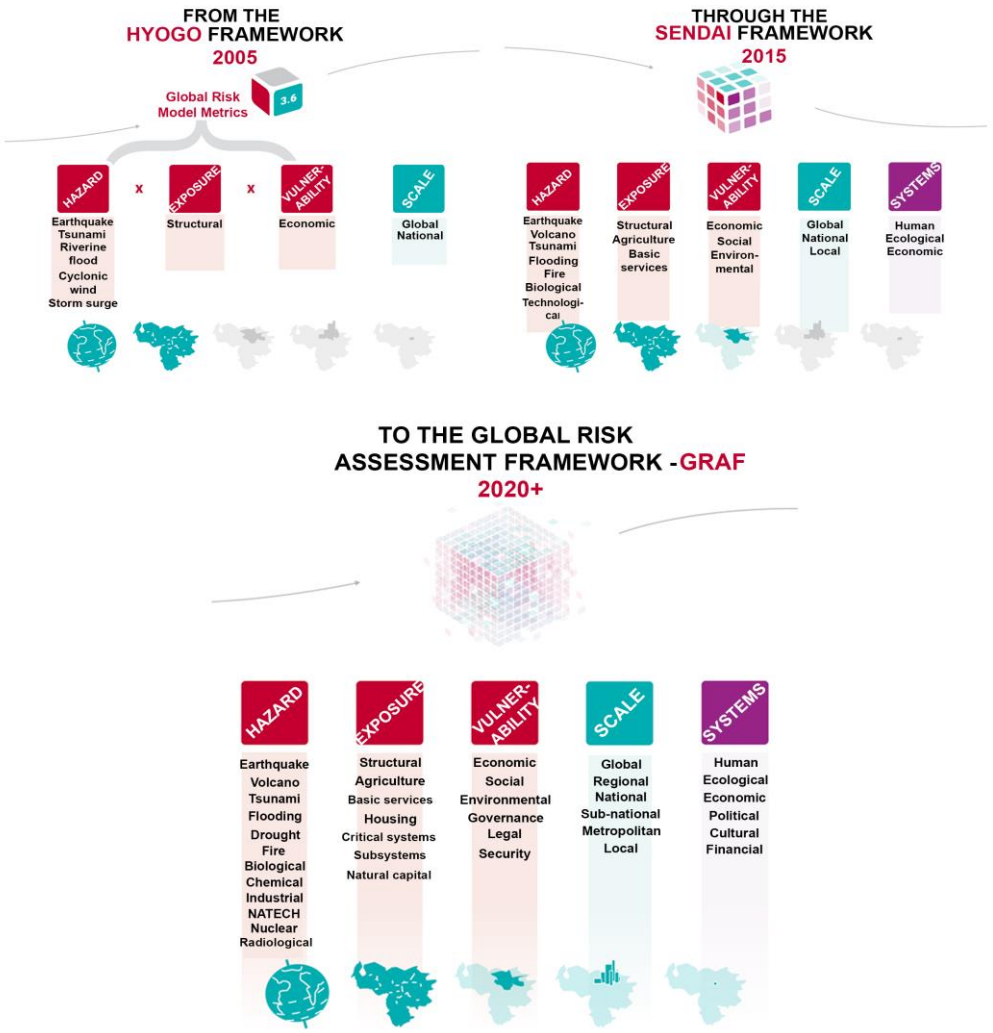

Figure 1-6 – Shift in the paradigm of Risk Assessment: from the 2005 Hyogo Framework, through the 2015 Sendai Framework to the Global Risk Assessment Framework.

Chapter 2. SEISMIC RISK ASSESSMENT

2.1 Abstract

While the more scientific field of earthquake engineering deals with the physical mechanisms induced by earthquakes, i.e., spectral-dependent ground motion, local site amplification, structural response, the more recent field of seismic risk assessment addresses which consequences this respective seismic ground motion may cause to a particular site, both for what concerns the built environment, building and infrastructure assets, or human factors related with the community. In this respect, seismic hazard becomes just one key component of any assessment. To estimate the risk to a certain region, in terms of expected damages and losses, three integral components must be quantified, namely seismic hazard, vulnerability (of buildings, infrastructure facilities, and population), and exposure of these assets in terms of their inventory and spatial distribution over the respective study area. In this chapter, the basic concepts forming the seismic risk assessment are reported to provide an overview of the methodology, the most known existing software and to underline the stakeholders' role.

2.2 **Introduction**

Proven that liquefaction of prone subsoil deposits occurs due to a strong seismic event (say M>5.5), before introducing any liquefaction risk assessment procedure, the definition of seismic risk and how it is assessed cannot be ignored. The unpredictable nature and the severe, widespread impact that they induced on the communities make Earthquakes one of the most lethal among natural disasters, resulting in an average of 27 000 deaths a year since 1990, 35 200 in the 2008-2017 decade (CRED, 2019). In 2018 Earthquakes have been the deadliest type of disaster, responsible for 45% of the total deaths, followed by flooding at 24%, which affected the highest number of people (50% of the total). The distribution of deaths and injured people due to earthquake disasters varies worldwide, depending on urbanization, economic development, and vulnerability of human-made constructions. To understand risk factors that expose a population to loss of life or major injuries has become the primary challenge to develop adequate awareness of seismic risk and put in place an effective preparedness or prevention plan.

In the definition given by United Nations Disaster Relief Office (UNDRO, 1979), the seismic risk for a selected area can be quantified as the expected number of lives lost, persons injured, damage to property, and disruption of economic activity due to Earthquakes which may affect the study area over a period. Thinking of the formal definition of Eq. 1.2:

Seismic Hazard (UNDRO, 1979) refers to the occurrence probability, for a given system in a specific time length, of a certain potentially damaging earthquake scenario. In practical situations, a seismic risk assessment procedure requires to define the probability P(r) that a given ground motion parameter will be exceeded in a period of (T) years.

Vulnerability is the possibility that a certain level of damage in structures/infrastructure, potential human and/or financial loss occur in the assessed area due to the selected hazard. The link between predefined intensity measures, which represent the magnitude of the phenomenon, and the expected damage is generally provided by fragility/vulnerability curves. These functions show in probabilistic terms the relationship between the level of an earthquake and the level of the expected damage/loss of either one of the previously mentioned entities. Thinking on buildings, lognormal fragility curves are commonly used: they allow to evaluate the probability that predefined structural and nonstructural damage states are reached for given

median estimates of seismic Intensity Measures, representing a building Engineering Demand Parameter "EDP". Fragility curves consider the variability and uncertainty associated with capacity curve properties, damage states, and ground shaking. The Hazus (FEMA, 1999) fragility curves distribute damage among Slight, Moderate, Extensive, and Complete damage states. For any given value of the spectral response, discrete damage-state probabilities are calculated as the difference of the cumulative probabilities of reaching, or exceeding, successive damage states. A building's probabilities reaching or exceeding the various damage levels at a given response level sum to 100%. Those functions can be constructed based on the observed damages experienced in past seismic events (Del Gaudio et al., 2019) and the non-linear structural analyses (Fotopoulou et al., 2018). In the past, the empirical approach was largely adopted worldwide, even if it is not the most accurate and complete since the database of damage observations may not include all the possible cases.

Lastly, the element at risk term is a quantification of the entities in the assessed area. This includes the people and buildings, the number and type of important infrastructures, and industrial and commercial activities. Based on previous European-project experiences like RISK-UE (https://cordis.europa.eu/), an exhaustive exposure model should emphasize the following aspects:

- Population density repartition;
- Main institutional actors and decision-makers;
- Presence of public buildings;
- Utility systems: Water, Sanitation, Electricity, Gas, Liquid fuel, Radio, Telecommunication, Transportation: Roadways, Railways, Harbours, Airports, …
- Essential facilities: Critical facilities (dangerous plants or industries); Strategic constructions in terms of crisis management (hospitals, fire, etc.); Main economic issues or facilities in terms of employment, production, trade, and services (industrial plants, trade centers, main services, etc.).
- Cultural and historical heritage.

2.3 **Stakeholders**

Focusing on earthquakes, the UNDRO guidelines preliminary identified Earth Scientists/Earthquake Engineers and Government authorities as main actors of the

process. The former were asked to catalogue existing earthquakes data, starting from preliminary studies on regional/continental scale also called “macrozonation” (which concerns the regional tectonic activity) up to the development of more detailed maps aimed to measure soil effects, reflecting local site conditions, estimate building acceleration in earthquakes and define relevant parameters to assess structural performance, i.e., “microzonation”. This huge activity primarily aimed to disseminate an adequate and interdisciplinary understanding of earthquakes’ effects and promote cooperation among experts and regulatory authorities to update national codes for earthquake – resistant building design currently. Besides, governments had to follow a protocol to understand the exposure (i.e., evaluate the presence of high-importance buildings, utilities, critical infrastructures) and define the acceptable risk since they were also responsible for implementing emergency plans for post-Earthquake disaster relief. Therefore, significant emphasis was given to the monitoring activities through the Institution of scientific organizations.

Such unprecedented activity carried out by the UNDRO Committee represented a preliminary and partial characterization of the seismic risk assessment since it was pursued mainly from a governmental viewpoint. Over the years, the society realized that earthquake is a multi-facet problem involving multiple actors (stakeholders), and therefore seismic risk mitigation became a multidisciplinary issue. The main categories of subjects interested in such risk assessment are listed below:

- Urban and territory planners
- Owner/manager of lifelines /services
- Emergency planners
- Investors/Owners of building assets
- Insurance Companies
- Designers

Each category has a different specific interest, summarized by the question reported in Table 2-1. Very often, interests are interconnected, and answers to multiple questions can be found in risk assessment. For instance, the assessment of building safety and performance in seismic conditions allows the owner to evaluate the possibility of investing money in the structural strengthening (or in the payment of an insurance rate) and an insurance company to fix the insurance premium. On the other hand, after a benefit/cost analysis, a structural engineer can address the design to minimize the seismic-induced annual loss or balance the estimated total loss and the cost of construction.

Table 2-1 End users of risk assessment

Stakeholder	Question
Urban and territory planners	Quantify hazard over the territory to plan the define land use, plan urban/industrial development, ultimately motivating people to abandon risky area
Owner/manager of lifelines/services	Estimate economic losses and increase the reliability of lifelines
Emergency planners	Increase awareness of risk among the population. Identify safe areas and verify their connectivity with the outer communication lines under catastrophic events
Investors/Owners of building assets	Determine seismic performance of their portfolio of buildings
Insurance Companies: estimate losses	Estimate losses to fix the premium of the insurance
Designers	Assess safety and serviceability of buildings or infrastructures and design remediation

2.4 **Uncertainty**

Although remarkable progress has been achieved in last decades to develop frameworks that support decision making for earthquake risk mitigation, prioritization of available options, pursuit of reliability and economy (e.g., Ellingwood 2001; FEMA/NIBS 2003; Crowley et al. 2005; Baker and Cornell 2008; Goda and Hong, 2008), some non-negligible uncertainties remain in the process.

Firstly, the knowledge of seismic phenomena unavoidably involves several uncertainties that make the assessment less reliable. The determination of ground motion and its occurrence probability, the role of subsoil, the fragility of building and infrastructure, and the quantification of values (e.g., Crowley et al. 2005; Kwona and Elnashai 2006; Goda and Hong 2008) all incorporate a noticeable degree of indeterminacy deriving from the quality, or even validity, scarcity and variability of the underlying data (Walley, 1991) and from the simplification necessarily introduced with models. The above uncertainty factors can be broadly categorized into:

- Aleatory, representative of unknowns that differ each time an experiment is run. Uncertainty comes from the impossibility of precisely knowing all the inputs of a phenomenon that are thus dealt statistically.

- Epistemic, also defined as systematic, due to things one could in principle know but doesn't in practice. This may arise from inaccuracy of measurement, an approximation of models that neglect certain effects, or some deliberately neglected data.

Epistemic uncertainty can be visualized with the concept of precision and accuracy in experimental measurement; even with an ideally perfect simulation of the phenomenology, randomness (aleatory uncertainty) of the input data due to imprecise knowledge leads to imprecise predictions; the most precise knowledge of input information may lead to inaccurate prediction due to approximate modeling (Figure 2-1).

One of the major challenges for seismic risk analysts is the estimate of uncertainty associated with earthquakes. Here the two above categories of uncertainty are combined. The current prediction of earthquake magnitude in a specific site is based on the statistical inference of historical data. Randomness is thus implicit in this prediction, being typically managed with the adoption of probabilistic models. However, one should admit that human experience is insufficient to predict all possible seismic scenarios and surprises must unavoidably be admitted beyond the expected range of situations. Although occurring in acknowledged seismic regions, the earthquakes of February 22nd, 2011 in Christchurch (New Zealand), March 11th, 2011 in Tohoku Oki (Japan), and May 21st, 2012 in Emilia Romagna (Italy) had some level of unpredictability. This highlights the limitation of our current methodologies based on the inference of statistical data and the necessity of introducing extrapolation functions or relaxing axioms of classical probability (e.g., total sum of the event probabilities equals one).

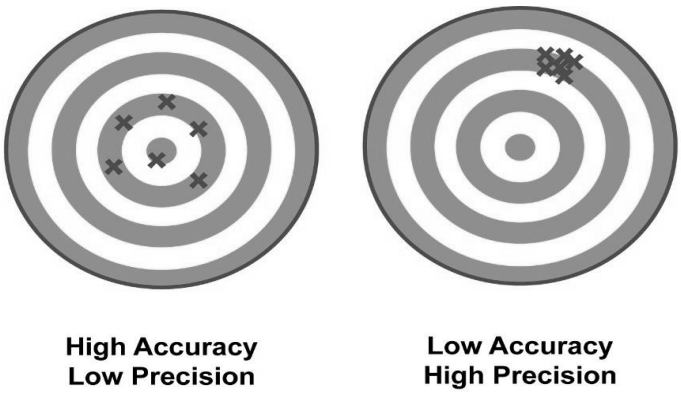

Figure 2-1 - Precision and accuracy.

Aleatory and epistemic uncertainties also affect the subsoil characterization, where noticeable effort must be produced to balance completeness and accuracy with a relatively limited amount of information. The usually low number of investigations implies that geotechnical models, i.e., stratigraphic conditions and constitutive models, are built introducing simplistic and generally conservative assumptions. Additionally, engineers are perfectly aware that, even with a great amount of information, the scattering of experimental results from laboratory or site tests is much larger for soils than for artificial construction materials.

Owing to unavoidable uncertainties and complexities of seismic risk and known that risk assessment is just a component of the management process (IEC/FDIS 31010:2009), non-physical factors, beyond characteristics of engineering materials and systems, like perception (e.g., expert versus public), criteria (individual versus societal, or voluntary versus involuntary), political process, and risk communication should not be neglected (Tesfamariam & Goda, 2013). In fact, due to these aspects and/or subjective consideration, objective risk assessment results may be disputed and, on occasion, overruled.

Notwithstanding the above situation, it is important to develop quantitative decision support tools for earthquake risk mitigation. Such tools are useful for quantifying/comparing seismic risks for different options and facilitating informed decision-making. Reducing uncertainties within tolerable levels and evaluating reliability of conclusions is of paramount importance for a successful risk assessment and must be thus continuously considered as the reference goal along the whole process.

2.5 **Qualitative vs quantitative risk assessment**

Risk assessment can be performed with quantitative or qualitative analyses depending on the problems under concern and the available knowledge. In fact, the choice of a quantitative or qualitative method depends on the availability of a metric for evaluating hazards and the level of analysis needed to make a confident decision.

Qualitative assessment is based on judgment and expert opinion to estimate proxies of risk and consequences. '. . . a man cannot, in general, tell what will happen, but his conception of nature of things, the nature of the men and their institutions and affairs, and the non-human would enable him to form a judgment as to whether any suggested thing can happen' (Zadeh, 1965). Qualitative methods offer analyses without detailed

information, are carried out with intuitive and subjective processes and may result in different outcomes/conclusions depending on those who use them. Albeit suspected of leading to subjective conclusions, they offer the possibility of considering factors hardly quantifiable, like those connected with human behavior, and sometimes lead to an adequate assessment of risk. An overview of the theories to transform qualitative into quantitative assessment (e.g., imprecise interval probability, possibility, and evidence theories) is provided by Tesfamariam & Goda (2013).

By contrast, quantitative analyses rely on probabilistic/statistical methods and databases that quantify the probability and consequent values. Quantitative analyses generally provide a more objective and unanimously acknowledged understanding. Still their efficacy relies fundamentally on the quality of available information, i.e., numerosity and accuracy of data, representing various possible situations.

When possible, a quantitative approach must be preferred to be more objective and examine the system in greater detail, but an integration with qualitative analyses should be considered. A combination is appropriate to sum the advantage of both approaches, becomes fundamental when not all factors can be parametrized.

2.6 **Risk perception and acceptance**

Unavoidably any decision based on risk assessment must end with tolerating some risk. Perception of the consequences is thus fundamental, and sometimes critical, for decision-making and risk management including recognizing and assessing risk and developing mitigation strategies. Risk acceptability depends on several factors, including the phenomenon (if controllable or not), the type and nature of consequences, short- and long-term effects, the gained benefits, the preparedness for natural hazards, and the influence of individual and total risk. The above questions are tightly connected with risk communication, i.e., those activities aiming at increasing the public's knowledge and awareness. Participation of the public (stakeholders) in the management of risk and policymaking is fundamental to promoting holistic strategies as decisions cannot be made by technical experts and public officials. Risk communication implies a continuous interaction among parties – risk experts, policymakers, and stakeholders.

As technical guidance to what risk level society is willing to accept, F-N curves can be used. For a given hazard, the F-N curves relate the annual probability of causing a number N of fatalities (F) to the number of fatalities, N. The term "N" on the x-axis of

the graph can be replaced by another quantitative measure of consequences, such as costs. An example of F-N curve is reported in Figure 2-2.a, defining four areas. Acceptable and unacceptable risk respectively refer to the level of risk requiring no further actions, being the level of risk which a society desires to achieve, and to the level requiring a mandatory reduction. As lower as reasonably practicable ALARP region represents situations where risk countermeasures should be evaluated and undertaken if assessed as advantageous. Lastly, in the area identified as "scrutiny" more detailed studies are required.

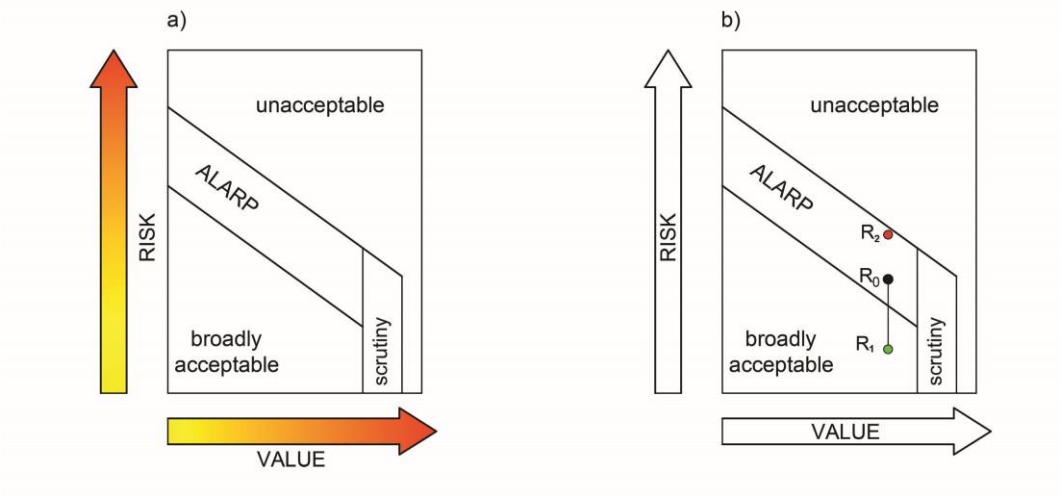

Figure 2-2 – Example of F – N curve (a) and Residual risk evaluation in the ALARP area (b) (modified after Nadim, 2009).

Once the pre mitigation risk R_0 has been evaluated through Equation 1.2, as shown in Figure 2-2.b, a benefit/cost analysis is required to evaluate the suitability of mitigation. In general terms, it may include a reduction of the hazard (active mitigation), a reduction of vulnerability (passive mitigation), or both the options (active and passive mitigation). Independently from the type, supposing a mitigation cost equal to U_d, the residual risk R'_d can be calculated:

$$R'_d = H'_a \times V'_p \times E'_{ap} + U_d \qquad \textit{Eq.2.1}$$

Where: *H', V'* and *E'* represent respectively the new terms of Hazard, Vulnerability, and Exposure after the mitigation. Starting from the same risk level R_0, a convenient situation is characterized by $R'_d = R_1 < R'_0$ and represented by the green point of Figure 2-2.b. This assumption justifies the adoption of countermeasures. On the other hand,

if $R'_d = R_2 > R'_0$ a situation of non-economic convenience is outlined. Even if the countermeasures effective reduce the hazard or vulnerability, their cost led to a residual risk greater than the pre-mitigation.

2.7 **Procedures and Software**

While the more scientific field of earthquake engineering deals with the physical mechanisms induced by earthquakes, i.e., spectral-dependent ground motion, local site amplification, structural response, the more recent field of seismic risk assessment addresses which consequences this respective seismic ground motion may cause to a particular site, both for what concerns the built environment, building and infrastructure assets, or human factors related with the community. In this respect, the seismic hazard establishes one key component of any assessment. To assess the risk to a certain region, in terms of expected damages and losses, three integral components must be quantified (Figure 2-3):

- hazard providing information on the seismic ground motion level and, in case of a probabilistic risk assessment, the ground motion's probability of occurrence;
- vulnerability (damageability) of buildings, infrastructure facilities, and population;
- exposure of these assets in terms of their inventory and spatial distribution over the respective study area.

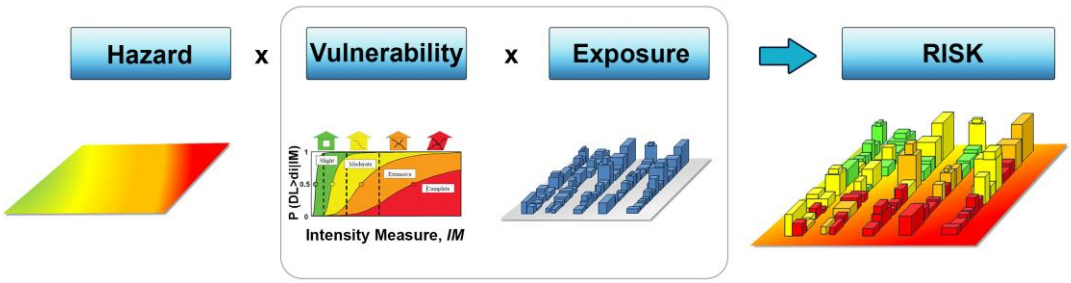

Figure 2-3 - Components of seismic risk assessment.

Software packages exist, some of which publicly available, enabling a complete assessment of the seismic risk based on a modular structure. The components of

earthquake loss estimation adopted by HAZUS (FEMA, 2003) are depicted in the flow chart of Figure 2-4. From the operative viewpoint, the methodology implemented in HAZUS is articulated as follows:

- Selection of scenario earthquakes and Probabilistic Earth Science Hazard "PESH" inputs;
- Selection of appropriate methods (modules) to meet different user needs;
- Collection of required inventory data, i.e., how to obtain necessary information;
- Costs associated with inventory collection and methodology implementation;
- Presentation of results including appropriate terminology, etc.;
- Interpretation of results, including consideration of model/data uncertainty.

Authors point out that one of the main differences in the types of risk assessment procedures consists of the time, effort and level of expertise needed to carry out analyses, that obviously turn out in a different detail and reliability of the analysis. Considering this issue, the software permits to run analyses with different level of complexity:

- Default Data Analysis requiring minimum effort by the user, input obtained by government agencies or published information, providing crude output as initial loss estimates to determine where more detailed analyses are warranted.
- User-Supplied Data Analysis requires more extensive inventory data and effort and expertise by the user to provide the best estimates of earthquake damage/loss with standardized methods of analysis.
- Advanced Data and Models Analysis incorporating results from engineering and economic studies carried out with external methods and software, requiring a high level of expertise with extensive participation by local utilities and owners of special facilities.

A similar approach is defined in SELENA, a software for SEismic Loss EstimatioN using a logic tree Approach, produced by NORSAR (https://www.norsar.no/). The structure of this software is depicted in Figure 2-5; SELENA allows for three analysis types that differ in the way the seismic input is considered: (1) deterministic analysis; (2) probabilistic analysis; and (3) real-time ground motion data. In general, spectral ordinates of seismic ground motion at different reference periods have to be provided for each geographical unit (i.e., census tract) to allow the construction of design spectra following a selectable seismic code provision. Once the seismic ground motion in each geographic unit is defined, the computation of physical damage to the building stock

is computed by applying one of the selectable Capacity Spectrum-based methods. Based upon the damage estimates, total economic losses related to these damages and the number of casualties, i.e., the number of injured people and fatalities, is conducted. Additional loss outputs are shelter demands (temporary housing) as well as debris estimates. Damage results are given in terms of cumulative probabilities of being in or exceeding one particular state following the classification scheme given by HAZUS-MH into none, Slight, Moderate, Extensive, and Complete damage.

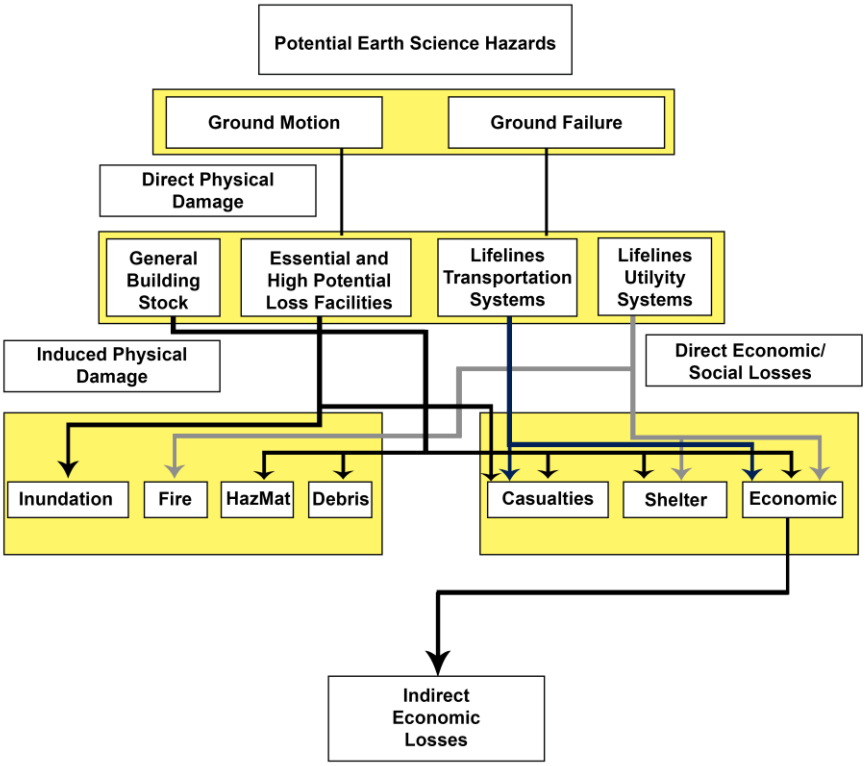

Figure 2-4 Hazus (Fema, 2003) flowchart for Earthquake Loss Estimation "ELE".

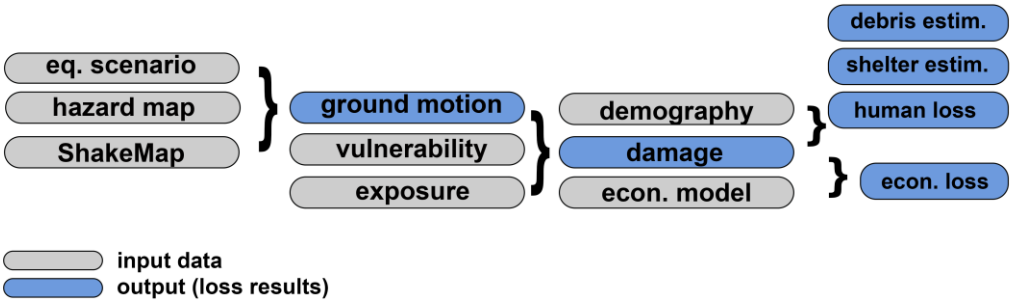

Figure 2-5 Risk assessment methodology defined in SELENA (NORSAR, 2003).

2.8 **Deterministic vs Probabilistic Assessment**

A common method of estimating the seismic performance of a system is based on the performance of Deterministic Seismic Hazard Analyses, "DSHA". Following this approach, strong ground motion involves assigning a Maximum Credible Earthquake to a specific fault. Once location (e.g., epicenter) and magnitude of the scenario earthquake are defined, an appropriate scenario earthquake location can be defined, for instance, from a database of seismic sources (faults) or specifying an event based on a database of historical earthquake epicenters. A specific attenuation relationship is then assumed to determine the PGA at the project site based on the geographic location of the study region and the type of fault. For example, Hazus code (FEMA, 2003) assumes (1) strike-slip (SS) faults, (2) reverse-slip (R) faults, (3) normal (N) faults (4) Interface (IF) events and (5) Interslab (IS) events.

The amplification of ground shaking to account for local site conditions is usually based on site classes and soil amplification factors. The 1997 NEHRP Provisions (FEMA, 1992) define a standardized site geology classification scheme and specify soil amplification factors for most site classes based, in part, on the average shear wave velocity of the upper 30 meters of the local site geology.

This procedure can be carried out for all seismic sources that contribute significantly to the ground motions at a site. Uncertainty in the resulting ground motion estimates can be assessed by incorporating the standard deviations in both seismicity rates and attenuation relationships. The advantage of this approach is that both the intensity of ground shaking (PGA) and the duration of the motions, as related to the earthquake magnitude, are known. The primary disadvantages of this approach include: (1) the PGA values do not necessarily reflect the cumulative, or aggregate, hazard in the region, and (2) assessing the influence of uncertainties in factors such as earthquake magnitude or source-to-site distance on the resulting PGA are accounted for by performing additional parametric studies of each variable.

In this way, only the largest reasonably possible earthquake associated with a source is accounted for. The recurrence interval of this Maximum Credible Earthquake and the temporal aspect of the seismic hazard are not specified (Dickenson, 2005). Deterministic analyses can accommodate seismicity rates associated with individual sources by incorporating the exposure interval of interest (e.g., 500 or 1000 years) and

estimating the magnitude of the event having this return period. This seismic hazard analysis method was common up through 1970's, and many practitioners continue to regard deterministic PGA analyses as independent of exposure interval. In contemporary practice, deterministic analyses are rarely performed without indirect accounting for the exposure time of interest.

The combination of DSHA to both a coded vulnerability taxonomy of buildings (e.g., EMS – 1998) and ad-hoc exposure models (e.g., Fardis, 1999; EPANTYK – 2009) allows quantifying for each seismic scenario the expected building damage rate, i.e., the one with the highest probability (Giovinazzi and Lagomarsino, 2004).

Even if open to improvements (Giannaraki et al., 2018), this method's application at urban scale represents an expeditious tool to estimate the impact of future earthquakes providing useful indications to the stakeholders involved in Rapid Risk Assessment (RRA). At a subnational scale, it can address the identification of the portion of building stock that needs to be strengthened; in conjunction with adequate loss models, it enables to evaluate the socio-economic impact and convenience of mitigation or the possibility of stipulating insurance policies.

Alternatively, seismic risk can be assessed based on Probabilistic Seismic Hazard Analyses (PSHA), i.e., after a probabilistic approach that combines all sources' contributions in a cumulative estimate of the ground motion parameter of interest. Probability distributions of key variables such as rupture location along a fault, location of random sources, seismicity rates, and ground motion estimates from attenuation relationships can be incorporated into one seismic hazard analysis. Other uncertainties such as the likelihood of activity along mapped faults, direction of fault rupture propagation, and predominant faulting style can be incorporated into the evaluation (e.g., Kramer 1996, Vick 2002, McGuire 2004). A primary advantage of probabilistic seismic hazard analysis is that by assigning locations and seismicity rates to all sources, the ground motion parameter of interest expected at a specific site can be determined along with its probability distribution, which is useful for illustrating uncertainty in the ground motion variable. Repeating the analysis for multiple locations, specified as grid points, throughout a region allows for the creation of contour maps of the ground motion parameters for specified exposure intervals. These maps have been referred to as "uniform" or "aggregate" hazard maps as all sources' contributions have been incorporated into a single ground motion value.

Once the Probabilistic Seismic Hazard Analysis has been completed, ground motion maps can be obtained for any specified exposure interval. This information forms the input of risk assessment. For a generic system with its lifecycle, risks of any

nature can be computed writing the following integral that convolutes the probability of demand p(D) (Hazard) and the consequent losses connected to the demand P(L|D) (Vulnerability):

$$P(L) = \int_D P(L|D) * p(D) \qquad \textit{Eq. 2.2}$$

The application of Equation to the assessment of liquefaction risk should separately disclose and quantify the uncertainties on:

- potentially critical scenarios
- models describing the response of the system
- quantification of relevant parameters
- risk evaluation

For seismic risk, Eq. 2.2 can be expressed by applying the performance-based earthquake engineering (PBEE) cascade methodology defined by the Pacific Earthquake Engineering Research (PEER) Center (Cornell and Krawinkler, 2000) and depicted in Figure 2-6.

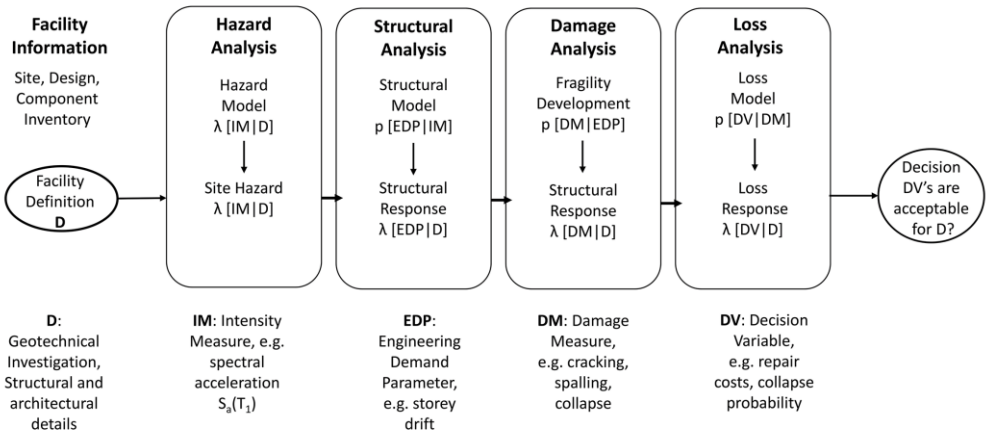

Figure 2-6 - Probabilistic definition of risk assessment (Cornell and Krawinkler, 2000).

Equation 2.2 is transformed as follows where the function p(D) is exploded considering the different factors defining the cascade phenomenon:

$$P(L) = \int_{IM} \int_{EDP} \int_{DM} P(VD|DM) * p(DM|EDP) * p(EDP|IM) * p(IM) \quad \textit{Eq. 2.3}$$

p(IM) is the probability that a seismic event of intensity measure IM occurs during the lifecycles of the system, p(EDP|IM) is the density probability of the engineering demand parameter (EDP) for the given IM, p(DM|EDP) is the probability that physical damage occurs on the structural component of the system for a given EDP and P(VD|DM) is a cumulative probability of the assumed evaluator of the system performance for a given damage DM (Lee and Mosalam 2006; Moehle 2003; Porter 2003; Comerio 2005; Krawinkler 2005; Mitrani-Reiser et al. 2006).

Chapter 3. PREDICTION OF LIQUEFACTION EFFECTS

3.1 Abstract

Liquefaction is a seismic phenomenon affecting loose, saturated, and cohesionless soils (such as sands and rarely gravels) in areas where a significative seismic hazard exists. Traditionally, expeditious simplified methods are used to determine the liquefaction potential by verifying the predisposing factors and then introducing a given seismic scenario. Despite most of the existing literature focused on liquefaction-induced surficial manifestations, i.e., all the liquefaction-induced phenomena (sand boils/ejecta, minor and extensive cracking, post-liquefaction 1D settlement) affecting ground in free field conditions, many studies have been carried out in recent years to quantify the shear-induced effects due to the presence of structures and the soil-structure interaction. After a mechanical characterization of the phenomenon, the most popular procedures to assess the liquefaction severity in free field conditions and buildings' presence are summarized in the following paragraphs.

3.2 **The phenomenon**

The term liquefaction was originally coined by Mogami and Kumo (1953) and then used in to indicate the manifestations of a complex phenomenon affecting loose, saturated, and cohesionless soils under seismic conditions. One of the most popular classification (Kramer, 1996) groups the liquefaction-related phenomena in two categories: flow liquefaction and cyclic mobility.

Flow liquefaction can occur when the shear stress required for the static equilibrium (of the soil mass) is greater than the shear stress of the soil in its liquefied state. Once triggered, the large deformations produced by flow liquefaction are driven by the static shear stress. The cyclic stress may bring the soil to un unstable state at which its strength drops sufficiently to allow the static stress to determine flow failure. Flow liquefaction is characterized by a sudden nature of the origin, the velocity of their development and the distance interested by such instability. In contrast, cyclic mobility occurs when the shear stress required for the static equilibrium is smaller than the shear stress of the soil in its liquefied state (e.g., gently slopes). In this case, the deformation produced by cyclic mobility develops incrementally under the seismic load, driven by both cyclic and static shear stresses, causing lateral spreading, which is defined as the horizontal displacement of a soil layer riding on liquefied soil either down a gentle slope or toward a free face like a river channel (Youd, 2018). In this case, when the underlying soil layer liquefies, the non-liquefied upper soil crust continues moving down until it reaches a new equilibrium position.

Level ground liquefaction represents a special case of cyclic mobility, characterized by the absence of the static shear stress capable of producing lateral deformation. Therefore, what happens during an earthquake is a chaotic movement of soil particles known as ground oscillation. From a mechanical viewpoint, Figure 3-1 illustrates the development of the liquefaction ground phenomenon. During strong earthquakes, say having a Richter magnitude greater than 5.5 (which reflects both the laboratory tests of Seed et al. (1975) relating the equivalent number of cycles to the earthquake magnitude, and the empirical observations of Ambraseyes (1988) that correlated the epicentral distance to the earthquake magnitude for sites where liquefaction happened and did not) and a PGA≥0.15g (NTC, 2018), a rapid increase in the porewater pressure is generated in such susceptible layers causing an upward flowing porewater. This mechanism may carry sand particles up to the ground surface,

where they are deposited in a generally conical pile called a sand boil. As a result, ground surface subsidence due to the soil particles' densification can be observed after the earthquake (Figure 3-1a).

Although flow liquefaction can lead to more dramatic consequences, cyclic mobility and level ground liquefaction can occur under many field situations. They are responsible for: subsurface soil liquefaction, which may determine low-moderate liquefaction-induced surficial damage, significant soil deformations, both horizontal (cracking) and vertical (settlements) capable of provoking severe damage to a variety of structures and infrastructures (Figure 3-1b) and lateral spreading, which will be more detailed described regarding the case studies.

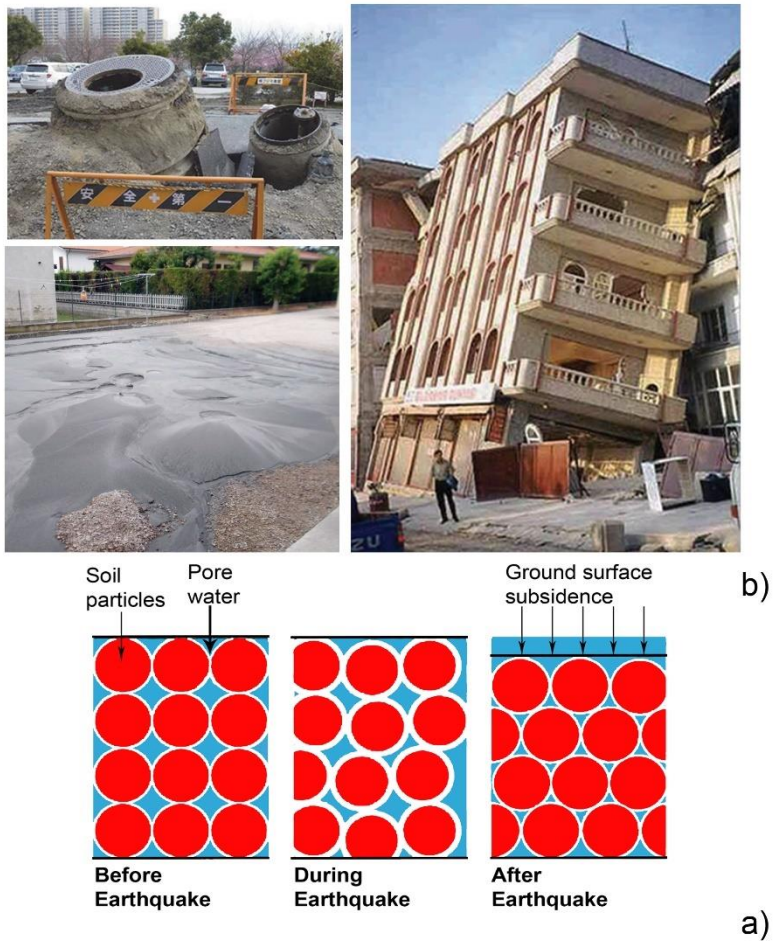

Figure 3-1 a) Development of the liquefaction process; b) examples of liquefaction-induced effects on soil, buildings, and water supply.

Considering the nature of the phenomenon, the estimation of liquefaction ground severity, which represents a risk equivalently if looking at the soil and a hazard for structure/infrastructure, implies several analyses to be carried out in a sequence. The first step is to estimate the susceptibility of subsoil to liquefaction on both the geological, i.e., estimating the tendency of geological formation to undergo liquefaction and geotechnical levels requiring that detailed soil profiles are analyzed. Then, the tendency of developing liquefaction under a given seismic input is determined through the triggering analysis. The last step implies evaluating the effects at the ground level; at this stage, indicators are adopted to broadly quantify the severity of liquefaction in free field conditions, neglecting the presence of buildings or infrastructures and their possible interaction with the subsoil.

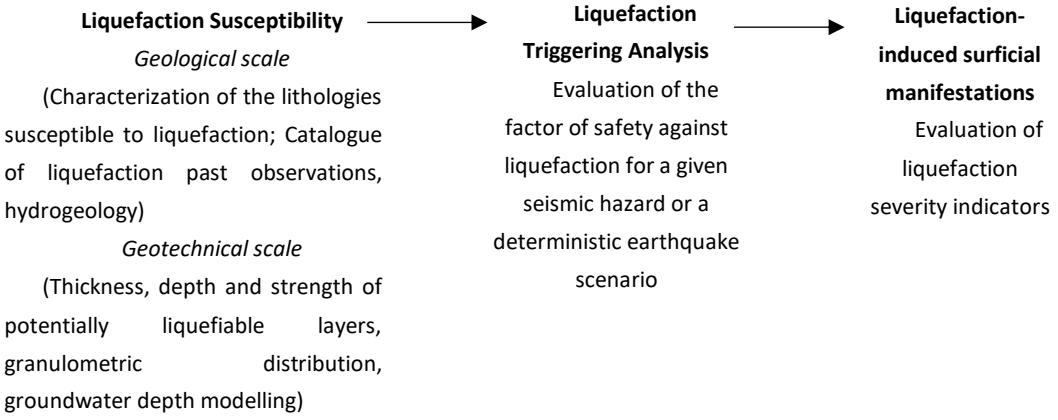

Figure 3-2 Flowchart of liquefaction hazard analysis (modified after Bird et al., 2006).

3.3 **Susceptibility**

The evaluation of liquefaction susceptibility represents a preparatory step of any liquefaction analyses, addressed to evaluate the physical properness of a soil to liquefy without introducing a specific seismic scenario, and therefore, it does not imply the occurrence of liquefaction, being the phenomenon dictated by the seismicity of the area. This step is normally accomplished by looking at the geological level, i.e., characterizing larger potions of territory and collecting available historical and geological data. In fact, past studies (Galli and Meloni, 1993) and ground post-earthquakes ground observations like the M_w 6.1 Emilia – Romagna (Italy) 2012, have

shown that liquefaction-induced phenomena are not randomly localized but are tightly related to the geology of the territory. In fact, since liquefaction recurrently happens at the same locations, the initial step for liquefaction susceptibility evaluation involves large-scale studies aimed at describing the geological/geomorphological conditions of a region or subregion as well as collecting the liquefaction observations following the historical earthquakes of the study area. Examples of historical liquefaction phenomena can be found in the catalogues developed by UNIPV (D2.4 Liquefact, 2019) and Galli (2000), which respectively collected all the recorded liquefaction manifestations after European and Italian historical earthquakes. The former includes approximately a thousand liquefaction manifestations mostly located in the Mediterranean area and ascribable to earthquakes of moderate magnitude (i.e., whose Mw ranges from 6 to 6.5).

Looking at the geological scale, the qualitative subsoil classification introduced by Youd and Perkins (1978) can be applied to the analysis of the selected area. Moving from the analysis of Geology, Hydrogeology, and Geomorphology, this criterion emphasizes the depositional environment and age of the deposit, observing that liquefaction susceptibility is rather high for Holocene or more recent (e.g., artificial) deposits, low or very low for Pleistocene or older ones (Figure 3-1). Since it is ascertained that the liquefaction resistance increases with the soil aging (Schmertman, 1991), a first issue consists in verifying the existence of Holocene (or more recent) loose deposits, which are considered very prone to liquefy Youd & Perkins, 1978). To this aim, geomorphological and surface geological Maps should be considered since they describe the geomorphology of the area, highlighting the presence of sandy and silty lithologies and relevant geomorphological elements such as rivers, meanders, levees/paleo-levees, and paleochannels. On the other hand, information about the land use, thickness of human-made deposits and the existing survey maps may help understand the urban development of the study area and reconstruct the subsoil profiles. For the European territory, a map of the potentially liquefiable lithologies shows a wide and heterogeneous distribution of liquefaction susceptibility over the continent, which characterizes the Iberian Peninsula, Italy, Balkan region, Greece, Turkey, and part of the Baltic area.

Table 3-1 Liquefaction susceptibility of sedimentary deposits (Youd and Perkins, 1978).

Type of Deposit	General Distribution of Cohesionless Sediments in Deposits	Likelihood that Cohesionless Sediments when Saturated would be Susceptible to Liquefaction (by Age of Deposit)			
		< 500 yr Modern	Holocene < 11 ka	Pleistocene 11 ka - 2 Ma	Pre-Pleistocene > 2 Ma
(a) Continental Deposits					
River channel	Locally variable	Very High	High	Low	Very Low
Flood plain	Locally variable	High	Moderate	Low	Very Low
Alluvial fan and plain	Widespread	Moderate	Low	Low	Very Low
Marine terraces and plains	Widespread	---	Low	Very Low	Very Low
Delta and fan-delta	Widespread	High	Moderate	Low	Very Low
Lacustrine and playa	Variable	High	Moderate	Low	Very Low
Colluvium	Variable	High	Moderate	Low	Very Low
Talus	Widespread	Low	Low	Very Low	Very Low
Dunes	Widespread	High	Moderate	Low	Very Low
Loess	Variable	High	High	High	Unknown
Glacial till	Variable	Low	Low	Very Low	Very Low
Tuff	Rare	Low	Low	Very Low	Very Low
Tephra	Widespread	High	High	?	?
Residual soils	Rare	Low	Low	Very Low	Very Low
Sebka	Locally variable	High	Moderate	Low	Very Low
(b) Coastal Zone					
Delta	Widespread	Very High	High	Low	Very Low
Esturine	Locally variable	High	Moderate	Low	Very Low
Beach					
High Wave Energy	Widespread	Moderate	Low	Very Low	Very Low
Low Wave Energy	Widespread	High	Moderate	Low	Very Low
Lagoonal	Locally variable	High	Moderate	Low	Very Low
Fore shore	Locally variable	High	Moderate	Low	Very Low
(c) Artificial					
Uncompacted Fill	Variable	Very High	---	---	---
Compacted Fill	Variable	Low	---	---	---

When the liquefaction susceptibility is ascertained by the presence of geological and geomorphological features of the area (like the ones listed in Table 3-1), more refined investigations at a more detailed scale allow determining the co-existence of paramount factors influencing the properness to the liquefaction phenomenon (i.e., grain size distribution, plasticity, and water level) as well as to build a 3D stratigraphic model. In this case, quantitative criteria are required to identify areas prone to local instability.

Considering the particle size analysis, soils with greater than 50% of their constituents passing the #200 sieve (i.e., fine-grained soils with grain sizes smaller

than 0.075 millimetres) were once considered non-liquefiable. Based on data provided in Wang (1979), Seed and Idriss (1982) proposed criteria for assessing the susceptibility of fine-grained soils to liquefaction, commonly referred to as the "Chinese criteria". These criteria are a function of percent clay (less than 15% by weight of particles < 0.005 mm), liquid limit (LL < 35%), and with an in-situ water content greater than 0.9 multiplied by the LL. Subsequent studies on the cyclic response of fine-grained soils following more recent earthquakes (e.g., Seed et al., 2003; Bray et al., 2004a, b; Bray and Sancio, 2006), indicated that the percentage of clay was less important than was the plasticity index (PI) of the soil. Also, they found that the ratio wc/LL was more important than was the LL alone in assessing the liquefaction susceptibility of fine-grained soils. Furthermore, the characteristics of the soil's cyclic behaviour and whether the soil's strength and compressibility were more aligned with clay than sand were identified as being important in evaluating the potential for ground failure of fine-grained soil deposits during earthquakes (Boulanger and Idriss, 2006). On the other hand, in the absence of more detailed laboratory or in-situ data, PI alone of the fine-grained soil was judged by Boulanger and Idriss (2006, 2008) to be a suitable proxy for determining whether the soil behaved as "clay-like" or "sand-like."

In the latter circumstance, the assessment of liquefaction potential over large areas implies the realization of geological and geotechnical models aimed at identifying source layers for liquefaction and the definition of zones having homogeneous stratigraphy to evaluate the local site effects on ground motion. A geotechnical model must be defined based on topography (DEM, DTM), monitoring activities (piezometers, wells), in-situ geotechnical (e.g., Boreholes, Standard Penetration Tests "SPT", Cone Penetration Tests "CPT") and geophysical investigations (Spectral Analysis of Surface Waves "SASW", Multichannel Analysis of Surface Waves "MASW", Cross-hole, Down-Hole, Micro-tremors…) and laboratory tests. Looking at the municipality level, when an adequate number of different in-situ tests exists, expeditious quantitative criteria to evaluate the liquefaction susceptibility based on the definition of the thickness and depth of saturated, sandy layers, which are assessed as potentially liquefiable, can be applied. One of them has been proposed by the University of Ferrara (2014) and the Group for the seismic microzonation of S. Agostino (FE), which developed a matrix of liquefaction susceptibility levels based on the size and position of the potentially liquefiable layer which can be evaluated from boreholes (and CPTs), which resulting susceptibility levels are summarized in Table 3-2.

Table 3-2 Punctual level of liquefaction susceptibility ("CMS"- University of Ferrara, 2014).

Crust Thickness (m)	Thickness of liquefiable layer (m)	Susceptibility level
< 5	> 0.4	L1
5-10	>1	L2
10-15	>2	L3
15-20	≥2	L4
≥ 20	0	N

Although CPTs cannot provide accurate predictions of soil type based on physical characteristics, such as, grain size distribution, they provide a measure of the soil mechanical properties (strength, stiffness, compressibility). Among the wide range of applications of CPT profiles, Robertson and Wride (1998) proposed a criterion that combines the measured tip resistance and sleeve friction to the in-situ tensional state, providing a repeatable index of the aggregate soil behaviour. Hence, the prediction of soil type based on CPT is referred to as Soil Behaviour Type (SBT), obtained through the index Ic defined by Robertson (1990). The main steps of the iterative procedure to evaluate the Soil Behaviour Type index from a CPT profile are summarized in Figure 3-3.

According to the classification proposed by Robertson and showed in Table 3-3, soils susceptible to liquefaction belong to classes 5 or 6, i.e., having an Ic greater than 1.31. Additionally, Robertson and Wride (1998) propose a default cut-off of the soil behaviour type index (Ic) equal to 2.60, which represents the approximate boundary between soil behaviour types 4 and 5. Beyond this value, the soil can be assumed as non-liquefiable (i.e., not susceptible to liquefaction), being both fine-grained and plastic. Although this cut-off criterion is generally accepted, it is also acknowledged that soils with Ic > 2.6 may undergo liquefaction under certain circumstances (Lai et al., 2020).

Robertson and Wride (1998) define a procedure to obtain the Ic profile relating the tip resistance and the sleeve friction to the in-situ tensional state. Accounting for the groundwater level, the non-liquefiable crust thickness, and the cumulative thickness of the potentially liquefiable layers can be evaluated exclusively depending on the lithology (Figure 3-3). In both the cases, the non-liquefiable crust thickness is evaluated according to Ishihara (1985), i.e., it is assumed equal to the depth of the first

liquefiable sandy layer (if there is a surficial cohesive soil) or equal to ground water depth if it is located within the sand deposits.

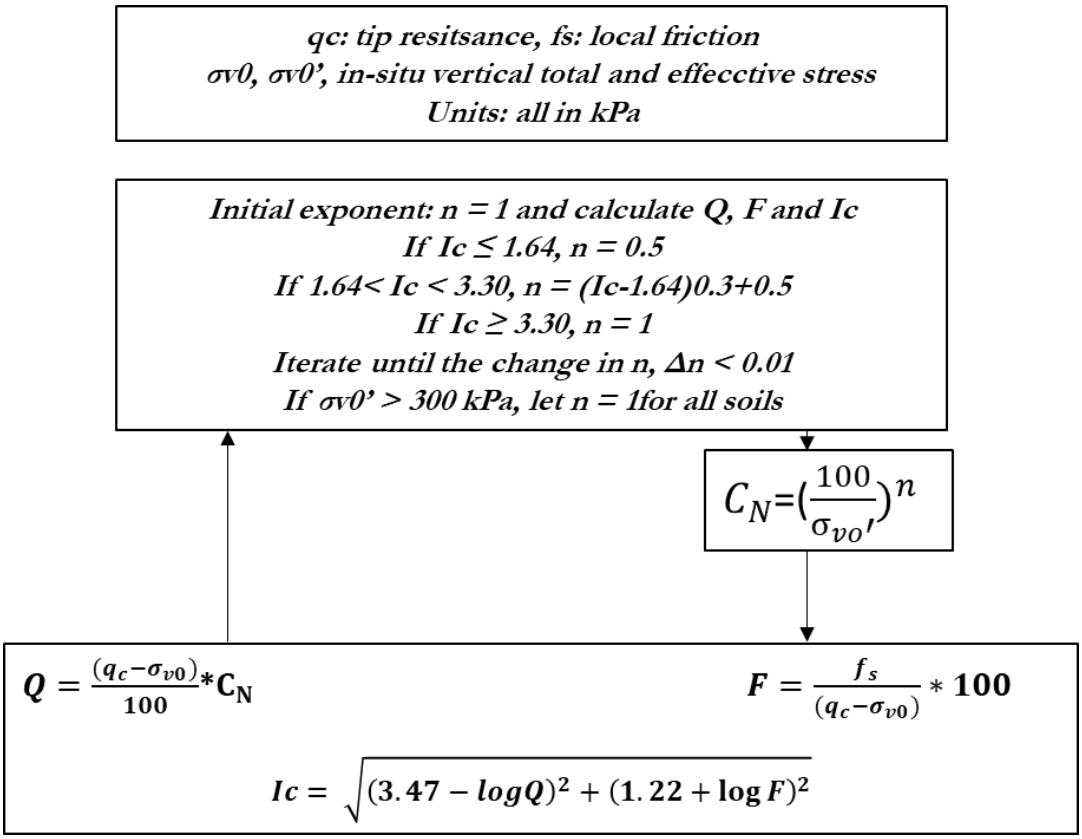

Figure 3-3 Schematic flowchart to evaluate the Soil Behaviour Type index (Robertson, 1998).

Accounting also for the groundwater level, the non-liquefiable crust thickness and the cumulative thickness of the potentially liquefiable layers (i.e., as the summation of all the layers belonging to Robertson SBT class 5 and 6) can be evaluated exclusively depending on the lithology. On the other hand, one of the major disadvantages of these "qualitative" criteria is that they do not account for the soil's strength, i.e., of their liquefaction resistance, since they do not consider several of the involved actors (grain sizes distribution and fine content, soil relative density Dr, the effect of soil aging..). In this sense, they only represent a preliminary rough indication of liquefaction susceptibility in terms of cumulative thickness of potentially liquefiable layers.

A new semi-automated procedure to derive an equivalent three strata model from a CPTu profile is proposed by Millen et al. (2020) after a series of studies that analyze the performance of different parameters used to define the strength of a potentially liquefiable layer. The criterion introduced by Millen et al. (2020) and briefly

summarized in Figure 3-5 schematizes a real subsoil profile to an equivalent three-layers model, the Equivalent Soil Profile ESP, identified by a thickness of crust and liquefiable layer and a mean Cyclic Resistance Ratio.

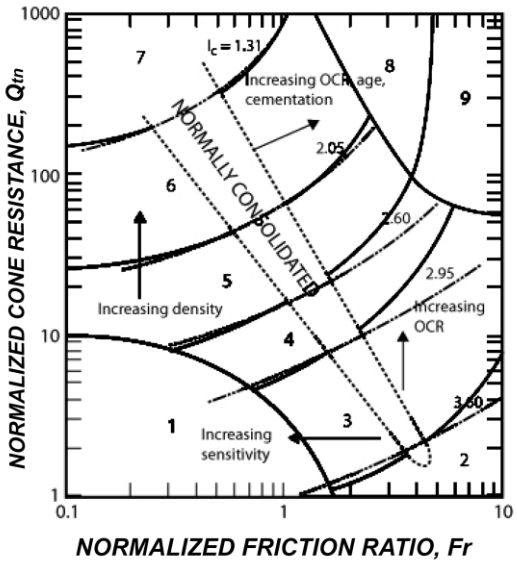

Figure 3-4 Normalized CPT Soil Behavior Type (SBTn) chart, Qt – F; (Robertson, 1990).

Table 3-3 Soil behaviour type index ranges and inferred soil types (Robertson & Wride 1998).

Zone	***Soil Behaviour Type***	***Ic***
1	*Sensitive, fine grained*	N/A
2	*Organic soils – clay*	> 3.6
3	*Clays – silty clay to clay*	2.95 – 3.6
4	*Silt mixtures – clayey silt to silty clay*	2.60 – 2.95
5	*Sand mixtures – silty sand to sandy silt*	2.05 – 2.6
6	*Sands – clean sand to silty sand*	1.31 – 2.05
7	*Gravelly sand to dense sand*	< 1.31
8	*Very stiff sand to clayey sand*	N/A
9	*Very stiff, fine grained*	N/A

The assimilation criterion, described in Figure 3-5, defines 22 equivalent soil classes, finding the best combination of H_crust, H_liq, and CRR that give the lowest value of the normed error showed in Equation 3.1. Such parameter will be used in future analyses to discriminate the profiles that can or cannot schematized with three-layers models.

$$\tilde{\delta} = \frac{\sum\left(CRR_{calc,i} - CRR_{fitted,i}\right) \cdot \Delta H}{CRR_{nonliq} \cdot H_{total}} \qquad \textit{Eq. 3.1}$$

Where $CRR_{calc,i}$ and $CRR_{fitted,i}$ are the real value of CRR at each dept and the CRR fitted to the potentially liquefiable layer by the automated procedure; *Htotal* is the total depth of the subsoil profile, and ΔH is the calculation step. CRR_{nonliq} is fixed equal to 0.6. The normed error (Eqn. 3.1.) is sensitive to the choice of CRR limit value set for the non-liquefiable soil and the maximum depth of the profile. The authors set the CRR limit equal to 0.6, taking the common value suggested in simplified procedures (e.g., Youd et al., 2001; Boulanger and Idriss, 2014). Higher values imply that soil layers with higher CRR would generate some error during fitting (Gerace, 2018). The maximum depth was taken as 20 meters, since the surficial consequences of liquefaction below such depths are considered negligible (Maurer et al., 2015).

The authors pointed out that the fitting of soil profiles with a three layers ESP model that gives errors lower than 0.05 is considered as optimal; if the error is contained in the range 0.05-0.15 the fitting is considered acceptable; if the error is larger than 0.15 the fitting with the three layers model is not applicable, and engineering judgment is required.

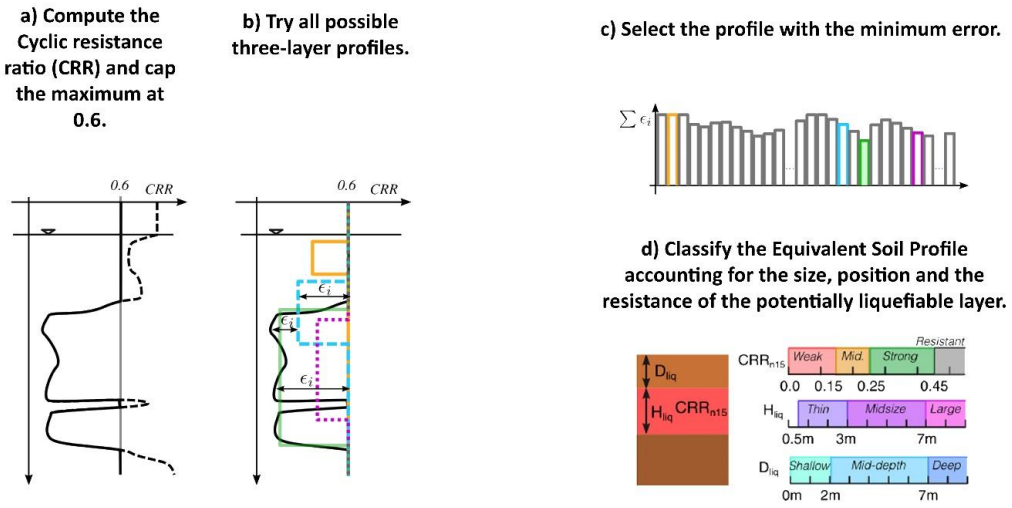

Figure 3-5 Scheme of the procedure to implement the CRR-fitted method and equivalent soil profile classification criteria.

3.4 **Triggering Analysis**

The existence of a liquefaction susceptibility does not automatically mean that liquefaction will occur during a future earthquake scenario. Therefore, liquefaction triggering analysis relating in-situ soil density and cyclic shear stress induced by ground shaking is required to verify such an opportunity. The most popular method to evaluate the liquefaction triggering implies the calculation of a liquefaction safety factor (FSL), obtained by dividing the cyclic stress ratio τ/σ'_v producing liquefaction (CRR) with the one induced by the earthquake (CSR). Following this approach, liquefaction is triggered at a given depth if FS_L is found less than 1.

$$FS_L(z) = \frac{CRR(z)}{CSR(z)} \qquad \textit{Eq. 3.2}$$

3.4.1 Cyclic Stress Ratio

A simplified method to estimate the CSR profile was developed by Seed and Idriss (1971) based on the maximum ground surface acceleration (a_{max}) at the site.

$$CSR_{M=7.5}\,(z) = 0.65 * \left(\frac{a_{max}}{\mathrm{g}}\right) * \left(\frac{\sigma_{\mathrm{vo(z)}}}{\sigma_{\mathrm{vo(z)}'}}\right) * r_d(z) \qquad \textit{Eq. 3.3}$$

Where:

σ_{v0}, σ_{v0}' = vertical total and effective stress at depth z, a_{max}/g = maximum horizontal acceleration (as a fraction of gravity) at the ground surface, and r_d is the shear stress reduction factor that accounts for the dynamic response of the soil profile.

The cyclic stress ratio required to initiate liquefaction (i.e., the liquefaction resistance, CRR) decreases with an increasing number of loading cycles; therefore, the seismic loading must be associated with a number of loading cycles. Earthquake magnitude is used as a proxy for the number of loading cycles because the duration of shaking and the associated number of loading cycles correlate with earthquake magnitude. The CSR is adjusted using a magnitude scaling factor (MSF) to compute an equivalent CSR for a reference M = 7.5.

$$CSR_{M=7.5}\,(z) = CSR_{M=m}\,(z) * \frac{1}{MSF} = 0.65 * \left(\frac{a_{max}}{g}\right) * \left(\frac{\sigma vo(z)}{\sigma vo(z)'}\right) * r_d(z) * \frac{1}{MSF} \qquad \textit{Eq. 3.4}$$

The magnitude scaling factor (MSF) accounts for duration effects (i.e., number and relative amplitudes of loading cycles) on liquefaction triggering. Several formulations (Andrus and Stokoe, 1997; Idriss and Boulanger, 2008) have been proposed to evaluate the Magnitude Scaling Factor, after the first developed by Seed and Idriss (1982), see Figure 3-6.

For instance, the MSF for sands used by Boulanger and Idriss (2014) was developed by Idriss (1999), who derived the following relationship:

$$MSF = 6.9 \cdot \exp\left(\frac{-M}{4}\right) - 0.058 \leq 1.8 \qquad \textit{Eq. 3.5}$$

The depth-dependent shear stress reduction coefficient, r_d, accounts for the nonrigid response of the soil deposit (characterized in the small strain regime by the shear wave velocity "Vs" profile at the site) and for the characteristics of the earthquake waves traveling through the soil. Seed and Idriss (1971) initially proposed a relationship between r_d and depth developed from a limited number of dynamic response analyses for a range of generic site conditions. Using additional site response analyses, Idriss (1999) modified the Seed and Idriss (1971) r_d relationship, also introducing the magnitude. The Idriss (1999) relationship is used to develop the triggering relationships of Idriss & Boulanger (2008) and Boulanger & Idriss (2014).

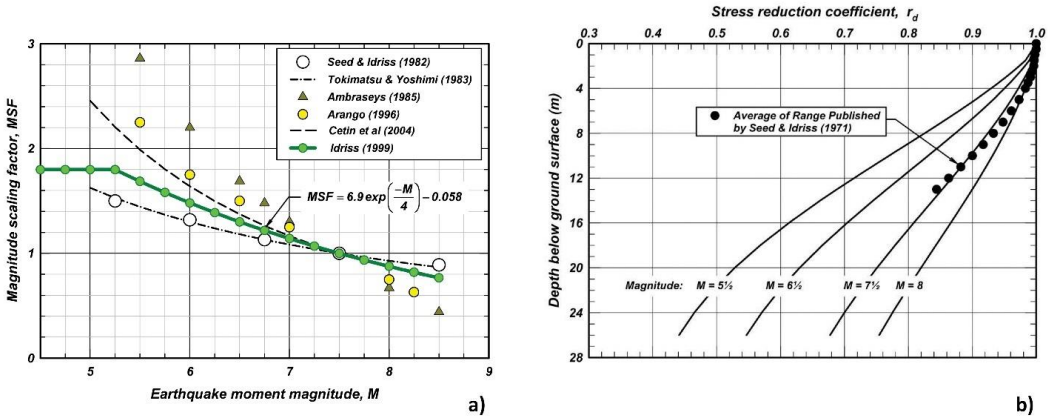

Figure 3-6: a) Magnitude scaling factor (MSF) relationships; b) Shear stress reduction factor, rd, relationships (Boulanger and Idriss, 2014).

After parametric site response analyses, Idriss (1999) concluded that the shear stress reduction coefficient, r_d, can be calculated using two functions of the depth, z, within the soil profile, namely α(z) and β(z), and the earthquake magnitude, M.

$$r_d = \exp\left[\alpha(z) + \beta(z) \cdot M\right] \quad \textit{Eq. 3.6}$$

$$\alpha(z) = -1.012 - 1.126 \sin\left(\frac{z}{11.73} + 5.133\right) \quad \textit{Eq. 3.7a}$$

$$\beta(z) = 0.106 + 0.118 \sin\left(\frac{z}{11.28} + 5.142\right) \quad \textit{Eq. 3.7b}$$

The 0.65 factor found in Eqn. 3.4 was originally proposed to relate the number of loading cycles from an irregular earthquake loading to the number of loading cycles from uniform cyclic loading. Although this value is somewhat arbitrary and was unnecessary once MSFs were introduced, 0.65 is still the standard due to historical precedent. CSR evaluation requires estimates of PGA, M_w, and r_d; since the required PGA is at the ground surface, it must account for the effects of the near-surface soil conditions on the ground shaking.

3.4.2 Cyclic Resistance Ratio

Empirical procedures were proposed to evaluate the CRR based on geotechnical and geophysical in-situ tests (CPT, SPT, and Vs profile). Among these, Robertson (1998), Idriss and Boulanger (2008) Boulanger and Idriss (2010; 2014) provide empirical formulations of the Cyclic Resistance Ratio based on the survey of liquefaction and the results of the most common in-situ tests (CPT and SPT), while Andrus and Stokoe (2000) and Kayen et al. (2013) propose methods to evaluate the CRR from Vs profiles.

In general terms, the calculation of the CRR requires geotechnical and geophysical in-situ tests (the measurement of the profile of SPT blow count, CPT tip resistance and sleeve friction, Vs profiles) as a function of depth and at multiple locations across the site. Then, correction factors are applied; for instance, to the measured SPT blow count, a first correction factor is required to define a stress- and energy-corrected SPT resistance $(N_1)_{60}$ based on the test setup. Furthermore, SPT blow counts recorded in hollow stem auger borings below the water table are particularly susceptible to error

due to soil disturbance. They may result in abnormally low blow count values. The SPT provides measurements at widely spaced intervals (often 1.5 m, but never less than the length of the split spoon sampler, 0.45 m), limiting the ability to use SPT measurements to identify thinner layers or detailed variations within a soil profile. On the contrary, the CPT provides continuous measurements along with a profile, representing a mighty mean to characterize thinner layers and detailed variations within strata. Pore-pressure data from piezocone penetration testing (CPTu) can provide additional information, both qualitative (e.g., whether the soil is dilatant or not) and quantitative (e.g., the steady-state porewater pressure). Depending on the measurement method, Vs may be used to identify thin layers and variations within strata, even if it has not the detail and the resolution of the CPT. A rigorous soil type characterization is required to perform liquefaction triggering analyses. Rigorously, since CPT and Vs methods do not provide a direct measure of soil type, additional boring and sampling or sampling using a special sampler adapted for use with CPT rigs are needed to determine soil type directly. When using liquefaction triggering methods that require Vs values to calculate the earthquake-induced CSR from site response analysis (e.g., Andrus and Stokoe, 2000; Cetin and Seed, 2004), Vs should be measured directly and not estimated by correlations with the SPT or the CPT. A comprehensive site investigation for liquefaction triggering could include all three characterization techniques: borings with SPT sampling (with hammer energy measurements—a stricter requirement than the use of the automatic hammer) to obtain blow counts and soil type; CPT soundings to obtain detailed profiles of in situ resistance, and Vs profiles to accurately assess the earthquake-induced CSR and to provide additional insights into the CRR.

One of the most popular CPT-based procedures to evaluate the Factor of Safety against liquefaction at each depth of a soil profile is the Boulanger and Idriss (2014), summarized in Figure 3-7.

Boulanger and Idriss (2014) calculate the Cyclic Resistance Ratio (CRR) from the measured CPT tip resistance, qc, the CPT sleeve friction, fs, and the effective vertical stress, σ'_v, in the soil. These are used to estimate an overburden correction factor, CN, and correct the tip resistance to account for the overburden stress, qc_1. The normalized overburden stress, qc_{1N}, is qc_1 divided by the atmospheric pressure (pa ~100 kPa). During the iteration (usually about 3 cycles), qc_1 is always based on the measured tip resistance, qc, while CN is based on the iteratively updated value for qc_{1N}. A second correction is made for the fines content, FC, allowing to evaluate an equivalent clean sand normalized tip resistance q_{c1Ncs}. With the assumed flat ground or uniform

surcharge for the regional-scale analysis, the correction for the effects of an initial static shear stress ratio is Kα=1. To characterize the soil behaviour type (SBT) and to evaluate the percentage of fines content, *FC*, the empirical correlations defined by Robertson (2015) are used.

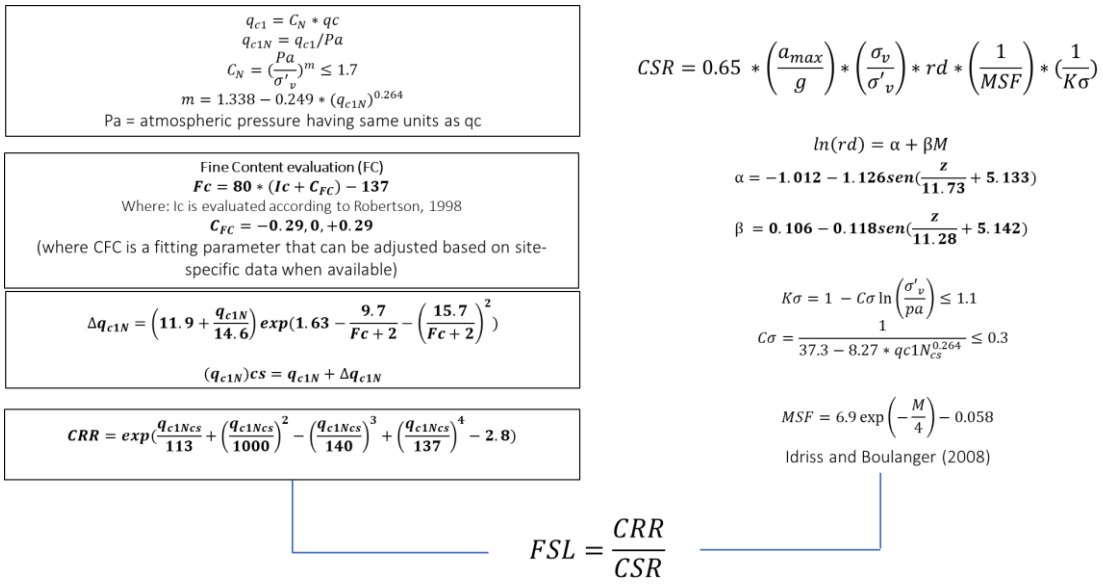

Figure 3-7: Flowchart of the Boulanger & Idriss (2014) CPT-based procedure.

Additionally, Boulanger and Idriss (2014) propose a SPT-based procedure to evaluate the CRR starting from the number of blows $N1_{60}$, normalized with respect to the atmospheric pressure Pa and increased to account for the fine content (Figure 3-8).

$$(N_1)_{60cs} = \mathrm{CN} \cdot \mathrm{CE} \cdot \mathrm{CB} \cdot \mathrm{CR} \cdot \mathrm{CS} \cdot \mathrm{N} + \Delta(N_1)_{60} \qquad \textit{Eq. 3.8}$$

where CN is the correction factor to adjust the blow count to reference stress of one atmosphere; CE is a correction factor for the kinetic energy of the hammer (i.e. hammer weight and height of fall); CB is a correction factor for the borehole diameter; CR is a rod length correction factor; CS is a correction factor for the configuration of the SPT sampler; N is the recorded blow count; and $\Delta(N_1)_{60}$ is the correction factor for the fines content. In this case, the soil behavior type index Ic (Robertson, 2015) can be evaluated with numerous empirical correlations between in-situ tests and geotechnical parameters.

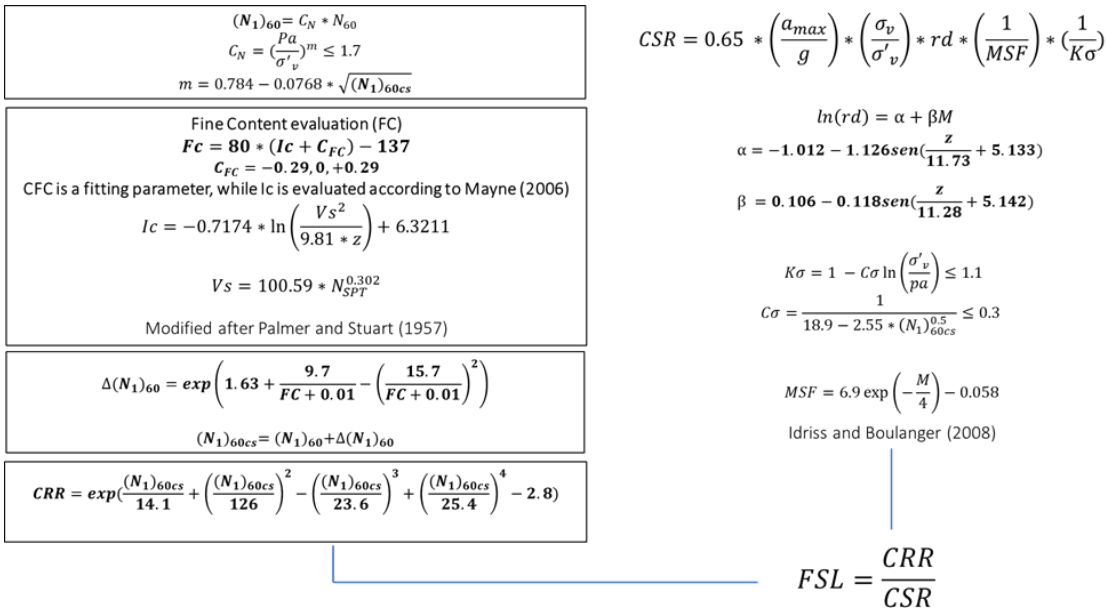

Figure 3-8: Flowchart of the Boulanger & Idriss (2014) SPT-based procedure for liquefaction triggering analysis.

Measuring shear wave velocity (Vs) is another test used to characterize soils in situ. Vs refers to the speed at which a shear wave (one type of wave generated by an earthquake) propagates through the ground. The speed of wave propagation depends on the density of the soil, the directions of wave propagation and particle motion, and the effective stresses in those two directions. Vs, by convention, refers to the shear wave speed at very small amplitudes. Vs is related to the shear modulus of the soil at small strain, G_{max}, and the mass density of the soil, ρ, by the equation:

$$Vs = \sqrt{\frac{G_{max}}{\rho}} \qquad \textit{Eq. 3.9}$$

Where ρ is equal to the total unit weight of the soil divided by the acceleration of gravity.

Vs measurements are economical and non-invasive since they do not need to penetrate the ground surface to make the measurement. The latter capability can be beneficial if soil profiles contain inclusions (i.e., gravel or cobble inclusions) that can make testing difficult or even prohibit SPTs and CPTs. There are many Vs measurement techniques, including downhole measurements (ASTM International, 2014a), cross-hole measurements (ASTM International, 2014b), suspension logging

(Nigbor and Imai, 1994), and non-invasive methods (Stokoe and Santamarina, 2000). Because non-invasive Vs tests do not provide soil samples, some drilling and sampling may still be required as part of a subsurface investigation.

Andrus and Stokoe (2000) propose an alternative method for calculating CRR using shear-wave velocity "Vs", which requires the calculation of a stress-corrected shear wave velocity V_{s1} and the evaluation of soil aging effect.

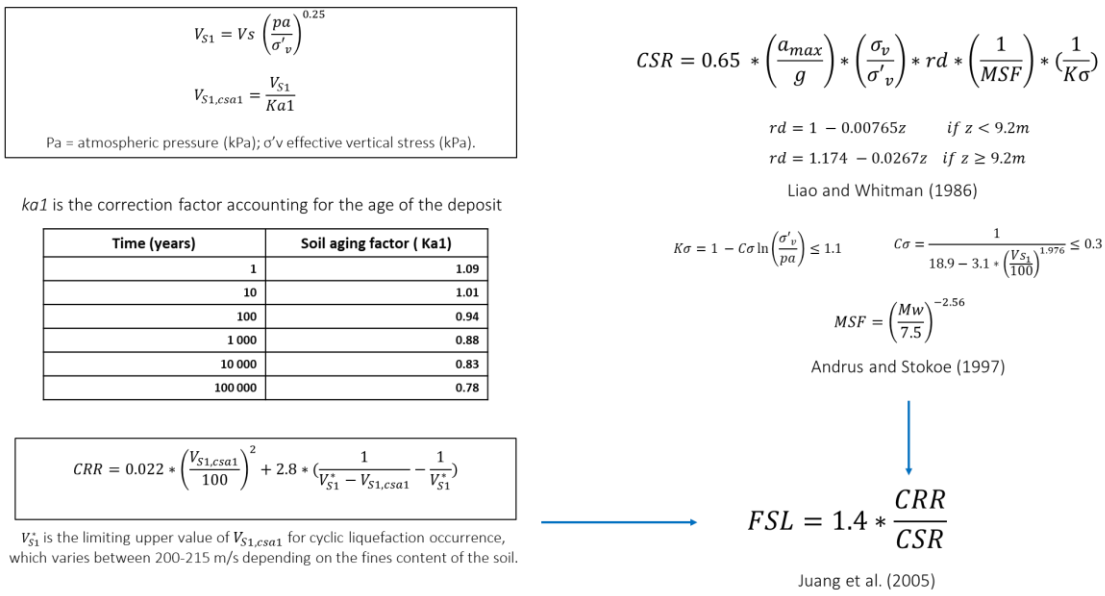

Figure 3-9 Flowchart of the Andrus & Stokoe (2000) procedure for liquefaction triggering evaluation.

Regarding the Factor of Safety, Juang et al. (2005) found that the traditional FSL is conservative for calculating CRR, resulting in lower factors of safety and over-prediction of liquefaction occurrence. To account for this, they introduce a multiplication factor of 1.4 to obtain a more realistic estimate of safety factor.

Recently, after an 11-years period of Vs site data collection and the development of probabilistic correlations for seismic liquefaction occurrence, new correlations for probabilistic/deterministic assessment of liquefaction potential from shear wave velocity were proposed by Kayen et al. (2013). Data coming from 301 liquefaction field case histories in China, Taiwan, Japan, Greece, and the United States were merged to previously published case histories to build a global catalogue of 422 case histories of Vs liquefaction performance. Then, after Bayesian regression and structural reliability methods, a probabilistic treatment of the Vs catalogue for performance-based engineering applications was developed.

3.4.3 Deterministic vs Probabilistic Assessment of Liquefaction Triggering

The most used relationships to evaluate the factor of safety (Robertson, 1998; Idriss & Boulanger, 2008; Boulanger & Idriss, 2014) are derived deterministically as medians of case history databases. As such, they are affected by uncertainties arising from the definition of CSR (model uncertainty on the triggering relationship) and the quality and interpretation of investigation (measurement or parameter uncertainty) (Toprak et al., 1999; Cetin et al., 2004). Analysing a database of 230 cases, Idriss & Boulanger (2010) derive the following relation estimating the conditional probability of liquefaction for known values of CSRM=7.5, σ'_v=1atm and the standard penetration resistance corrected for the presence of finer soil N1,60,cs:

$$P_L\left((N_1)_{60cs}, CSR_{M=7.5,\sigma'_V=1atm}\right) = \Phi\left[-\frac{\frac{(N_1)_{60cs}}{14.1}+\left(\frac{(N_1)_{60cs}}{126}\right)^2-\left(\frac{(N_1)_{60cs}}{23.6}\right)^3+\left(\frac{(N_1)_{60cs}}{25.4}\right)^4-2.67-ln\left(CSR_{M=7.5,\sigma'_V=1atm}\right)}{\sigma_{ln(R)}}\right] \quad \textit{Eq. 3.10}$$

The authors find that a standard deviation $\sigma_{ln(R)}$ equal to 0.13 correctly represents variability.

An alternative to the stress-based approaches, Zhu et al. (2015, 2017) provide empirical functions to predict liquefaction probability at a different scale. The use of readily accessible predictor variables (such as $Vs_{,30}$) led its success among the insurance sector that takes advantage from the applicability to rapid response and loss estimation over large areas. Additionally, advantages of the Zhu et al. (2015) model include the use of simple variables that do not require engineering judgment (except the selection of ground motion ShakeMaps or GMPEs) and the possibility to relate the outcome with the annual insurance rate that a landlord is supposed to invest.

For a given set of predictor variables, the probability of liquefaction is given by the function:

$$P\,[liq] = \frac{1}{1+e^{-x}} \quad \textit{Eq. 3.11}$$

where X is a linear function of the predictor variables accounting for the geology and the expected seismicity of an area.

The Zhu et al. (2015, 2017) geospatial liquefaction model (GLM) is based on globally available geospatial explanatory variables that are proxies for density, saturation, and dynamic loading. In particular, the Zhu et al. (2015) was developed after logistic regression of data considering four earthquakes from New Zealand and Japan in which liquefaction observations were spatially complete across each region. In Zhu et al. (2017), the model was updated by including 23 earthquakes from China, Taiwan, Japan, and the United States.

3.5 **Permanent Ground Deformation**

Once the Factor of Safety against liquefaction has been calculated at each depth, the effects of liquefaction at ground level (free field) are normally predicted (e.g. NZGS, 2016; DPC, 2017) with indicators of severity that empirically synthesize the paramount factors dictating liquefaction in free field conditions. Although with differences among each other, all of them are computed as integral over fixed depths of a function of the safety factor $f_1(FS_L)$ weighted with a function of depth from the ground level w(z), Eqn. 3.12:

$$INDEX = \int_{Zmin}^{Zmax} f_1(FS_L) * w(z)dz \qquad \textit{Eq. 3.12}$$

Table 3-4 reports a list of the most common indexes, namely the Liquefaction Potential Index *"LPI"* (Iwasaki et al., 1978); Ishihara-inspired Liquefaction Potential Index *"LPI_{ISH}"* (Maurer et al., 2015); one-dimensional volumetric reconsolidation settlement *"Wv"* (Zhang et al., 2002); Lateral Displacement Index *"LDI"* (Zhang et. Al., 2004); Liquefaction Severity Number "*LSN"* (van Ballegooy et al., 2014). Despite simplicity that makes these indicators appealing for an extensive assessment, they suffer the implicit limitation of quantifying the subsoil response with a sum of contributions from all potentially liquefiable layers (FSL<1) located at different depths, ignoring in this way any possible mechanical and hydraulic cross-interaction between susceptible layers located at different depths (Cubrinovski, 2017).

Table 3-4: Severity liquefaction indicators proposed in the literature

INDEX	REFERENCE	f_1(FSL)	w(z)	Z
LPI	Iwasaki, 1978	$1 - \text{FSL}$ if FSL < 1 0 if FSL ≥ 1	$10 - 0.5z$	$Z_{min} = 0$ $Z_{max} = 20m$
LPI_{ish}	Maurer, 2015	$\{^{1 - FSL \quad if \quad FSL \leq 1 \cap H1 \cdot m(FSL) \leq 3}_{0 \quad otherwhise}$ $m(FSL) = \exp\left(\frac{5}{25.56(1 - FSL)}\right) - 1$	$\frac{25.56}{z}$	$Z_{min} = H1$ $Z_{max} = 20m$
Wv	Zhang et al., 2002	$\varepsilon_v = \varepsilon_v\ (FSL, qc1N_{cs}\ )$	-	$Z_{min} = 0$ $Z_{max} = \max depth$
LDI	Zhang et al., 2004	$\gamma_{max} = \gamma_{max}\ (FSL, qc1N)$	-	$Z_{min} = 0$ $Z_{max} < 23m$
LSN	van Ballegooy, 2014	$\varepsilon_v = \varepsilon_v\ (FSL, qc1N_{cs}\ )$	$\frac{1000}{z}$	$Z_{min} = 0$ $Z_{max} = 20m$

3.5.1 Liquefaction Potential Index (Iwasaki et al., 1978)

The Iwasaki et al. (1978) Liquefaction Potential Index LPI is the summation of liquefaction severity in each soil layer, which in turn is a function of the Factor of Safety (FSL), weighted by a depth factor that decreases linearly from 10 to 0 over the top 20 m. The LPI value is between 0 (representing no liquefaction expected) and 100 (representing extreme liquefaction effects expected to the ground surface). By weighting soils to have an increasing influence on LPI as depth decreases, this parameter can represent the beneficial effects of an increasing non-liquefied surface layer thickness, or crust.

The authors defined the Liquefaction Potential Index (LPI) of a 20 m deep soil profile as:

$$LPI = \int_0^{20m} F_1(z) \cdot w(z) dz \qquad \textit{Eq. 3.13}$$

where:

$w(z) = 10 - 0.5 \cdot z$

$\text{F}_1(\text{z}) = \{ \begin{matrix} 1 - \text{FS}_\text{L} & \text{if FS}_\text{L} < 1 \\ 0 & \text{if FS}_\text{L} \geq 1 \end{matrix} \}$

z is the depth below the ground surface in metres;

FS_L (z) = the Factor of Safety against Liquefaction at the depth z.

3.5.2 LPI Ishihara inspired (Maurer, 2015)

After Ishihara (1985) experience, who recognized the important role of the upper non-liquefiable crust's thickness (H_1) in mitigating the surficial liquefaction manifestations, Maurer et al. (2015) derived a new index to assess liquefaction-induced ground manifestations: the Ishihara inspired LPI, LPI_{ISH}, developed as a result of the rebuilding efforts in Christchurch. The modifications proposed to the LPI framework try better to capture the trends in the Ishihara boundary curves, to include the influence of the thickness of the non-liquefied crust (i.e., H_1) on the surficial liquefaction manifestations. Maurer et al. (2015) defined LPI_{ISH} as:

$$LPI_{ISH} = \int_0^{20m} F(FS_L)\frac{25.56}{z}dz \qquad \textit{Eq. 3.14}$$

Where:

$$F(FS_L) = \begin{cases} 1 - FS_L & if \quad FS_L \leq 1 \cap H_1 \cdot m(FS_L) \leq 3 \\ 0 & otherwise \end{cases}$$

$$m(FS_L) = \exp\left(\frac{5}{25.56(1 - FS_L)}\right) - 1$$

Where:
H_1 is defined the same as H_1 in the Ishihara (1985) procedure;
z is the depth to the layer of interest in meters below the ground surface
FS_L is the factor of safety against liquefaction at a given depth, z.

As compared to the Iwasaki et al. (1978) LPI procedure, the LPI_{ISH} incorporates the concept of a limiting cap thickness and utilizes a power-law, rather than linear, depth weighting function. LPI_{ISH} weighs the contribution of liquefaction triggering towards producing surficial manifestation more for depths between 0 and 3 m, and less for depths between 3 and 17 m. It can be shown that LPI_{ISH} = 100 for a profile with FS = 0 over the entire 20 m, and with groundwater at a depth of 0.4 m. Because of the power law form of the depth weighting function, the authors recommend that a minimum H_1 of 0.4 m should be used in computing LPI_{ISH}, regardless of whether liquefiable soils are present at shallower depths. The new LPI_{ISH} framework has been tested against a total of 60 liquefaction case studies from the 1989 Loma Prieta (USA), 1994

Northridge (USA), 1999 Kocaeli (Turkey), 1999 Chi-Chi (Taiwan), 2010 Darfield (New Zealand) and 2011 Christchurch (New Zealand) earthquakes, showing a better performance in reducing false-positive predictions (cases where manifestations were predicted but not observed).

3.5.3 Liquefaction-induced ground displacements

Liquefaction-induced ground settlements are essentially vertical deformations of superficial soil layers caused by the densification and compaction of loose granular soils following earthquake loading. Several methods have been proposed to calculate liquefaction-induced ground deformations, including numerical and analytical methods, laboratory modelling and testing, and field-testing-based methods. Semi-empirical approaches using data from field tests are likely best suited to provide simple, reliable, and direct methods to estimate liquefaction-induced ground deformations for low to medium-risk projects and to provide preliminary estimates for higher risk projects. The post-liquefaction volumetric strain can then be estimated using Eqn. 3.15, that corresponds to Figure 3-10 for a given CPT sounding.

For sites with level ground, far from any free face (e.g., riverbanks, seawalls), it is reasonable to assume that little or no lateral displacement occurs after the earthquake, such that the volumetric strain will be equal or close to the vertical strain. If the vertical strain in each soil layer is integrated with depth using the following equation:

$$w_v = \sum_{i=1}^{j} \varepsilon_{vi} \cdot \Delta z_i \qquad \textit{Eq. 3.15}$$

Where:

w_v is the calculated liquefaction-induced ground settlement at the CPT location;

ε_{vi} is the post-liquefaction volumetric strain for the soil sublayer i;

Δz_i is the thickness of the sublayer i;

j is the number of soil sublayers the result should be an appropriate index of potential liquefaction-induced ground settlement at the CPT location due to the design earthquake.

At each layer, the Factor of Safety (FS_L) and the normalised tip resistance, qc_{1N}, are used to calculate the post-liquefaction volumetric densification strain, ε_v. These strains are interpolated from the curves proposed by Zhang et al. (2002), except that the CPT tip resistance is corrected to remove the effect of overburden stress using the iterative Idriss and Boulanger (2014) procedure.

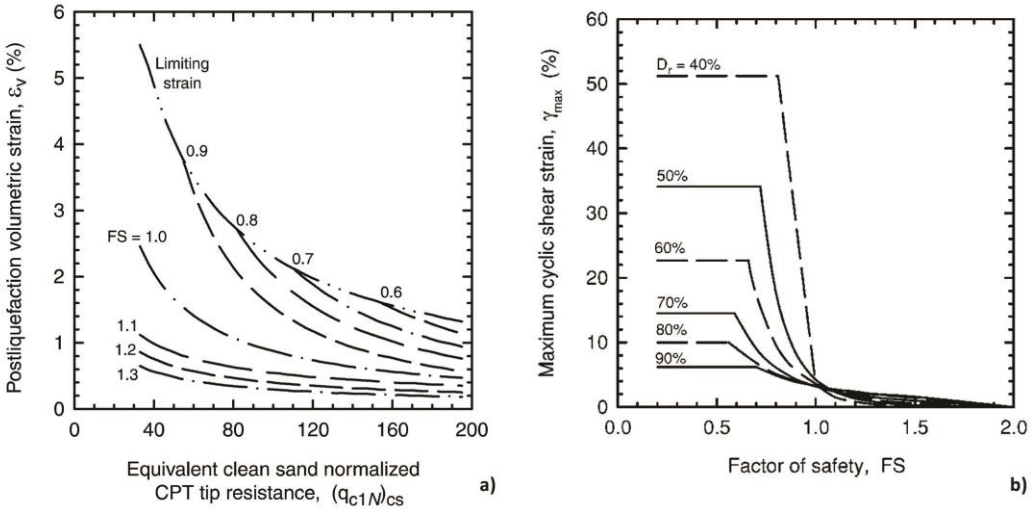

Figure 3-10 a) Relationship between post-liquefaction volumetric densification strains, Ɛv, and normalized CPT tip resistance, qc1N for different factor of safety; b) relationship between maximum cyclic shear strain and factors of safety for different relative densities (Zhang et al., 2002; 2004).

The Settlement indicator integrates the volumetric densification strains, Ɛv, calculated using the Zhang et al. (2002) method, over the total depth of the CPT profile, Z, using:

$$w_{V1,d} = \int_0^Z \varepsilon_v(z)\,dz \qquad \textit{Eq. 3.16}$$

Where:

- ε_v (z) is the volumetric densification strain at depth, z, based on Zhang et al. (2002);
- Z is the total depth of the CPT profile;
- *z* is the depth in metres below the ground surface.

There are always volumetric densification strains when the excess pore pressure rises during shaking, so strains are included for all factors of safety up to FS_L = 2.0 (i.e., including non-liquefied layers). Settlements calculated using this method for deeper CPT profiles are typically greater than settlements calculated for shallower CPT profiles. The calculated values are therefore not strictly comparable between CPT profiles.

For sites where lateral displacement cannot be neglected (e.g., riverbanks, seawalls), Zhang et al. (2004) propose a semiempirical approach to estimate the

liquefaction-induced lateral displacement by integrating the maximum cyclic shear strains with depth (LDI) and amplifying it to account the geometrical effect.

$$LDI = \int_0^{Z\,max} \gamma_{max} dz \qquad \textit{Eq. 3.17}$$

Where:
Z max [m] is the maximum depth below all the potential liquefiable layers with a calculated FS<2.0 (in any case minor than 23 m that is beyond the range of liquefaction); γ_{max} is the maximum cyclic shear strain, depending on Dr and FSL (Figure 3-10). Then, knowing the ground slope (S) or/and free face height (H) and the distance to a free face (L), the lateral displacement (LD) is estimated using either:

$$LD = (S + 0.2) \cdot LDI \quad for\ (0.2\% < S < 3.5\%) \qquad \textit{Eq. 3.18}$$

for gently sloping ground without a free face, or:

$$LD = 6 \cdot \left(\frac{L}{H}\right)^{-0.8} \cdot LDI \quad for\ (4 < L/H < 40) \qquad \textit{Eq. 3.19}$$

for level ground with a free face of Figure 3-11.

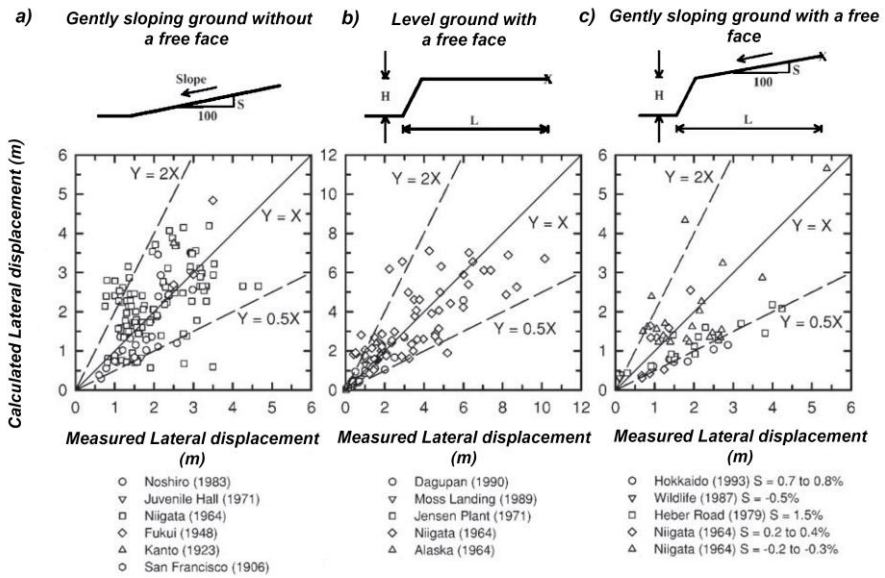

Figure 3-11 Measured vs calculated lateral displacements for: a) gently sloping ground without a free face; b) level ground with a free face; and c) gently sloping ground with a free face (Zhang et al., 2004).

The proposed approach is recommended within the ranges of earthquake properties and ground conditions, namely moment magnitude of the earthquake between 6.4 and 9.2, peak surface acceleration between 0.19*g* and 0.6*g*, and free face heights less than 18 m.

In other words, semiempirical approaches: use laboratory test results to define a limiting shear strain as a function of soil density and some measure of earthquake loading; integrate the limiting shear strain over the depth of the profile, and then regress the result against case history data, usually as a function of some measure of slope geometry. However, due to the simplicity and basis in actual lateral spreading observations, practitioners mostly use empirical regression models to estimate lateral spreading-induced displacements. One of the most popular was initially presented by Bartlett and Youd (1995) and then modified by Youd et al. (2002). They related an extensive database of lateral spread case histories from Japan and the western United States to many statistically evaluated soil and earthquake parameters (e.g., SPT blow counts $(N_1)_{60}$, the cumulative thickness of saturated layers, slope geometry, earthquake moment magnitude and distance from the seismic source, Etc.). With the same principles used in probabilistic seismic hazard analysis defined by the PEER framework, Franke and Kramer (2014) introduce a procedure to develop performance-based estimates of liquefaction-induced lateral spread displacement to provide an update to design criteria and account to the significant level of uncertainty.

3.5.4 Liquefaction Severity Number (LSN) (van Ballegooy et al., 2014)

By combining the effect of volumetric strains (Zhang et al., 2002) with a hyperbolic weight function, the Liquefaction Severity Number "*LSN*" was developed to assess the performance of residential land in Canterbury in future earthquakes after its validation against the residential land damage observed during the 2010-2011 Christchurch Earthquake Sequence. For a given CPT profile, the LSN results from the summation of the post-liquefaction volumetric reconsolidation strains calculated for each soil layer divided by the depth to the midpoint of that layer:

$$LSN = 1000 \int_0^{20m} \frac{\varepsilon_v(z)}{z}\, dz \qquad \textit{Eq. 3.20}$$

being:

$\varepsilon_v(z)$ is the volumetric densification strain at depth, z, based on Zhang et al. (2002); z is the depth in metres below the ground surface.

The value of LSN is theoretically between 0 (representing no liquefaction vulnerability) to a very large number (representing extreme liquefaction vulnerability). The hyperbolic depth weighting function (1⁄z) can yield a very large value only when the groundwater table is very close to the ground surface, and soil layers immediately below the ground surface liquefy.

The general performance of layers undergoing liquefaction with a description of the effects from excess pore pressure and liquefaction is summarized in Figure 3-12.

PERFORMANCE LEVEL	EFFECTS FROM EXCESS PORE WATER PRESSURE AND LIQUEFACTION	CHARACTERISTICS OF LIQUEFACTION AND ITS CONSEQUENCES	CHARACTERISTIC F_L, LPI
L0	**Insignificant**	No significant excess pore water pressures (no liquefaction).	$F_L > 1.4$ LPI=0 LSN <10
L1	**Mild**	Limited excess pore water pressures; negligible deformation of the ground and small settlements.	$F_L > 1.2$ LPI = 0 LSN = 5 – 15
L2	**Moderate**	Liquefaction occurs in layers of limited thickness (small proportion of the deposit, say 10 percent or less) and lateral extent; ground deformation results relatively small in differential settlements.	$F_L \approx 1.0$ LPI < 5 LSN 10 – 25
L3	**High**	Liquefaction occurs in significant portion of the deposit (say 30 percent to 50 percent) resulting in transient lateral displacements, moderate differential movements, and settlement of the ground in the order of 100mm to 200mm.	$F_L < 1.0$ LPI = 5 – 15 LSN = 15 – 35
L4	**Severe**	Complete liquefaction develops in most of the deposit resulting in large lateral displacements of the ground, excessive differential settlements and total settlement of over 200mm.	$F_L << 1.0$ LPI > 15 LSN > 30
L5	**Very severe**	Liquefaction resulting in lateral spreading (flow), large permanent lateral ground displacements and/or significant ground distortion (lateral strains/stretch, vertical offsets and angular distortion).	

Figure 3-12 General performance levels for liquefied deposits (NZGS, 2016).

3.6 **Settlement prediction**

The main limitation of the previous empirical procedures is that none considers the influence of a building and soil-structure interaction (SSI) on the extent of excess pore pressure generation, the liquefaction hazard, and the resulting settlements. However, this becomes very important near the built facilities. In fact, for a given hazard, the physical damage induced by liquefaction on structures and infrastructures depends on their typology, planimetric extension and capability to adsorb absolute and differential movements. These aspects make the estimate of physical impact more complex than the assessment of liquefaction occurrence in the subsoil (Bird et al., 2006). Uncertainties basically stem from the following reasons:

Coupling of liquefaction and ground shaking

Identify damage mechanisms and define the demand for liquefaction

Classify damage into levels

Categorize structure response into homogenous groups

The above concerns become even more relevant and problematic for buildings due to the larger variety of structural typologies and construction materials adopted worldwide. The issue of combined ground shaking and liquefaction has been largely debated. More often buildings that have undergone liquefaction do not exhibit ground shaking damage, giving the idea that a base isolation could be induced by the liquefied soil on the building. However, evidence of buildings damaged by both shaking and liquefaction suggest that severe ground shaking might take place before the groundwater pressure builds up. Bird et al. (2005) claim that the differential settlement induced by liquefaction on framed buildings causes a drift of columns added to that produced by shaking and thus structures previously affected by shaking are more vulnerable to liquefaction. Following this idea, these authors propose a cumulative analytical methodology considering permanent shaking deformation as a reduction of the building capacity against liquefaction. The connection between the two mechanisms is even more evident for masonry structures.

Focusing solely on the effects of liquefaction, a list of possible building damages is provided by van Ballegooy (2014), together with the threshold movements defining the level of damage. Differential settlements or horizontal movements dictated by

inhomogeneous load distributions and stratigraphic conditions (e.g., inherent variability of homogeneous subsoil and boundary between liquefied and non-liquefied soils) are recognised among the most critical causes of damage. Rigid body movements like uniform settlement, tilting and horizontal sliding may add, increasingly affecting aesthetic, serviceability and, ultimately, the stability of buildings. The relative weight among mechanisms is mainly dictated by the stiffness of the structural system with a paramount role of its foundation, whether made of isolated footings, continuous beams or pads, pile reinforcement. Classification of severity levels cumulatively, including shaking and liquefaction, has been proposed by Bird et al. (2006). They define four classes of damage, namely slight, moderate, extensive and complete based on repairability of the building. However, as pointed out by the same authors, general applicability of this criterion is affected by the strong dependency of the fixed limits on the type of structure, on the suitability of buildings and foundation to sustain repair works, plus several other factors dictated by the local practice. van Ballegooy et al. (2014) distinguishes damage according to the deformation mechanisms activated on the building and the extent of settlement. A more general classification of damage on buildings of different typology, not just referred to liquefaction, is provided by Poulos et al. (2001) where a distinction is made among the type of structure (framed, masonry, bridges) and level of damage. In all cases, predicting the overall kinematics of buildings is not easy, moreover for large-scale assessment where geotechnical and structural information are largely incomplete. Following a methodology adopted for the serviceability limit state analysis of foundations under static loads (Grant et al., 1974), differential settlements quantified by the relative rotation β have been related to the absolute settlements of the building.

Once the equivalence between absolute settlement and distortion is established, it is readily seen that the classification criteria defined by van Ballegooy et al. (2014) and Poulos et al. (2001) lead to similar limit values of settlements. In both cases (Figure 3-13), the damage is triggered for absolute settlements in the range 10-100 mm, being severity dependent on the building type. Absolute settlements may thus be considered as Engineering Demand Parameters for the estimate of damage. Despite some popular empirical procedures (e.g., Tokimatsu and Seed, 1987; Zhang et al. 2002, 2004) that focus on the free-field response of liquefied soils, centrifuge studies (e.g., Dobry and Liu, 1994; Dashti et al., 2010b; Bertalot and Brennan, 2015) have highlighted that the presence of loaded footings near the ground level significantly influences the pore pressure build-up and alters the mechanisms that govern deformation and settlements.

In the following, three among the most recent mechanical based formulas to evaluate the liquefaction induced absolute building settlements, namely the Karamitros et al. (2013), Bray and Macedo (2017) and Bullock et al. (2018) are briefly introduced.

a)

Dwelling Foundation Damage Categories

Type of Damage	Minor	Moderate	Major
Stretching	0 to 5mm	5 to 30mm	>30mm
Hogging	0 to 20mm	20 to 50mm	>50mm
Dishing	0 to 20mm	20 to 50mm	>50mm
Racking/Twisting	0 to 10mm	10 to 30mm	>30mm
Tilting	0 to 20mm	20 to 50mm	>50mm
Abrupt Differential Movement	0 to 10mm	10 to 20mm	>20mm
Global Settlement	0 to 50mm	50 to 100mm	>100mm

b)

Type of structure	Type of damage/concern	Criterion	Limiting value(s)
Framed buildings and reinforced load bearing walls	Structural damage	Angular distortion	1/150 – 1/250
	Cracking in walls and partitions	Angular distortion	1/500 (1/1000-1/1400) for end bays
	Visual appearance	Tilt	1/300
	Connection to services	Total settlement	50 – 75 mm (sands) 75 – 135 mm (clays)
Tall buildings	Operation of lifts & elevators	Tilt after lift installation	1/1200 –1/2000
Structures with unreinforced load bearing walls	Cracking by sagging	Deflection ratio	1/2500 (L/H=1) 1/1250 (L/H = 5)
	Cracking by hogging	Deflection ratio	1/5000 (L/H = 1) 1/2500 (L/H = 5)
Bridges – general	Ride quality	Total settlement	100 mm
	Structural distress	Total settlement	63 mm
	Function	Horizontal movement	38 mm
Bridges – multiple span	Structural damage	Angular distortion	1/250
Bridges – single span	Structural damage	Angular distortion	1/200

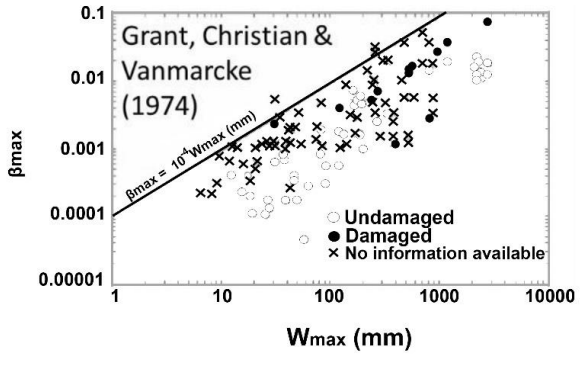

c)

Figure 3-13 Type and level of damage caused on buildings by liquefaction (van Ballegooy, 2014); b) Classification of damage for different building typologies (Poulos et al., 2001); c) empirical relation between maximum absolute settlement and angular distortion for shallow and piled foundations (Viggiani et al., 2012).

3.6.1 Karamitros et al. (2013)

Based on the results of one basic numerical and 18 parametric analyses (considering different soil, excitation, and superstructure characteristics), Karamitros et al. (2013) provide a simplified analytical formula for the computation of the seismic settlements of strip and rectangle footings resting on liquefiable soil with a clay crust. Such settlement is associated with a ‘‘sliding-block’’ type of punching failure through the clay crust and within the liquefied sand layer. The basic idea supporting their study is that liquefaction-induced settlements are correlated to the seismic excitation characteristics and the post-shaking degraded static factor of safety. At the same time,

the effect of shear-induced dilation of the liquefied subsoil is also considered. The adopted model combines the bounding surface plasticity theory with a vanished elastic region to predict all fundamental aspects of the monotonic and the cyclic response and liquefaction of sands.

The proposed expression for the dynamic settlement ρ_{dyn} (i.e., the settlement during shaking) is shown in Eqn. 3.21, being *c* a foundation aspect ratio correction (where *c'*=0.003), a_{max} the peak bedrock acceleration, T the representative period of the motion, N the number of cycles of the excitation, Z_{liq} the thick liquefiable sand layer, B the structure width and FS_{deg} the degraded static factor of safety of the foundation.

$$\rho_{dyn} = c a_{max} T^2 N \left(\frac{Z_{liq}}{B}\right)^{1,5} \cdot \left(\frac{1}{FS_{deg}}\right)^3 \quad \textit{Eq. 3.21}$$

$$c = c' \left(1 + 1{,}65 \cdot \frac{L}{B}\right) \leq 11{,}65c'$$

$$a_{max} T^2 N = \int_{t=0}^{t} |v(t)| dt$$

FS_{deg} in Eqn. 3.21 can be calculated as the degraded bearing capacity ($q_{ult,deg}$) divided by the bearing pressure (q) (Eqn 3.22b). The foundation bearing capacity failure mechanism is simulated by the Meyerhof and Hanna (1978) model for a crust on a weak layer using the degraded friction angle in (Eqn 3.22a) where r_u is the average excess pore pressure ratio of the liquefied sand and φ_0 is the initial friction angle. The superficial crust is beneficial, and there is an upper bound beyond where failure occurs entirely within the crust and does not get affected by the liquefiable layer.

$$\varphi_{deg} = tan^{-1}(1 - r_u) tan(\varphi_0) \quad \textit{Eq. 3.22a}$$

$$FS_{deg} = \frac{q_{ultdeg}}{q} \quad \textit{Eq. 3.22b}$$

Such methodology was evaluated against results from many relevant centrifuge and large-scale experiments, as well as against observations of the performance of shallow foundations in the City of Adapazari, during the 1999 Kocaeli Earthquake. Even if good agreement was found among analytical predictions and liquefaction-induced settlements, the authors suggest respecting the parameters of numerical analysis in future applications.

3.6.2 Bray & Macedo (2017)

Moving from the idea that a significant amount of settlements is induced by the distortional strains generated close to the foundation toe, Bray and Dashti (2014) proposed to express the total settlement (w_{max}) as a sum of three contributions, shear-induced (w_s), volume-induced (w_v) and ejecta-induced (w_e):

$$w_{max} = w_s + w_e + w_v \qquad \textit{Eq. 3.23}$$

Based on two-dimensional numerical analyses, Bray and Macedo (2017) developed a probabilistic procedure for the settlement of structures due to deviatoric deformations. After performing a set of nonlinear dynamic SSI effective stress analyses on 105 different models, they suggest that practitioners compute the different terms of Eq. 3.23 as follows:

- integrate with depth the volumetric strain computed with the procedure suggested by Zhang et al. (2002) to compute wv;
- estimate the settlement due to sand ejecta (w_e) with an empirical function, built from case histories, of liquefaction indicators like the Liquefaction Severity Number LSN (van Ballegooy et al., 2014), the Liquefaction Potential Index LPI defined by Iwasaki et al. (1978);
- compute the shear-induced settlement using the following equation Bray and Macedo (2017):

$$\begin{aligned} ln(w_s) = c1 + 4.59 \cdot ln(Q) - 0.42 \cdot ln(Q)^2 + c2 \cdot LBS \\ + 0.58 \cdot ln(tanh(H_{L/6})) - 0.02 \cdot B + 0.84 \\ \cdot ln(CAVdp) + 0.41 \cdot ln(S_{a1}) + \varepsilon \end{aligned} \qquad \textit{Eq. 3.24}$$

where w_s is expressed in mm, Q is the unitary contact pressure on the foundation (kPa), HL(m) the thickness of the liquefiable layer and B (m) the lower planimetric dimension of the building footprint. CAV_{dp} (g*s) is the cumulative absolute velocity (Campbell & Bozorgnia, 2011) and Sa_1 is the spectral acceleration at T = 1.0 s (g). The use of CAV for the characterization of the seismic signal responds to the concept that liquefaction is more dictated by the energy released by the earthquake rather than by its peak intensity.

Relevance is assumed by the index $LBS = \int \frac{\varepsilon_{shear}}{z} dz$ computed integrating with depth the shear deformation ε_{shear} (Zhang et al., 2002) below the foundation plane. It

also dictates the two coefficients c1 and c2, equal respectively to -8.35 and 0.072 for LBS ≤ 16, -7.48 and 0.014 otherwise.

The term computed by Eqn. (3.24) represent the median of the results of numerical analyses. In fact, the authors suggest quantifying the uncertainty connected with the use of a simplified formulation with a probabilistic normal function having a variation coefficient ε=0.5 in the natural logarithmic units.

3.6.3 Bullock et al. (2018)

In a recent study, Bullock et al. (2018) present a comprehensive predictive relation for the settlement of shallow-founded structures on liquefiable ground during earthquakes. The relation is derived interpolating with a non-linear regression and latent variable analysis the results of an extensive fully coupled three-dimensional numerical parametric study of soil–structure systems, validated with centrifuge experiments and adjusted with case history observations to capture all mechanisms of settlement below the foundation, including volumetric and deviatoric strains as well as ejecta. In particular, the study considered 421 models, each subjected to 150 ground motion records, and the predicted liquefaction-induced settlement includes both volumetric and deviatoric deformations beneath a structure on a mat foundation. The initial predictive model was calibrated and adjusted with a case history database consisting of 50 cases of liquefaction-induced structural settlements from six different earthquakes to correct the results for sedimentation and ejecta effects not effectively captured by the numerical models.

The resulting probabilistic building settlement model incorporates the influence of the soil profile, the presence and properties of the structure and the characteristics of the ground motion, thus providing engineers with a comprehensive procedure for predicting liquefaction-induced settlement of a mat-founded building. The formula is written as:

$$\ln(\bar{S})_{num} = f_{so} + f_{fnd} + f_{st} + s_o \ln(CAV) \qquad \textit{Eq. 3.25}$$

where $\ln(\bar{S})_{num}$ is the natural logarithm of the median predicted numerical foundation settlement (mm) and f_{so}, f_{fnd} and f_{st} are functions that capture effects due to the characteristics of the soil profile, foundation and the structure, respectively.

The first term is computed as:

$$f_{so} = \left[\sum_i H\left(H_{S,i} - 1 + \varepsilon\right) f_{S,i} f_{H,i}\right] + [c_0 + c_1 ln(CAV)] F_{LPC} \qquad \textit{Eq. 3.26}$$

$$S, i_{(SPT)} = \begin{cases} a_0 & N_{1,60,i} < 12.6 \\ a_0 + a_{1,SPT}\left(N_{1,60,i} - 12.6\right) & 12.6 \le N_{1,60,i} < 17.2 \\ a_0 + 4\, a_{1,SPT} & 17.2 \le N_{1,60,i} \end{cases}$$

$$S, i_{(CPT)} = \begin{cases} a_0 & q_{c1N,i} < 112.4 \\ a_0 + a_{1,CPT}\left(q_{c1N,i} - 112.4\right) & 112.4 \le q_{c1N,i} < 140.2 \\ a_0 + 27.8\, a_{1,CPT} & 140.2 \le q_{c1N,i} \end{cases}$$

$$f_{H,i} = b_0 H_{S,i} \exp\left[b_1 (max(DSI)^2 - 4)\right]$$

H(-) is the Heaviside step function; ε is an infinitesimal positive quantity to make H(-) equal to 1 for an argument of zero; FLPC is a flag that is equal to 1 if a low-permeability layer is present above the uppermost susceptible layer; $N_{1;60}$ is the corrected standard penetration test (SPT) blow count in the i^{th} layer; $q_{c1N;i}$ is the corrected, normalized cone penetration test (CPT) tip resistance in the ith layer; $H_{S;i}$ is the thickness of the i^{th} susceptible layer; and $D_{S;i}$ is the depth from the bottom of the foundation to the center of the i_{th} susceptible layer. The term related to the presence of a low-permeability cap indicates that its influence is dependent on motion intensity.

The second term is computed as:

$$f_{fnd} = f_q + f_{B,L} \qquad \textit{Eq. 3.27}$$

$$f_q = \{d_0 + d_1\, ln[min(CAV, 1000)]\} \ln(q)\ exp\left\{d_2\, min\left[0,\ B - max\left(D_{S,1}, 2\right)\right]\right\}$$

$$f_{B,L} = \{e_0 + e_1\, ln[max(CAV, 1500)]\}\, [\ln(B)]^2 + e_2(L/B) + e_3 D_f$$

where q is the bearing pressure of the foundation (in kPa), B is the width of a rectangular foundation (m); L=B is its unitless length-to-width ratio, and D_f is the depth from the surface to the bottom of the foundation (m). $D_{S;1}$ is the depth to the centre of the uppermost susceptible layer with $N_{1;60}$ less than 17.2 blows (q_{c1N} less than 140.2). The exponential decay term included in f_q reduces the influence of q for

profiles where there are no loose susceptible layers within the foundation's depth of influence. This decay term, determined to maximize model performance with respect to the numerical database, engages for layer depths greater than B (taken here as the depth of influence), rather than 1.2 B (per Tokimatsu et al., 2019) or 1.5B (per Boussinesq's solution), which were based on the size of stress bulbs beneath a square footing. Using a threshold of B rather than either of these values offered improved model R2 and reduced bias for models with deep layers and multiple layers. This slight difference may be the result of a highly non-linear and elastoplastic soil response considered in this numerical study, which contradicts simplifying assumptions used by previous researchers in their formulation of the foundation's zone of influence.

The form and intensity threshold captured the effects of the foundation dimensions well (as demonstrated later in this paper). The orders of scaling (natural logarithm squared for B and linear for L=B and D_f) were determined by inspection to minimize residuals.

The third term is:

$$f_{st} = \{f_0 + f_1 \, ln[min(CAV, 1000)]\}h_{eff}^2 + f_2 \, min[(M_{st}/10^6, 1)] \qquad \textit{Eq. 3.28}$$

where h_{eff} is the effective height of the structure (m), and M_{st} is the inertial mass of the structure (kg). The orders of the terms in this equation reflect the expectation that the building's effective moment of inertia should affect its ratcheting behaviour, which in turn influences settlement. An upper and a lower bound are given to CAV are included to allow the functional form to capture the trends discussed in points (e), (f), and (i) in the previous section describing trends in the numerical model.

3.6.4 Discussion of settlement prediction methods

One main question arises on the Intensity Measure relevant for liquefaction hazard; to this regard, Kramer and Michell (2006) argue that because of the complexity of the liquefaction process, an ideal ground motion parameter does not exist. Although with different hypotheses, each of these analytical formulas agrees in defining the seismic input through cumulative intensity measures. While traditional liquefaction triggering analysis evaluate the CSR by combining peak ground acceleration and magnitude (e.g.,

Seed and Idriss, 1971), in recent studies Karimi and Dashti (2017) observed that the evolutionary settlements of structures depend on intensity, duration and frequency content of the ground motion and concluded that cumulative energy is more appropriate to represent intensity measure, more than peak variables which are commonly used in free field liquefaction triggering analyses. They propose the cumulative absolute velocity (Campbell & Bozorgnia, 2011) as a potential candidate as also recently assumed by Bray & Macedo (2017) in the standardized form CAVdp and Bullock et al. (2018).

Table 3-5 and Table 3-6 resume the most known peak and cumulative-energy variables used as seismic Intensity Measures. About them, Luco and Cornell (2007) formally defined the quality of an IM for predicting a DP in terms of "efficiency" and "sufficiency." An efficient IM results in relatively small variability around its predictions of the engineering demand parameter (i.e., smaller uncertainty in probabilistic predictive models). A sufficient IM results in projections of DP unbiased on all earthquake source, path, and site parameters that affect the IM. Further, Bullock et al. (2019.a) highlight the importance of considering both predictive performance (efficiency and sufficiency) and predictability in IM selection when developing probabilistic models applicable to future scenario analyses. Predictability refers to the availability and efficiency of ground motion models (GMMs) for predicting a given IM. In this context, some IMs can be predicted by the available GMMs (e.g., PGA, CAV); others require additional effort (e.g., $Sa_{,avg}$ and CAV_{DP}). A complete and more exhaustive dissertation about them can be found in Bullock et al. (2019.a).

Table 3-5 Definition of a subset of the principal peak transient and duration related Intensity Measures.

IM	**Definition**	**Units**
PGA - Peak Ground Acceleration	$\max_t(\lvert a(t)\rvert)$	g
PGV- Peak Ground Velocity	$\max_t(\lvert v(t)\rvert)$	cm/s
PGD – Peak Ground Displacement	$\max_t(\lvert d(t)\rvert)$	cm
EPV – Effective Peak Velocity	$SV\ (T_s \approx 1)/2.5$	
SA - Spectral Acceleration	$SA(Ts)$	g
TP - Predominant Period	$T(\max(SA))$	s
D595 – Significant Duration	$t(0.95Ia) - t(0.05Ia)$	s
I_c – Characteristic Intensity	$a_{rms}^{1.5}(D_{595})^{0.5}$	cm $^{1.5}$ s $^{-2.5}$

Table 3-6 Definition of a subset of the principal ground motion Cumulative Measures.

IM	Definition	Units
I_a - Arias Intensity (Arias 1970)	$\frac{\pi}{2g}\int_0^{\infty}[a(t)]^2dt$	cm/s
CAV - Cumulative Absolute Velocity	$\int_0^{\infty}\lvert a(t)\rvert dt$	cm/s
CAV,dp – Standardized version of the Cumulative Absolute Velocity (Campbell and Bozorgnia, 2011)	$\sum_{i=1}^{N}(H(PGA_i-0.025)\int_{i-1}^{i}\lvert a(t)\rvert dt)$	g-s
SI – Response Spectrum Intensity (Housner, 1959)	$\int_{0.1}^{2.5}PSV\ (\xi=0.05,T_s)/dT$	cm
$a_{max}T^2N$ - (Karamitros et al., 2013)	$\pi^2\int\lvert v(t)\rvert dt$	m
$Sa_{,avg}$ - mean of the log spectral accelerations at a set of periods of interest	$\frac{1}{N}\sum_{i=1}^{N}\ln Sa(c_i*T_i)$	g-s
a_{rms} - Root Mean Square Acceleration (Vanmarcke and Lai, 1977)	$\sqrt{\frac{1}{D_{95}}\int_{T1}^{T2}[a(t)]^2dt}$ Where $D_{95}=T_2-T_1$	g

Looking at the fundamental mechanisms driving the absolute settlements, Karamitros et al. (2013) recognize the shear deformation of the foundation soil, which accumulates during shaking because of the inertia forces developing in the foundation subsoil, following a Newmark-type sliding-block mechanism. This hypotehsis differs from Tokimatsu and Seed (1987) and Ishihara and Yoshimine (1992) experiences, which attributed their free-field settlements to post-shaking excess pore pressure dissipation causing the densification of soil. Covering only deviatoric mechanisms, Bray and Macedo (2017) suggest combining the evaluated shear-induced settlement to the volumetric deformation term calculated with the Zhang et al. (2002) procedure. However, van Ballegooy et al. (2014) observed that ground settlement associated with sand ejecta accounted for nearly 90% of the land damage in residential neighborhoods

resulting from the 2011 earthquake in Christchurch, New Zealand. This contribution is difficult to quantify with traditional indicators. On the contrary, Bullock et al. (2018) perform a comprehensive series of 3D analyses, covering both (volumetric and deviatoric) deformation mechanisms. Finally, they account for sedimentation and ejecta contribution effects by correlating with an extensive case histories database.

Concerning the subsoil modelling, Karamitros et al. (2013) emphasize the beneficial role of a non-liquefiable soil crust in both reducing the seismic settlements and increasing the post-shaking static bearing capacity. In a practical application, Bray and Macedo (2017) schematize the subsoil as a three-layer profile whose thickness of the liquefiable layer (H_L) is estimated as the summation of the layers with safety factor against liquefaction lesser than 1.0. This implies preliminary liquefaction triggering analysis of available CPT-profiles. Bullock et al. (2018) introduce a multi-layer subsoil modelling which exacerbates the contribution to the total settlement of the top susceptible liquefiable layer and the presence of a low-permeability silt crust above it which may increase settlement by slowing down the drainage and amplifying the pore pressure, strength loss and deformations in the soil. Differently from the previous models, the Bullock et al. (2018) procedure does not require an initial liquefaction triggering analysis (e.g., Youd et al., 2001; Boulanger & Idriss, 2014) since the extent of soil softening and the likelihood of triggering below the foundation are explicitly accounted by introducing the structural inertial effects.

Another debated question concerns the role of structural inertial effects. The first existing empirical procedures to evaluate settlements account for structures only as a surcharge load or only consider the foundation width in relation to the thickness of the liquefiable layer (e.g. Liu & Dobry, 1997) like Karamitros et al. (2013) do. To overcome this limitation, Bray & Macedo (2017) developed a probabilistic procedure for the settlement of structures allowing practitioners to combine the predictions of this model with estimates of volumetric-type deformations and ejecta to predict the total settlement of structures. After experiments and case history/physical model studies (Sancio et al., 2004; Karimi et al., 2018) which have shown that the building dynamic properties that control inertial interaction can influence pore pressure generation and, hence, a building's settlement and particularly tilt potential, Bullock et al. (2018) explicitly introduced the role of building mass, stiffness, and height in their formula.

Table 3-7 Main features of the above defined method for liquefaction induced settlement evaluation.

INDEX	REFERENCE	IMs	SUBSOIL MODELLING	BUILDING MODELLING
ρ_{dyn}	Karamitros et al., 2013	$a_{max}T^2N = \int_{t=0}^{t} \lvert v(t) \rvert dt$	Three-layer model	Foundation bearing pressure.
W_s	Bray and Macedo, 2017	CAV_{dp}, Sa1.0	Three-layer model	Building geometry, depth and contact pressure on foundation.
S_{adj}	Bullock et al., 2018	CAV	Multi-layer model. Accounts to the presence of a Low/High permeability cap.	Building geometry, inertial mass, foundation embedment depth, foundation contact pressure.

3.7 **Procedures and Software**

In Hazus (FEMA, 1999), a procedure to estimate liquefaction hazard based on geological data concerning the depositional environment and age of the subsoil is proposed and accomplished with the following steps. Firstly, the geological susceptibility is evaluated with a qualitative rating based upon general depositional environment, and geologic age of the deposit is given following Youd and Perkins (1978). Estimate the probability of liquefaction combining susceptibility of the soil, amplitude and duration of ground shaking and depth of groundwater with the following formula:

$$P[\,\text{Liquefaction}_{sc}] = \frac{P[\,\text{Liquefaction}_{sc} | PGA = a]}{K_M \cdot K_W} \cdot P_{ml} \qquad \textit{Eq. 3.29}$$

where the conditional liquefaction probability $P[\,\text{Liquefaction}_{sc} | PGA = a]$ is expressed for the above-given susceptibility categories based on the state-of-practice empirical procedures, as well as the statistical modelling of the empirical liquefaction

catalogue presented by Liao et al. (1986) for a magnitude 7.5 earthquake and an assumed groundwater depth of five feet. Correction factors to account in for moment magnitudes (M) and groundwater depths (d_w) different than respectively 7.5 and 5 feet, are given by Equations 3.30 and 3.31 (Seed and Idriss, 1982; Seed et. al., 1985; National Research Council, 1985) and represented graphically in Figure 3-14:

$$K_M = 0.0027M^3 - 0.0267M^2 - 0.25M + 2.9188 \qquad \textit{Eq. 3.30}$$

$$K_W = 0.022d_w + 0.93 \qquad \textit{Eq. 3.31}$$

Where M and d_w respectively are the earthquake moment magnitude and the groundwater depth.

For a given subsoil category, liquefaction is unlikely to occur over the whole portion of the geologic map, and this should be considered in assessing the probability of liquefaction at any given location. Considering that non-susceptible portions are expected to be smaller for higher susceptibilities a probability factor that quantifies the proportion of a geologic map unit deemed susceptible to liquefaction (i.e., the likelihood of susceptible conditions existing at any given location within the unit) is inserted. For the various susceptibility categories, default values are provided in Figure 3-14.

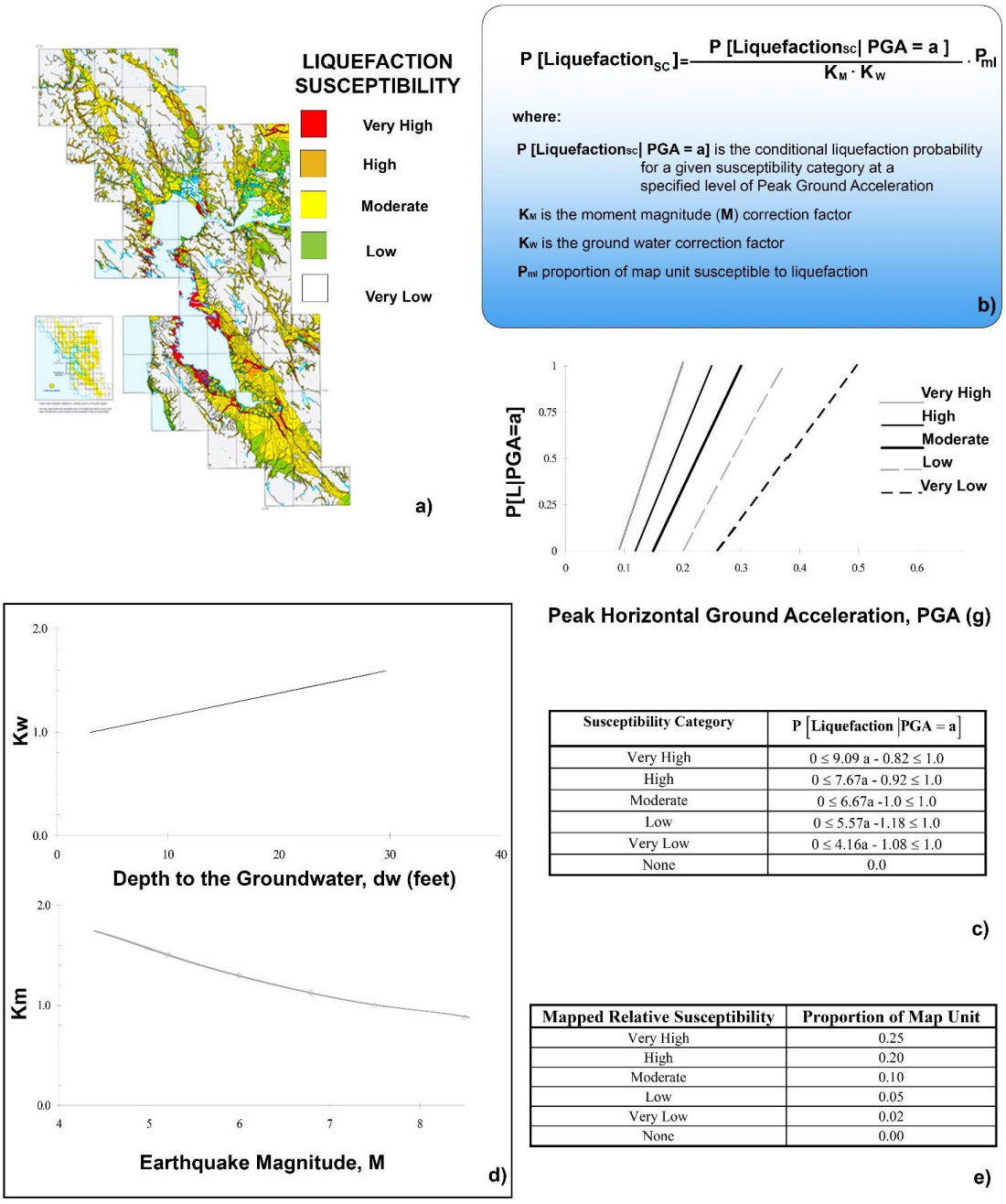

Susceptibility Category	P [Liquefaction |PGA = a]
Very High	0 ≤ 9.09 a - 0.82 ≤ 1.0
High	0 ≤ 7.67a - 0.92 ≤ 1.0
Moderate	0 ≤ 6.67a -1.0 ≤ 1.0
Low	0 ≤ 5.57a -1.18 ≤ 1.0
Very Low	0 ≤ 4.16a - 1.08 ≤ 1.0
None	0.0

c)

Mapped Relative Susceptibility	Proportion of Map Unit
Very High	0.25
High	0.20
Moderate	0.10
Low	0.05
Very Low	0.02
None	0.00

e)

Figure 3-14 – a) Liquefaction geological susceptibility Map (Youd & Perkins, 1978); b) Conditional liquefaction probability for a given susceptibility class; c) Conditional liquefaction probability for a given susceptibility category at a specified level of peak ground acceleration; d) groundwater depth and Moment Magnitude (Seed and Idriss, 1982) Correction Factors for Liquefaction Probability Relationships; e) Proportion of the map susceptible to liquefaction (Power et al., 1982).

The HAZUS procedure allows to estimate the Lateral Spreading Permanent Ground Displacements with the following relationship (provided by Youd and Perkins, 1987) with the ground motion attenuation relationship developed by Sadigh et. al. (1986) as presented in Joyner and Boore (1988):

$$E[PGD_{SC}] = K_{\Delta} \cdot E[PGD|(PGA/PL_{SC}) = a] \qquad \textit{Eq. 3.32}$$

where $E[PGD|(PGA/PL_{SC}) = a]$ is the expected ground displacement for a given susceptibility category under a specified level of normalized ground shaking (PGA/PGA(t)), PGA(t) is the threshold ground acceleration necessary to induce liquefaction (Figure 3-15).

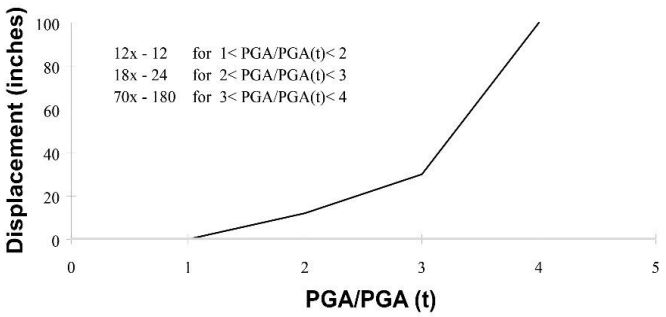

Susceptibility Category	PGA(t)
Very High	0.09g
High	0.12g
Moderate	0.15g
Low	0.21g
Very Low	0.26g
None	N/A

Figure 3-15: Lateral spreading displacement relationship (after Youd & Perkins, 1978; Sadigh et al., 1986) and threshold ground acceleration (PGA(t)) corresponding to zero probability of liquefaction.

KD is the displacement correction factor introduced to account for Moment magnitudes different than 7.5 (Seed and Idriss, 1982), expressed by Eqn. 3.33 and plotted in Figure 3-16.

$$K_{\Delta} = 0.0086M^3 - 0.0914M^2 + 0.4698M - 0.9835 \qquad \textit{Eq. 3.33}$$

HAZUS also report a simple methodology to estimate ground settlement associated with liquefaction. The latter is assumed to be related to the susceptibility category assigned to an area according to Tokimatsu and Seed (1987) that indicate strong correlations between volumetric strain (settlement) and soil relative density (a measure of susceptibility). Considering that experience has shown that deposits of higher susceptibility tend to have increased thicknesses of potentially liquefiable soils, the ground settlement is computed multiplying a characteristic settlement amplitude appropriate to the susceptibility category (Figure 3-16) with the probability of liquefaction computed with for a given ground motion level.

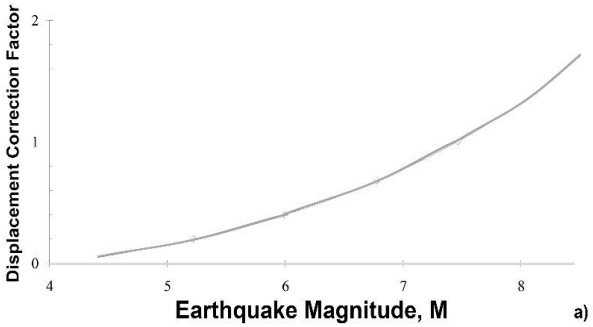

Relative Susceptibility	Settlement (inches)
Very High	12
High	6
Moderate	2
Low	1
Very Low	0
None	0

b)

Figure 3-16: Displacement correction factor, KD for Lateral spreading displacement relationship (after Seed & Idriss, 1982); Ground settlements amplitudes for liquefaction susceptibility categories (after Tokimatsu & Seed, 1987).

The above-described procedure enables to estimate the probability and, with relatively high uncertainty, the effects of liquefaction, but at a very large geographical scale. Considering that subsoil characterisation is based on geological information (environment and age of the deposit), the results do not allow to distinguish the situation at the scale of buildings or even on aggregates. The challenge for the user is to translate regional/local data, experience and judgment into site-specific relationships. HAZUS provides just a series of comments related to this issue to drive user-defined risk assessment procedures (called Expert-Generated Ground Failure Estimation) based on the collection of geotechnical data.

Chapter 4. MULTILEVEL RISK ANALYSIS

4.1 Abstract

Population, structures, utilities, and socio-economic activities form together an integrated system of interdependent entities. About them, the extensive physical damage produced on buildings and lifelines is only a part of the impact of liquefaction, as injuries are aggravated by the prolonged reduced serviceability of the critical infrastructures, i.e., those systems and organizations that deliver goods and services fundamental for the functioning of society and economy. This implies that the challenge for liquefaction risk assessment on buildings comes from the need to investigate the concurrent factors in liquefaction triggering (namely the seismicity and subsoil response) and the purpose of quantifying the liquefaction-induced physical impact and the consequent economic loss. To this aim, adequate fragility and economic models must be introduced depending on the building structural typology and intended use. In this chapter, a procedure to assess the liquefaction risk on buildings is defined, highlighting the non-negligible role of geostatistics tools and error propagation in evaluating such risk over urban areas.

4.2 **The cascade process of liquefaction**

Liquefaction is a seismic-induced hazard and, as a secondary seismic hazard, it involves different factors in a cascade process that starts with the release of energy associated with rapid movement on active faults, the propagation of motion through layers of different properties, the generation of excess pore pressure in the shallower subsoil portions and finally to the damage on structures and infrastructures. The liquefaction impact on constructions moves from a physical level (structural damage) to the losses for the community that involve serviceability consideration. All these aspects form the logical scheme depicted in Figure 4-1, whose elements act in a way that the output of the lower level forms the input of the upper level. This chain scheme may be applied from bottom to top to compute the holistic risk or interrupted at intermediate levels to assess risk on specific subsystems (ground, physical asset, service, community).

In any case, the response of each element must be characterized, defining a correlation between input and output variables, individually or in conjunction with the closer elements depending on the relevance of the interaction between the two systems.

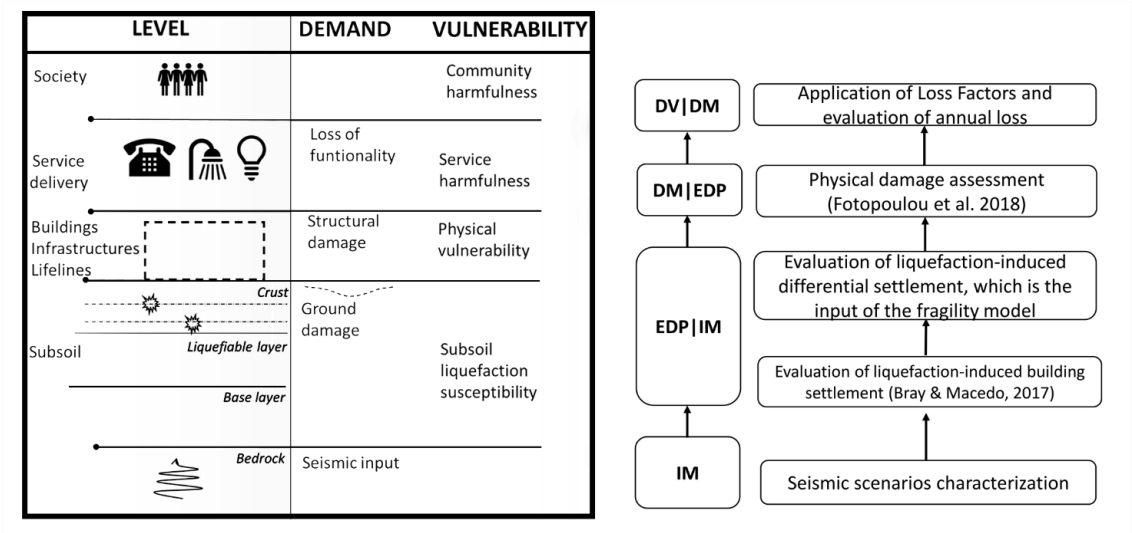

Figure 4-1 The cascade scheme implemented for liquefaction risk assessment and the PBEE equation are here specified to the evaluation of risk on buildings.

Considering the intrinsic nature of the phenomenon together with the cause-and-effect diagram governing initiation and development of liquefaction, the PBEE approach (Cornell and Krawinkler, 2000) of Eqn. 3.2 can be adapted:

$$P(L) = \int_{IM} \int_{EDP} \int_{DM} P(VD|DM) * p(DM|EDP) * p(EDP|IM) * p(IM) \qquad \textit{Eq. 4.1}$$

Following the logic of the systemic risk, the earthquake represents the primary hazard factor, and liquefaction occurs if the soil has specific characteristics, namely a grain size distribution composed of sand with limited fine content, sufficiently low density and saturation. Therefore, the combination of earthquake and subsoil response determines the demand for the structure located at the ground level. However, physical damage for the latter can be computed considering the subsoil-structures as a unique coupled system or evaluating the response of the two components separately. In the first case, the earthquake intensity measure IM also becomes the engineering demand parameter EDP and the vulnerability function p(DM|EDP) quantifies the response of the subsoil-structure system for the given seismic input. In the second case, the soil response provides the demand function p(EDP|IM) for the structure, and physical vulnerability is computed considering the p(DM|EDP) function for the sole structure. The resulting physical damage represents the demand for the delivery capability of the system whose vulnerability is defined by a function that relates the loss of serviceability to the different levels of damage. Finally, the latest level of risk assessment concerns the community: it is harmed by the loss of safety and serviceability and risk can be assessed in terms of deaths, injuries, loss of incomes, damage to cultural and environmental heritage.

The terms of Eqn. 4.1 can be quantified in different manners, sometimes with a probabilistic inference of statistical observations, sometimes applying theoretical models with stochastically variable inputs, sometimes with less objective procedures. For instance, it is customary to express the severity of damage in terms of financial losses based on expert judgement, qualitative estimates or even rules of thumb that make the process unavoidably subjective.

In Figure 4-1, the fundamental aspects of multilevel analysis are implicitly introduced since for each entity (e.g., subsoil, structure, infrastructure..) it is possible to evaluate the risk by defining the convolutional integral of the PBEE. Once the element understudy has been identified (characterized by its vulnerability to the liquefaction phenomenon), the input represents the demand (i.e., everything is below

the selected element in the cascade process). On the other hand, the output represents the risk for the selected element and, in turn, the hazard factor if looking at the following item. Considering liquefaction, the risk for the ground represents the hazard for buildings and infrastructures, and the physical damage of the building represents the hazard for the loss of functionality which in turn represents the hazard for the loss of function from a social point of view.

Although the risk can be assessed looking at each entity, the next paragraphs will focus on urban aggregates.

4.3 Risk Assessment

The assessment of liquefaction risk carried out over large areas implies to identify on a local basis the different factors forming risk (hazard, vulnerability and exposure) and, for each type of analysis, characterise the mechanisms defining and quantify the most suitable representative parameters. Looking at the building/city block resolution level, the analysis of liquefaction-induced permanent ground deformation becomes a preparatory phase to assess the risk, since it moves from the susceptibility to the expected liquefaction severity in free field conditions.

For buildings subjected to liquefaction, the sequence depicted in the right part of Table 4-1, which terms will be explained in the following paragraph, is employed. The basic steps in a liquefaction risk assessment are:

Hazard Analysis that includes the identification of earthquake sources, modelling of the occurrence of earthquakes from these sources, estimation of the attenuation of ground motions between these sources and the study area, evaluation of the site effects of soil amplification, evaluation of liquefaction propensity, triggering and liquefaction-induced permanent ground deformations (PGDf).

Inventory Collection: (depending on the study detail level) identification of structures and infrastructure exposed to damage, classification of the built asset according to their vulnerability to damage, classification of the occupancy of the buildings and facilities.

Damage Modelling: modelling of the performance of the inventory classes underground shaking and seismic liquefaction, development of damage functions (the relationship between levels of damage and corresponding demand), estimation of the

combined damage to the inventory by introducing relationships between damage and a series of earthquake intensity measures (IMs) or Liquefaction Severity Indicators.

Loss Estimation: estimation of direct losses due to damage repair costs, estimation of indirect losses due to loss of function of the inventory, estimation of casualties caused by the selected scenario and estimation of social impact on the whole community.

4.3.1 Hazard Analysis

Liquefaction hazard can be defined for a generic structure as the probability that a given value of the liquefaction severity indicator (demand) will be produced in a specific time interval (e.g., the lifetime of the structure). The practice of characterizing liquefaction hazard through these indicators is applied in many countries to quantify risk on structures and infrastructures present in a given territory (e.g. ICMS-LIQ 2017, MBIE, 2016, Yasuda and Ishikhawa, 2018). Moreover, liquefaction severity indicators can be seen as proxies of the permanent ground deformation (PGDf) (Bird et al., 2006) or, more generally, of damage and as the "liquefaction demand" for the assessment of the response of the overlying structures and infrastructures, characterized by their own vulnerability.

As described in Chapter 3 and summarized in the Flowchart of Figure 4-2, the output of liquefaction hazard assessment is represented by maps of liquefaction severity indicators, obtained from geostatistical interpolation of the punctual results. Despite such indicators are derived from the safety factors along with the investigated profile and can be formally referred to a common structure (see Eqn. 3.12), each indicator differs from the other. Thus, a different performance is expected when applying them to estimate liquefaction hazard over the investigated area.

The classical LPI (Iwasaki, 1978) index adopts a linear weight function of the complement of FSL to 1, reaching zero at a depth equal to 20 m. According to this formulation, there is no contribution where FSL>1. The modification introduced to this indicator by Ishihara (e.g. Maurer, 2015a) considers the presence of a crust and adopts a hyperbolic weight function, giving in this way larger importance to the shallower liquefiable strata. The settlement w_v (Zhang et al., 2002) puts the function f_1(FSL) equal to the vertical deformation, expressed as a function of the safety factor and the normalized CPT resistance. Differently from the previous two, this method

computes a contribution even when FSL>1. The Liquefaction Severity Index (LSN) (van Ballegooy, 2014) adopts the same function f_1(FSL) of Zhang et al., (2002) but introduces a hyperbolic weight function.

Therefore, the objective of validation is to evaluate the predictive capability of the adopted indicators comparing the value assumed in an investigated profile with the effects observed in the surrounding area after an assigned earthquake. In the following, the above-described procedure (Figure 4-2) is applied on two different examples, respectively the case studies of 22nd February 2011 Christchurch (New Zealand) M_W=6.2 and the event of May 20th 2012 in Terre del Reno (Italy) M_W=6.1 Earthquakes.

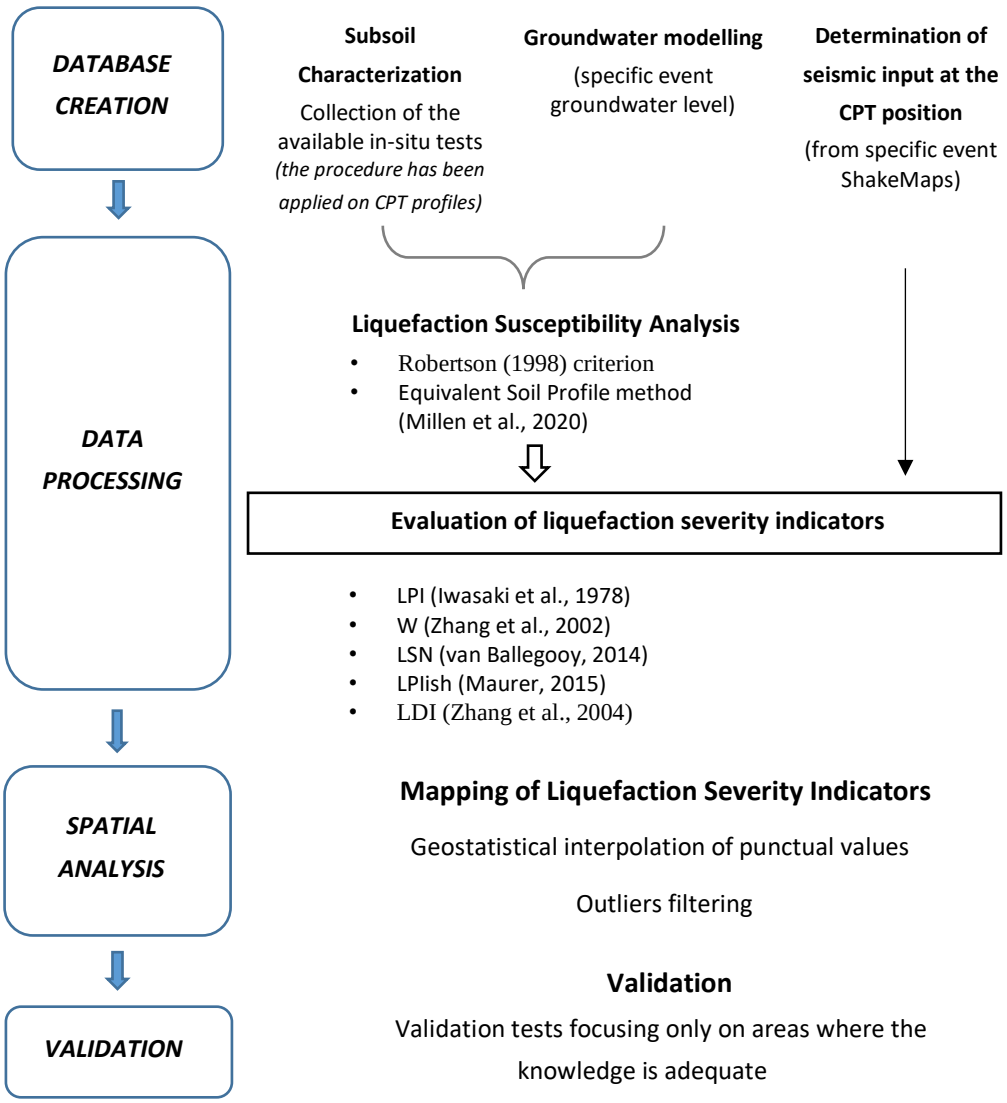

Figure 4-2 Flowchart for liquefaction hazard analysis and validation of the obtained results.

4.3.2 A generalized indicator for combined liquefaction and lateral spreading

Since almost all the indicators account to 1D topographic conditions, a preliminary study is here in carried out about lateral spreading. Lateral spreading is a particular liquefaction-induced phenomenon that typically occurs in sloping grounds or level ground close to waterways/open faces (e.g., riverbanks, streams), where this slope may drive the liquefied soil mass (heavy liquid) to move in the down-slope direction. The process will continue until equilibrium is re-established, or resisting forces reach the level of driving forces.

This means that the temporal evolution of lateral spreading is closely related to the development of excess pore water pressures and soil liquefaction in the spreading deposit. While spreading due to the biased seismic loads might be initiated at the early stages of strong shaking during the pore pressure build-up, the magnitude of lateral spreading displacements will increase substantially once the soils liquefy, because soil liquefaction will dramatically reduce the stiffness and strength of soils and will reduce their shear resistance to levels below the amplitude of the driving shear stresses. The spreading may continue even after the strong shaking has diminished and is influenced by a number of factors such as the available soil resistance (soil properties and in-situ state), driving stresses (topography, and ground motion characteristics), dissipation of excess pore water pressures (dynamic permeability and water flow conditions) and magnitude of lateral displacements (change of overall soil volume during spreading). Trying to enumerate the factors affecting lateral spreading, the following aspects should not be neglected (Cubrinovski et al., 2012): a complex interplay of the topography, soil characteristics and conditions, temporal and spatial development of pore pressures and strains in the ground during cyclic loading, residual strength and stiffness of liquefied soils, conditions for dissipation of excess pore water pressures, mode of deformation and characteristics of ground motion (earthquake loads).

The modeling of such a complex phenomenon, influenced by numerous aspects, collides with the practical need to have a synthetic and reliable indicator capable of predicting the triggering of lateral spreading. Also, the use of traditional indicators of liquefaction severity (LPI, LSN, W) can lead to a significant underestimation of the consequences of lateral spreading since almost all these indicators only account for 1D geometrical conditions. From the perspective of semiempirical approaches, Zhang et

al. (2004) propose an expeditious approach to estimate liquefaction-induced lateral displacements. The authors combined SPT- and CPT- based methods to evaluate the liquefaction potential with laboratory tests to estimate the potential maximum cyclic shear strains for saturated sandy soils under seismic loading and an amplification factor accounting to the topography. In their procedure, Zhang et al. (2004) suggest calculating a lateral displacement index "LDI" by integrating the maximum cyclic shear strains with depth; then, empirical amplification functions derived from case histories are applied to characterize the site geometry, ascribable to three different conditions: gentle sloping ground without a free face, gently sloping ground with a free face and level ground with a free face.

The lateral displacement index "LD" defined by Zhang et al. (2004) is dimensionally a length (L). Therefore, it can only be used and tested against the prediction of lateral displacement. However, in practical situations, a punctual validation of the forecast is difficult to be achieved due to the lack of punctual horizontal displacement measures. On the contrary, in cases where measurements of horizontal displacements are available, ad-hoc studies should be carried out to evaluate the horizontal correlation distance, i.e., the maximum within which the measured effects can be attributed to the surveyed vertical.

Furthermore, due to the small number of worldwide case histories that implies the processing of a small number of CPT/SPT profiles and a limited number of PGAs, the authors do not provide a classification range describing the severity of possible manifestations, like the ones proposed by Iwasaki et al. (1978) and Sönmez (2003) for the LPI. The proposed topographic functions only reflect a limited number of geometries (12 sites for gently sloped without free face and 4 with a free face).

Despite the Zhang et al. (2004) framework is robust since it accounts for the soil relative density Dr (%), observers may thus argue that it is only applicable in a limited number of situations and engineering judgment and additional data are required respectively in interpreting the results or trying to customize the LD indicator to further scenarios. Filling this gap, i.e., to generalize the Zhang et al. (2004) framework by introducing a novel indicator capable of predicting the whole range of liquefaction-induced surficial manifestations, including lateral spreading, is the purpose of the present study.

Taking advantage of the Zhang et al. (2004) experience and preserving the formal structure of the most adopted among the liquefaction severity indicators (Eqn. 3.12), the functional form of the herein proposed Generalized LD "GLD" is shown in Eqn. 4.2:

$$GLD = TF \int_0^{z_{max}} \gamma_{max} * w(z) dz \qquad \textit{Eq. 4.2}$$

Where:

γ is the shear strain (expressed as a decimal) computed (as for Figure 3-10b) as a function of the normalized CPT resistance $(qc_{1N})_{cs}$ and the liquefaction safety factor FSL and TF is the topographic factor computed; w(z) is the weight function.

The correcting factor TF of Eqn. 4.2 expresses the influence of the local topography on the liquefaction hazard. It is derived by adapting the Zhang et al. (2004) topographic factor, in a way that provides a value equal to 1 when 2D conditions are not verified. The analytical formula is reported in Eqn. 4.3, respectively, for the case of sloped ground and free faces (Figure 3-11):

$TF = 1.2 + S$ for sloped ground *Eq. 4.3a*

$TF = 1 + 6 \cdot \left(\frac{L}{H}\right)^{-0.8}$ for free face with L/H≤40 *Eq. 4.3b*

$TF = 1$ if S = 0 or L/H>40 *Eq. 4.3c*

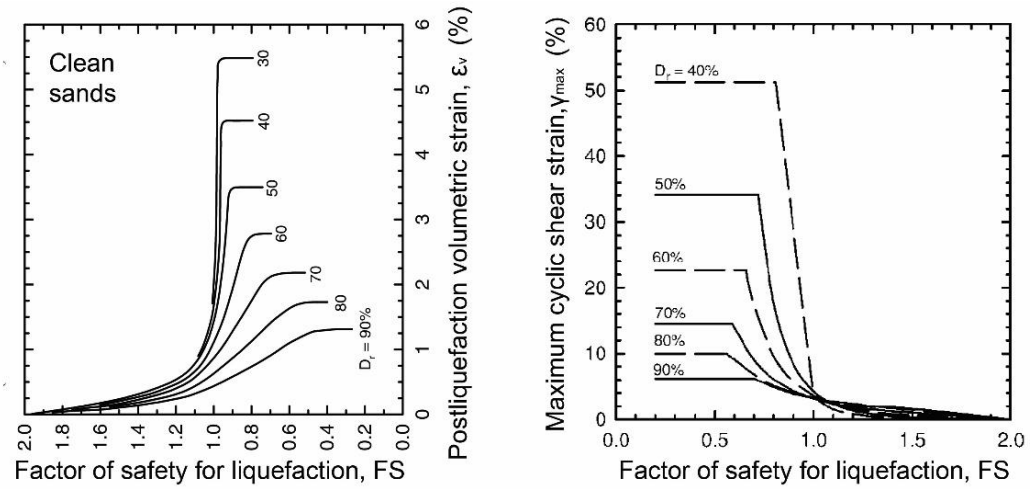

Figure 4-3 Post liquefaction volume strain (a) and maximum cycle shear stain (b) as function of relative density and Liquefaction Safety Factor (FSL) (modified from Ishihara & Yoshimine, 1992).

S in Eqn. 4.3a represents the slope steepness, expressed as a percentage. H and L in eq. 4.3b are the height of the free face and the distance from the free face's toe. Concerning the topography, the factor TF applied in the GLDI framework maintains a similar mathematical formulation to the Zhang et al. (2004) LDI, since it plays a role in determining lateral spreading in the presence of sloped ground (Eqn. 4.3a) or free face (Eqn. 4.3b). Conversely, in the case of a sub-horizontal ground surface (S=0) and

absence of free faces (L/H>40), no topographic amplification is required (TF = 1), but this does not imply that liquefaction is unlikely to occur. Lastly, when both the effects (of S and H) are found over a site, the topographic factor should be evaluated by applying both Eqn. 4.3a and Eqn. 4.3b and taking the maximum among them.

On the other hand, the introduction of the weight function w(z) of Eqn. 4.4 represents an innovative term if compared to the Zhang et al., (2004) original approach.

$$w(z) = \left(1 - \frac{\pi}{2} \cdot \left(atan\left(\frac{z}{z_{max}}\right)\right)^{n1}\right)^{n2} \qquad \textit{Eq. 4.4}$$

Where:
Z is the i-th layer depth (m);
Zmax is assumed to equal 20 m;
n1, n2 respectively equal to 5 and 20 in a way that emphasizes both the severity of liquefaction if happening in the upper 10 meters and decreasing the surficial manifestations for deeper triggering.

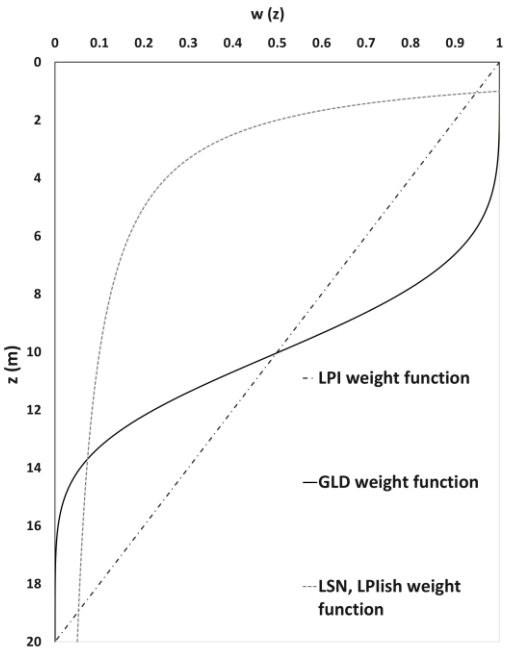

Figure 4-4 Comparison among the adopted weight functions in evaluating liquefaction severity indicators.

A comparison among the adopted weighted functions w(z) is showed in Figure 4-4. Despite with different laws (i.e., Iwasaki et al. in the LPI propose a linear attenuation law, while van Ballegooy et al. (2014) and Maurer et al. (2015a) adopt hyperbolic

functions in defining their LSN and LPIish), all of them are consistent in exacerbating the relevance of liquefaction-induced effects when liquefiable layers are shallow, say <5-6 m considering hyperbolic functions, considering negligible the liquefaction-induced manifestations if the phenomenon is triggered at greater depth (>12-15m).

The procedure to evaluate the GLDI on a given CPT profile is summarized in Figure 4-5: similarly to any other liquefaction severity indicator, the integral of the maximum shear strain is evaluated and weighted by the depth. Lastly, it is multiplied by the topographic factor TF, evaluated as shown in Figure 4-6, dependently from near profile geometric conditions (H, L and S) which can be determined from the Digital Elevation Model of the area.

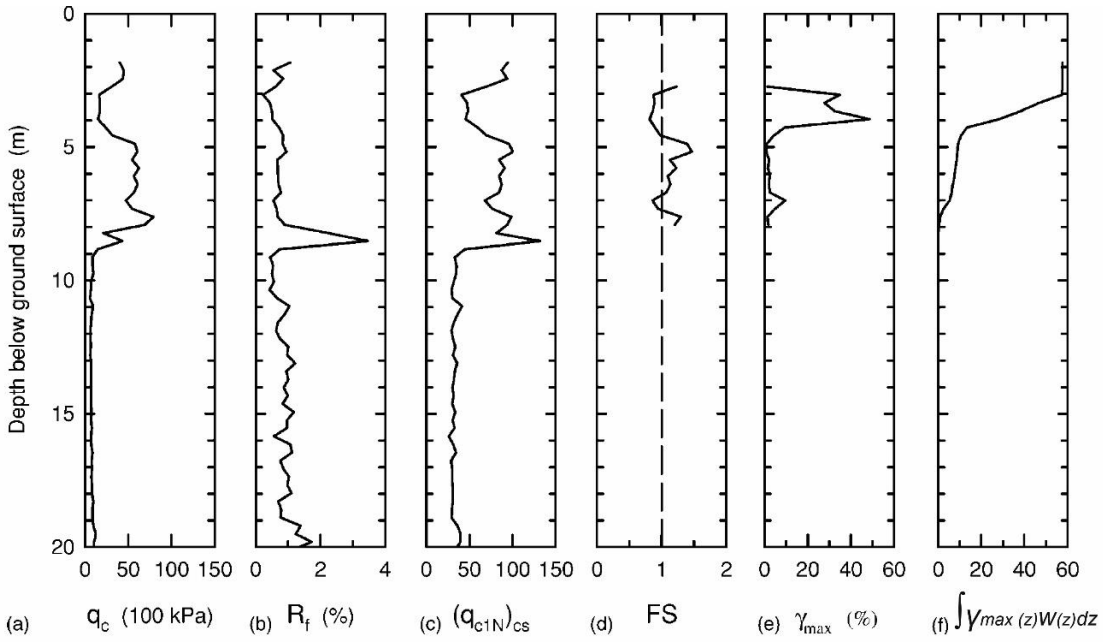

Figure 4-5 Schematic procedure to assess the integral of the maximum shear strain from a generic CPT profile.

In conclusion, the new index GLD preserves the logical structure of the Zhang et al. (2004) "LD" extending its application to a wider variety of conditions, not only in cases where lateral spreading occurs. Similarly to other prediction variables, its computation in a fixed geographical position requires the seismic input definition, with expected Magnitude and Peak Ground Acceleration PGA, the CPT tip resistance and sleeve friction profiles necessary to compute FSL, $(q_{c1N})_{cs}$ and consequently γ. Finally, topographic characteristics like maximum slope steepness, the height of the possible

free face and distance of the considered point from the toe are also needed. In case of S = 0 or L/H>40, the herein adopted topographic factor is placed equal to 1; as a consequence of the functional correlations shown in Figure 4-3, this provides GLD values proportional to the Zhang et al. (2004) "LDI" and the van Ballegooy et al. (2014) "LSN".

In the following Chapters, examples of application and testing of the performance of the GLD indicator will be presented applied to real case studies.

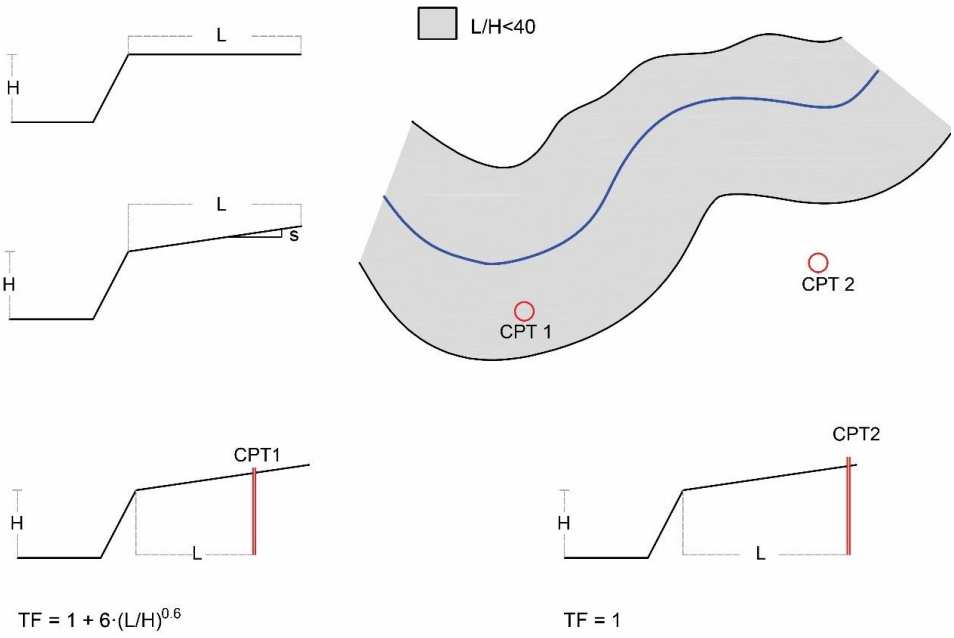

Figure 4-6 evaluation of the topographic factor TF (modified after Zhang et al., 2004).

4.3.3 Vulnerability of buildings

A fundamental issue for the application of Eqn. (1) is the definition of vulnerability that passes through the identification of a representative parameter, EDP in the equation, and the expression of the p(EDP|IM) and p(DM|EDP) functions. The physical damage induced by liquefaction on buildings depends on the intensity of the ground shaking and pore pressure build-up, coupled with the capability of structures to adsorb absolute and differential movements. As a preliminary step of the analysis, it should be considered that prior to experiencing settlements buildings affected by earthquakes undergo shaking that may produce additional damage. The coupling between ground shaking and liquefaction effects on buildings form the subject of

previous studies carried out on empirical or theoretical basis. Some events, like the one occurred in Adapazari, Turkey, after the 1999 Kocaeli Earthquake (Bakir, 2002), showed that the buildings damaged by liquefaction suffered limited effects of shaking and vice versa. This evidence suggests that the liquefied soil may act as a sort of natural seismic isolator for the shaken buildings, also raising the extreme idea of inducing liquefaction into selected soil layers to reduce the more severe damage of shaking (e.g. Mousavi et al., 2016). This conceptual scheme implies the idea that shaking prevails in the initial phases of the earthquake whereas liquefaction overlaps in a second phase, with the result that a combination of both gives the whole earthquake damage. However, while liquefaction reduces the effects of shaking, the consequence in the opposite direction is less evident, with the practical consequence that the estimate of liquefaction damage can be performed autonomously from shaking. Concerning the definition of EDP, Bird et al. (2006) theoretically and van Ballegooy et al. (2014) empirically focus on the differential settlements as the major cause of damage. This option matches closely with the definition of damage given by Boscardin and Cording (1989) and adopted in design standards, e.g. the Eurocode PrEN 1997-1 (CEN, 2008), that express the serviceability performance of buildings in terms of distortion. A recent study by Fotopoulou et al. (2018) uses differential settlement as EDP into the definition of four liquefaction fragility curves for buildings, each referred to damage limit states (Table 4-1). Fragility curves are statistical tools that quantify the probability that a system undergoes a given performance state (e.g. damage level) as functions of the engineering demand parameter. A fundamental requirement for their definition is the taxonomic classification of buildings into classes that group homogenous elements, i.e. buildings having similar typology, extension, structural stiffness and weakness (e.g. Brzev et al., 2013). In choosing the buildings classification, a compromise must thus be unavoidably sought between particularization and available knowledge. In fact, a more particular classification would give to more reliable prediction but at the expenses of a deeper knowledge of the building characteristics, rarely viable in territorial analyses. The fragility criterion defined by Fotopoulou et al. (2018) chosen for the present study represents a compromise between immediateness and accuracy. It refers to low code reinforced concrete buildings, i.e. designed without specific seismic regulation, resting on shallow isolated footings. They have been obtained from statistical analyses of the results of non-linear numerical calculation considering two possible failure mechanisms, flexural damage of beams and shear failure of columns, induced by random differential displacements applied at the foundation. An example of fragility curves for two stories buildings is given in Figure 4-7, while a table of the

parameters (median A and dispersion β) of the log-normal distribution for 2, 4 and 9-storey buildings is reported in Table 4-1.

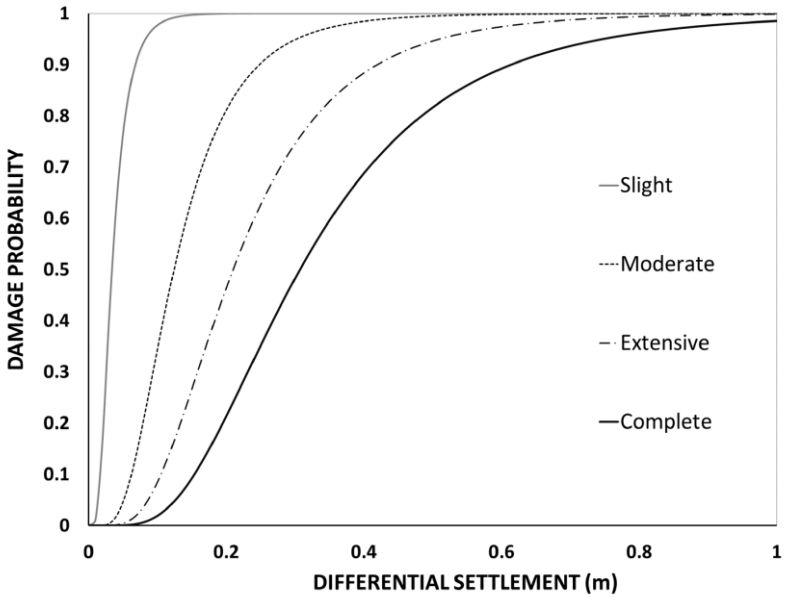

Figure 4-7 Example of fragility curves for a two stories low code framed building (adapted from Fotopoulou et al., 2018).

Table 4-1 Median and dispersion of differential settlements associated to different damage levels for low code reinforced concrete buildings of 2, 4 and 9 stories (from Fotopoulou et al., 2018).

		Level of damage							
		Slight		Moderate		Extensive		Complete	
		A(m)	β	A (m)	β	A(m)	β	A(m)	β
Number of storeys	2	0.034	0.54	0.124	0.54	0.210	0.54	0.307	0.54
	4	0.027	0.50	0.098	0.50	0.176	0.50	0.305	0.50
	9	0.022	0.50	0.083	0.50	0.156	0.50	0.270	0.50

Damage evaluation with the above curves implies to estimate the differential settlements of earthquake solicited buildings. This evaluation is normally affected by significant uncertainty, being dictated by the nonhomogeneous subsoil conditions (Ishihara and Yoshimine, 1992), distribution of loads and structural properties of the buildings. Knowing these factors in detail is difficult, even for the study of a single building under static conditions, and thus alternative simplified approaches are pursued, that base the estimate of differential settlements on the values of absolute

settlements (e.g., Grant et al., 1974; Viggiani et al., 2012). The estimate of differential settlements is moreover difficult when dealing with large scale analyses where information become somehow vaguer. However, data on age and structural typology, plan dimensions, height and number of stories of buildings obtained from databases can be exploited to perform a preliminary risk assessment. With this aim, a two-step calculation is proposed in the present study, extending to liquefaction assessment the previously recalled procedure adopted for static conditions: firstly, absolute settlements are quantified with a simplified formula that includes the dependency on seismic input, subsoil characteristics and simple building properties; then a relation between differential and absolute settlements is inferred from the results of parametric numerical calculations where the coupling between heterogeneous liquefiable subsoil and structures having variable flexural stiffness is accounted for.

4.3.4 Absolute vs Differential Settlements

The factors influencing differential settlements of buildings recalled in the Eurocode 7 - PREN 1997 (CEN, 2008) include occurrence and rate of settlements; variation of ground properties; loading distribution; construction method and sequence of loading; stiffness of structures.

Compared to Bray and Macedo (2017) and Bullock et al. (2018), which provide estimates of the absolute building settlement, Bullock et al. (2019.b) propose three different approaches to calculate the probabilistic distribution of building residual and peak transient tilts depending on the available information. In the present study, the role of the above factors on the differential settlements is quantified with a specific calculation. Neglecting the effects of the construction sequence, not related to liquefaction, and considering for simplicity a uniform load distribution on building foundations, the effects of settlement rate, the variation of subsoil properties and stiffness of the structure have been evaluated performing a parametric numerical analysis (ITASCA V2D, 2016). The performed analysis shows that, while the settlement distribution depends on different factors like seismic motion, subsoil layering and properties, foundation width, soil-foundation contact, building inertia etc. (e.g., Karimi et al., 2018; Ramirez, 2019; Tokimatsu et al., 2019), the ratio between distortion and absolute settlements depends mainly on the stiffness of the structure-foundation complex and the variability of subsoil properties.

The studied subsoil scheme consists of three-strata (Figure 4-8), an intermediate liquefiable layer whose stress-strain response has been simulated with the critical state-

based plasticity model (PM4 sand; Ziotopoulou & Boulanger, 2013), a lower base and an upper crust whose stress-strain response has been simulated with hysteretic models coupled with Mohr-Coulomb (MC) failure criterion. For the sake of validation, the model has been inspired to the case study of a building in Terre del Reno (Emilia-Romagna, Italy) struck during the earthquake of May 20th, 2012 (M_w 6.1). Figure 4-8 shows a summary of the model characteristics, geometrical mesh, and constitutive parameters. Further details can be found in Modoni et al. (2019). In the first series of analyses, the flexural stiffness of the building-foundation system is pointed out. The studied scheme, depicted in Figure 4-8, includes a 10 m long plate of variable flexural stiffness modulus EI (from 0 to 260 MN*m), carrying a uniform load (50 kPa). To estimate the influence of seismic input, the calculation is performed for three different acceleration time histories, the one recorded during the May 20th, earthquake in Emilia Romagna and the other two scaled times 0.7 and 1.6, respectively. The plot of Figure 4-9.b, reporting the angular distortion β (defined in Figure 4-9.a) as a function of the maximum settlements w_{max} shows a clear correlation between the two variables. Both depend significantly on the seismic input, but the angular distortion can be significantly restrained, increasing the slab stiffness. It is also worth noting that the dots representative of EI=0 matches closely the curve proposed by Grant et al. (1974) that represents the upper bound of observation under static conditions. Multiple analyses performed with a different set of characteristics (e.g., soil relative density, layers thicknesses, foundation width, etc.) have shown a limited influence of these factors on the β - w_{max} relation.

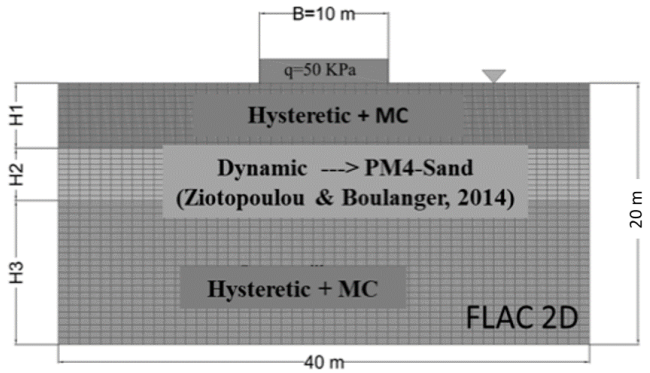

Figure 4-8 Numerical model implemented to study the absolute vs differential settlement relation.

Table 4-2 General properties defined in the numerical modelling.

ρ: soil density; K: bulk modulus; G: shear modulus; n: porosity; k: soil permeability; ϕ: friction angle; c: cohesion.

	General Properties						
Layer	P (kg/m³)	K (MPa)	G (MPa)	n	k (m/s)	Φ (°)	c (kPa)
Clayey crust	1250	65.8	14.1	0.48	8.15E-12	-	50
Deeper clayey layers	1330	388	83	0.55	1.02E-13	-	50
Sandy Layer	1449	13.79	29.88	0.44	2.00E-06	33	-

Table 4-3 Damping and PM4 Sand parameters.

L_1 and L_2: soil damping parameters; D_r: relative density; G_0: small-strain shear stiffness; h_{po}: plastic modulus calibration parameter; n^d: dilatation surface calibration coefficient; n^b: bounding surface calibration coefficient; A_{d0}: dilatancy calibration coefficient.

	Damping		**PM4 Sand**					
Layer	L1	L2	Dr	G_0 (Mpa)	h_{po}	n^d	n^b	A_{d0}
Clayey crust	-3	0.5	-	-	-	-	-	-
Deeper clayey layers	-2.2	0.3	-	-	-	-	-	-
Sandy Layer	-	-	variable	500	0.4	2.2	0.1	0.1

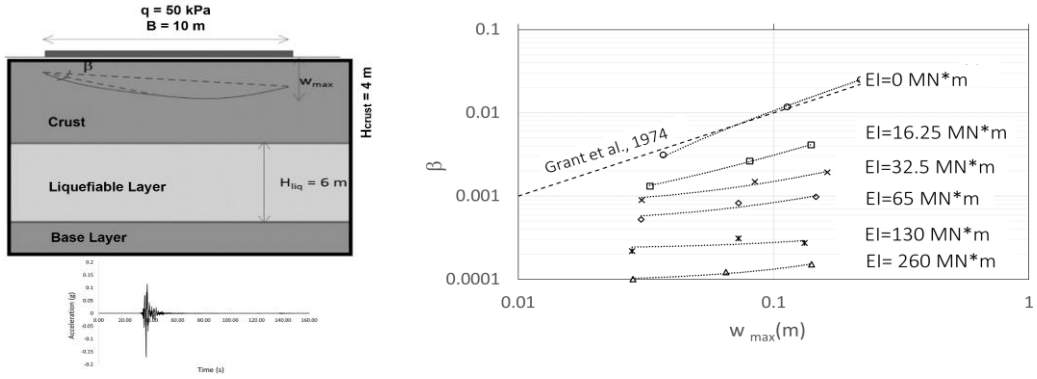

a b

Figure 4-9 (a) Scheme adopted for the numerical calculation; and (b) angular distortion vs. maximum settlement for variable seismic input and flexural stiffness of the foundation raft.

The second considered factor is the variability of subsoil properties, claimed by Ishihara & Yoshimine (1992) as one of the main causes of differential settlements. This issue has been investigated by introducing in the above numerical model the spatial variability of relative density in the liquefiable soil layer and performing random field analyses (Fenton & Griffiths, 2000). The definition of spatial variability requires an autocorrelation function that reproduces the spatial dependency within relatively short distances and a stochastic function characteristic of the spatially uncorrelated variability, i.e., at larger distances. These functions have been derived from the investigation carried out in Terre del Reno (Italy). Therefore, the spatially correlated variability has been modeled with an anisotropic exponential function having vertical autocorrelation distance equal to 0.77 m, found with a maximum likelihood criterion (Honjo & Kazumba, 2002) on the profiles of CPT tests Figure 4-10; the horizontal autocorrelation distance has been given considering literature indications (Studlein et al., 2012) that suggest values variable between 2 and 5 m depending on the depositional history of the deposit. Proven that the differential settlement is directly related to the ratio between the characteristic length of foundation and the correlation distance, a value equal to 2.0 m (i.e., the lower defined by Studlein et al., 2012) has been assumed in the present study to maximize the soil heterogeneity. The Markov correlation function's choice is justified by the simplicity of the model, primarily due to the definition of a process where the future only depends on the

present and not on the entire history, which fits with almost all the engineering applications.

After verifying the goodness of fit, the random variability of relative density has been modeled by assigning a lognormal probability function with a mean equal to 0.36 based on the interpretation of the CPTs available in the study area (Robertson & Wride, 1998; Idriss & Boulanger, 2008) (Figure 4-10). The standard deviation found in this specific case is equal to 0.07, but this value has been parametrically varied in future analyses for the sake of generality (Modoni et al., 2019). The lognormal distribution of the relative density agrees with both the study of Fenton (1999) and most of the real geotechnical situations, where variables are not symmetrically distributed. Last but not the least, negative values of geotechnical variables like the soil relative density that may result from a normal distribution do not have a physical meaning.

Fields of relative density like the one depicted in Figure 4-11 can be randomly generated with the local average subdivision method (Fenton & Griffiths, 2000) and considered as input for calculation of settlements.

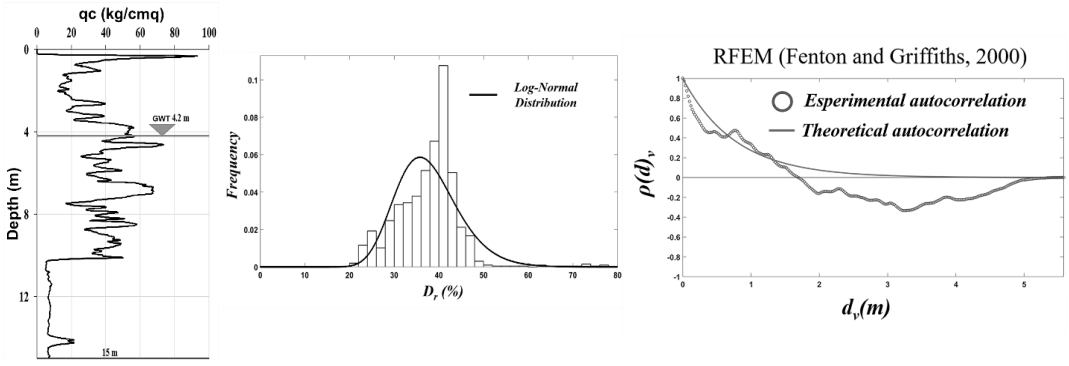

Figure 4-10 Random field analysis: derivation of random and spatial variability models.

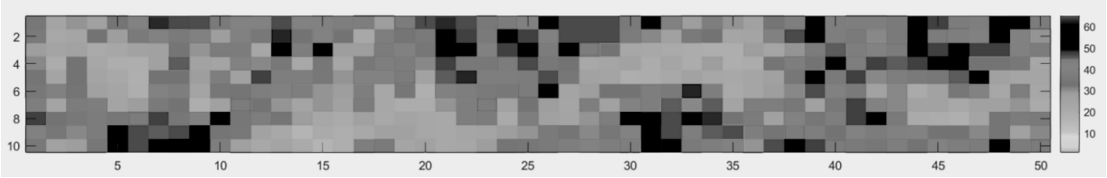

Figure 4-11 example of random field of relative density for the liquefiable layer.

The numerical analyses have been performed assigning random fields of relative density to the liquefiable layer in the liquefaction scheme of Figure 4-8, a 10 m wide slab with a uniform unit load equal to q = 50 kPa. Nil flexural stiffness (EI = 0) has

been assigned to the slab to infer the most conservative condition according to Figure 4-9.b, i.e., the one that amplifies differential settlements. As before, the seismic input has been assigned scaling times 0.7, 1.0, and 1.6, the acceleration time history of May 20th, 2012 event in Terre del Reno. The variability of subsoil properties has been parametrically varied, assigning different variation coefficients to the log-normal random distribution (CV = 0.1, 0.2, and 0.3). Together with the low assumed values of autocorrelation distances, these quantities should provide conservative estimates of the differential settlement (see Studlein et al., 2012). For each combination of factors, twenty random fields of relative density have been generated and subjected to the numerical calculation. This number has been chosen considering the time necessary for one calculation. Absolute and differential settlements have been estimated from the deformation of the slab, as shown in the sketch of Figure 4-12.a. The plot of Figure 4-12.b readily shows that, despite a large variation of settlements generated by seismic inputs of largely different intensity, a direct proportionality can be inferred between differential (δ_{max}) and absolute (w_{max}) values.

Based on this observation, the following linear relation is adopted between these two variables:

$$\delta_{max} = \alpha \cdot w_{max} \qquad \textit{Eq. 4.5}$$

Figure 4-12.b shows the statistical distribution of the coefficient α, from which a normal distribution having mean value equal to 0.53 and standard deviation equal to 0.08 is inferred.

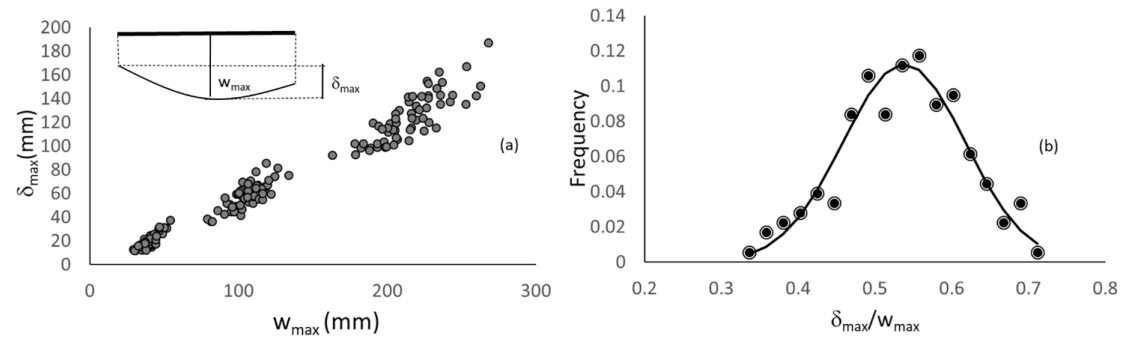

Figure 4-12 (a) Differential (δ_{max}) vs. absolute (w_{max}) settlements from the parametric random field analysis; and (b) statistical distribution of the coefficient α defined in Eqn. (5).

4.3.5 Loss model

The computation of losses associated with damage (DV|DM) is the last step of the assessment procedure depicted in Figure 4-1. Several studies have proposed to define damage/losse relations based on socio-economic consideration (e.g., Lee and Mosalam, 2006; Moehle, 2003; Comerio, 2005; Krawinkler, 2005; Mitrani-Reiser et al., 2006). Focusing for simplicity on the repair losses, i.e., neglecting other indirect costs, a deterministic evaluation scheme defined in Hazus (FEMA, 2003) has been adopted in the following. This scheme introduces four different damage limit states (Slight, Moderate, Extensive, and Complete) and associates to each of them a loss cost (rc_i) expressed as a percentage of the total demolition and reconstruction cost (RC_i). The ratios $(rc/RC)_i$ are defined in the code for 33 different building categories. Table 4-4 shows an example for residential and industrial buildings.

Combining the loss factors with the probability of reaching each of the four defined damage states (Pds_i) enables to compute the Mean Damage Rate (MDR) as follows:

$$MDR = \sum_i P_{ds_i} * (rc/RC)_i \qquad \textit{Eq. 4.6}$$

The economic losses due to the combination of physical damage and the loss of serviceability can be determined following the Hazus (FEMA, 2003) procedure. Considering the generic building, the method proposes to calculate the total loss by adding the repair cost to the loss of income arising from the non-use of the building. The repair cost, tot_rc_i, results from the structural and non-structural damage (rc_i), including those related to the business inventory (INV_DAM_i), if present.

In general, assumed the total demolition and reconstruction cost RC_i and estimated the annual gross product of the Company $PROD_i$, the total loss due to the physical damage and loss of business inventory could be evaluated as follows:

$$\begin{aligned} tot\_rc_i &= rc_i + INV\_DAM_i \\ &= RC_i \left(\sum_{ds} P_{i_{ds}} \cdot \left[\left(\frac{rc_i}{RC_i} \right)_{ds_i} \right] \right) \\ &+ Prod_i \left(\sum_{ds} P_{i_{ds}} \cdot [(INV/Prod)_i \cdot INV\_damage_i] \right) \end{aligned} \qquad \textit{Eq. 4.7}$$

Where (rc_i/RC_i), $(INV/PROD)_i$ and the fraction of damaged stocks are listed in Table 4-4; for each of the building typology defined in Hazus and P_{ids} is the probability of reaching predefined damage limit states.

An additional term that corresponds to the total loss accounts for the building's lack of functionality and is related to the time needed for building restoration FLT_i. The latter differs according to the building use; in this calculation, they were considered equal to the costs of renting an alternative structure for housing and to the loss of income for industrial activities.

$$ul_i = \sum_{ds}(INC_i \cdot FLT_i) \cdot P_{i\_ds} \qquad \textit{Eq. 4.8}$$

The loss of functionality FLT_i (expressed in days) associated with each damage limit state was assessed as a product of the time necessary to restore the generic function of the building BRT_i and a reduction factor linked to the possibility of transferring the activity elsewhere, SIM_i (FEMA, 2003).

$$FLT_i = BRT_i \cdot SIM_i \qquad \textit{Eq.4.9}$$

Table 4-4 reports the loss factors values considered in the above-described procedure.

Table 4-4 Loss factors introduced in the risk assessment procedure, as reported in the Hazus code (FEMA, 2003).

		Slight	*Moderate*	*Extensive*	*Complete*
RES1 Residential buildings	*rc/RC*	0.02	0.10	0.45	1.00
	INV/PROD	-	-	-	-
	INV_damage	-	-	-	-
	BRT (days)	5	120	360	720
	SIM	0	0.5	1.0	1.0
IND Industrial buildings	*rc/RC*	0.02	0.10	0.355	1.00
	INV/PROD	0.05	0.05	0.05	0.05
	INV_damage	0.0	0.0	0.0	0.50
	BRT (days)	10	90	240	360
	SIM	0.5	1.0	1.0	1.0

4.3.6 Remediation

The decision-making to mitigate risk applies to the above-defined holistic model, including the multiscale connections outlined in Figure 4-1. Briefly recalling the fundamental steps, liquefaction is triggered when a relatively high seismic demand combines with susceptible subsoil. The phenomenon may turn or not into the damage of buildings and infrastructures depending on their physical fragility. Damaged systems become progressively unable to withstand their function, and thus, depending on its severity, physical damage turns into a lack of serviceability. The consequences for society depend on the relevance of the function provided by the infrastructure for the served community, on the repairability/replaceability of this function or, in more general terms, on the preparedness of the community to withstand its absence. Interrupting this chain is the scope of mitigation, acting separately on one component of the system, or undertaking a holistic strategy aimed to reduce the overall impact on society.

The Japan Geotechnical Society (JGS, 1998) envisages three different intervention classes (Figure 4-13), acting respectively on auxiliary facilities supporting/replacing the function of the concerned infrastructure, on the physical reinforcement of the structures or of the ground. In general, mitigation actions can be subdivided into two main categories, strategic or non-technical when aimed at improving the functionality of the considered system with the creation of auxiliary facilities or with modified management to face critical situations, or technical when operating on the physical systems with structural reinforcement or ground improvement.

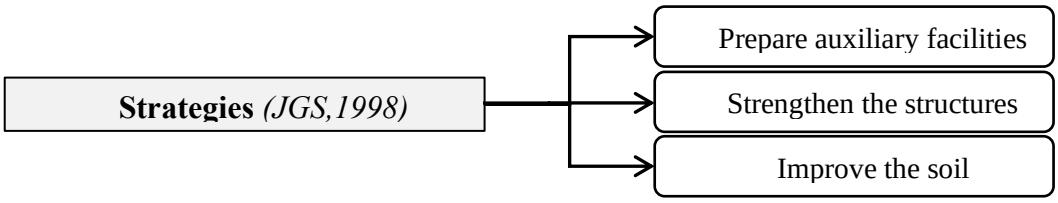

Figure 4-13 Strategies for liquefaction risk mitigation.

Non-technical strategies generally require an analysis of the behavior of a system under critical scenarios and to prepare a series of actions able to reduce the impact on the community and improve its resilience. From a technical viewpoint, being the liquefaction phenomenon ruled by the concurrence of different factors, i.e., non-plastic

soil in a loose state, saturation, hampered drainage, various mitigation techniques may be carried out to interrupt the chain of mechanisms responsible for the phenomenon. Soil susceptibility may be reduced by decreasing the contractive tendency upon cyclic loading, e.g., utilizing dynamic compaction (Mayne, 1984), vibratory techniques (Kirsch and Kirsch, 2016) or blasting (Lyman, 1941), or adding a finer plastic material (El Mohtar et al., 2013) to reduce the mobility of grains upon shaking. Triggering may be avoided by preventing the excess pore pressure build-up with induced partial desaturation (Mele et al., 2018) or facilitating its exhaust with horizontal and vertical drains (Chang et al., 2004). Other possible countermeasures consist of limiting the impact on the superstructure by reinforcing foundations with piles, columnar or lattice wall inclusions created with jet grouting (Yamauchi et al., 2017), deep soil mixing (Nguyen et al., 2012), or stone columns (D'Appolonia, 1954). Reinforcements have the twofold scope of reducing shear strains in susceptible soils and transfer loads to deeper non-liquefiable strata.

A list of possible ground improvement solutions describing principles, drawbacks, and costs is provided by the JGS (2011). From a purely mechanical viewpoint, the function of ground improvement can be classified as follows, being the single ground improvement technique able to reach one or more of the following goals:

Densification: reducing the volume contraction tendency of the soil upon shaking

Stabilisation: reducing the mobility of grain and volume contraction tendency of the soil upon shaking

Drainage: reducing the pore pressure build-up

Desaturation: preventing the pore pressure build-up

Reinforcement: reducing the shear strain into liquefiable soil and transferring loads to more competent strata.

From a technical viewpoint, Olarte et al. (2017) show the importance of evaluating holistically the potential tradeoff of liquefaction mitigation, which on the one hand may reduce foundation settlements and rotations and, on the other hand, may increase ground shaking intensity, resulting in more significant drifts and structural damages. These authors performed a series of centrifuge tests to rank the effectiveness of three liquefaction countermeasures (i.e., densifications, drainages and in-ground structural reinforcements) in preventing the liquefaction-induced damage on a 3-story steel moment frame structure. In parallel, Ramirez et al. (2019) conducted 3D, nonlinear, solid-fluid, fully-coupled, effective stress, dynamic finite element (FE) simulations in the object-oriented, open-source, finite element (FE) computational OpenSEES platform (Open System for Earthquake Engineering Simulation, Mazzoni et al., 2006)

to evaluate the influence of prefabricated vertical drains (PVDs) on the performance of soil-foundation-(mitigation)-structure (SFMS) systems.

Olarte et al. (2019) found that settlement and rotation of the foundation strongly depend on the drainage conditions, soil properties, and seismic motion, and each mitigation strategy can reduce them. On the other hand, the adopted techniques differently impacted the generation of excess pore pressures in the underlying soil, the foundation accelerations, and transient rotations. Ground densification reduces excess pore press generation, permanent foundation settlement, and tilt, but also amplifies the accelerations and forces experienced in the superstructure. Prefabricated vertical drains reduce the duration of large excess pore pressures in the underlying soil, minimizing the permanent and transient foundation settlement and tilt more than other mitigation methods, while amplifying the seismic demand and flexural deformations in the superstructure. More enormous excess pore pressures and liquefaction that boosted the foundation's permanent settlement and tilt than other mitigation methods have been recorded due to the presence of in-ground walls that limited the water flow and amplified accelerations.

Given the above, the choice of the optimal solution must come out for each application from a series of consideration involving not only technical efficiency but also: the feasibility of treatments concerning the scope of the project and the existing boundary conditions, taking into account also environmental issues and, last but not least, cost-effectiveness. A classification of the considered methods considering all these aspects is summarized in Table 4-5 where a score is given to each technique. This classification serves as a primary judgment on the suitability of the different techniques to different possible situations and as a tool for the first selection of mitigation strategies following a risk analysis. Therefore, a grade and a relative weight are first given to the following fields, considering their relevance for the project:

- Site conditions, considering if the ground improvement concerns free field or is addressed to existing buildings/infrastructures, distinguishing in this case if the structure is in operation or out of order;
- Subsoil characteristics, distinguishing the type of soil to be treated (with the presence of fine component), stratigraphy (crust of non-liquefiable soil), depth of the portion to be treated (<3m; 3-12 m; 12-18 m; 18-25 m);
- Extension of the ground to be treated (<1000 m^2; 1000-5000 m^2; >5000 m^2);
- Foundation type of the building/infrastructure under concern (shallow or deep);
- Constraints like the presence of buildings nearby (presence of buildings or utilities);

- Environmental restraints;
- Cost.

Then, the considered ground improvement methods have been evaluated considering each of the above issues. For instance, impacting techniques like deep dynamic compaction or blasting are discouraged near existing buildings giving a nil grade. Finally, each grade given to a technique with reference to a specific issue is weighted for the relevance of the issue. In this way, a score is obtained for all the techniques; it drives the stakeholders (managers, technical and non-technical personnel) to get oriented on the most suitable solution.

Table 4-5 : Evaluation of ground improvement methods for liquefaction mitigation (D7.4, Liquefact, 2019).

LEGEND		
APPLICABILITY	Good	3
	Medium	2
	Low	1
	Not applicable	0
RELEVANCE	Very important	4
	Important	3
	Medium important	2
	Less important	1
	Not applicable	0

List of G.I. technologies:
Deep dynamic compaction
Vibro compaction
Blasting compaction
Compaction grouting
Low pressure grouting
Earthquake drains
Induced partial saturation
Vibro replacement
Deep soil mixing
Jet grouting

Question		RELEVANCE	Relative weight	DEEP DYNAMIC COMPACTION		VIBRO COMPACTION				BLASTING COMPACTION		COMPACTION GROUTING		LOW PRESSURE GROUTING		EARTHQUAKE DRAINS				INDUCED PARTIAL SATURATION				VIBRO REPLACEMENT		DEEP MIXING		JET GROUTING	
						Deep		Shallow / Replacement								Vertical		Horizontal		Vertical		Horizontal							
			(%)	Applicability	Weighted score	Applicability	Weighted score	Applicability	Weighted score	Applicability	Weighted score	Applicability	Weighted score	Applicability	Weighted score	Applicability	Weighted score	Applicability	Weighted score	Applicability	Weighted score	Applicability	Weighted score	Applicability	Weighted score	Applicability	Weighted score	Applicability	Weighted score	Applicability	Weighted score
1. Site conditions	1.1) Free field	4	16.0	3	48	3	48	3	48	3	48	3	48	3	48	3	48	3	48	3	48	3	48	3	48	3	48	3	48
	1.2) Existing buildings in operation			0	0	0	0	0	0	0	0	1	16	1	16	1	16	3	48	1	16	3	48	0	0	0	0	1	16
	1.3) Existing buildings out of order			0	0	0	0	0	0	0	0	2	32	2	32	2	32	3	48	2	32	3	48	0	0	0	0	2	32
2. Soil type	2.1) Gravel soils	4	16.0	2	32	2	32	2	32	2	32	2	32	3	48	1	16	1	16	2	32	2	32	1	16	1	16	3	48
	2.2) Sandy soils			3	48	3	48	3	48	2	32	3	48	3	48	3	48	3	48	3	48	3	48	2	32	2	32	3	48
	2.3) Inorganic silts, clays silts of low to medium plasticity			1	16	0	0	0	0	0	0	1	16	0	0	1	16	1	16	1	16	1	16	3	48	3	48	2	32
3. Stratigraphy	3.1) Soil crust	2	8.0	1	8	2	16	3	24	1	8	3	24	3	24	3	24	3	24	3	24	3	24	2	16	3	24	3	24
	3.2) No soil crust			3	24	3	24	3	24	3	24	3	24	3	24	3	24	3	24	3	24	3	24	3	24	3	24	3	24
	3.3) Layered liq/non liq soils			1	8	2	16	3	24	1	8	1	8	3	24	3	24	0	0	3	24	3	24	3	24	3	24	2	16
4. Depth of the zone to be treated (based on case histories)	4.1) <3 m	4	16.0	3	48	3	48	3	48	2	32	1	16	1	16	1	16	2	32	3	48	1	16	3	48	3	48	2	32
	4.2) 3-12 m			3	48	3	48	1	16	3	48	3	48	3	48	2	32	3	48	3	48	3	48	3	48	3	48	3	48
	4.3) 12-18 m			1	16	2	32	0	0	2	32	3	48	3	48	3	48	2	32	3	48	2	32	2	32	3	48	3	48
	4.4) 18-25 m			0	0	1	16	0	0	0	0	2	32	2	32	2	32	1	16	3	48	1	16	1	16	2	32	3	48
5. Size of area to be improved	5.1) Small (<1000 m^2)	1	4.0	0	0	0	0	3	12	0	0	3	12	3	12	3	12	3	12	3	12	3	12	0	0	3	12	3	12
	5.2) Medium (1000-5000 m^2)			1	4	1	4	2	8	1	4	3	12	3	12	3	12	2	8	3	12	2	8	1	4	3	12	3	12
	5.3) High (>5000 m^2)			3	12	3	12	1	4	3	12	3	12	3	12	3	12	1	4	3	12	1	4	3	12	3	12	3	12
6. Foundation type	6.1) Shallow foundations	1	4.0	0	0	3	12	3	12	1	4	3	12	3	12	3	12	3	12	3	12	3	12	3	12	3	12	3	12
	6.2) Deep foundations			0	0	1	4	0	0	0	0	1	4	3	12	3	12	1	4	3	12	3	12	0	0	3	12	2	8
7. Project constrains	7.1) Low overhead clearance	2	8.0	0	0	0	0	0	0	0	0	2	16	3	24	2	16	3	24	2	16	3	24	0	0	0	0	2	16
	7.2) Adjacent structures			0	0	0	0	1	8	0	0	3	24	3	24	3	24	2	16	3	24	2	16	0	0	3	24	3	24
	7.3) Existing utilities			0	0	0	0	1	8	0	0	2	16	2	16	2	16	2	16	2	16	2	16	0	0	0	0	2	16
8. Presence of subsurface obstructions		2	8.0	0	0	0	0	0	0	0	0	2	16	2	16	2	16	3	24	2	16	3	24	0	0	1	8	2	16
9. Environmental compatibility		2	8.0	3	24	3	24	3	24	1	8	2	16	2	16	3	24	3	24	3	24	3	24	3	24	2	16	2	16
10. Cost (per sq. m. of treated area)		3	12.0	3	24	3	24	1	8	3	24	1	8	1	8	2	16	2	24	2	16	2	16	3	24	1	8	1	8
Total			100.0																										

4.3.7 Cost/benefit analysis

In risk assessment, the effectiveness of mitigation should also be evaluated from the cost/benefit viewpoint. This implies to compare on a financial basis the budget spent on mitigation with the reduction of losses. Considering that mitigation, when undertaken, is a cost while losses depend on the probability of liquefaction occurrence, the benefit/cost analysis should be performed on an annual basis considering the residual lifecycle of the structure/infrastructure under concern.

There are different criteria to compute the annualized cost of mitigation. One of the most adopted is to equally distribute the invested capital over the lifecycle of the structure, adding the interest rate (fixed or variable). The question can be seen as equivalent to borrow the capital necessary for mitigation from a bank at a fixed rate mortgage and pay it back with a constant annual amount. In this way, the annualized cost sustained for mitigation is the amount paid by the borrower every year that ensures that the loan is paid off, in full of interest, at the end of its term.

This cost should be compared with the annualized benefit, i.e., the earthquake losses saved per year, which for a probabilistic assessment is computed by integrating the product between losses given by earthquakes of different intensity and their annual occurrence probability. In the hypothesis of 100% efficiency of mitigation in preventing the liquefaction-induced damage, benefit/cost analyses are performed considering several unitary treatment costs. For each of them, the annual mortgage rate is compared with the reduction in the annualized total loss, which is calculated as defined by the PBEE methodology.

$$Annual\ Loss = \sum_i AFE_i \cdot (tot_{rc_i} + ul_i) \qquad Eq.4.10$$

In the case of new building construction, the annual loss is calculated to evaluate different design approaches to choose the most convenient solution (Blockley, 2013).

4.3.8 Methodology

The above relations form the sequence of steps summarized in the flow chart of Figure 4-14, conceived to estimate losses on a portfolio of buildings. The procedure implies identifying and characterize each building with reference to the implemented calculation, i.e., determining the geographical coordinates of the centroid, its structural

typology, extension, and the number of stories, the latter necessary to identify the appropriate fragility function and estimate unit load. The subsoil is determined with the depth, width, and relative soil density of the liquefiable layer, which implies processing all available investigations (boreholes, CPT profiles) as described in Chapter 3. Conjugating this information with the base seismic input, the local seismic response can be analyzed at the building position to determine the parameters necessary for the analysis's further steps. They consist of estimating the maximum absolute settlement of the building with Eqn. (3.23), transform it into a differential settlement with Eqn. 4.5, and computing the probability associate with each damage level through the procedure described in Figure 4-7 and Table 4-1.

Finally, the estimate of losses can be obtained by multiplying each of these probabilities with the cost associated with the corresponding damage level (Eqn. 4.6). The physical damage computed on each building is a fraction "*MDR"* of the total demolition/reconstruction cost. Depending on the building use, the translation of physical damage into economic loss requires introducing a reconstruction and relocation/temporary rental costs (respectively *RCi* of Eqn. 4.7 and *INCi* of Eqn. 4.8) and defining the annual business revenue PRODi (Eqn. 4.7).

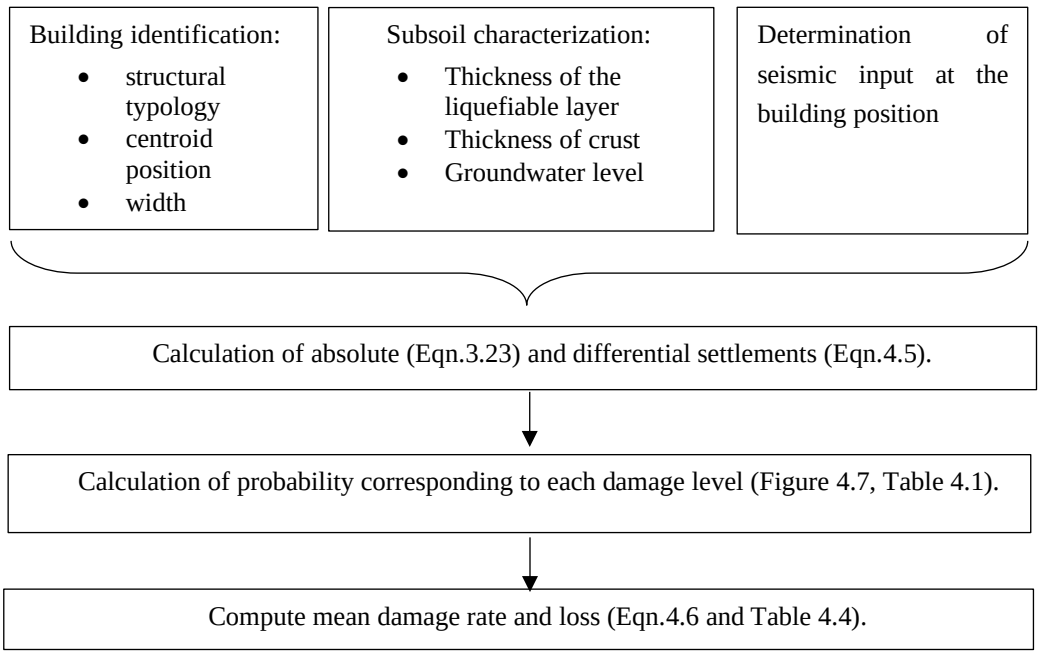

Figure 4-14 Flow chart for the estimate of losses on a building.

The calculation can be performed for a selected seismic scenario, assigning the corresponding seismic input, or for the entire lifecycles of the building. In this second case, the seismic input must be defined in probabilistic terms, considering the seismic

hazard of the area: the resulting annual loss (evaluated through Eqn. 4.10) represents the benefit in the following benefit/cost analysis.

4.4 **Data management and Uncertainty**

Earthquake-induced liquefaction disasters *EILD* has often struck densely urbanized areas with severe consequences for the population. Although not being the only event of such a size, the case of the February 2011 (Mw6.2) Christchurch Earthquake is probably the most impressive example of liquefaction induced damage in an urban environment. Due to the widespread liquefaction, a diffuse and unprecedented economic loss was experienced by most of the Region, involving the community in a slow, tiring, and still ongoing reconstruction process. This and other recent events such as the Mw9.0 2011 Tohoku (Japan) Earthquake, the Mw6.1 2012 Emilia (Italy) Earthquake, the Mw 7.3 2016 Kumamoto (Japan) Earthquake have clearly shown the importance of being prepared for a community by implementing adequate emergency plans to face the post-earthquake scenarios, whose main purpose is to reduce the total loss, provide reasonable living conditions to the affected population and speed up the recovery to normality. To this aim, Local Authorities and the Scientific Community recognized the usefulness of organizing pre-existing data and post-earthquake surveys into Geodatabases to facilitate emergency management and data-sharing among the stakeholders. Taking advantage of the previous experiences, developing of a community database of liquefaction-related phenomena and case histories has been recently initiated by the Pacific Earthquake Engineering Research (Stewart et al., 2016). PEER's Next Generation Liquefaction (NGL) project takes advantage of the partnership between PEER and various public agencies (in the United States, Japan, New Zealand, and Taiwan) to build a robust collection of worldwide liquefaction case histories, including laboratory tests, physical modelling and numerical studies on key aspects of liquefaction triggering and related phenomena. Finally, the current approaches for decision-making against risk rely on tools capable of handling analyses characterized by a spatial multiscale approach, in a way that emphasizes both the spatial distribution of the phenomena and the spatial relationships with the territory elements and human activities. To this aim, the modern Geographical Information Systems (GIS) provide an efficient supporting tool in any risk assessment procedures.

For liquefaction risk assessment procedures, a GIS Platform allows the following activities:

- The management of geographical information at different resolution levels, which in turn enables them to constantly update the amount of georeferenced data coming from different public/private stakeholders;
- The combination of different data format (raster images, vectors, tables, spreadsheets …) which can be easily assessed, read, and combined to process the input data automatically;
- The possibility of post-processing the obtained results through dynamic and interactive Maps, which allow performing quantitative spatial and reliability analyses.

Such flexibility in their structure, their wide range of applications, and the existence of different opensource GIS Platforms have encouraged the interaction among different disciplines (geology, geotechnical/structural engineering, insurance..) and stakeholders allowing not only to manage post-Earthquake emergencies but also to extend the analysis to wider fields of applications. These aspects resulted in the development of consolidated Platforms, whose data acquisition, implementation, and presentation are governed by national and International Standards, e.g., the INSPIRE Directive (Infrastructure for Spatial Information in the European Community), which sets the minimum conditions for interoperable sharing and exchange of spatial data across Europe (https://inspire.ec.europa.eu/). On the other hand, the above concerns imply dealing with a huge amount of data from different sources, added in different periods, and continuously updated. Such data availability represents an advantageous situation to the processing purpose, but it inevitably introduces significative uncertainty factors whose control can be partially managed through statistics and geostatistics methods.

4.4.1 Uncertainty in data measurements

Even considering with probabilistic models the uncertainty associated with the ground-motion estimation and the likelihood of liquefaction triggering, the above procedures are affected by other uncertainties related to measurement biases of in situ data (Baecher & Christian, 2003). Despite a tendency to discipline the execution and interpretation of subsoil investigation to improve consistency, quality, and reliability (e.g., NZGS, 2016), a major part of data presently available for risk assessment has been obtained in previous times without of date standards. An attempt to fill this gap

is proposed by Madiai et al. (2016), who performed an experimental study to convert the mechanical CPT results into equivalent electrical CPT data. Based on the analysis of more than 4000 couple of points measured to the same depth, the authors propose to correct the equivalent normalized tip resistance (q_{c1ncs}) and the Soil Behaviour Type index Ic as shown in Figure 4-15.

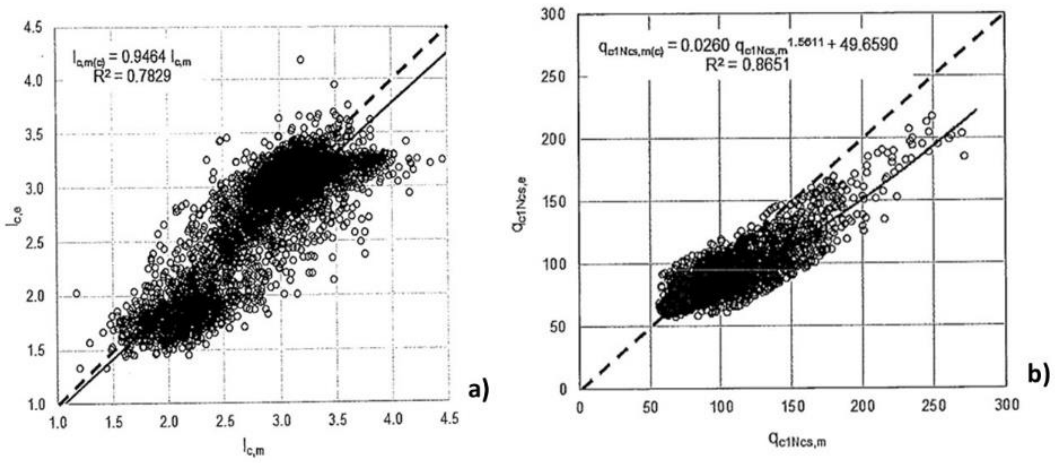

Figure 4-15 a) Ic values calculated from CPTm and CPTe data and best regression model adapted to mechanical CPT data; b) qc1n,cs values calculated from CPTm and CPTe data by following the procedure of Boulanger & Idriss (2014) and best regression models.

4.4.2 Geostatistical Analysis of Data

Regionalized phenomena, i.e., whose characteristics refer to space and present a spatial structure or organization, can be modelled through a geostatistics approach that defines a regionalized variable z(x) as the realization of the random distribution Z(x). It can be modeled through the fitting of a spatial analytical function called variogram.

In geostatistics (Matheron, 1965), the value of a variable in a generic point of the map is computed as a linear interpolation of the values obtained on the investigated profiles. A series of actions (displayed in Figure 4-16) consisting in the mathematical definition of the spatial structure governing the investigated variable is preparatory to the geostatistical interpolation. Firstly, considering pairs of samples, the squared difference between the values is calculated. The resulting dissimilarities are plotted against the distance among ample pairs “h” in geographical space, forming the

variogram cloud. The subsequent step concerns the sliced of the variogram cloud into classes according to separation in space. The average dissimilarities in each class form the sequence of values of the experimental variogram. It can be observed that the average dissimilarity between values increases proportionally to the increase in spacing between the pairs of sample points. For large distances, the experimental variogram reaches a sill that can be equal to data variance. A relevant aspect is the behavior at the origin of the variogram, which indicates the type of continuity of the regionalized variable: differentiable, continuous but not differentiable, or discontinuous. This last case is a symptom of the so-called nugget-effect, meaning that no spatial correlation exists among the measured points or equivalently that the values of the variable change abruptly at a microscopic scale, like gold grades when a few gold nuggets are contained in some samples. On the contrary, a non-zero slope of the variogram near the origin indicates spatial structure. An abrupt change in slope indicates the passage to a different structuration of the values in space. Theoretical variograms, based on the analytical model, and the kriging interpolator allow the model to describe such transitions and visualize the different spatial associations of the values separately as maps.

The maps displayed in the following chapters have been obtained by interpolating the theoretical variograms through ordinary kriging. Among the different types of kriging, it gives the optimal predictions under the assumption that the process is second-order stationary and is distributed normally. That observed values are a realization of a stationary stochastic process of a simple structure. This model is the weighted linear combination of the observation with the white noise process. Thus, the optimal predictor will be accepted by minimizing the mean squared prediction error. The observed values are first used to estimate the unknown parameters of the process and compute the empirical semivariogram. These observed values, parameters, and semivariogram are used to produce the best linear unbiased predictor of the unobserved point. For each variable, the standard error map (obtained as a by-product of the kriging operation) is overlapped to the prediction map, providing a quantitative measure of the uncertainty. Obviously, the smaller the variance, the better will be the results. On the contrary, in the lack of new data, areas characterized by a high level of uncertainty will be discarded from the analysis.

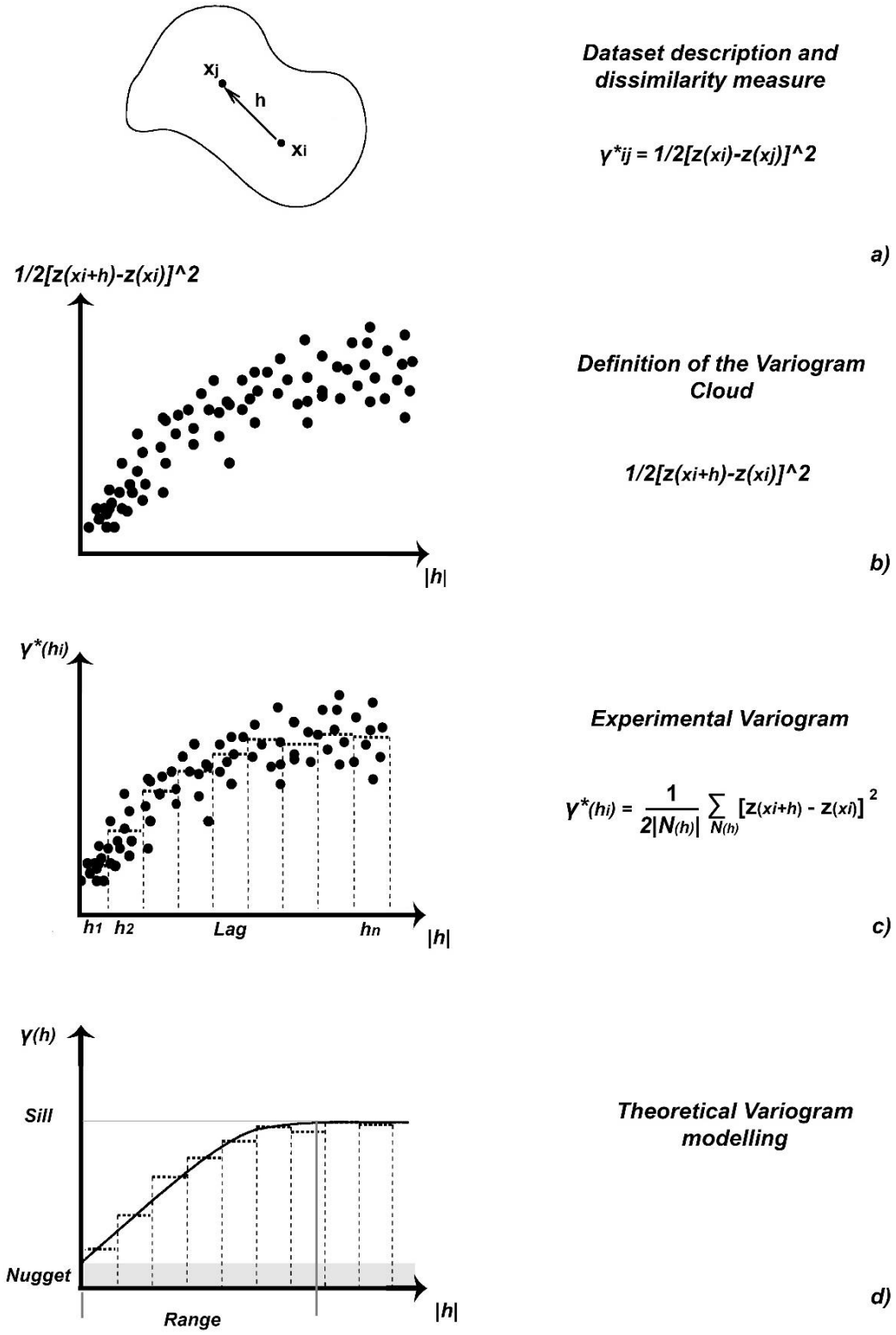

Figure 4-16 Subsequent steps in the modelling of a regionalized variable according to the geostatistics method (modified from Wackernagel, 1998).

Definitely, starting from the dataset of measures/samplings x_i, for any distance h and any N(h) pairs of distant points h, the variogram modeling process can be achieved in two steps:

Building the experimental variogram through the function:

$$\hat{\gamma}(h) = \frac{1}{2|N(h)|}\sum_{N(h)}[z(x_i + h) - z(x_i)]^2 \qquad \textit{Eq. 4.11}$$

where $|N(h)|$ number of pair.

Find a mathematical function capable of best fitting the experimental variogram. In Figure 4-17, the most applied interpolators in regionalized variable studies (namely the spherical and exponential models) are showed (Chilès and Delfiner, 1999):

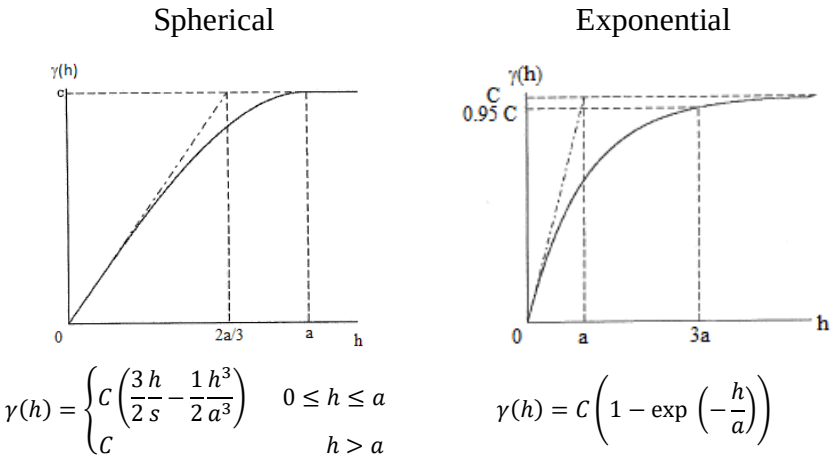

Figure 4-17 Example of analytical functions used to fit the variogram.

The difference with a straight interpolation with mathematical functions (e.g., polynomial) consists of the fact that estimates are considered as statistical variables, and thus a standard error term, which is a proxy of the standard deviation, is associated with them. The main advantage of this information is that the reliability associated to the estimate is known (a large standard deviation implies a greater uncertainty and lower reliability). In this way, the analysis's quality can be improved, confining it to the zones where estimates are more robust. Regarding geotechnical and site characterization problems, it is immediate to understand that standard deviation drops

where more investigations are close to each other, while it assumes intolerable values where the investigation is limited or totally missing. Hence, the standard deviation map can be viewed as a tool to increase completeness of the analysis, filling the gap of information with additional investigation.

A paramount difficulty of risk assessment for systems spread over large territories is evaluating variables (e.g., subsoil properties) from the investigation outcomes performed in a discrete number of positions. Sometimes, the original information is affected by inconsistencies, like, for example, largely different variable values are measured even for boreholes close to each other. Possible reasons for such a discrepancy can be sought in different directions, like, for instance, different standards adopted in the execution of tests, to a wrong location of the borehole. This inconsistency of investigation represents one of the major causes of error in interpolating information over the areas, resulting in punctual values of a given variable, which markedly differ from the spatial trend inferred from contiguous investigations. To identify such singularity and quantify uncertainty of the estimate in each position, geostatistical tests (Chilès and Delfiner, 2012) are beneficial. In territorial studies of liquefaction, geostatistical tools have been adopted, for instance by Baker and Faber (2008) to compute the distribution of liquefaction potential indicators in the city of Adapazari (Turkey), by Pokhrel et al., (2015) to map the Liquefaction Potential Index (Iwasaki et al., 1978) from SPT results in the city of Urayasu (Japan) and by Zhu et al. (2017) to quantify the probability of liquefaction based on CPTu data.

Geostatistical tools can be recurrently used to assess the quality of available information and filter low-quality ones. An issue related to the collection of subsoil information over large areas is that investigations are rarely performed with the same standard, and data are not always consistent each other. This inconsistency frequently stems from different execution, reporting, interpretation standards, other sources like mispositioning the investigation sites over the map, etc. Geostatistical based tests like the boxplot (Montgomery et al., 2012) enable to evaluate the quality of data from the continuity of information estimated from nearby investigation. A boxplot test represents an expeditious but not arbitrary criterion to filter anomalous data, being possible to analyze and manage data in a fully automatic way, i.e. without the need for the operator to pick singularly data and drive outcomes. Once problematic data are identified, it is possible to verify the origin of inconsistency, correct errors or eventually discard the datum. The beneficial effects can then be measured with a reduction of the estimate standard error.

For a given variable, a boxplot shows the three quartiles on a rectangular box representing respectively the 25, 50 (i.e. the median value) and 75 percentiles. The interquartile range IQR is defined as the difference between the third and the first quartiles:

$$IQR = Q_3 - Q_1 \qquad \textit{Eq. 4.12}$$

Each point falling outside from the interval Q_1-1.5*IQR and Q_3+1.5*IQR is assessed as a potential outlier, extreme outlier if considering the interval Q_1-3.0*IQR and Q_3+3.0*IQR.

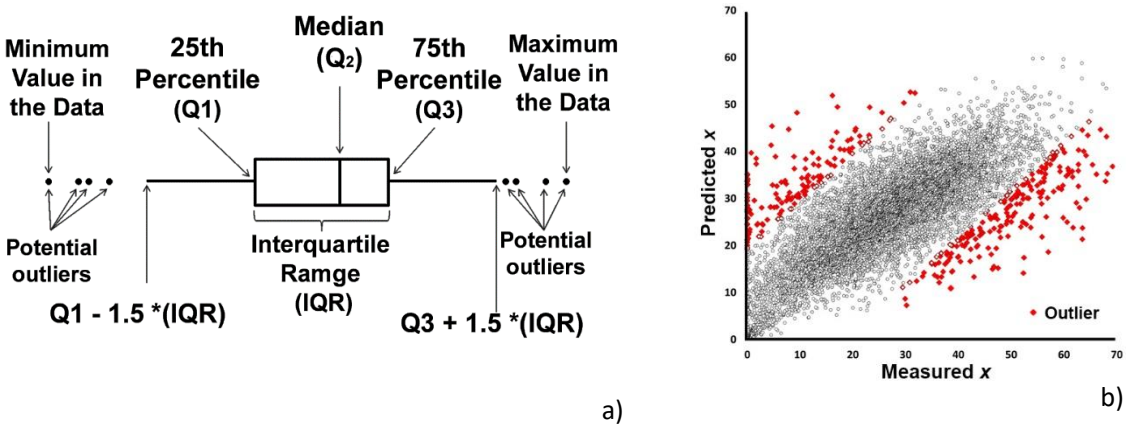

Figure 4-18 – a) Box plot test and identification of outliers; b) Example of cross validation to remove inconsistent data for a given variable x.

In the present case, the tolerability criterion has been fixed considering the 25 and 75 percentiles of the standard deviation of estimate and discarding the data assessed as outlier through the boxplot criterion, red points of Figure 4-18.

4.4.3 Error Propagation Theory

Evaluating the role of uncertainty in the assessment of risk is a special case of error propagation. The basic idea is that uncertainties in input parameters propagate through the rest of the calculation and affect the result. For example, an engineer might estimate a factor or a property (a seismic intensity measure, the parameters of a soil model, etc.), use them in some cascade calculation process, and use results to compute risk. Each of these steps involves errors on its own, and uncertainties in the original estimate

will affect the numbers calculated at each subsequent step. The study of error propagation aims to deal rationally with this problem (e.g., Baecher & Christian, 2003). In cascade phenomena like liquefaction, the uncertainty that arises at a certain level propagates at the upper levels, and methodologies are needed to evaluate effects (e.g., Kaplan, 1981; Paté-Cornell, 1994; Bradley et al., 2009; Ching et al., 2009). Well-established reliability methods, such as FOSM, FORM/SORM, and Monte Carlo simulation, provide useful techniques for quantifying the propagation of uncertainty at the upper level (Nadim, 2007) and reveal which parameters contribute most to the uncertainty and probability of failure. In the First Order Second Moment approach (Ang and Tang, 1984), the analytical approximations for the mean and standard deviation of a parameter of interest are provided as a function of the mean and standard deviations of the various input factors, and their correlations by mean of the first terms of a Taylor series. The FOSM approximation only provides estimates of the mean and standard deviation, which are not sufficient by themselves for evaluating the failure probability. To estimate the failure probability, one must assume the safety margin's distribution function or the safety factor beforehand. Compared to the previous FOSM method, the pioneering work of Hasofer and Lind (1974) provided a geometric interpretation of the reliability index as a measure of the distance (in dimensionless space) between the peak and multivariate distribution of the uncertain parameters and a function defining the failure condition. Their approximation implies transforming a general random variable into a standard Gaussian vector; to locate the point of maximum probability density within the failure domain and estimate the probability of failure. SORM analyses define the limit state function as the FORM for compete information, although approximating them with a second-order function (Breitung, 1984). However, for geo-problems, the probabilities of failure obtained with SORM are very close to FORM's values (Lacasse and Nadim, 1999). The Monte-Carlo simulation is a procedure, which simulates stochastic processes by repeating many times deterministic analyses, i.e., calculation where input values are randomly selected in proportion to their joint probability density function. It is a powerful technique, applicable to both linear and non-linear problems, but can require many simulations to provide reliable distribution of the response (Nadim, 2007).

Notwithstanding the above situation, it is essential to develop quantitative decision support tools for earthquake-related risks mitigation. Such tools are helpful to quantify/compare risks for different options and to facilitate informed decision making. Reducing uncertainties within tolerable levels and evaluating reliability of conclusions is of paramount importance for a successful risk assessment and must be

thus continuously considered the reference goal along the whole process. Taking advantage of the existing literature (Baecher & Christian (2003), the main assumptions of the FORM method are first introduced and then contextualized to the liquefaction chain phenomenon.

The study of Baecher & Christian (2003) starts by recognizing that the result of the calculations can be considered a function "g" of the several input parameters and variables (X_1, X_2, . . .,X_n) evaluated at some points (x_1, x_2, . . . , x_n):

$$g = g(x_1, x_2, \dots x_n) \qquad \textit{Eq. 4.13}$$

If only one independent variable X appears and the value of "g" is known for some value of X, say $\bar{X}$, then the value of g can be found for any other value x by using the Taylor series showed in Eqn. 4.14.

$$g(x) = g(\bar{X}) + \frac{1}{1!}(x - \bar{X}) \cdot \frac{dg}{dx} + \frac{1}{2!}(x - \bar{X})^2 \cdot \frac{d^2g}{dx^2} + \frac{1}{3!}(x - \bar{X})^3 \cdot \frac{d^3g}{dx^3} + \cdots$$

Eq. 4.14

However, in the study of error propagation, more than one independent variable usually appears and, therefore, a generalization of Eqn. 4.14 is needed. In this case, the initial value of each independent variable Xi is usually taken equal to its mean value, μXi. An equivalent form of the Taylor series for multiple variables is shown in Eqn. 4.15.

$$\begin{aligned} g(x_1, x_2, .., x_n) &= g(\mu x_1, \mu x_2, .., \mu x_n) + \frac{1}{1!}\sum_{i=1}^{n}(x_i - \mu x_i) \cdot \frac{\partial g}{\partial x_i} \\ &+ \frac{1}{2!}\sum_{i=1}^{n}\sum_{j=1}^{n}(x_i - \mu x_i)\left(x_j - \mu x_j\right) \cdot \frac{\partial^2 g}{\partial x_i \partial x_j} \\ &+ \frac{1}{3!}\sum_{i=1}^{n}\sum_{j=1}^{n}\sum_{k=1}^{n}(x_i - \mu x_i)\left(x_j - \mu x_j\right)(x_k - \mu x_k) \cdot \frac{\partial^3 g}{\partial x_i \partial x_j \partial x_k} + \cdots \end{aligned}$$

Eq. 4.15

If all the terms *(xi – μXi)* are small, their squares, cubes, and higher powers will be even smaller and thus can be ignored. This means that only the first-order terms are included. Hence methods based on this assumption are called First Order Reliability

Methods (FORM) and derive from the Hasofer–Lind (1974) approach. From the first order terms adoption the approximation of Eqn. 4.16 is derived.

$$g(x_1, x_2, .., x_n) \approx g(\mu x_1, \mu x_2, .., \mu x_n) + \frac{1}{1!}\sum_{i=1}^{n}(x_i - \mu x_i) \cdot \frac{\partial g}{\partial x_i}$$

Eq. 4.16

Consequently, the expected value "μ" and the variance "σ^2" of g can be found through Equations 4.17 and 4.18.

$$\mu_g \approx g(\mu x_1, \mu x_2, \ldots \mu x_n)$$ *Eq. 4.17*

$$\sigma_g^2 \approx E\left[\left(\sum_{i=1}^{n}(x_i - \mu x_1)\frac{\partial g}{\partial x_i}\right)^2\right]$$ *Eq. 4.18*

Then, multiplying the expression in brackets by the probability density function and integrating over the complete range of probabilities leads to an expression for the variance. In this case, care must be taken to multiply out the terms before interchanging the order of integration and summation. The result is showed in Eqn. 4.19.

$$\sigma_g^2 \approx \sum_{i=1}^{n}\sum_{j=1}^{n}\rho x_i X_j \sigma X_i \sigma X_j \frac{\partial g}{\partial x_i}\frac{\partial g}{\partial x_j} = \sum_{i=1}^{n}\sigma_{Xi}^2\left(\frac{\partial g}{\partial x_i}\right)^2 + \sum_{i=1}^{n}\sum_{j\neq 1}^{n} COV(X_i, X_j)\frac{\partial g}{\partial x_i}\ \frac{\partial g}{\partial x_j}$$

Eq. 4.19

Equation 4.19 requires the values of some partial derivatives, although only sometimes it is possible to differentiate the function "g" and evaluate the corresponding terms exactly. In the more common situation, the partial derivatives must be found numerically. The easiest way to do this is to use central differences that implies to evaluate the function g with each of the variables set at its mean value (estimate of μg in Eqn 4.17). In turn, the partial derivative for each variable is found by increasing and decreasing the variable by a small amount, finding the difference between the two resulting values of "g", and dividing the difference by twice the small increment.

Example of error propagation in the liquefaction induced physical damage

With reference to the cascade process summarized by the convolutive integral of PBEE, the evaluation of the uncertainty in the term p(EDP|IM) of Eqn. 4.1 is a special case of error propagation. In particular, the EDP corresponds to the liquefaction-induced differential settlement evaluated at the building centroid for a given intensity measure IM of the seismic scenario. Since in the herein defined approach, differential settlements are correlated to the absolute ones based on numerical analyses (Eqn. 4.20), the evaluation of building differential settlement implies a cascade process starting from the definition of the geotechnical subsoil model as well as the spatial interpolation of representative variables consisting in the 1D post-liquefaction settlement and the contribution of ejecta material (respectively terms Wv and We of Eqn. 4.21).

$$\delta w = \alpha \cdot w_{max}$$

Eq. 4.20

where: W_{max} is the total absolute building settlement calculated with the Bray and Macedo (2017) formula and α is the scaling factor.

$$Wmax = Wv + We + Ws$$

Eq. 4.21

As pointed out by Bray and Dashti (2010), the absolute settlement has been calculated by the sum of volumetric deformation (Zhang et al., 2002) and shear-induced deformations evaluated through the Bray and Macedo (2017) formula (Eqn. 4.22) assumed as independent variables. In this phase, the contribution of ejecta-sand material has been neglected in the lack of building-by-building records of ejecta liquefied material.

$$Wmax = Wv + Ws = Wv + \exp(c1 + 4.59 \cdot \ln(Q) - 0.42 \cdot \ln(Q)2 + c2 \cdot LBS + 0.58 \cdot \ln(\tanh(HL/6)) - 0.02 \cdot B + 0.84 \cdot \ln(CAVdp) + 0.41 \cdot \ln(Sa1) \cdot \exp(\varepsilon)$$

Eq. 4.22

It can be observed that significative uncertainties in the estimate of differential settlements arise from:

the spatial variability of geotechnical variables, which includes both the subsoil properties (relative density, measured CPT tip resistance and sleeve friction, evaluated indicators of liquefaction severity) and the characterization of the geometric stratigraphic model (meaning the assessment of a crust thickness and thickness of the liquefiable layer);

the building characterization, i.e., geometry (plan regularity/irregularity), load distribution, building mass, inertial effects, foundation types, and depth.

Concerning the former issue, geostatistics interpolation tools (like the kriging showed in Par. 4.6.2) allow to spatially characterize a given variable through its mean and normed error (or standard deviation), which is a proxy of the error estimate. About the stratigraphy, the application of the ESP method (Millen et al., 2020) is herein recommended to build the geotechnical model of the subsoil since its normed error allows to prove the consistency with the hypothesis of three strata model. On the contrary, engineering judgment should be introduced in defining the subsoil model when the normed error is found greater than a critical value of 0.15, as suggested by the authors.

Despite a rigorous application of the FORM method would require an explicit evaluation of the error made in defining the building contact pressure on the foundation, many National and International Standards (NTC, 2018; CEN-2004a) agree in the use of a semi-probabilistic approach assessing the building's loads, which are defined in terms of characteristic values accounting to all the uncertainties in materials, actions.

Lastly, the calculation method employed to evaluate the shear-induced deformation is usually affected by an error since it is obtained from data regression among numerical modeling and observations. To capture this contribution, Bray and Macedo introduce in their study a normally distributed random variable epsilon, having zero mean and 0.50 standard deviation in logarithmic units.

The application of Eqn. 4.19 to the absolute total settlement, leads to calculating the variance $\sigma^2(w_{max})$ as expressed in Eqn. 4.23. Despite in more common applications the above-defined "g" function is not tractable (but partial derivates must be numerically evaluated), in this situation, it is possible to differentiate the function w_{max} and evaluate the corresponding terms exactly.

$$\sigma^2\,(w_{max}) \approx \sigma^2(w_v)\cdot\left(\frac{\partial w_{max}}{\partial w_v}\right)^2 + \sigma^2\,(HL)\cdot\left(\frac{\partial w_{max}}{\partial HL}\right)^2 + \sigma^2(LBS)\cdot\left(\frac{\partial w_{max}}{\partial LBS}\right)^2 + \sigma^2(\varepsilon)\cdot\left(\frac{\partial w_{max}}{\partial \varepsilon}\right)^2 + COV(HL, w_v)\cdot\left(\frac{\partial w_{max}}{\partial HL}\right)\cdot\left(\frac{\partial w_{max}}{\partial w_v}\right) + COV(HL, LBS)\cdot\left(\frac{\partial w_{max}}{\partial HL}\right)\cdot\left(\frac{\partial w_{max}}{\partial LBS}\right) + COV(LBS, w_v)\cdot\left(\frac{\partial w_{max}}{\partial LBS}\right)\cdot\left(\frac{\partial w_{max}}{\partial w_v}\right)$$

Eq. 4.23

Where the recalled partial derivates have been calculated as follows:

$$\frac{\partial Wmax}{\partial Wv}=1$$

Eq. 4.24

$$\frac{\partial W_{max}}{\partial LBS} = exp(c1 + 4.59\cdot ln(Q) - 0.42\cdot ln(Q)^2 + c2\cdot LBS + 0.58\cdot ln(tanh(HL/6)) - 0.02\cdot B + 0.84\cdot ln(CAVdp) + 0.41\cdot ln(Sa1) + \varepsilon)\cdot exp(c2\cdot LBS)\cdot c2$$

Eq. 4.25

$$\frac{\partial W_{max}}{\partial HL} = exp(c1+4.59\cdot ln(Q)-0.42\cdot ln(Q)^2 + c2\cdot LBS - 0.02\cdot B + 0.84\cdot ln(CAVdp) + 0.41\cdot ln(Sa1) + \varepsilon)\cdot\left(-0.096667\cdot tanh\left(\frac{HL}{6}\right)^2 + 0.096667\right)\cdot tanh\left(\frac{HL}{6}\right)^{-0.42}$$

Eq. 4.26

$$\frac{\partial Wmax}{\partial \varepsilon} = exp(c1+4.59\cdot ln(Q)-0.42\cdot ln(Q)^2 + c2\cdot LBS + 0.58\cdot ln(tanh(HL/6)) - 0.02\cdot B + 0.84\cdot ln(CAVdp) + 0.41\cdot ln(Sa1))\cdot exp(\varepsilon)$$

Eq. 4.27

Finally, the differential settlements at each building centroids are evaluated by applying Eqn. 4.20. At this step, the error propagation theory allows evaluating not only a deterministic value of differential settlement (e.g., the mean value "δ_m") but also to characterize the variance σ^2 (δ_m), which can be evaluated as showed in Eqn. 4.28.

$$\sigma^2(\delta_m) = \sigma^2(\alpha)\cdot w_{max} + \alpha\cdot\sigma^2(w_{max})$$

Eq. 4.28

Where α is normally distributed, having a mean value equal to 0.54 and standard deviation equal to 0.08. On the other hand, w_{max} in Eqn. 4.28 represents a median absolute settlement of a normal distribution, as demonstrated by the introduction of the ε term (Bray and Macedo, 2017). This assumption is justified by numerical analyses (see Chapter 4) that showed a statistical independence between α and the maximum liquefaction-induced absolute settlement w_{max}.

The aim of the previous steps of calculation is to define for each building a probabilistic distribution of differential settlements induced by a selected seismic scenario, which also reflects the level of uncertainty in the geotechnical modelling of the subsoil. It is evident that: the less is the error in the estimate of the subsoil properties and spatial variability, the less will be the evaluated standard deviation of differential settlement and the more accurate the prevision model will be. In this context, the application of the FORM method in both evaluating the liquefaction-induced building absolute settlement and relating it to the differential one allows defining for a given earthquake scenario the Gaussian distribution of differential settlements (defined by the mean and standard deviation calculated as per Eqn. 4.20 and Eqn. 4.28).

Proven that, for a normal distribution (having mean "μ" and standard deviation "σ"), the 95.5% and 99.7% of the entire dataset respectively range in $\mu \pm 2\sigma^2$ and $\mu \pm 3\sigma^2$, (see Figure 4-19), an example of cumulative distribution functions considering the 95.5% of the entire differential settlements distribution induced by a predefined seismic scenario is showed in Figure 4-20.a. According to the adopted model (Fotopoulou et al., 2018), the curves of Figure 4-20.a relate the evaluated differential settlements to their probability of exceedance.

However, in the logic of the cascade scheme, a liquefaction-induced differential settlement represents for a building both the result of a given seismic input and the building structural demand also classified as engineering demand parameter "EDP", responsible for structural/non-structural damage. In this situation, fragility models like the Fotopoulou et al. (2018) are normally introduced to quantify the liquefaction-induced physical impact: they link differential settlements to four predefined damage limit states. Although fragility curves represent a probabilistic estimate of building damage, a more rigorous application of the error propagation theory implies to join the fragility model considering the whole range of possible EDPs and weighting each value by its probability of exceedance. It means that for a building, the probability of

undergoing a given damage limit state, which accounts for the entire range of possible EDPs, can be determined through Eqn. 4.29.

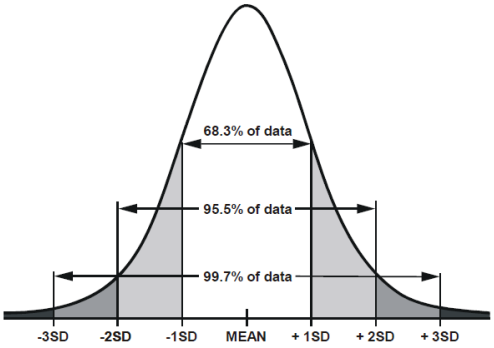

$$p\,(DL \geq 1\,) = \sum_i p(D1|\delta w_i) * p(\delta w_i)$$

$$p\,(DL \geq 2\,) = \sum_i p(D2|\delta w_i) * p(\delta w_i)$$

$$p\,(DL \geq 3\,) = \sum_i p(D3|\delta w_i) * p(\delta w_i)$$

$$p\,(DL \geq 4\,) = \sum_i p(D4|\delta w_i) * p(\delta w_i)$$

Eq. 4.29

Figure 4-19 Areas under the normal curve that lie between 1, 2 and 3 standard deviation on each side of the mean.

Figure 4-20.b highlights the difference between two possible approaches in evaluating the physical impact: the former estimates the term P(D>d|δ) deterministically, i.e., only considering one value of the EDP (e.g., the median value of the differential settlement, or a defined quantile). It is represented by the black line of Figure 4-20.b. The latter introduces all the EDP values ranging for instance in $\mu \pm 2\sigma^2$, each of them weighted by its density probability function. This approach is displayed through the areas below each damage state fragility curve of Figure 4-20b.

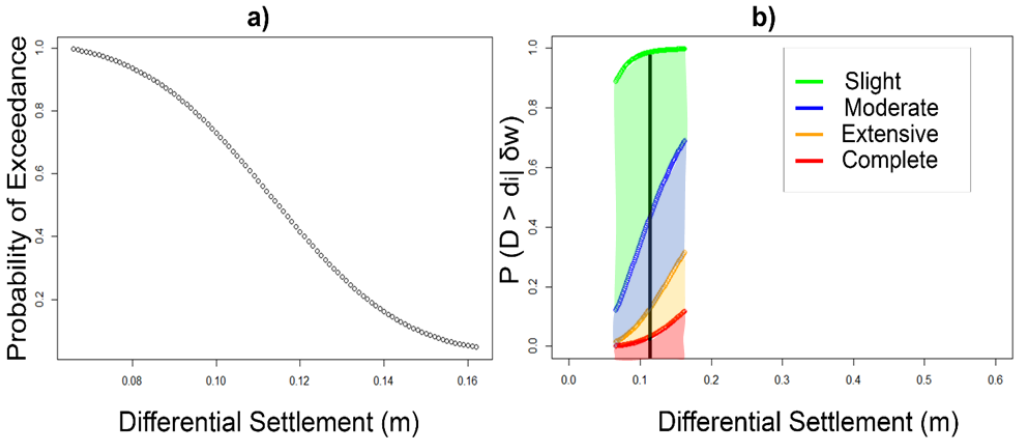

Figure 4-20 Probability of exceedance of a liquefaction-induced building differential settlement for a given scenario; b) evaluation of liquefaction-induced physical impact on buildings, namely in a deterministic (solid line) and probabilistic (areas below each curve) ways.

4.5 **Validation criterion and Performance evaluation**

Each risk assessment procedure needs a phase of validation aimed at quantifying the reliability of the obtained results. One of the main concerns of validation is to find a suitable criterion that quantifies the predictive capability of the adopted models. As done for the selected case studies of Christchurch (New Zealand) and Terre del Reno (Italy), the method based on the Receiver Operating Characteristic (ROC) Curve (Kongar et al., 2015) can be adopted at each level to assess liquefaction impact. It establishes a binary classification of predictions and observations in a way that, for a specific event and an adopted predictive model, data can be summarized into 2 x 2 confusion matrices like the one showed in Table 4-6.

Table 4-6 Example of confusion matrix based on binary classification.

		Predicted Class	
		Yes	No
Actual Class	Yes	True Positive (TP)	False Negative (FN)
	No	False Positive (FP)	True Negative (TN)

In the two-class case, a single prediction has four possible outcomes: true positives (TP), true negatives (TN) represent the correct classification, false positives (FP), and false negatives (FN) (Figure 4-21). Considering on the vertical axis the outcome of an event with a clear threshold defining damage (positive event) and on the horizontal axis a candidate predictive variable, a favourable situation is the one depicted in case A of Figure 4-21 with positive and negative events/predictions defined with clear thresholds. The Receiver Operative Curve "ROC" reports the true positive ratio (also defined as recall), i.e., the ratio of positive prediction over the number of positive events (showed in Eqn. 4.30), on the vertical axis and the false positive ratio, i.e., the number of positive predictions over the number of negative events, on the horizontal axis (Eqn. 4.31).

$$True\ Positive\ Rate = \frac{TP}{TP+FN} \qquad \textit{Eq. 4.30}$$

$$False\ Positive\ Rate = \frac{FP}{FP+TN} \qquad \textit{Eq. 4.31}$$

For a zero threshold of the prediction variable, the true positive and false positive ratios are equal to 1. When the predictive threshold increases, the false positive becomes progressively true negative values (the false positive ratio reduces to zero), while the true positive values persist (the true positive ratio constantly remains equal to 1). Therefore, the ROC curve heads leftward to the vertical axis. Thereafter, when the predictive threshold is further increased, the true positive values become progressively false negative (the true positive ratio reduces to zero), and the curve moves to the origin of the axes. In this optimal condition, the size of the Area below the Receiver Operating Curve (Area Under Curve – AUC) is equal to 1. In the case of poorly performing predictive models, the dots in the binary plot are randomly distributed in the binary classification plot (case B in Figure 4-21). Consequently, there is a simultaneous reduction of True Positive and False Positive occurrences with increasing the prediction threshold. The Receiver Operating Curve describes a 1:1 line in the false positive-true positive ratio plot, and the size of AUC is equal to 0.5. The value of AUC is thus used to estimate the quality of prediction.

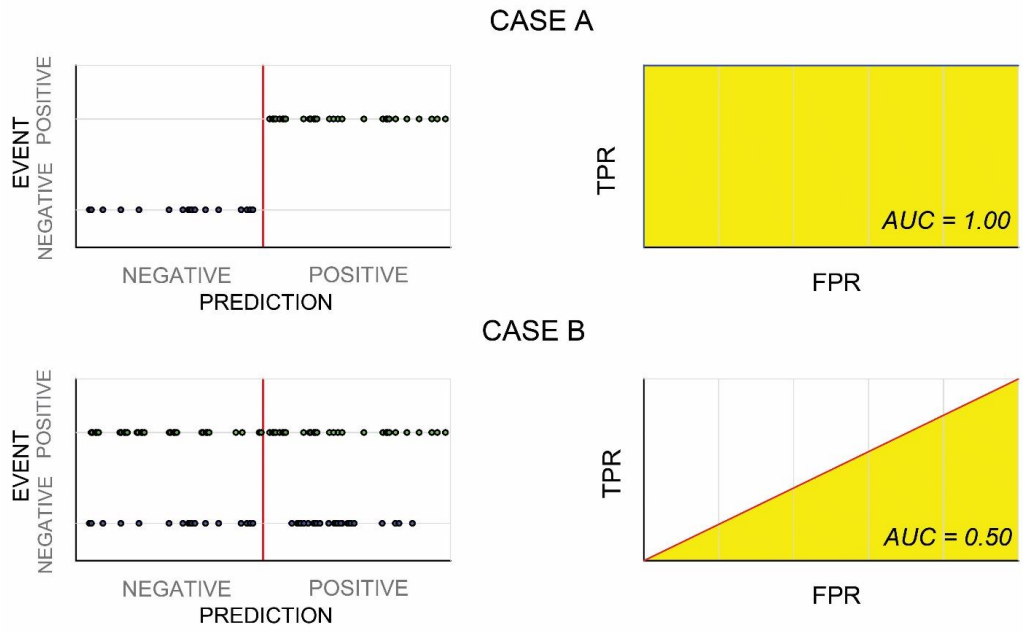

Figure 4-21 Validation criterion (Kongar et al., 2015).

In addition to the TPR, FPR, other synthetic indicators of the goodness of estimate can be calculated. Precision (Eqn. 4.32a) is referred to as a positive predicted value, and recall (Eqn. 4.32b) refers to the true positive rate or sensitivity. The F-measure showed

in Eqn. 4.33 combines Precision and Recall, having the best value at 1 and the worst at 0.

$$Precision = \frac{TP}{TP+FP} \quad \textit{Eq. 4.32a}$$

$$Recall = \frac{TP}{TP+FN} \quad \textit{Eq. 4.32b}$$

$$Fmeasure = 2 \cdot \frac{precision \cdot recall}{precision+recall} \quad \textit{Eq. 4.33}$$

Alternatively, the Youden (1950) J-stats index can be calculated for diagnostic tests as a proxy of the performance. It ranges from 0, meaning that the test gives the same proportion of positive results for positive and negative events (i.e., the test is useless) through 1 indicating that there are no false positives or false negatives (i.e., the test is perfect).

$$J - stats = sensitivity + specificity - 1 = \frac{TP}{TP+FN} + \frac{TN}{TN+FP} - 1 \quad \textit{Eq. 4.34}$$

Similarly, the overall success and failure rates (OSR and OFR), defined respectively as the percentages of successful and unsuccessful prediction can be computed to evaluate the prediction performance on the entire set of events.

$$Overall\ Success\ Rate = \frac{TP+TN}{TP+TN+FP+FN} \quad \textit{Eq. 4.35a}$$

$$Overall\ Failure\ Rate = \frac{FP+FN}{TP+TN+FP+FN} \quad \textit{Eq. 4.35b}$$

Once the validity of the predictive method is ensured, the last step consists in defining the optimal threshold of the predicted variable able to classify negative and positive events. To this aim, increasing values of the threshold are considered, and the Matthews Correlation Coefficient defined in (Powers, 2011) has been computed for each of them. The maximum value of this function provides the best estimate of the threshold characterising the event.

$$MCC = \frac{TP\ X\ TN - FP\ X\ FN}{\sqrt{(TP+FP)(TP+FN)(TN+FP)(TN+FN)}} \quad \textit{Eq. 4.36}$$

Chapter 5. CASE STUDY 1: CHRISTCHURCH CITY

5.1 Abstract

The city of Christchurch (≈370 000 inhabitants at that time), in the Canterbury Region of the South Island of New Zealand, was repeatedly struck by earthquakes during the 2010-2011 seismic sequence known as Christchurch Earthquake Sequence "C.E.S." (Cubrinovski, 2013). Among the thousands of earthquakes, the most noticeable (Mw 6.2) occurred on February 22nd, 2011, just below the city resulting in 185 fatalities and diffuse devastation to dwellings and infrastructures. Liquefaction played a major role in causing the displacement of about 15 000 families, the temporary abandonment of nearly 20 000, the demolition of 8 000 buildings, and the removal of 900 000 tons of liquefied soil (Tonkin & Taylor, 2013). In this chapter, the liquefaction risk assessment is firstly tested and validated, comparing predictions with liquefaction-induced effects observed in Christchurch (New Zealand) after the 22nd February 2011 Mw 6.2 earthquake. Then, the physical/economic impact on reinforced concrete framed ("RC-F") residential buildings is calculated accounting for the area's seismic hazard; this analysis allows to judge the economic convenience of different mitigation options.

5.2 The 2010 – 2011 Christchurch Earthquake Sequence "C.E.S."

The city of Christchurch (pop. 366.100, 2013) in New Zealand, is an important industrial and agricultural centre and the second-largest city in the country. It is located on the eastern (Pacific) coast of the South Island, in the Canterbury Region (Figure 5-1). From a geological viewpoint, the setup of the Canterbury Plains consists of recent alluvial deposits laid down by the Waimakariri River and fine marine sediments deposited on the coastal margin of the floodplain and in estuaries and lagoons. To the south of the city, the alluvial deposits become shallower against the basalt rock composing the volcanic cone of Banks Peninsula (Figure 5-1.b).

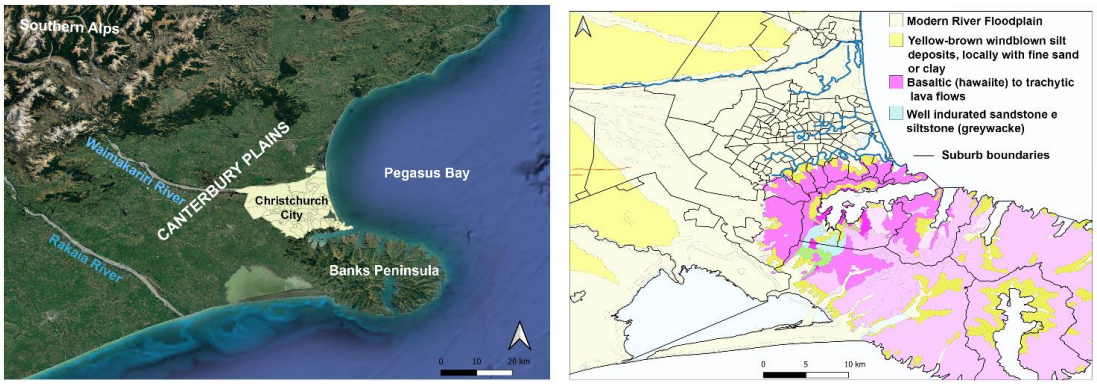

Figure 5-1 Overview of Christchurch the Canterbury Region (a); Geology of Christchurch City (b).

Between September 2010 and December 2011, the Canterbury Region suffered a severe earthquake sequence known as the Christchurch Earthquake Sequence (C.E.S.) that produced huge damage to buildings and infrastructural assets. The 2010 – 2011 seismic sequence includes several thousand of events, four of them with Richter Magnitude ≥ 6 and precisely: the M7.1 4th September 2010 Darfield earthquake, the 22nd February 2011 Christchurch Earthquake and the 13th June 2011 and the 26th December 2011 aftershocks. The characteristics of the main events are summarised in Table 5-1. In particular, the 22 February event was the most destructive since it provoked 185 fatalities. Despite the September 2010 event developed a larger magnitude if compared to the 22nd February 2011 earthquake, the observed effects on the City were less dramatic since its epicentre was located farther from the Central

Business District of Christchurch; 44 km vs 10 km (Figure 5-2). Because of the vicinity to the fault location, some of the recorded ground motions in the central Christchurch strong motion stations had 5% damped spectral accelerations that surpassed the 475-year return period design motions by a factor of two.

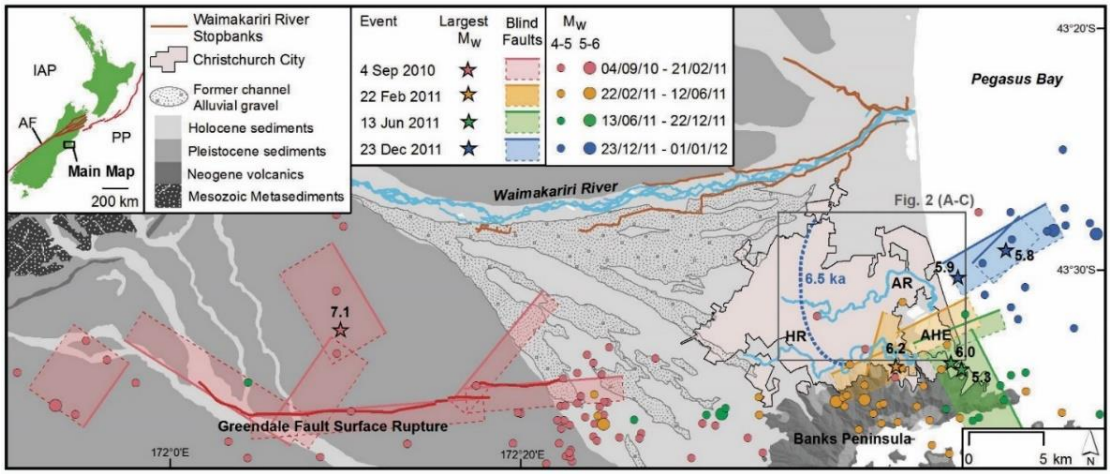

Figure 5-2 Geologic and seismic context of Christchurch through the 2010–2011 Canterbury Earthquake Sequence "CES" (Hughes et al., 2015).

Table 5-1 Description of the main events in the C.E.S.: Earthquake Richter M_L and moment magnitude Mw (www.from geonet.org.nz), PGAh and PGAv, PGV from (Bradley et al., 2014).

Earthquake name and date	Lat	Long	M_L	Mw	PGA Horizontal (g)	PGV Horizontal (cm/s)	PGA Vertical (g)
Darfield Earthquake (2010.09.03)	-43.538	172.164	7.1	7.1	0.76	115	1.3
October 2010 aftershock	-43.626	172.564	5.1	4.8	0.28	16	0.21
Boxing Day aftershock (2010.26.12)	-43.554	172.662	4.9	4.7	0.27	18	0.52
Mw6.2 Christchurch Earthquake, (2011.02.22)	-43.566	172.691	6.3	6.2	1.41	81	2.21
February Aftershock I (2011.22.02)	-43.589	172.661	5.8	5.5	0.56	44	0.93
February Aftershock II (2011.22.02)	-43.590	172.634	5.9	5.6	0.75	29	0.69
April Aftershock (2011.04.16)	-43.613	172.760	5.3	5	0.68	32	0.48
June Aftershock (2011.06.13)	-43.568	172.753	5.6	5.3	0.45	28	0.69

Mw6.0 Christchurch Earthquake (2011.06.13)		-43.564	172.743	6.4	6	1.54	102	1.14
June 21 Aftershock (2011.06.21)		-43.599	172.525	5.4	5.2	0.26	11	0.62
December Earthquake (2011.12.23)	Mw5.8	-43.486	172.796	5.9	5.8	0.31	30	0.98
December Earthquake (2011.12.23)	Mw5.9	-43.530	172.743	6	5.9	0.44	44	0.39

Such intense ground shaking caused substantial damage to many buildings including widespread liquefaction and lateral spreading. Liquefaction impact on the entire community was devastating. It caused the displacement of about 15,000 families, the temporary abandonment of nearly 20,000, the demolition of 8,000 buildings (including 70% of the building in the CBD), the removal of 900,000 tons of liquefied soil (Tonkin & Taylor, 2013), the failure of 700 km (140km completely out of service) of wastewater pipes (Cubrinovski et al., 2011a) and the fault of 11kv cables up to 86% in areas where moderate to severe liquefaction happened (Giovinazzi et al., 2011). Liquefaction was particularly severe in the residential area located North-East to the CBD as a result of strong ground shaking, high water table (median groundwater depth ≈1m from the surface) and loose sandy soils characterized by surficial CPT tip resistance of about 2-4 MPa in the top 5-6 meters or an SPT blow count of 7-8 (Cubrinovski et al., 2011d). Additionally, the ground slope and the presence of the Avon River increased the lateral-spreading susceptibility of these deposits significantly. Therefore, that area was named "*The Red Zone*" after the earthquake, since all buildings were completely damaged and subsequently demolished (Figure 5-3). Diffuse losses have involved the community in a slow, tiring and still ongoing reconstruction process. Although not being the only event of such a size, the case of Christchurch is probably the most impressive example of liquefaction-induced damage in an urban environment.

To better understand the liquefaction impact of the February 2011 seismic event and its magnitude over the territory, Figure 5-4 reports a comparison with the extent of liquefaction-induced damage observed after the September 2010 and June 2011 Earthquakes.

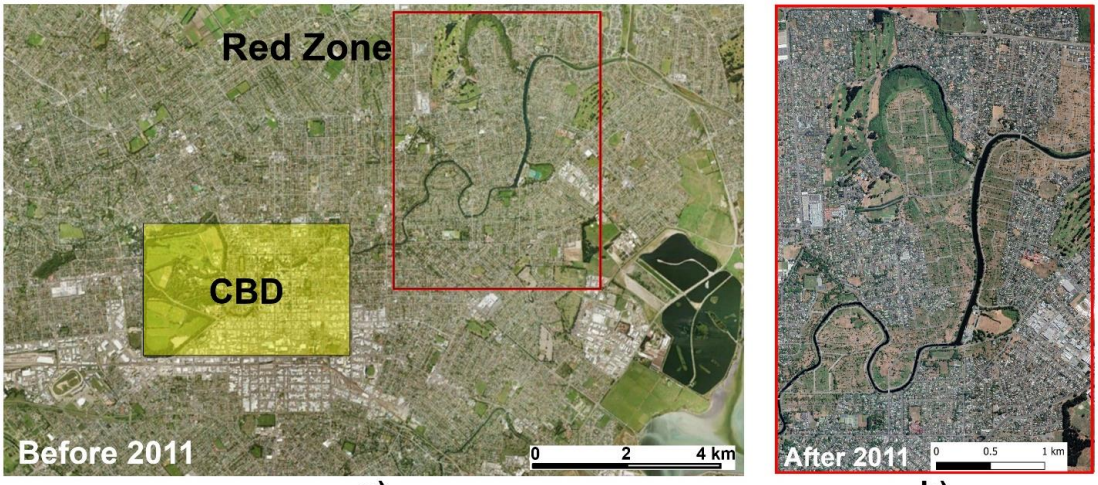

Figure 5-3 a) Study area identification; b) evolution of landscape in the red zone of Christchurch after the 2010-2011 seismic sequence.

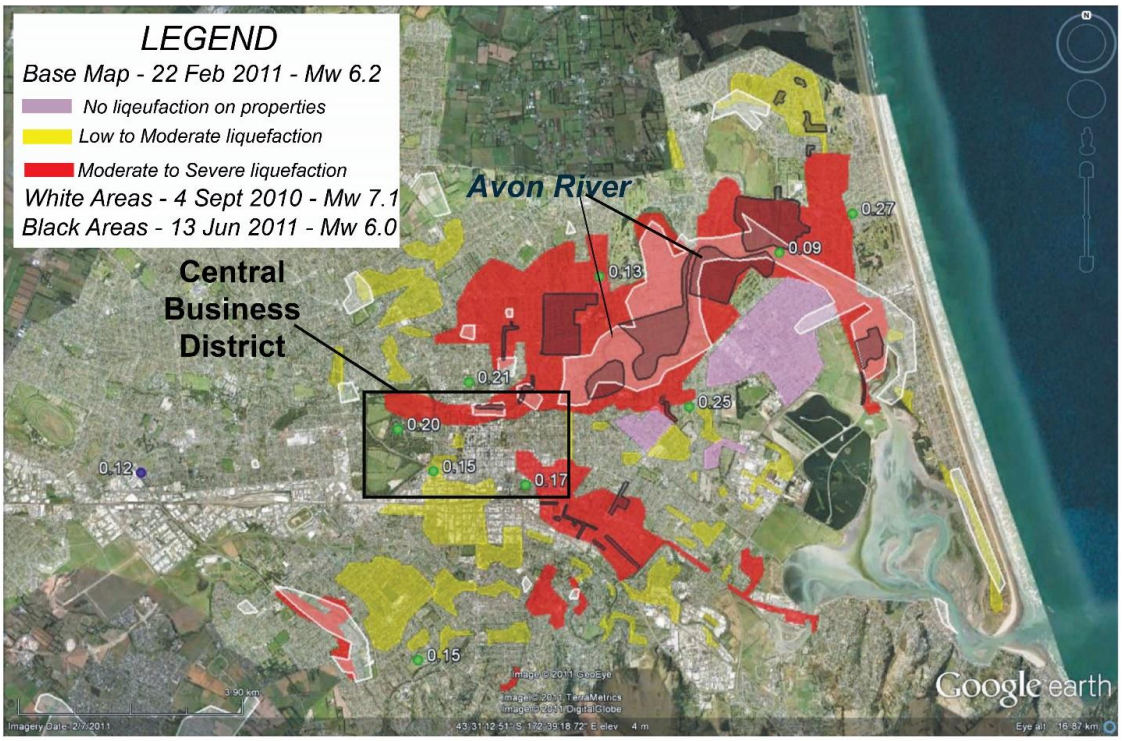

Figure 5-4 Preliminary liquefaction map documenting areas of observed liquefaction in the 4 September 2010 (white contours), 22 February 2011 (red, yellow, magenta areas), and 13 June 2011 (black contours) earthquakes. Note that only parts of Christchurch were surveyed and that the aim of the surveys was to capture only general features and severity of liquefaction manifestation as observed from the roads (zoning is therefore not applicable to specific properties), (Cubrinovski et al., 2011b).

Along the Avon River, particularly to the east of CBD, severe lateral spreading occurred, causing horizontal displacements at the riverbank on the order of several tens of centimeters to more than two meters (Cubrinovski et al., 2012). At ten locations along the Avon River, lateral spreading measurements conducted after the 22 February 2011 earthquake showed permanent lateral displacements ranging from two to three times the removal measured after the September earthquake. Such increased spreading movement agrees with the more severe liquefaction observed in these areas during the February event. Additionally, the permanent ground deformation surveying indicated that ground cracks associated with lateral spreading extended as far as 100-200 meters from the river. Other aerial observation methods suggest that the effects of spreading might have been even beyond these distances. An example of lateral spreading along the Avon River is shown in Figure 5-5.

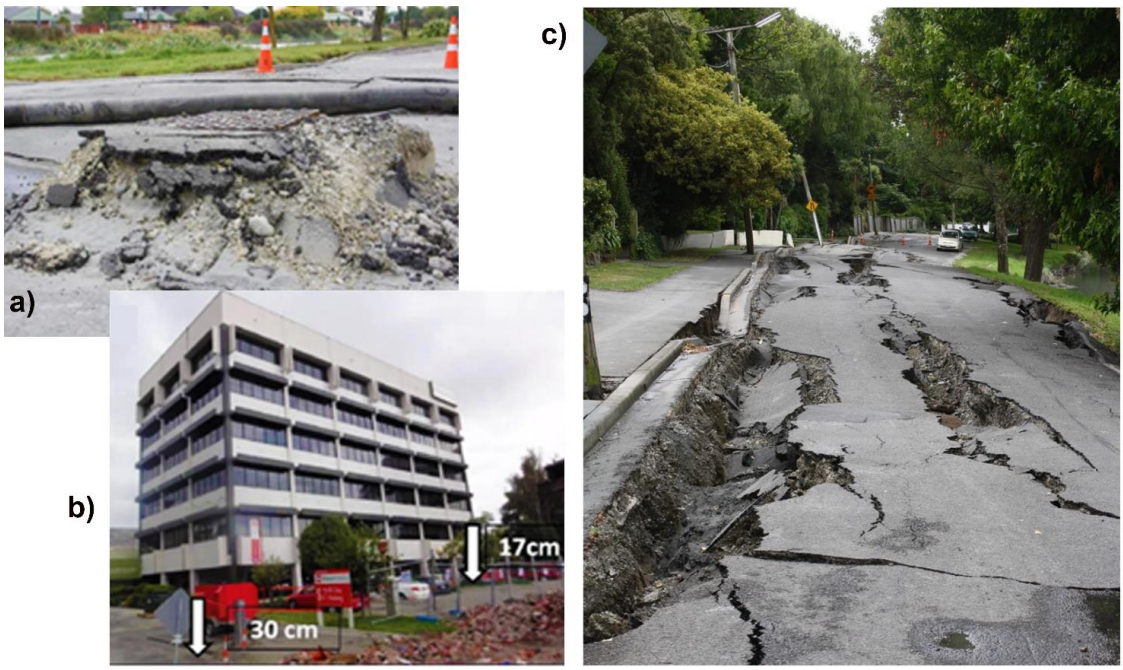

Figure 5-5 Examples of liquefaction-induced damage: a) flotation of pipe below causes the manhole to rise; b) building on pile foundations in area of severe liquefaction showing large settlement of the surrounding soils relative to the foundation beams c) effect of lateral spreading on the roadway.

Immediately after the main events of the sequence, a huge number of in-situ tests was carried out by several teams of geotechnical engineers to evaluate liquefaction vulnerability and quantify the liquefaction-induced land damage, and estimate the damage to residential properties, public buildings, lifelines, and more generally infrastructures (van Ballegooy et al., 2014). Such activity led to the creation of the

Canterbury Geotechnical Database (CGD) that Tonkin and Taylor company developed initially for the Canterbury Earthquake Recovery Authority (CERA) to manage the rebuild of Christchurch following 2010-2011 Canterbury Earthquake Sequence "C.E.S.". Following the success of the Canterbury Geotechnical Database (CGD), the Ministry of Business, Innovation and Employment (MBIE) encouraged the development of the New Zealand Geotechnical Database "NZGD" https://www.nzgd.org.nz. As of May 2019, the NZGD database contained over 35 800 cone penetration tests (CPT), 18 700 boreholes, 1 000 piezometers with accompanying groundwater monitoring records, 6 000 laboratory tests (plus other data and maps), and it is constantly updated. This unprecedented documentation available after the earthquake sequence enables the validation of different components of the model and discloses the importance of disregarded factors.

5.3 **Hazard Analysis**

The assessment of liquefaction hazard for Christchurch's city has been performed following the analyses described in the flow chart of Figure 4-2. Since it results from the combination of liquefaction susceptibility and seismic hazard, the first step of this analysis concerns the subsoil characterization.

The subsoil data used in the present and the following analyses have been extracted from the New Zealand Geotechnical Database (NZGD-https://www.nzgd.org.nz/), whose amount of information offers such a unique occasion to investigate separately the different factors involved in liquefaction and to quantify the reliability of the adopted predictive models. As per May 2019, the NZGD database contained over 35 800 cone penetration tests, 18 700 boreholes, 1 000 piezometers with accompanying groundwater monitoring records, 6 000 laboratory test records (plus other data and maps), and it is continuously updated.

Focusing on CPT profiles, the database creation, and preparatory information collecting has consisted of the following steps:

- individual scrutiny of more than 13 000 CPT profiles available for the Christchurch City territory from the NZGD. Since a standard worldwide format for CPT measurements does not exist, one of the main disadvantages of such a large amount of information is that data includes raw and partially processed data, often provided in different formats (i.e., .pdf, .txt, .csv, excel

spreadsheet..). Additionally, the organization of columns and the units of measures whom whit data is provided may vary from a stakeholder to another. All these aspects have required an initial phase of data standardization preparatory to the following automated processing. Each CPT has been converted in homogenized ASCII files, reporting as first four columns respectively the depth (m), the measured CPT tip-resistance "qc" (MPa), the measured CPT sleeve-friction "fs" (MPa) and the generated pore pressure "u" (MPa);

- reconstruction of the depth to groundwater table over the study area prior to the 22 February 2011 Earthquake. The Map obtained from geostatistical interpolation of the groundwater level at each CPT location and available piezometers measurements is showed in Figure 5-6.

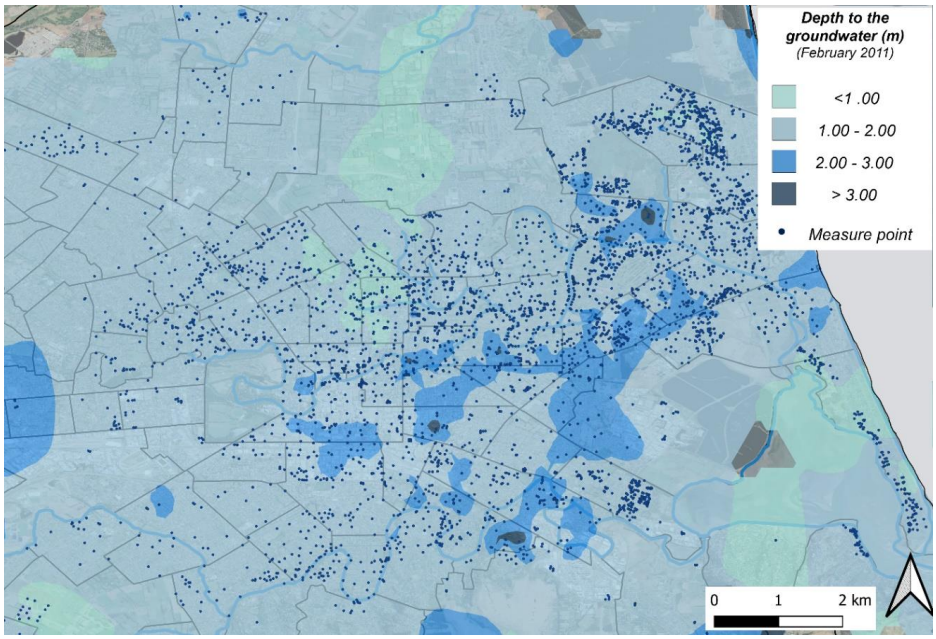

Figure 5-6 Map of groundwater depth at February 2011 (NZGD).

After the subsoil database creation, the liquefaction susceptibility analysis of CPT profiles consists of the automated application of Robertson (1998) and the Millen et al. (2020) Equivalent Soil Profile criteria. These two assessments have been respectively performed through scripts developed in the open source "Rstudio" (r-project.org) and "Python" environments.

The liquefaction hazard analysis, consisting in the evaluation of the most popular liquefaction severity indicators (Table 3-4), requires the introduction of seismic

ground motion: and therefore, the 22 February Christchurch Earthquake contour map of PGA derived from Canterbury Geotechnical Database (2015) ("Ground Motion", Map Layer CGD5170-30 June 2015, retrieved [date] from https://canterburygeotechnicaldatabase.projectorbit.com/) and displayed in Figure 5-7 has been considered as seismic input at each CPT location.

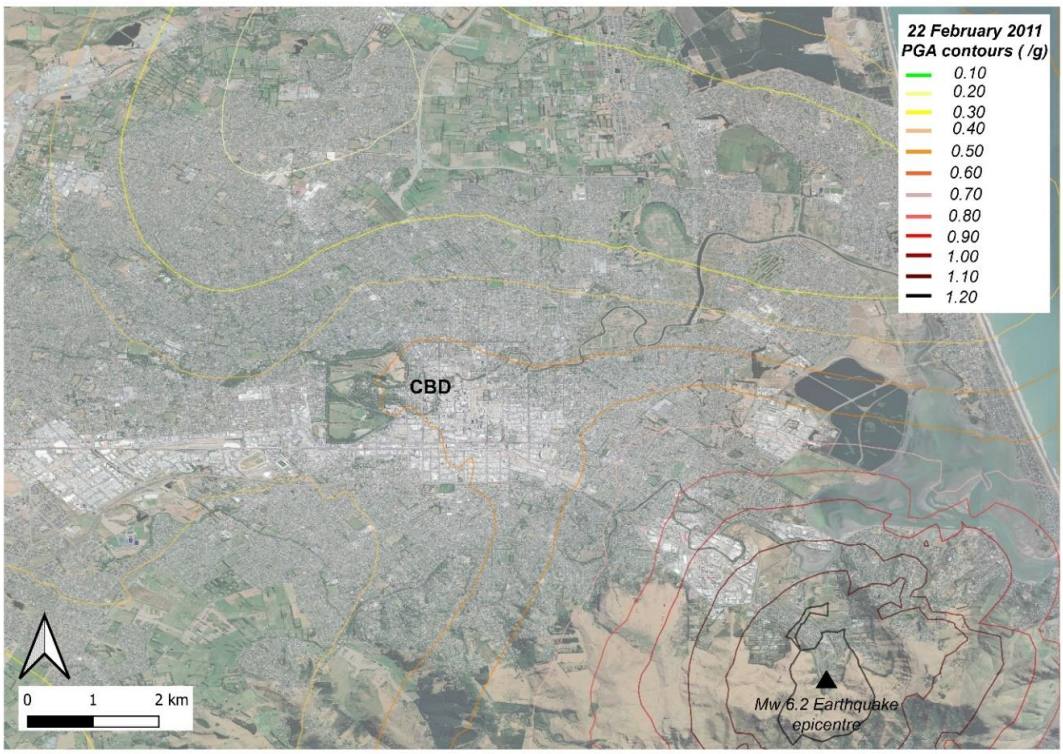

Figure 5-7 22 February 2011 event spatial distributions of Peak Ground Acceleration (Canterbury Geotechnical Database (2015) "Ground Motion", Map Layer CGD5170 - 30 June 2015).

The subsequent liquefaction hazard analysis consisting of evaluating of the most known liquefaction severity indicators has been carried out in the R-studio environment that includes dedicated packages for statistical and geostatistical analyses.

Firstly, the application of geostatistics tools and boxplot test (Montgomery et al., 2012) to the obtained results enabled anomalous data filtering. In this phase, accomplished in GIS Platform, the cross-validation test shown in Figure 5-8 directly compares for a given point the measured and interpolated values of a selected variable, providing an expeditious and graphical indication of inconsistent data, i.e., all those data incoherent with the outlined spatial trend. In particular, thinking on the boxplot

test, the tolerability criterion has been fixed considering the 25 and 75 percentiles of the error distribution (Q1 and Q3), the interquartile range (IQR = Q3 - Q1) and discarding the data falling outside the interval (i.e., Q1-1.5*IQR; and Q3+1.5*IQR). For example, the LSN outliers identification and localization over the territory added to the LSN standard error mapping are shown in Figure 5-8 b,c.

Finally, the maps obtained only accounting for consistent data allow to estimate the spatial distribution of significant variables in terms of their mean values and standard errors and discriminate areas where the knowledge is not adequate. In the lack of new data measurements, these areas will be removed from further risk analyses. As an example, Figure 5-8 shows the distribution of mean values and standard errors of the Liquefaction Severity Number LSN (van Ballegooy et al., 2014) computed for the February 22nd, 2011 earthquake in the central area of the city (Christchurch CBD).

In the following, only maps obtained after geostatistical data filtering are presented, covering areas where further investigation is required since they show an estimated standard error more significant than 25%.

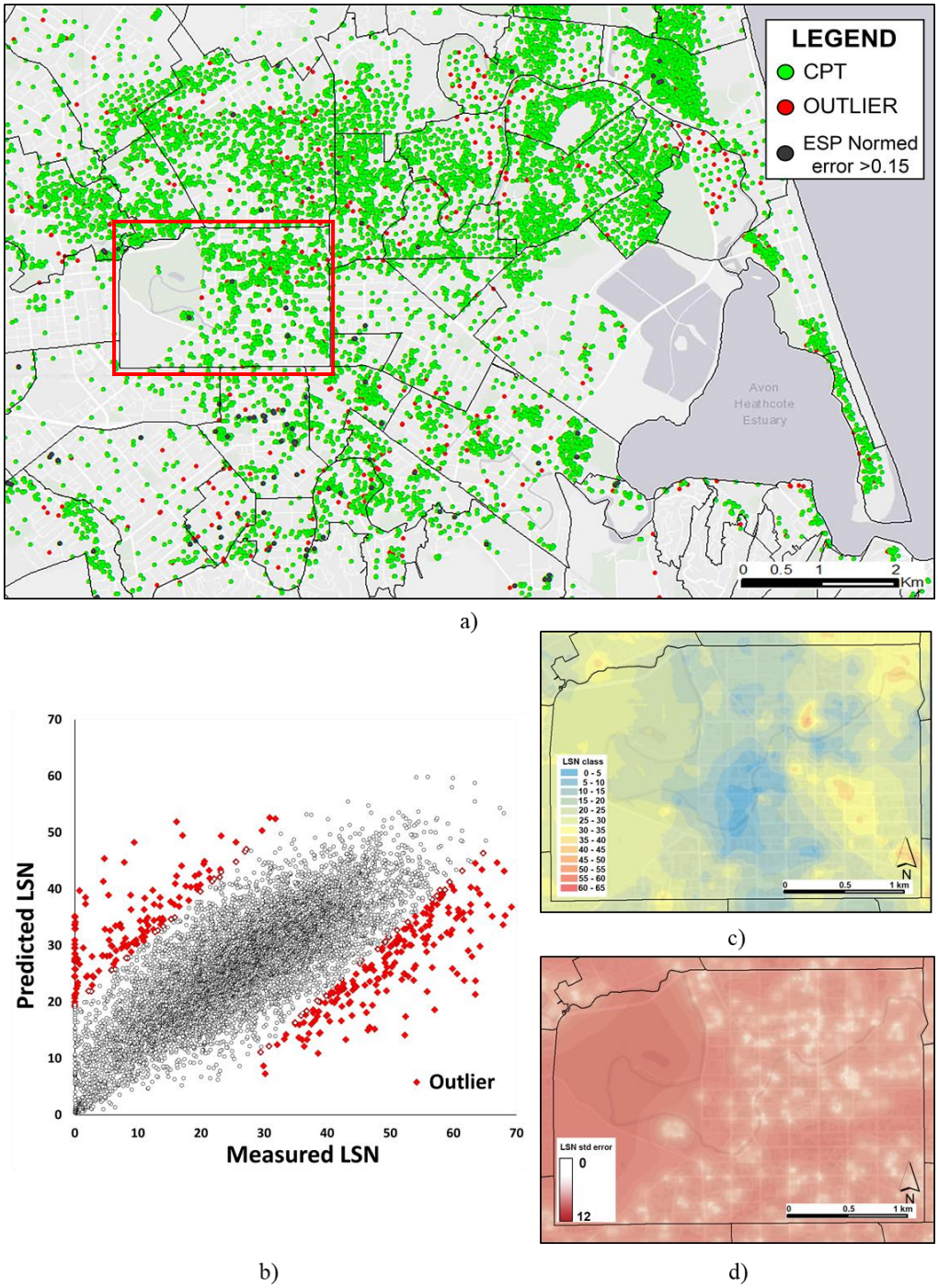

Figure 5-8 a) a) Map of Christchurch with the position of CPT tests; b) outlier test implemented for the filtering of inconsistent data based on the estimate of LSN; LSN (c) and LSN Standard error Maps (d) in the Central Business District.

5.3.1 Liquefaction susceptibility of the area

Proven that the geology of the Canterbury Plain confirmed that a liquefaction susceptibility exists in almost all the territory of Christchurch City, the quantitative susceptibility analysis consisted in the application of the Robertson (1998) criterion and the Millen et al. (2020) ESP method to the total number of homogenized CPTs. A preliminary data filtering of the original CPT dataset taken from the NZGD, individually scrutinized and homogenized, highlighted around 4 000 profiles shallower than 10 m. They were removed from the following analyses. They were removed from the following analyses.

In Figure 5-9, the mapping of cumulative thickness of liquefiable layers "CTL" resulting from the processing of CPTs deeper than 10m with the Robertson (1998) Ic-based criterion is displayed. The obtained results highlight a significant presence of potentially liquefiable soils in part of the CBD and large areas of Eastern Christchurch, where the cumulative thickness is found up to 16-20 m. Conversely, according to the Robertson (1998) criterion, a very low/low liquefaction susceptibility can be evaluated in the West/North West suburbs of Christchurch (corresponding to CTL<2-3m).

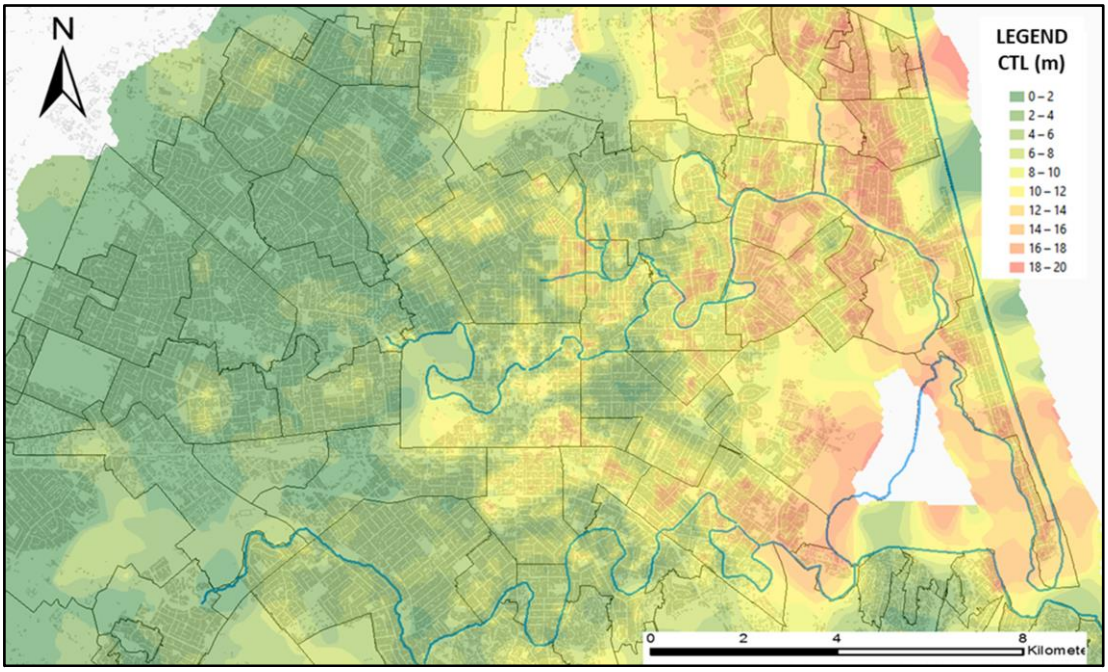

Figure 5-9 Map of the cumulative potentially liquefiable layers, obtained by summing the thickness of all the saturated sandy layers in the first 20 meters depth.

In addition to the previous one, the Millen et al. (2020) susceptibility criterion which schematizes each CPT profile to an equivalent three-layer model (the Equivalent Soil Profile ESP) identified by a thickness of crust and liquefiable layer and a mean Cyclic Resistance Ratio is applied. A preliminary step consists of the analysis of the normed error (Eq. 3.1), which both ranks the robustness of the ESP method and the consistency with the 3-layered subsoil modelling. Figure 5-10a shows that over a number of 8818 processed CPT profiles, only 106 (1.2%) gave errors larger than 0.15, indicating the presence of multiple liquefiable layers separated by large non-liquefiable layers. However, the scattered position of these tests over the map (Figure 5-10b) shows that the equivalence is rather affected by uncertainties linked to the execution and interpretation of the tests more than by local systematic variations of the stratigraphy. In all cases, engineering judgment is needed to focus on these tests and decide on the acceptance/rejection of the equivalence.

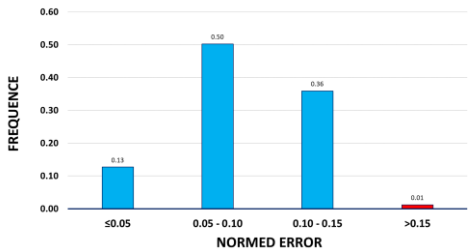

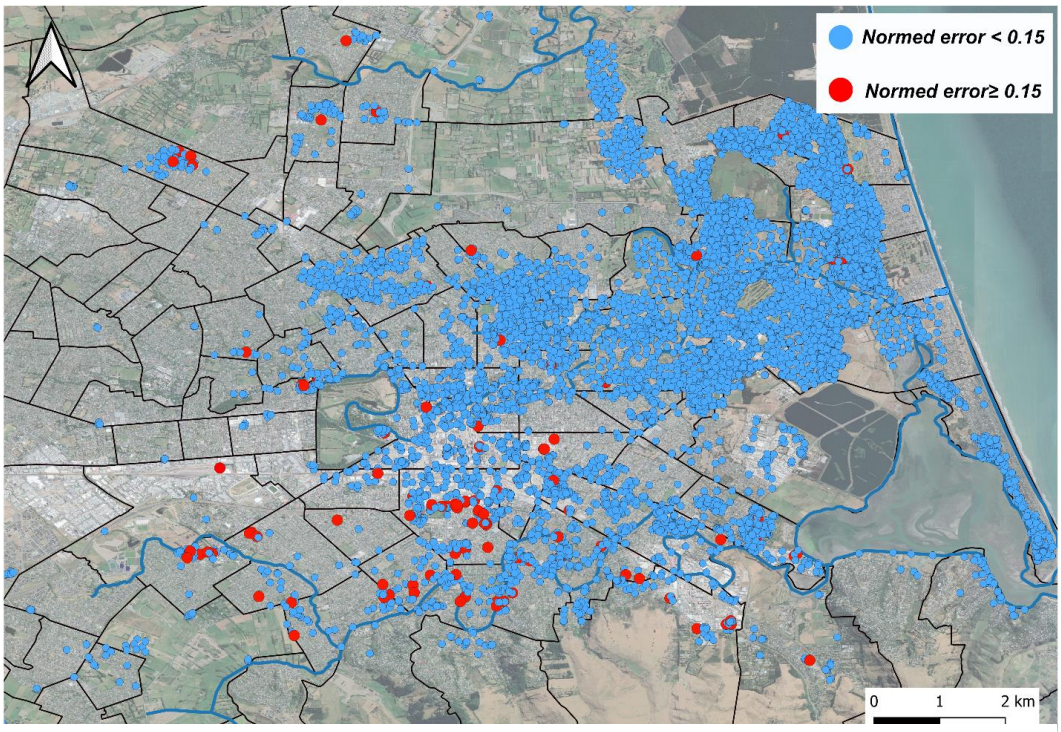

Figure 5-10 Histograms of the normed errors showing the equivalence of soil profile to the ESP model (a) and position on the map of Christchurch of the profiles with error>0.15 (b).

A detailed analysis of typical profiles helps to understand the importance of normed errors. Table 5-2 shows three selected profiles are representative of the above-defined classes (with normed errors, respectively N.E<0.05, 0.05<N.E.<0.15, 0.15<N.E.). The LSN indicator (computed for the earthquake scenario of Feb 22nd, 2011) has been added to the table. As can be seen, the values calculated on the real and equivalent soil profiles are similar when the standard error is lower than 0.05. At the same time, their difference becomes intolerable for larger standard normed errors.

Table 5-2 Example of analysis for three typical subsoil profiles with different normed errors.

ID	Max Depth (m)	GWT (m)	PGA (g)	Hc (m)	Hliq (m)	CRR	ESP	LSN direct	LSN esp	Norm_err
912	38.1	1.70	0.50	1.70	8.2	0.161	MLS	33.6	36.6	0.016
2	40.5	2.50	0.54	7.51	4.8	0.371	SMX	11.2	1.1	0.111
220	24.3	1.06	0.45	9.29	10.6	0.131	WLD	55.2	18.6	0.175

Figure 5-11 shows the CPT test analysis for the profile with the low error (0.016) catalogued in the present study as #912. Here the ESP equivalence is largely acceptable, and the characterization of the soil profile with three layers is appropriate as there is only one and easily recognizable liquefiable layer. The profile of the Factor of Safety against Liquefaction (FSL) highlights the presence of a continuous shallow sandy layer with FSL<1, extended up to a depth of 10 m. Strata having FSL<1 can also be recognized at different depths, but they are rather scattered and do not represent continuous layers.

Therefore, this profile is adequately described with a crust thickness (H_crust) equal to 1.71 m, a thickness of the liquefiable layer (H_liq) equal to 8.2 m, and an average CRR of 0.16. According to the ESP method, the CPT 912 is classified as MLS since it is characterized by a large (thickness >7m), shallow (depth <2m) liquefiable layer with intermediate liquefaction (CRR=0.161 i.e., in the range 0.15-0.25). The results are still acceptable but to a lesser extent, in the case of CPT catalogued with #2, characterized by a standard normed error of 0.111 (Figure 5-12). Here two distinct liquefiable layers can be identified within the first 20 m, an upper one at 7-12 meters depth and a lower at 15-20 meters depth. A non-liquefiable layer around 2-3 meters thick can be recognized between them. In the ESP method, the second layer is not considered and the CPT_002 is classified as SMX type: strong since it is characterized by a relatively high CRR (0.25-0.5) and midsize because the liquefiable thickness H_{liq} is around 5 meters.

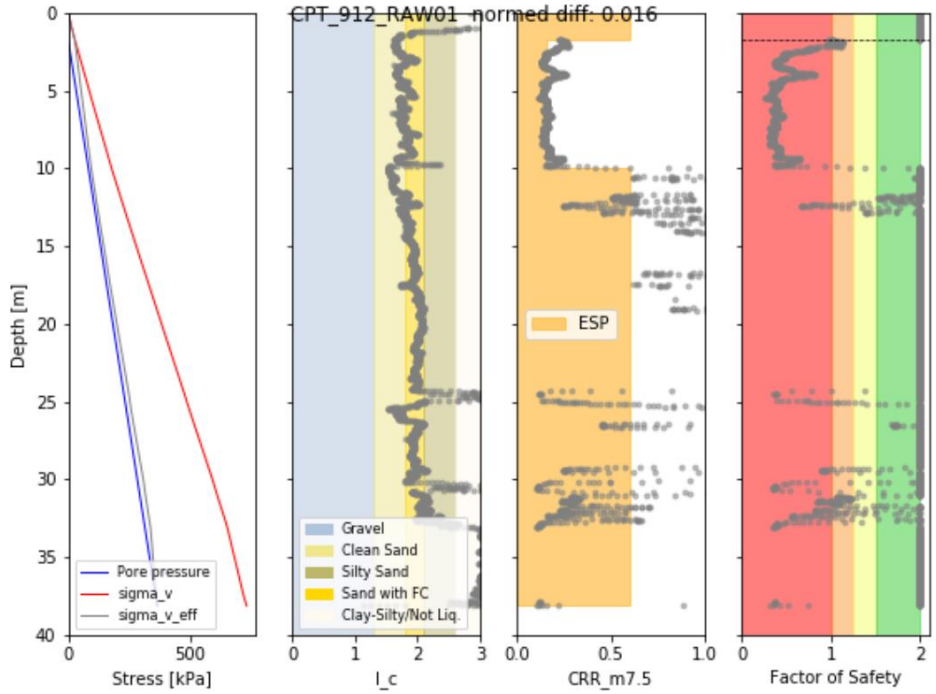

Figure 5-11 CPT profile #912, for which the equivalent soil profile method is consistent with the real soil profile (St.N.E.<0.05).

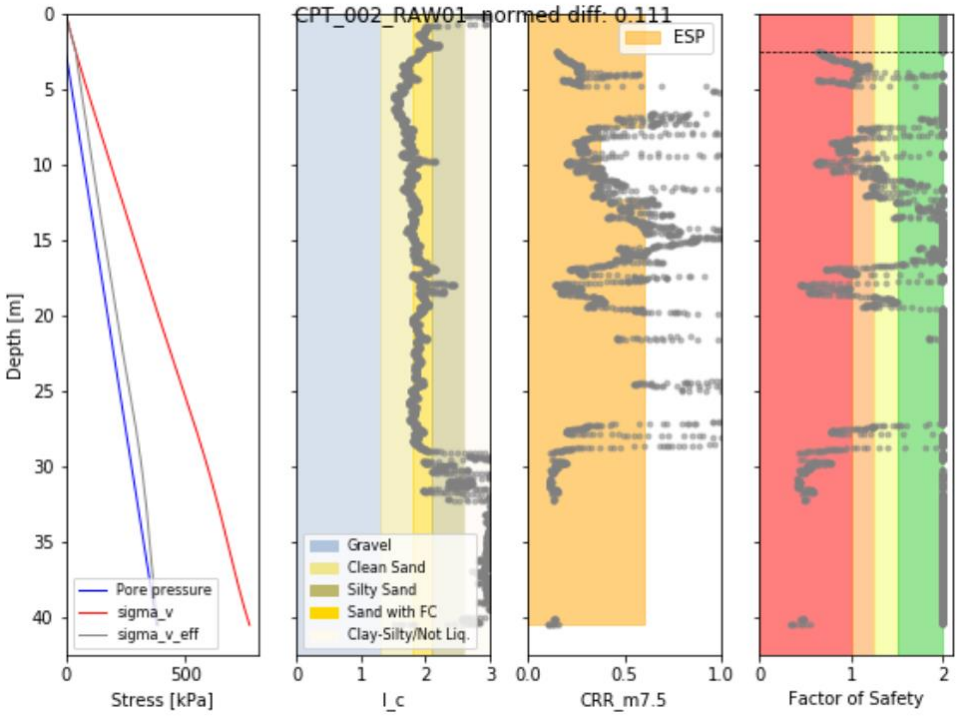

Figure 5-12 CPT profile #2 showing an average agreement between the equivalent soil profile and the real one (0.05<St.N.E.<0.15).

Finally, the third example (CPT #220) concerns a test where the ESP equivalence is not acceptable, and further analyses for liquefaction assessment are needed (Figure 5-13). In fact, the results of such CPT are characterized by an average error of 0.175. Here the profile is classified as WLD according to a large weak liquefiable layer. Still, the equivalence method does not account for the presence of a thick shallow liquefiable layer extended in the first 2-4 m of depth from the ground. Moreover, the same CPT profile highlights a second liquefiable lens of 5-7 m deep. The ESP method thicknesses the crust (H_{crust}) larger than 9 meters, which implies a deep liquefaction phenomenon. The large normed error clearly identifies a poor fit, and engineering judgment would be required to generate a suitable equivalent profile.

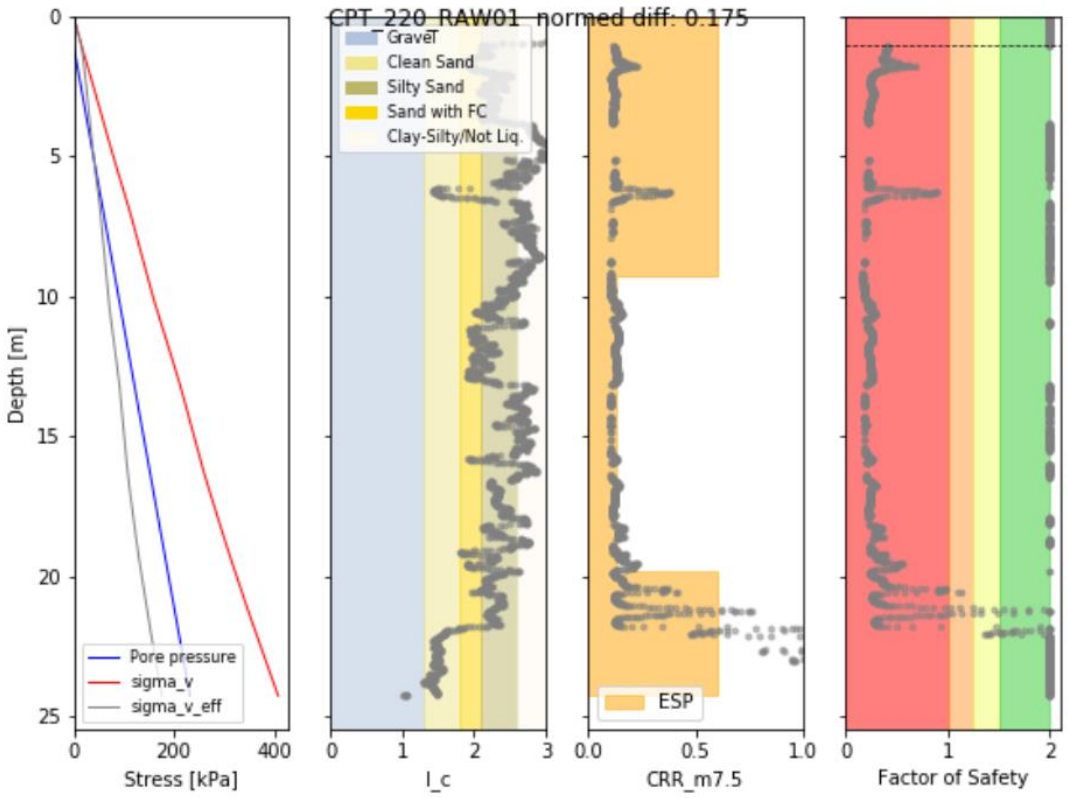

Figure 5-13 CPT profile #220 showing an example of profile where ESP equivalence is not acceptable, and a specific engineering evaluation is required (0.15<ST.N.E.).

After analyzing normed errors largely confirmed the goodness of fitting, the subsoil profiles have been classified into equivalent soil profile classes. An overview of the obtained ESP classes over the territory of Christchurch is presented in Figure 5-14. It

showed that most of the Central Christchurch profiles are assessed as Weak/Mid Resistance to liquefaction (yellow and red points of Figure 5-14). For these areas, ground observation surveys after the CES's major earthquakes revealed moderate to severe liquefaction and lateral spreading, confirming that liquefaction susceptibility is high in the CBD area and along the Avon River. On the contrary, the green points representing Strong subsoil profiles are concentrated in the Northern boundary of the City. In contrast, only a negligible group of Resistant profiles (0.5% of the entire dataset) is observed.

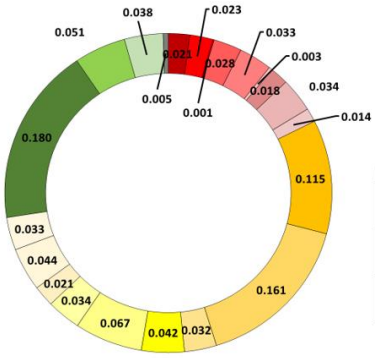

WLS WLM WLD WMS WMM WMD WTS WTM
WTD MLS MLM MLD MMS MMM MMD MTS
MTM MTD SLX SMX STX RXX

		WEAK	%	MID	%	STRONG	%	RESIST	%
LARGE	Shallow	WLS	2.11	MLS	11.54	SLX	18.02	RXX	0.51
	Mid.	WLM	2.29	MLM	16.13				
	Deep	WLD	0.11	MLD	3.18				
MIDSIZE	Shallow	WMS	2.80	MMS	4.23	SMX	5.11		
	Mid.	WMM	3.28	MMM	6.72				
	Deep	WMD	0.34	MMD	3.38				
THIN	Shallow	WTS	1.83	MTS	2.11	STX	3.82		
	Mid.	WTM	3.42	MTM	4.35				
	Deep	WTD	1.39	MTD	3.31				

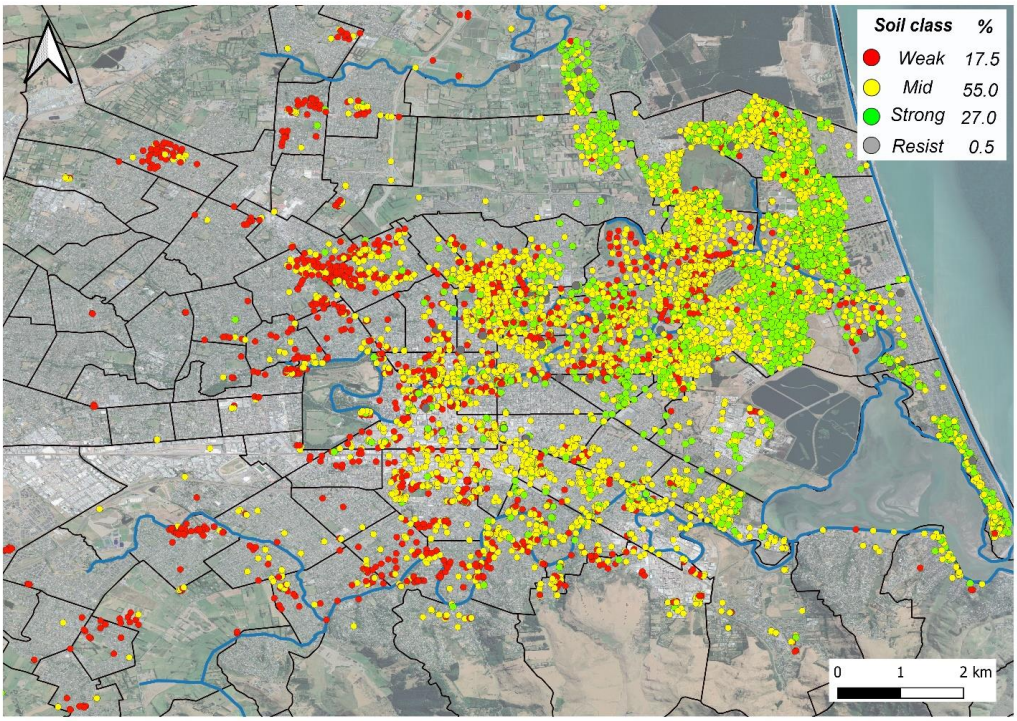

Figure 5-14 Statistical distribution of the Equivalent Soil Profiles in Christchurch (a) and overview of the spatial distribution of subsoil classes (b).

5.3.2 Mapping of liquefaction severity indicators

Considering the February 2011 (Mw 6.2) Earthquake, the hazard analysis consisted in the evaluation of the most widely adopted liquefaction severity indicators, namely: LPI (Iwasaki et al., 1978), w_v (Zhang et al., 2002), LSN (van Ballegooy et al., 2014), LPIish (Maurer, 2015a). The factor of safety has been determined by applying the Boulanger & Idriss (2014) procedure, adopting a cutoff equal to 2.6 to the soil class indicator I_c as suggested for the regional assessment of liquefaction susceptibility by Tonkin & Taylor (2013 – Appendix A). The computed values of all indicators correspondingly to the CPT positions have been interpolated with geostatistical kriging to obtain maps covering the territory. During the following spatial analysis, a filter was applied to the dataset of CPT profiles removing those not consistent with the spatial trend (outlier) following the procedure described in the previous Chapter and summarized in Figure 4-18.

The maps of different indicators are reported in Figure 5-15, Figure 5-18. Taking advantage of the possibility given by this analysis to estimate uncertainty, the standard error distribution was studied, and the area affected by errors larger than 25% have been removed from the present analysis (and represented with grey color).

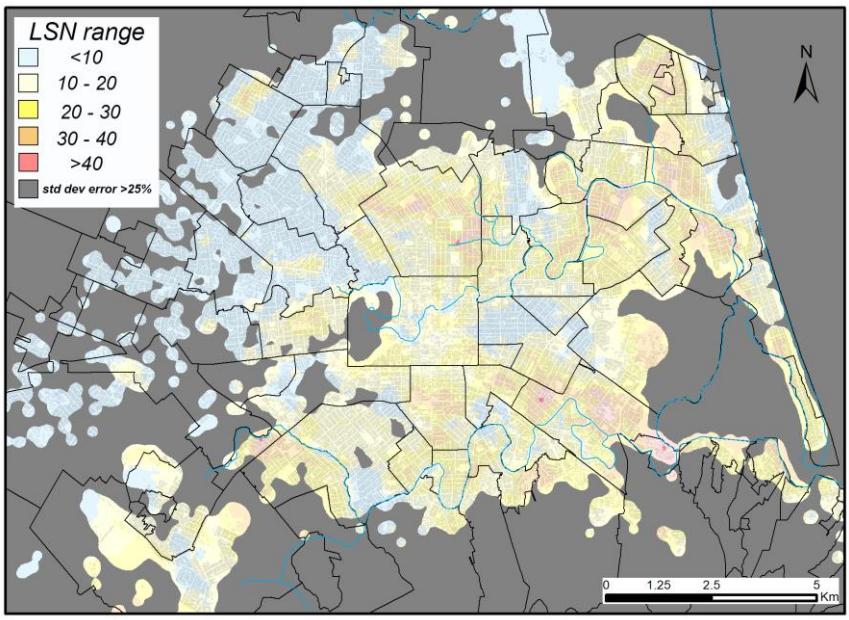

Figure 5-15 Geostatistical interpolation of "LSN" (van Ballegooy et al., 2014) on the entire territory of Christchurch; estimate error map was overlaid to the indicator Map to cut the areas where knowledge is not adequate.

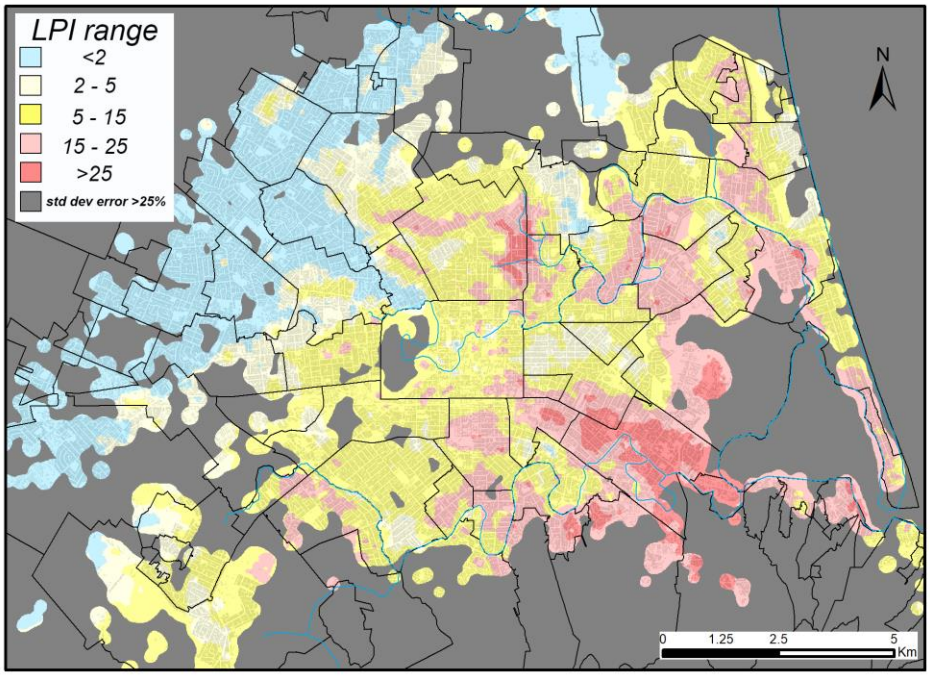

Figure 5-16 Geostatistical interpolation of "LPI"(Iwasaki et al., 1978) on the entire territory of Christchurch; estimate error map was overlaid to the indicator Map to cut the areas where knowledge is not adequate.

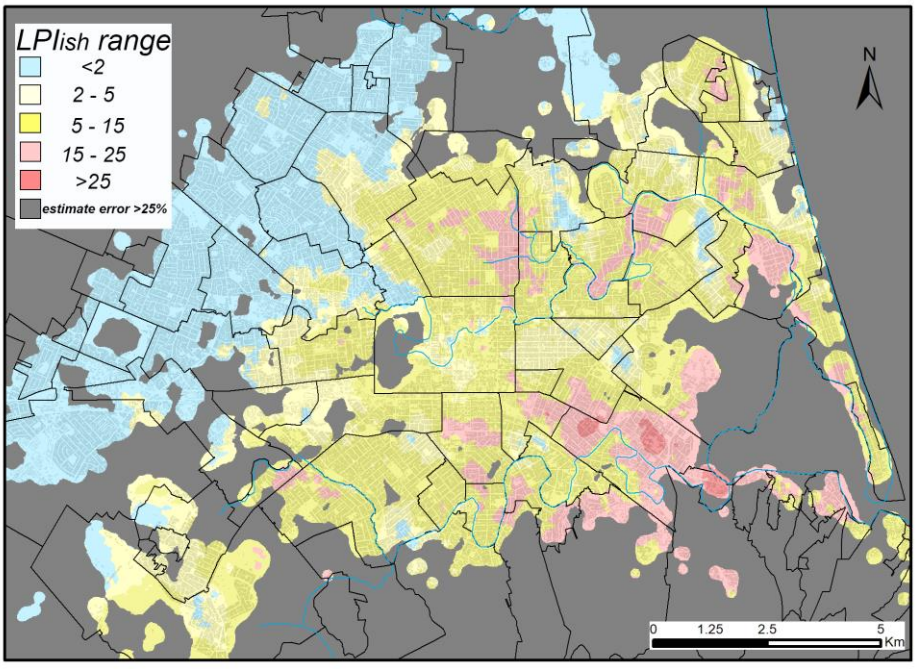

Figure 5-17 Geostatistical interpolation of "LPIish" (Maurer, 2015a) on the entire territory of Christchurch; estimate error map was overlaid to the indicator Map to cut the areas where knowledge is not adequate.

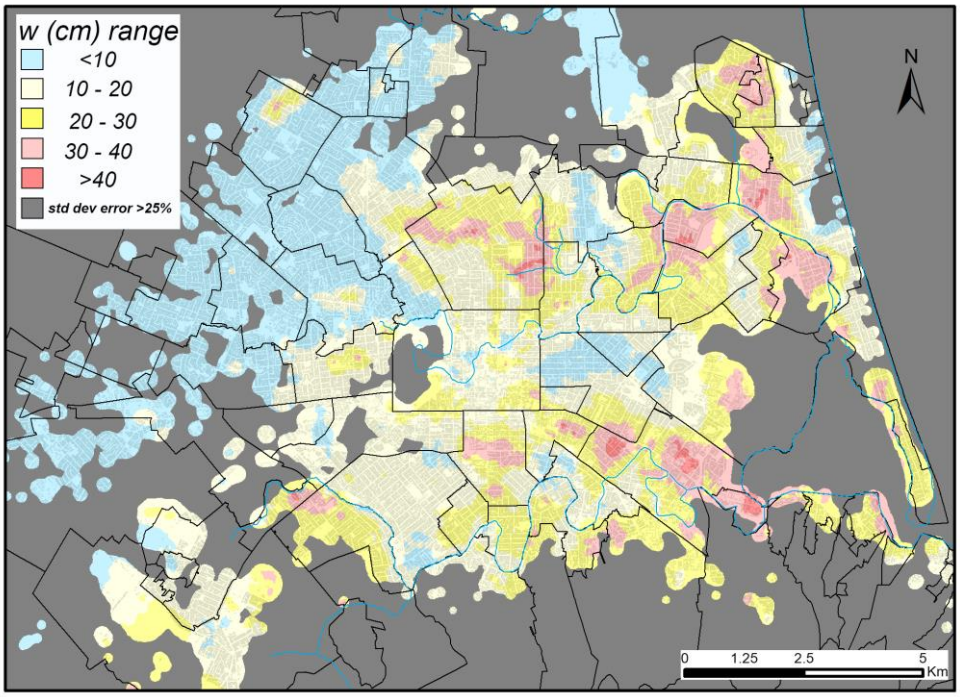

Figure 5-18 Geostatistical interpolation of liquefaction-induced 1D settlement "w" (Zhang et al., 2002) on the entire territory of Christchurch; estimate error map was overlaid to the indicator Map to cut the areas where knowledge is not adequate. Survey of liquefaction-induced ground damage.

Although different from each other, all maps highlight a heterogeneous distribution of values over the territory area with a stronger concentration of potentially liquefiable layers along the end portions of the watercourses (North East and South East portions). This trend reflects the geological and hydrogeological features of the territory, consisting of alluvial deposits of various composition but having major sandy components along the Avon and Heathcote Rivers. This preliminary observation may induce thinking that each of the evaluated liquefaction severity (free field) indicators performs in the same way if compared to the liquefaction ground observations. However, it only represents a qualitative starting point in the correlation between predictive models and observations. Therefore, a quantitative evaluation of their performance based on analytical criteria will be displayed in the following paragraphs.

5.3.3 Lateral Spreading

The 2010-2011 Earthquake sequence also highlighted lateral spreading as one of the most impactive liquefaction-induced effects, responsible for the most severe damage to buildings and infrastructure, especially in the Avon River area. Despite the slope of the ground surface being very small or negligible, namely less than 1%, maximum permanent horizontal ground displacements at the Avon riverbanks are typically in the range between 0.5 m and 1.5 m. A representative section located along the Avon River is reported in Figure 5-19. Scrutiny of the stratigraphy presented in Figure 5-19 shows that each of the three layers could contribute to liquefaction and lateral spreading; however, Cubrinovski and Robinson (2015) identified the intermediate (loose) fine sand to silty sand layer as the critical layer. On the investigated sites exhibiting large-displacement lateral spreads, they were located at depths corresponding to the bottom of the river channel. It had consistently low equivalent clean sand normalized CPT tip resistance in the range between 55 and 75. On the contrary, overlying silty soils and the underlying medium dense, fine sand layers were localized near the riverbanks and were generally not encountered away from the river.

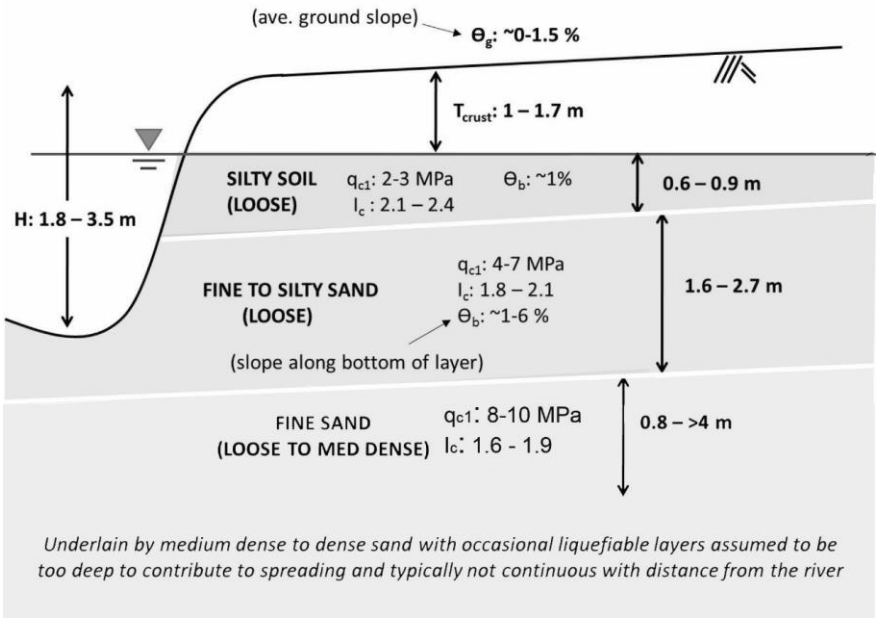

Figure 5-19 Characteristic soil profile of large-displacement lateral spreads (modified after Robinson, 2015).

Thinking on lateral spreading, the liquefaction hazard analysis considering the 22 February 2011 Christchurch Earthquake consisted of applying the Zhang et al. (2004) semiempirical approach to the available CPT dataset. This approach implies combining a CPT-based method to evaluate the factor of safety against liquefaction and the integral of the shear deformation with the topography of the area, which in Christchurch is mostly dictated by the presence of the Avon River and its meanders. Considering the latter issue, Figure 5-19 shows that the Christchurch's typical situation is characterized by the presence of a free face height with gently sloping. And therefore, the topographic factor "TF" has been evaluated with Eqn. 3.19, where the height "H" has been defined as the difference between the CPT ground level and the bottom of the river channel (derived from the Digital Elevation Model). Lastly, for each CPT, the term "L" has been derived by measuring the distance between the profile and the free face in a GIS environment.

Figure 5-20 reports the map of the Zhang et al. (2004) lateral displacements LD evaluated for the 22 February 2011 event; it shows that the estimated lateral displacement along the Avon River and its Northern meanders ranges from 0.25 m to >2 meters, being consistent with the observations described by Cubrinovski and Robinson (2015) based on LiDAR measurements (CGD, 2013). Is it obvious from the topography of Figure 5-19, the LiDAR data depict and quantify global patterns of movement, which show movements predominantly towards the Avon River. However, for lateral the spreading phenomenon, a punctual comparison between prediction and observation cannot be achieved because detailed measurements of lateral displacement at each CPT location are not available.

Figure 5-20 highlights a limitation of the Zhang et al. (2004) Lateral Displacement arising from the topographic amplification factor definition. Since the term "TF" (Eqn. 3.19) depends on the ratio between the distance and height from the free face being zero for L/H>40 if looking at the evaluated "TF" for the whole territory of Christchurch they show only a limited susceptibility to lateral spreading.

Furthermore, the geometry of a representative section (like the one reported in Figure 5-19) highlights that the free face's height ranges in 1.8 – 3.5 m, which according to the Zhang approach means that any LD effect can be evaluated among 72 – 140 m. On the other hand, Cubrinovski and Robinson (2015) observed that the zone affected by the spreading generally extends from the riverbanks up to 150-200 m.

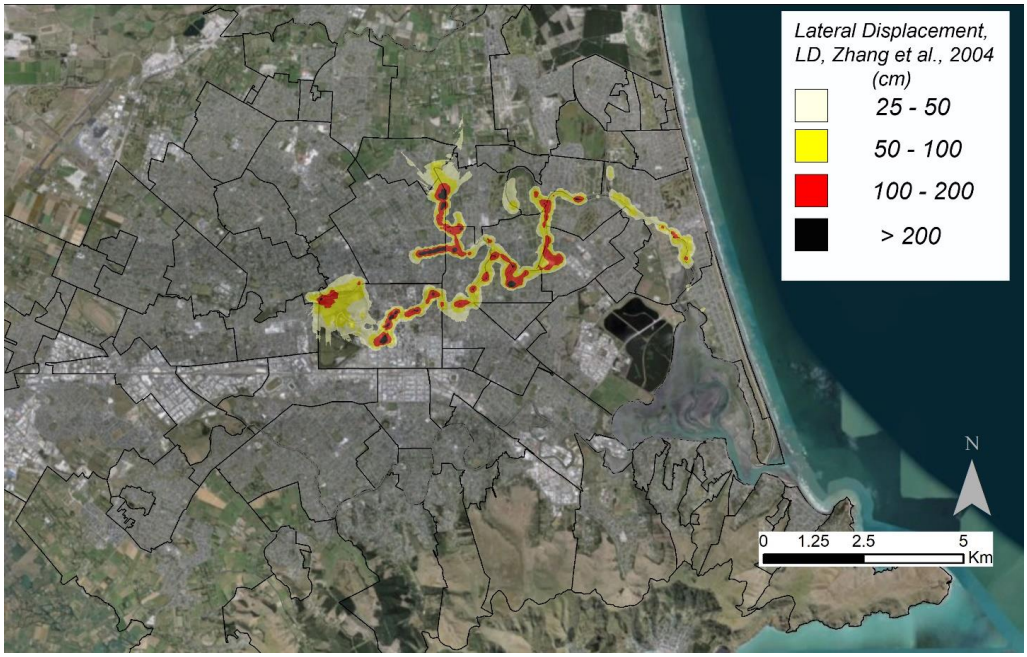

Figure 5-20 Mapping of "LD" (Zhang et al., 2004) along the Avon River after geostatistical interpolation.

These empirical observations have suggested that the application of the Zhang et al. (2004) original framework to the Christchurch Case study may lead to a significative misprediction of Lateral Spreading-induced displacements. To avoid this kind of critical situations, the herein defined GLD, which aim is to generalize the LD concept to all the possible liquefaction-induced phenomena, has been evaluated on the whole set of CPT profiles. With the same logic of the Zhang et al. (2004), the factor of safety FS and the maximum cyclic shear strain have been calculated. On the other hand, the topographic factor "TF" has been evaluated by applying Eqn. 4.3; it is assumed equal to 1 if L/H>40 or the slope is negligible.

A Map of the interpolated GLD values obtained for the 22 February Earthquake is shown in Figure 5-21. From a qualitative viewpoint, the general trend depicted is consistent with liquefaction-induced damage pattern displayed in Figure 5-21. In particular, by combining the effect of subsoil properties, seismicity with the contribution of topography the GLD indicator depicts quite well the Christchurch "Red Zone", i.e. the suburb districts along the Avon River where buildings experienced heavy damage resulting from severe liquefaction and lateral spreading (see Figure 5-3 and Figure 5-4).

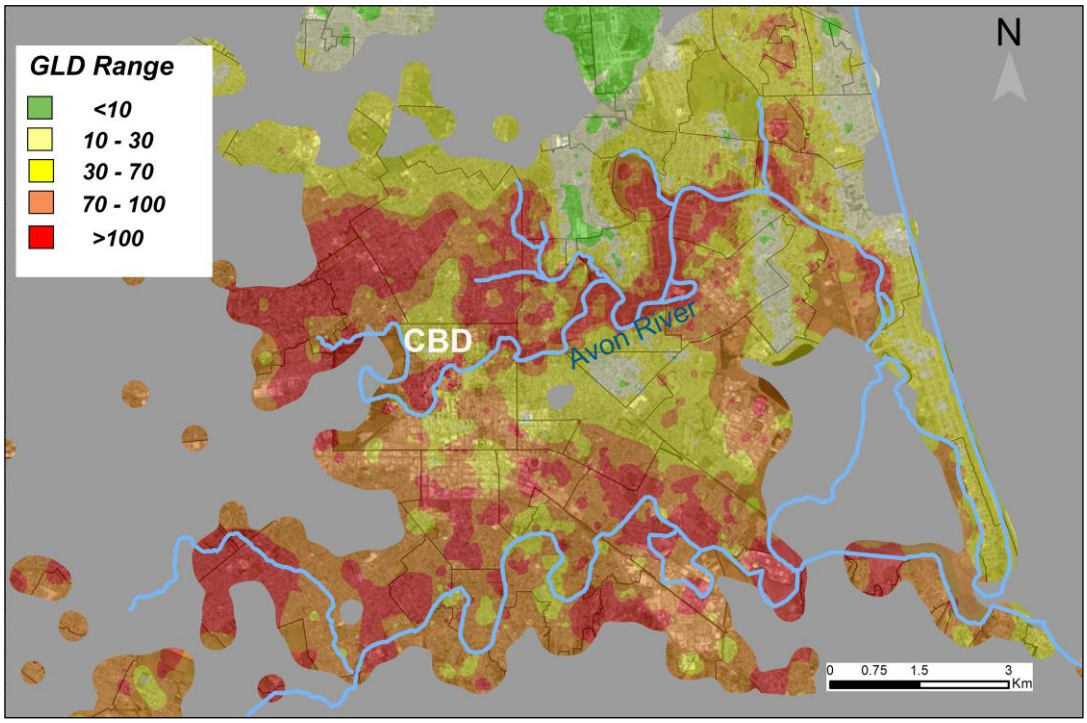

Figure 5-21 Mapping of generalized lateral displacement index, "GLD" after geostatistical interpolation.

Furthermore, the evaluation of a generalized indicator for combined liquefaction and lateral spreading gives the possibility to validate its performance by comparing the map of Figure 5-21 with post-earthquake damage observations.

In fact, following the major Canterbury earthquake events, a survey of damage to land and dwelling foundation was undertaken as part of the coordinated response by the agencies of the NZ government. The mapping of liquefaction-induced land damage was carried out immediately after the September 2010, February 2011, and June 2011 earthquakes to assess the extent and severity of the surface effects. Observations were categorized according to the quantity of ejected material observed on the ground surface and to the presence/absence of cracks and lateral spreading. Each of these three categories was further subdivided according to its severity. In particular, the map of land damage for the 22 February 2011 event (Figure 5-22a) classifies the areas where no liquefaction was observed with blue and green color, the areas characterized by minor to moderate sand ejecta and cracks with yellow, and the areas affected by severe liquefaction, major cracks and lateral spreading with red. For completeness, the same classification after the September 2010 event is reported in Figure 5-22b.

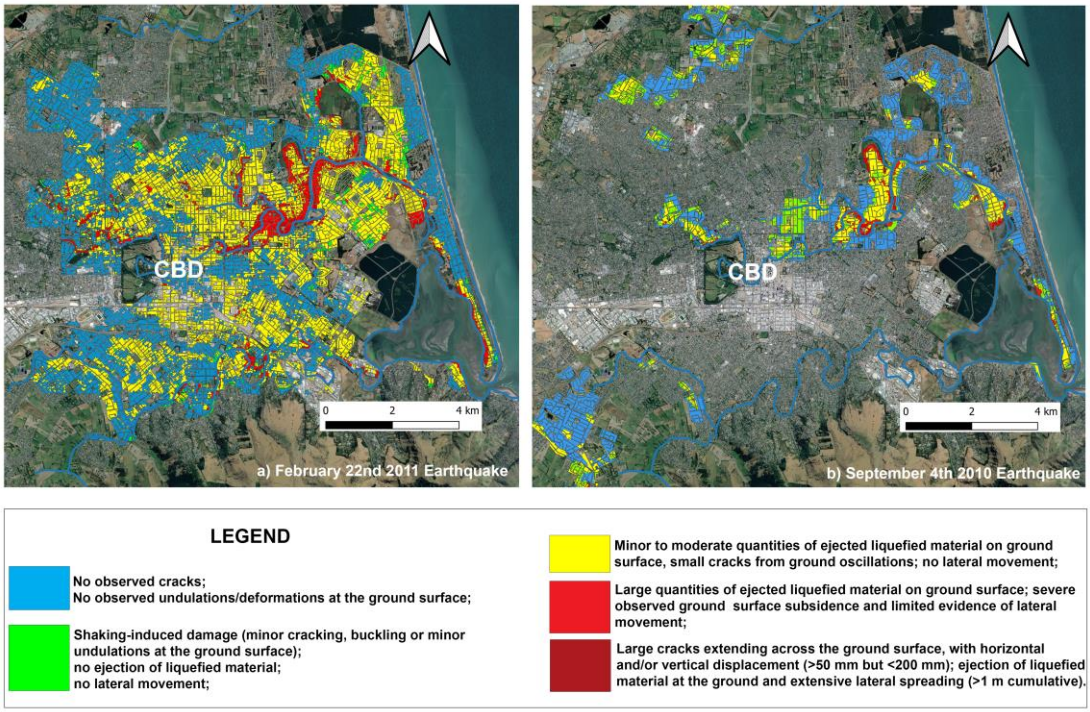

Figure 5-22 Liquefaction and Lateral Spreading Observations from Canterbury Geotechnical Database (2013). Map Layer CGD0300 – retrieved on 22nd September 2016 from https://canterburygeotechnicaldatabase.projectorbit.com/.

5.3.4 Validation of Liquefaction Severity Indicators

Firstly, the traditional liquefaction severity indicators are here validated for the February 2011 (M_w 6.2) earthquake comparing the prediction obtained from each CPT profile with the damage level corresponding to the same position after the earthquake. According to the criterion adopted for validation, defined by Kongar et al., (2015), punctual values of the liquefaction severity indicators have been computed at each CPT location, and the values have been compared with the event. Taking advantage from the ESP method and the geostatistics tool, CPT profiles having a normed error greater than 0.15 and/or differing from the spatial trend have been assessed as outliers. Concerning the latter, yellow, orange and red areas in Figure 5-23 represent zones affected by liquefaction (positive event). In the validation test, threshold values have been varied between the minimum and maximum observed values and the Receiver Operator Curve has been built (Kongar et al., 2015). Then the area under the curve AUC is calculated, by combining the True Positive/Negative Ratio and the False Positive/Negative Ratio. Finally, the Mathews Correlation Coefficient "MCC" has

been evaluated to identify the optimal threshold of each indicator in liquefaction-induced ground damage prediction.

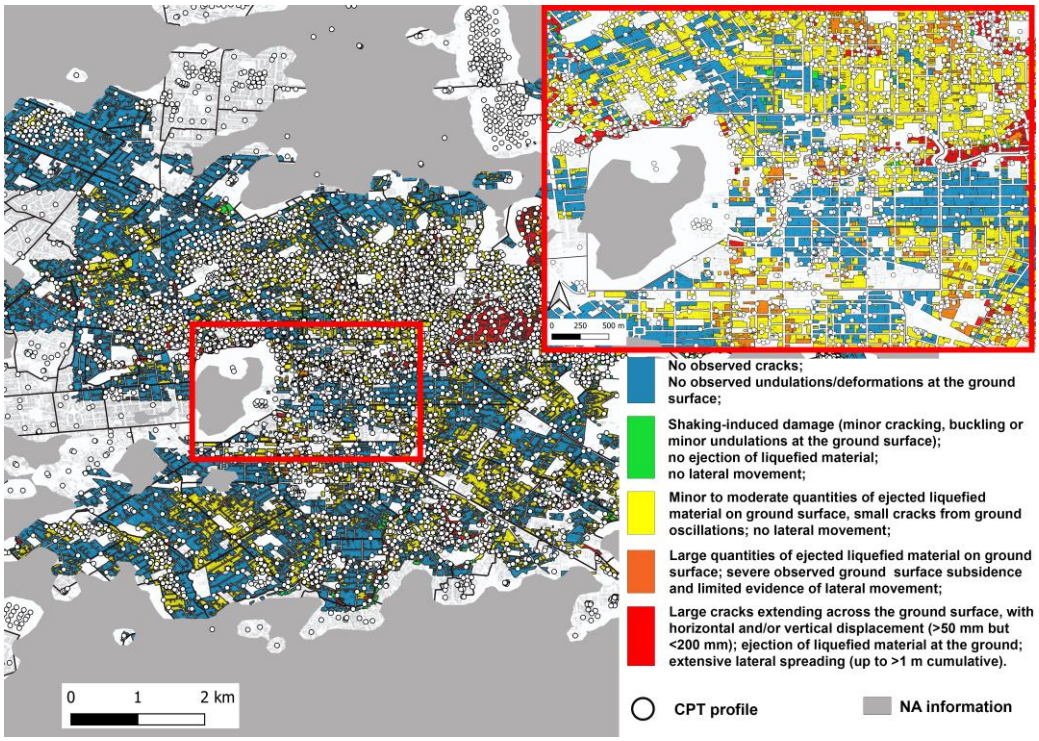

Figure 5-23 Map of liquefaction-induced ground damage superposed to the location of CPT tests; grey areas were removed from the analysis due to inadequate knowledge.

A preliminary observation on the "MCC" formula points out that success and failure of prediction (for both positive and negative occurrence) are considered in the same way, i.e. without distinguishing the consequences of misprediction. To account for this issue, Maurer et al. (2015b) propose to set the optimal decision thresholds evaluating the economic consequences of misprediction, i.e. multiplying the terms of Eqn. 4.36 with weighting factors. Despite this issue becomes relevant when risk assessment is preparatory for remediation of buildings, this logic has not been introduced in the present step of thr analysis, i.e. the same weight has been given to all terms, to avoid subjective consideration on the cost of repair and remediation. Alternatively, when the Matthews coefficient does not provide a clearly defined optimal threshold, other indicators like the maximum value of the Youden (1950) "j-stats" can be assumed to determine an optimal threshold.

Inthea first step, the effectiveness of traditional indicators has been tested in discriminating among liquefaction/non-liquefaction. The results of this analysis, reported in Figure 5-24, show a fairly good predictive ability of all indicators, with minimal differences among the different methods. The parameters defined by the validation test are summarized in more detail in Table 5-3.

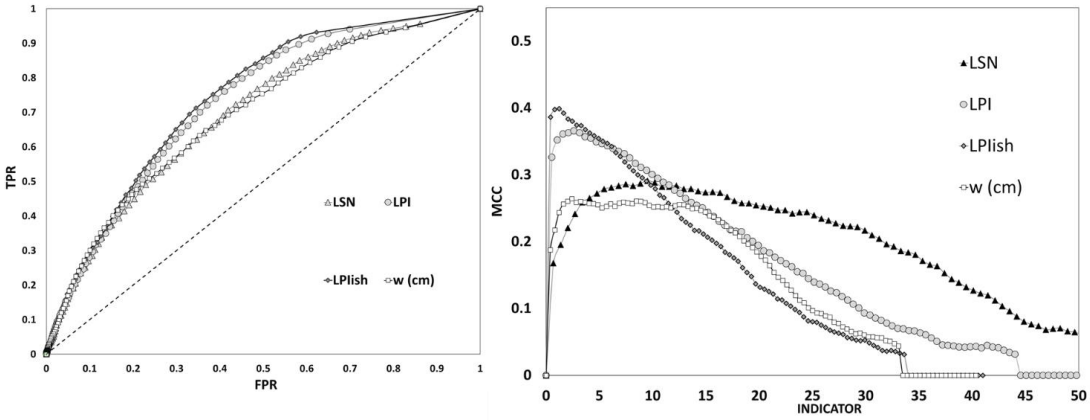

Figure 5-24 ROC curves and MCC functions after geostatistical error filtering.

Table 5-3 General performance of traditional indicators in predicting the occurrence of liquefaction, after geostatistical filtering of outliers.

Liquefaction Severity Indicator	AUC	OPTIMAL THRESHOLD (MCC)	TPR	FNR	TNR	FPR	OSR (%)	OFPR (%)	OFNR (%)
LPI	0.74	≈2	0.88	0.12	0.45	0.55	74.6	16.5	8.9
W (cm)	0.70	≈3-4	0.84	0.16	0.39	0.61	70.4	18.8	10.8
LPIish	0.76	≈1	0.90	0.10	0.44	0.56	76.0	17.3	6.7
LSN	0.70	≈10	0.85	0.15	0.42	0.58	71.7	15.4	12.9

One of the critical issues points of the simplified analysis based on indicators is its representativeness in case of multiple liquefiable alternated with non-liquefiable layers. As observed by Cubrinovski and van Ballegooy (2017), the dense alternation of liquefiable and non-liquefiable layers creates the conditions for a more complex dynamic response (called system response by the authors) of the deposit, where liquefaction does not affect all layers, as postulated by the indicators, but affects some of them selectively and propagates with time to closer layers.

In the further step of the analysis, a distinction has been made among the CPT tests considering only those fulfilling the equivalence criterion defined by the Equivalent Soil Profile. Out of the entire database, around 1 000 profiles (corresponding to the 13%) with a normed error< 0.05 have been selected. The repetition of the binary test considering only these profiles shows a remarkable improvement in the performance of traditional liquefaction severity indicators. It is also interesting to note that the optimal threshold values for each indicator, i.e. those better defining the prediction of positive/negative event (reported in Table 5-4), are consistent with the typical values defined by the authors of each method. Therefore, this analysis confirms the validity of all methods for the subsoil stratigraphy, where a unique liquefiable layer can be identified.

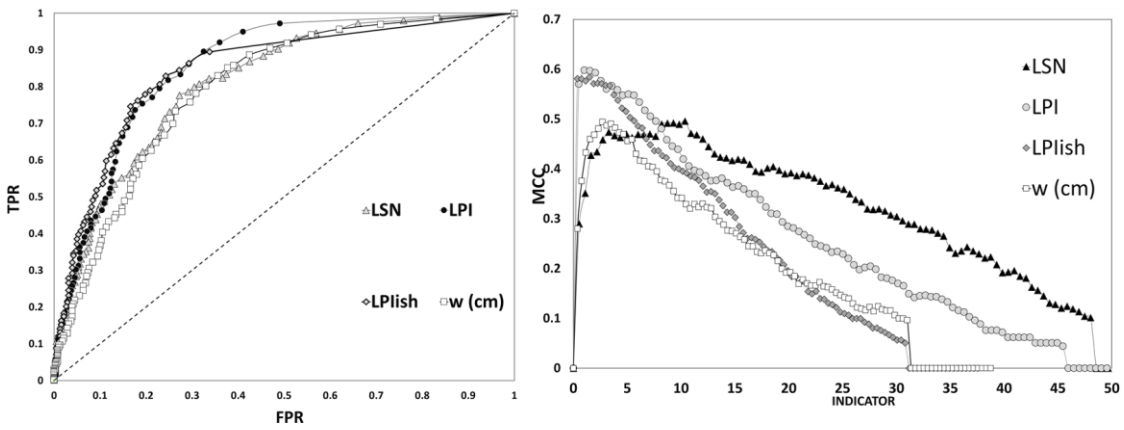

Figure 5-25 ROC curves and MCC functions after geostatistical error filtering, for CPTs consistent with the three-layers profiles (ESP normed error<0.05).

Table 5-4 General performance of traditional indicators in predicting the occurrence of liquefaction, after geostatistical filtering of outliers, for CPTs consistent with the three-layers profiles.

Liquefaction Severity Indicator	**AUC**	**OPTIMAL THRESHOLD (MCC)**	**TPR**	**FNR**	**TNR**	**FPR**	**OSR (%)**	**OFPR (%)**	**OFNR (%)**
LPI	0.87	≈2	0.90	0.10	0.67	0.33	80.8	12.8	6.4
W (cm)	0.80	≈4	0.85	0.15	0.62	0.38	76.3	14.6	9.1
LPIish	0.88	≈1	0.84	0.16	0.73	0.27	79.9	10.8	9.3
LSN	0.82	≈10	0.78	0.22	0.73	0.27	75.7	7.5	16.8

At the same time, a reduction in the performance can be observed for each indicator versus the most severe liquefaction-induced damage levels: this is quantified by ROC value up to 20-30% smaller if compared to the previous hypothesis of three strata-layered profiles. The worst situation is observed when traditional indicators are employed in predicting severe cracks and lateral spreading. Despite the evaluated optimal thresholds significantly increase if compared to the lower liquefaction induced damage levels, for all the indicators the AUC range in 0.58 – 0.66 (as shown in Table 5-5,), i.e. values representative of poor performance. It is noticeable that the TPR range in 0.38 – 0.42, meaning that most of the positive events of lateral spreading are underestimated by the traditional indicators. These results are not surprising as lateral spreading takes place under bi-dimensional conditions that are not considered in the definition of traditional indicators.

Table 5-5 General performance of traditional indicators in predicting lateral spreading, after geostatistical filtering of outliers, for CPTs consistent with the three-layers profiles.

Liquefaction Severity Indicator	**AUC**	**OPTIMAL THRESHOLD (MCC)**	**TPR**	**FNR**	**TNR**	**FPR**	**OSR (%)**	**OFPR (%)**	**OFNR (%)**
LPI	0.65	≈22.5	0.42	0.58	0.79	0.21	79.1	20.3	0.6
W (cm)	0.58	≈20	0.38	0.62	0.79	0.21	78.2	21.1	0.7
LPIish	0.66	≈18	0.38	0.62	0.86	0.14	85.3	14.0	0.7
LSN	0.65	≈38.5	0.42	0.58	0.89	0.11	88.5	8.5	3.0

In the following phase, the validation method proposed by Kongar et al. (2015) has been applied to assess the performance of the generalized indicator in predicting liquefaction induced damage. As shown in Figure 5-22, ground liquefaction evidence resulting from each of the main events of the CES were categorized in four classes: minor (including sand boils and punctual phenomena of liquefaction), minor to moderate cracking, severe cracking and lateral spreading. For each condition, the values indicating the performance of prediction are reported in Table 5-6, while Figure 5-26 shows the area under the curve AUC for lateral spreading. The introduction of 2D geometrical conditions in the results in a stable capability of the proposed GLD indicator to capture observations, being the ROC curves higher than the plane bisecting line, with an AUC ranging in 0.76 – 0.85. Also, when the hypothesis of three strata

model is ascertained, namely the normed error is found minor than 0.05, it can be observed that the AUC values are usually 10-15% greater than the corresponding AUC given by traditional indicators. This evidence suggests both a stable performance of the generalized LD in capturing liquefaction ground observations and an improvement if compared to traditional indicators.

On the other hand, in defining the optimal generalized LD thresholds according to the criterion of Matthews (1975), the "MCC" function can reach a plateau since this variable depends on the total number of TP, TN, FP, FN. In such cases, the maximum value of j-stats indicator can be assumed alternatively to the "MCC".

The general parameters associated to the GLD and summarized in Table 5-6 show its robustness in forecasting the different types of liquefaction induced phenomena. As an example, looking at the binary test performed for lateral spreading assuming an optimal GLD threshold = 100, an important improvement in the performance of GLD (concerning the before evaluated traditional indicators) consists in the reduction of the False Negative cases which represent the most dangerous type of error (azure versus red points of Figure 5-27).

Observers may argue that sometimes the evaluated Overall Success Rate (OSR) is not particularly exciting (e.g., 62.2% for minor cracks). Still, when looking at the Overall Failure Rate (OFR), it can be observed that the most relevant contribution is represented by the Overall False Positive Ratio instead of the Overall False Negative Ratio (34.3% against the 3.5%). This results in a more conservative approach.

Table 5-6 Performance of the generalized indicator "LD" in predicting the observed liquefaction-induced damage levels after the application of the validation test.

DAMAGE LEVEL	AUC	OPTIMAL THRESHOLD	TPR	FNR	TNR	FPR	OSR (%)	OFPR (%)	OFNR (%)
Liquefaction/No Liquefaction	0.85	10-12	0.83	0.17	0.68	0.32	77.0	12.7	10.3
Minor to Moderate Cracking	0.78	≈25-30	0.79	0.21	0.59	0.42	62.2	34.3	3.5
Moderate to Severe Cracking	0.76	≈60-70	0.65	0.35	0.72	0.28	71.0	25.9	3.1
Lateral Spreading	0.83	≈90-100	0.68	0.32	0.78	0.22	79.5	19.2	1.3

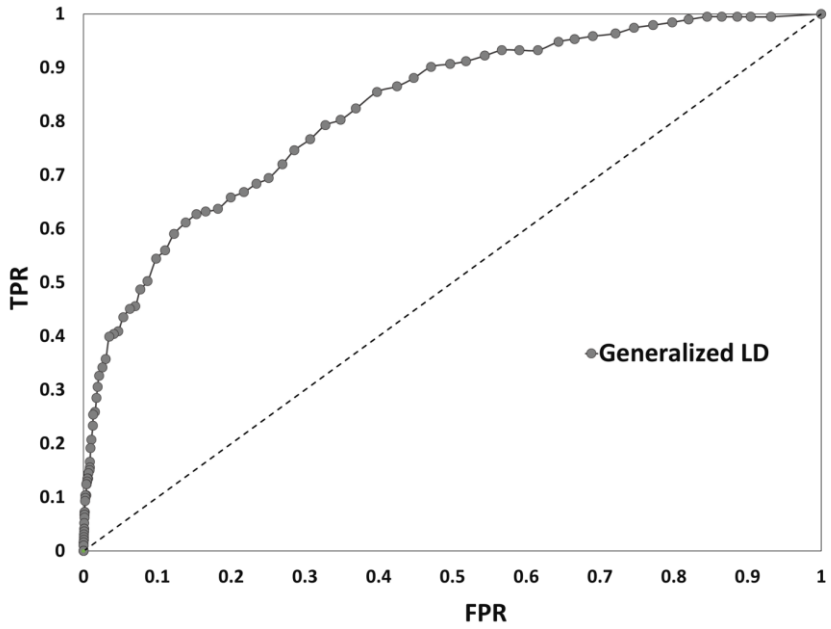

Figure 5-26 ROC curve of the generalized indicator LD vs lateral spreading observations for CPTs consistent with three-layers profiles (namely CPTs having an ESP normed error < 0.05).

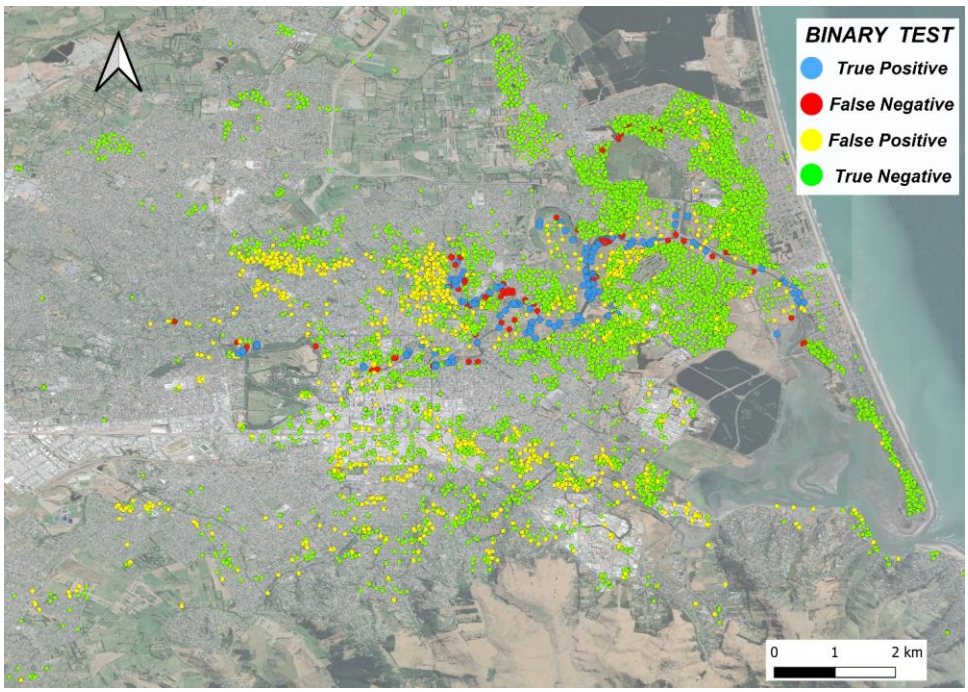

Figure 5-27 Generalized LDI binary test for lateral spreading, assuming an optimal threshold equal to 100.

5.3.5 Semi-empirical based soil fragility curves for liquefaction (free field)

Taking advantage from the huge amount of available CPT and the post-seismic surveys showing liquefaction-induced ground observations, the Christchurch City case study offers an unprecedented chance to test the most widely used liquefaction severity indicators refining them with the introduction of new criteria like the Ishihara (1985) based LPI that accounts to the presence of a non-liquefiable crust thickness or the equivalent soil profile method which provides a quantitative measure of liquefaction susceptibility and an indicator of the validity of the three-layered model.

Additionally, a so huge number of liquefaction-induced evidence induced by ground accelerations ranging in (0.15 – 0.60g) on several susceptible subsoils forms an unprecedented dataset allowing to derive probabilistic relationships between the expected liquefaction ground severity and the observed damage.

To this aim, many approaches (like the PBEE) adopt lognormal functions to link the mechanical evolution of liquefaction (empirical or numerical modelling of the phenomenon) with damage measures (predefined damage limit states or observations). Despite most of the existing literature is focused on liquefaction-induced damage on buildings (Fotopoulou et al., 2018) and infrastructures like embankments and pipe networks (Syner-G, 2013; Liu et al., 2015), only a few studies have tried to link the expected values of liquefaction severity indicators to predefined liquefaction-induced surficial observations. A preliminary study to derive free field liquefaction fragility curves is proposed by Maurer et al. (2017). The authors analyzed two separate datasets: the former made of case histories resulting from 20 global earthquakes; the latter includes observations from three events in Christchurch (the 2010 Mw7.1 Darfield Earthquake, the 2011 and 2016 Christchurch respectively Mw6.2 and Mw5.7 Earthquakes). In each case, profiles experiencing PGA lower than 0.15g were removed from the calculation.

The obtained functions express the probability of observing liquefaction ground evidence (which severity ranges from no to severe) as a function of three different liquefaction severity indicators (LPI, LPIish and LSN). Each of the liquefaction severity indicators has been evaluated with four alternative liquefaction-triggering models: Robertson (1998), Moss et al. (2006), Idriss and Boulanger (2008), Boulanger and Idriss (2014).

The probability of the surface manifestation of liquefaction reaching/exceeding a manifestation severity, MS, given a computed Liquefaction Demand Measure LDM value, FMS(LDM), is idealized by a typical lognormal distribution (e.g., Bradley, 2010):

$$F_{MS}(LDM) = \phi\left(\frac{Ln\left(\frac{LDM}{x_m}\right)}{\beta}\right) \quad \textit{Eq. 5.1}$$

where Φ denotes the Gaussian cumulative distribution function; x_m is the distribution median, and β is the logarithmic standard deviation. Among the entire range of approaches aimed at fitting functions to data, the maximum likelihood method described in Porter (2016) is employed. It identifies the model parameters with the highest likelihood of producing the observed data.

The case histories are grouped into m classes of LDM, where bins have index i, average value LDM_i, and contain n_i cases, of which f_i are cases in which observed manifestations reached or exceeded MS. Assuming quantity f_i can be estimated from a binomially distributed random variable; F_i, gives the probability of observing quantity f_i among n_i cases; Eqn. 5.2. gives the probability of an individual case exceeding MS:

$$P\left[F_i = f_i\right] = \frac{n_i!}{f_i!(n_i - f_i)!} \cdot p_i^{f_i} \cdot (1 - p_i)^{n_i - f_i} \quad \textit{Eq. 5.2}$$

In Eqn. 5.2, p_i is defined by Eqn. 5.1, evaluated at LDM_i. Lastly, the values of parameters xm and β that maximize the likelihood of producing the observed data are determined. This likelihood is given by the product of the probabilities in Eq. 5.3, multiplied over all bins:

$$L(x_m, \beta) = \prod_{i=1}^{m} P[F_i = f_i] \quad \textit{Eq. 5.3}$$

With the same logic of Maurer et al. (2017), a set of empirical fragility curves for liquefaction ground observations are derived on Christchurch case study merging the post 22 February liquefaction ground observations to the available information of CPT profiles. As a preliminary step, the application of the ESP method allowed to select those profiles consistent with the three-layers hypothesis, the same on which the performance of liquefaction severity indicators showed the best predictive capability.

Despite this implies to remove a significative number of profiles from the original, more than 1000 CPT profiles with an ESP normed error lower than 0.05 (Figure 5-8) are considered. On this subset, the traditional liquefaction severity indicators (LPI, LPIish, Wv and LSN) have been evaluated. The factor of safety against liquefaction has been evaluated with the Boulanger & Idriss (2014) triggering model, adopting an Ic cut-off of 2.60 for the liquefiable layer (Robertson, 1998; Tonkin and Taylor, 2013 - A) and the Boulanger – Idriss (2014) relation to evaluate the Fine Content, FC (%). On the other hand, the severity of surficial liquefaction manifestations has been classified in minor, moderate and severe with the same criteria shown in Figure 5-22. Since lateral spreading is not captured by the most known 1D liquefaction severity indicators, that does not account to geometry, it is not included in the above-mentioned damage classification. On the contrary, it will be separately considered by the generalized LD indicator.

The fragility functions obtained after the application of the Equivalent Soil Profile method and the geostatistical spatial filter of outliers, having all the form presented in Eq. 5.1, are summarized in Table 5-7. For each damage level, the xm and β values are provided and, when possible, compared with the corresponding set proposed by Mauer et al. (2017). Despite with differences among each other, i.e. among mean and standard deviation values associated to a given damage level, the two sets of functions show an acceptable consistency for each the indicators. Additionally, the maximum calculated value for each indicator is reported, meaning that discretion should be used in using the obtained fragility functions out from the suggested range.

Table 5-7 Summary of liquefaction soil fragility-functions and comparison with the Maurer (2017) results.

	Damage	**LPI**			**LPIish**			**LSN**		
	Level	**Xm**	**β**	**Range**	**Xm**	**β**	**Range**	**Xm**	**β**	**Range**
Maurer et al. (2017)	MINOR	6.3	1.059	*LPI ≤58*	3.97	1.292	*LPI_{ish} ≤52*	15.9	1.131	*LSN ≤65*
	MODERATE	18.98	1.154		14.3	1.417		39.9	1.164	
	SEVERE	56.7	0.827		53.98	1.036		198.6	1.304	
This study	MINOR	4.7	1.117	*LPI ≤51*	2.4	1.446	*LPI_{ish} ≤38*	13.5	1.011	*LSN ≤55*
	MODERATE	25.1	0.947		23.4	1.10		45.0	1.11	
	SEVERE	54.1	1.110		45.0	1.120		167.4	1.685	

Indicator	**Damage Level**	**Parameters**		
		Xm	**β**	**Range**
Wv (cm)	MINOR	5.4	1.21	*Wv ≤39 cm*
	MODERATE	30.6	1.206	
	SEVERE	100	1.710	

As an example, the suite of functions developed for use with LPI is plotted in Figure 5-28. The obtained functions relate the probability of each manifestation severity, MSi, to a computed value of LPI, which reflects the general distribution of liquefaction ground evidence observed after the 22 February 2011 Earthquake and shown through the histograms plot of Figure 5-29. From Figure 5-28, it can be observed that the probabilities of manifestations being at least minor, moderate, and severe at LPI = 10 are 75%, 16.5%, and 6.5%, respectively. Equivalently, these curves provide the probability that a manifestation will be in a severity class. This is illustrated by the black segments denoted as P (No damage), P (minor damage), P (moderate damage), and P (severe damage) and respectively representing the probability that MS will be none, minor, moderate, and severe. Again, using LPI = 10 as an example, the probabilities of manifestations being none or minor, moderate, and severe are 25%, 59%, 10%, and 6.5%, respectively (Figure 5-29).

In Figure 5-30, the LPI fragility functions showed in Figure 5-29 are plotted together with the Maurer et al. (2017) fragility-functions, which parameters are listed in Table 5-7. About the LPI, Figure 5-30 shows that the two models agree quite well in predicting the minor damage, while small differences exist concerning the moderate and severe levels (ranging in 10 – 20%). Considering the severe damage, the graph seems to suggest that the consistency of three-layered profiles hypothesis results in a more conservative estimate of its probability of occurrence.

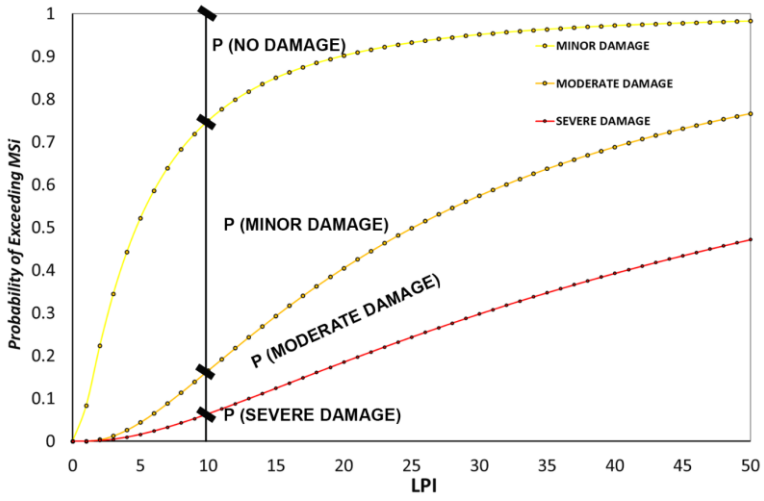

Figure 5-28 Probability of exceedance of a manifestation severity, MSi, given an LPI value and the respective probabilities that manifestation severity is none, minor, moderate, and severe.

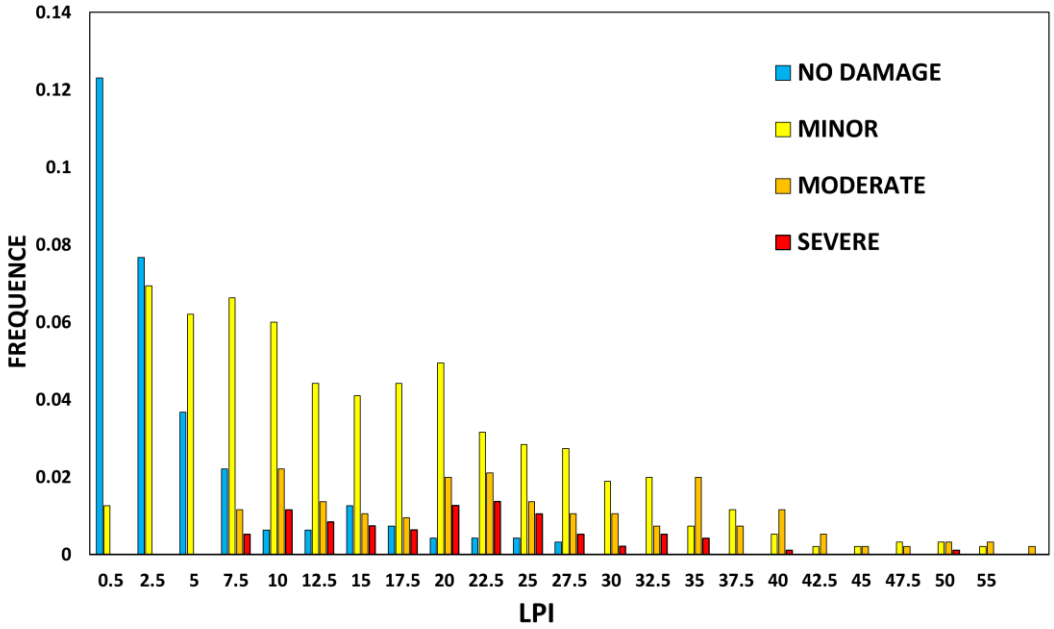

Figure 5-29 General frequence of manifestations being in a severity class, MSi, given an LPI.

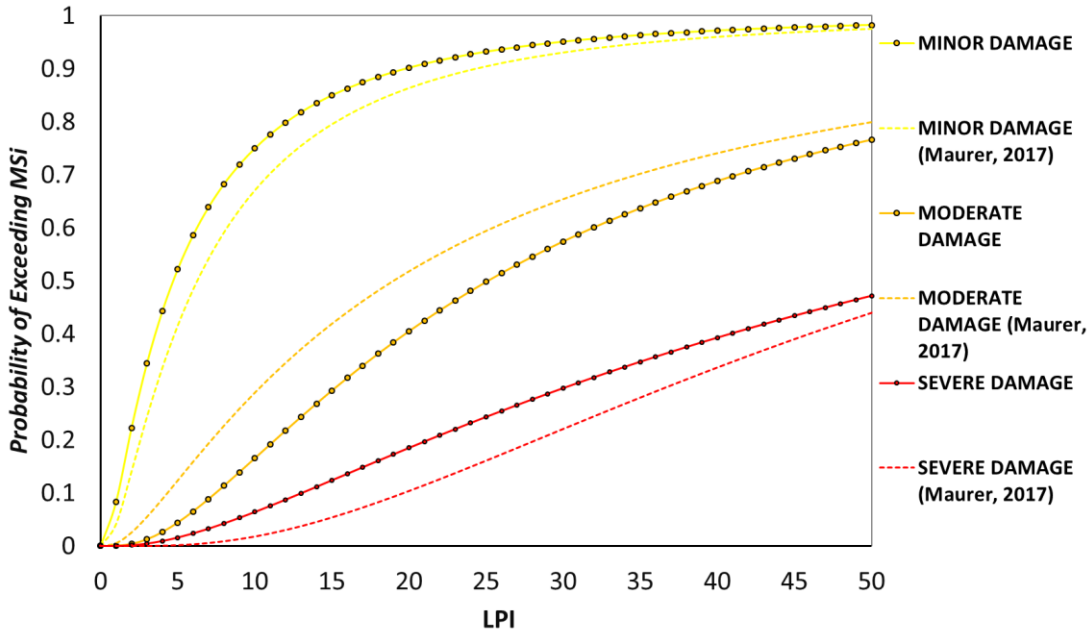

Figure 5-30 Comparison of the herein developed fragility curves given an LPI value and the corresponding proposed by Maurer et al. (2017).

With the same logic, semi-empirical fragility functions of the generalized GLD indicator have been derived for the 22 February earthquake, starting from the application of the Equivalent Soil Profile and the geostatistical spatial filtering of outliers. The Boulanger & Idriss (2014) procedure and the Robertson (1998) chart, have been respectively applied to evaluate the factor of safety against liquefaction and the soil behaviour type index Ic, assuming an Ic cut off equal to 2,60. On the other hand, liquefaction-induced ground damage levels ranging from no observed damage to lateral spreading have been considered (Figure 5-22). The mean xm and standard deviation β values corresponding to each damage level are summarized in Table 5-8, which also reports the maximum calculated value (i.e. the Range column).

Table 5-8 Summary of liquefaction soil fragility-functions as a function of the generalized indicator LD.

	Damage Level	Parameters		
		Xm	β	Range
GEN LD	MINOR	17	1.448	*GEN LD ≤300*
	MODERATE	80	1.184	
	SEVERE	130	0.909	
	LATERAL SPREADING	170	0.540	

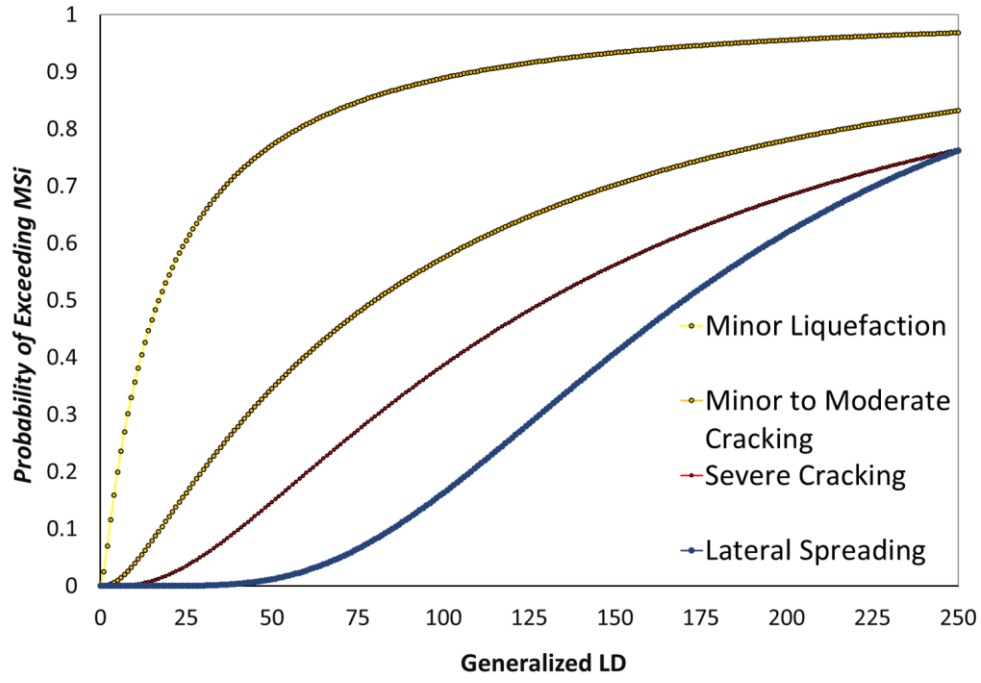

Figure 5-31 Probability of observing a manifestation severity, MSi, given a GEN LD value.

5.4 **Risk Analysis**

Firstly, the methodology described in the Flowchart of Figure 4-14 has been applied to the Christchurch building stock as back analysis of the 22 February event; then, a further analysis based on the PBEE approach will be implemented considering the residential RC-F building stock of Christchurch. In both cases, the analysis requires to collect and process data of different nature, referring them to their geographical position, cross information and compute the different terms of damage and risk. Regarding the 22 February event, building typology and characteristics together with subsoil composition and properties for the city of Christchurch have, thus, been combined in a GIS platform to predict damage with the scheme of Figure 4-14 and compare estimates with the post-earthquake survey of buildings.

5.4.1 Typology, characteristics and damage of buildings

The data on buildings have been recovered from the Canterbury Earthquake Building Assessment (CEBA) database (Lin et al., 2014; 2016). This database was developed based on post-earthquake data collected by Christchurch City Council (CCC), the Canterbury Earthquake Recovery Authority (CERA), and Tonkin and Taylor Limited to quickly assess buildings health state and identify possible danger to the public safety. It provides several information on damaged buildings, including addresses, year of construction, structural attributes like typology, systems and construction material, the current state of conservation, number of stories and fundamental period (T_y), peak ground and spectral acceleration (PGA, $S_a(T_y)$) plus other information (Fikri et al., 2018). About 10 777 damaged buildings were documented in the CEBA database following the Canterbury earthquakes, of which 6 062 were classified as residential (56%) and 3528 (33%) as commercial (Lin et al., 2016). The distribution of buildings over the territory (Figure 5-32.a,b) shows that the largest part consists of relatively light wooden structures (61%), with one or two stories, a lower percentage (16%) is made of heavier masonry walls. In comparison, the remaining part consists of reinforced concrete (21%) or steel frames (2%). While wooden buildings are distributed all over the city area, the reinforced concrete buildings are mainly concentrated in the central part of the city, around the Christchurch CBD (Figure 5-32.c).

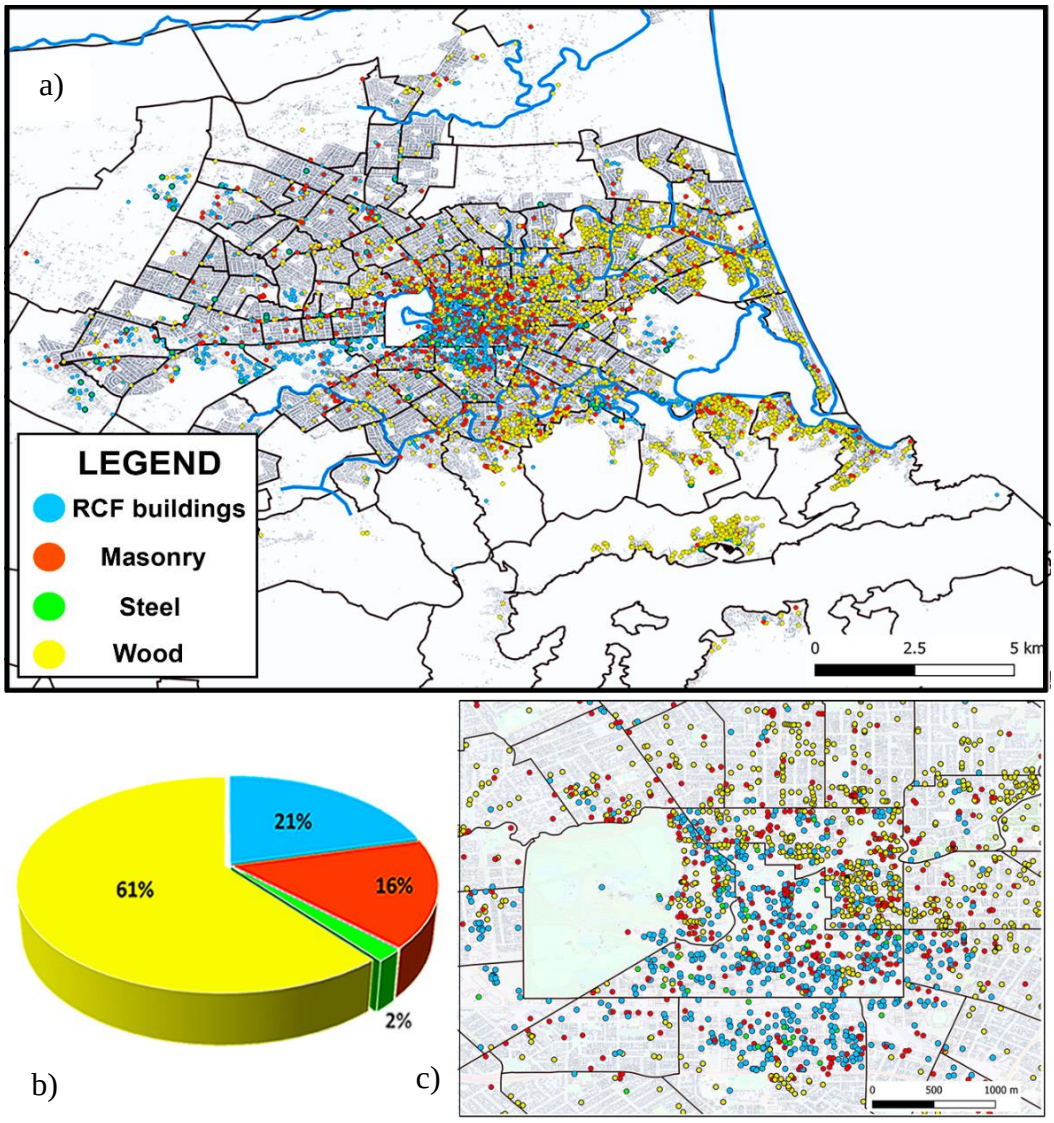

Figure 5-32 Distribution of building typology in the city of Christchurch (a,b) and its CBD (c), from CEBA database.

After each major earthquake events, a detailed survey of the damage occurred to land and dwellings was undertaken by teams of geotechnical engineers coordinated by the agencies of the NZ Government. Maps of liquefaction-induced damage (like the ones showed in Figure 5-22) were produced to assess the extent and severity of the surface effects. Thinking on buildings, different types of damage were observed, in a strict dependency with the structural typology: the damage on wooden buildings was mainly due to ground cracks and sand ejecta, with a negligible role of the building due its limited weight and weak foundation (Figure 5-33a); the damage to taller reinforced

concrete buildings was due to differential deformation occurred at the foundation level, more heavily affected by the building presence (Figure 5-33b).

a) b)

Figure 5-33 Type of damage on wooden; and (b) reinforced concrete buildings (from Cubrinovski et al., 2011c) (the yellow arrows in figure b represent the settlement distribution along the building).

Comparing the two plots of Figure 5-22, it readily emerges that the Central Business District, that hosts the reinforced concrete buildings analyzed in the present study was not affected by the September 2010 earthquake. Hence, an interaction between the two events seems unlikely. On the contrary, some overlapping of liquefied zones in the Red Zone may lead to suppose that the previous event could have increased the liquefaction susceptibility of the soil shaken by the second event. The effects of multiple earthquakes on the liquefaction susceptibility of soil are controversial and largely debated in the literature (Cubrinovski et al., 2011d; van Ballegooy et al., 2014). Considering the different distribution of evidence shown by Figure 5-22 and the relatively limited subsidence recorded after the September 2010 event (https://www.nzgd.org.nz/) this influence has been herein neglected and prediction for the earthquake of February 22nd, 2011 has been performed independently from the past event.

Subsequently, another survey named Detailed Engineering Evaluation (DEE) was completed for business and multi-stories residential buildings (Lin et al., 2014). Based on these reports, damage induced by liquefaction was classified as minor, moderate or major according to the criterion introduced by van Ballegooy et al. (2014) that defines severity classes (Level: #1 minor, #2 moderate and #3 major) for different types of foundation damage (Figure 5-34a). The map with the classification of damage for the buildings of Christchurch is plotted in Figure 5-34b.

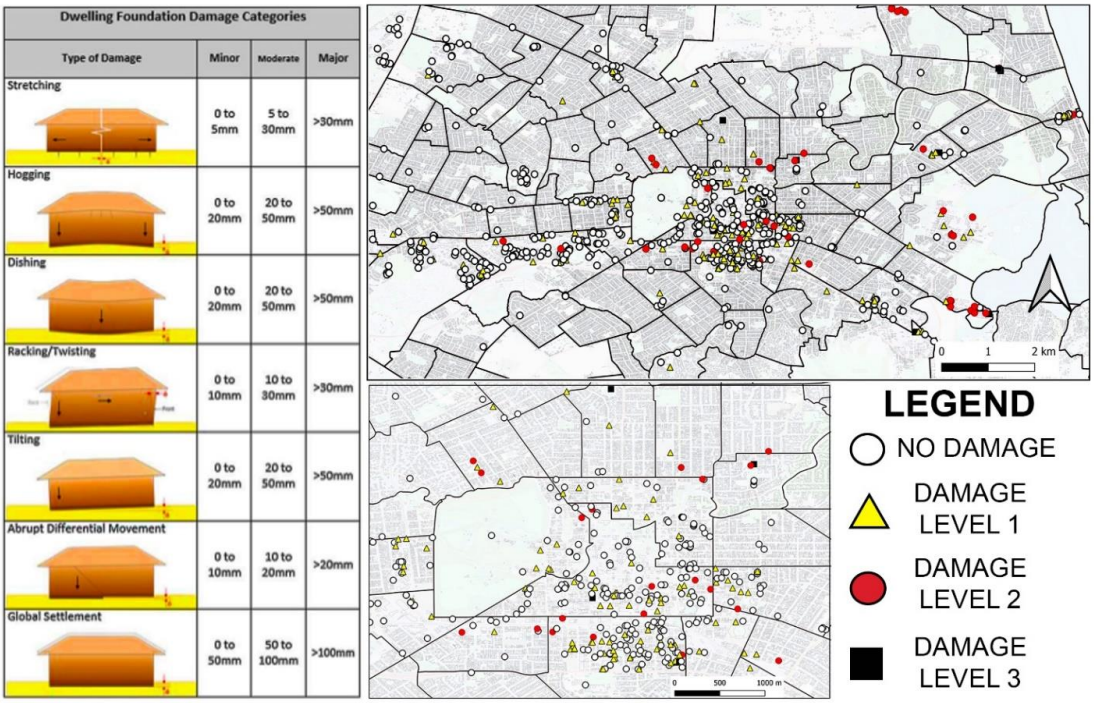

Figure 5-34 a) Damage survey criterion from van Ballegooy et al. (2014); and b) mapping of the observed liquefaction-induced building damage.

5.4.2 Subsoil composition and properties

In the present analysis, about 9 000 Cone Penetration Test (CPT) profiles extending below 10 m depth from the ground surface and uniformly distributed over the studied territory have been considered. Such an unprecedented density of territory coverage with subsoil data enables to reconstruct with sufficient accuracy the distribution of the different variables over the territory. The subsoil characterization is schematized in the flowchart of Figure 4-14. The NZGD also enables to verify the applicability of models and to identify possible limitations of the performed analysis. In this specific case, the models adopted to evaluate absolute and differential settlements (e.g., Eqns. (3.23) and (4.5)), but also the empirical indicators foreseeing the effects of liquefaction (e.g. *LSN*), postulate a relatively simple mechanism where liquefaction occurs in a unique layer underlying a non-liquefiable crust. The boxplot test led to discarding about 400 samples over the total number of CPT profiles.

More complex effects, like those envisaged by Cubrinovski and van Ballegooy (2017), must, on the contrary, be expected for the alternation of susceptible and non-susceptible layers. Therefore, the application of the above-defined models to the specific situation could result inappropriate and lead to significant errors. To exclude this issue, the equivalence of the subsoil profile derived from each CPT profile to a three-layers model is verified with a criterion defined by Millen et al. (2020), which application to the total number of 8 300 CPT shows intolerable normed errors (with an assumed threshold equal to 0.15), i.e. the schematization with a three-layer model is unacceptable for a limited number of cases (106 profiles, about 1.2% of the total). These profiles are mostly distributed in the southern part of the city with just a few spot-like exceptions in the other parts. This result suggests that the subsoil of Christchurch CBD can be reasonably assumed as an adherent to the three-layers model (see Figure 5-8.a) and authorize to apply this schematization with enough confidence.

Additionally, the analysis of outliers shows that the information from CPT is largely consistent all above the territory, apart from a limited fraction of data reported with red dots in Figure 5-8a. The nature of this inconsistency stems from a small variation of the test results coupled with the implemented automatic processing that lead to misclassify some soil layers and obtain thicknesses of crust and liquefiable layers inconsistent with the local spatial distribution computed with kriging. This error could be corrected scrutinizing these CPT profiles individually but, considering the very huge number of CPT available in the present study, all inconsistent profiles have been removed. In general, this measure has produced an improvement of the estimate certified by a lower standard error (Figure 5-8.c)

5.4.3 Estimate of damage on reinforced concrete buildings

With the above databases, the procedure illustrated in Figure 4-14 has been implemented as follows to estimate the damage induced on the reinforced concrete buildings by liquefaction during the February 22nd, 2011 earthquake:

- selection of reinforced concrete buildings resting on subsoil that can be outlined with a three-layer model;
- evaluate the absolute settlement w_{max} of each building with Eqn. (3.23); the unit load Q is estimated multiplying the number of stories times a load per unit area equal to 10 kPa (this value assumed as a summary of different loading

contribution); S_{a1} and CAV_{dp} have been estimated considering the ground motion recordings within the Christchurch CBD (Bray and Macedo, 2017);

- evaluate differential settlement as a function of the absolute settlement by using Eqn. (4.5), where α is assumed to be equal to the median value (0.54) of the observed distribution;
- compute the probability associated with each damage level with the functions given in Figure 4-7 and Table 4-1;
- compute the Mean Damage Rate (*MDR*) with the loss factors for each damage level expressed in Table 4-4.

Despite numerous assumptions and approximation inherent in its definition, *MDR* has been adopted here as an indicator of damage, considering that it incorporates multiple factors such as the released seismic energy, subsoil, and building characteristics. Looking at the global map of Figure 5-35.a, the buildings located in the western part of Christchurch assume generally low *MDR* values (<0.15), consistently with the limited seen effects of liquefaction (Figure 5-23). These values increase in the southern and eastern parts of the CBD, where subsoil becomes more susceptible. The information given by the map of Figure 5-35b overlap quite closely with the distribution of *LSN* plotted in Figure 5-8.c. However, it is also seen that largely different values (<0.15 and >0.60) occur for buildings located at a relatively small distance, i.e., in similar subsoil conditions. This result is dictated by the number of stories, as taller buildings determine higher loads transferred to the foundation and are characterized by a higher vulnerability, per the lower median of the fragility function defined in Table 4-1.

a) b)

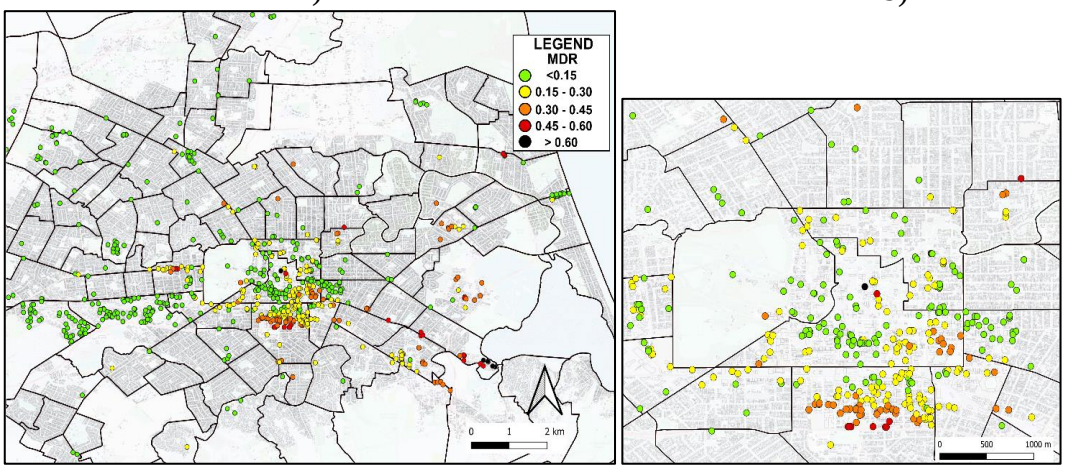

Figure 5-35 MDR *computed on reinforced concrete buildings for the M_w6.2 22nd February 2011 Earthquake: (a) general map of the city; and (b). enlargement in the CBD.*

5.4.4 Validation

The effectiveness of prediction is seen comparing the estimated MDR (Figure 5-35) with the damage observed after the February 22nd, 2011 event (Figure 5-34) and evaluating the performance of the method with a quantifying indicator. The method based on the Receiver Operating Curve – ROC (Kongar et al., 2015) is adopted with this aim. It compares prediction and observation in 2x2 contingency tables, classifying each occurrence as true positive (TP), true negative (TN), false positive (FP) and false negative (FN). Then, considering that the prediction outcomes (positive or negative) depend on the threshold assumed for the characteristic variable, the method computes the true positive ratio (TPR i.e., the fraction of positive events predicted as positive), and the false positive ratio (FPR i.e., the fraction of negative events predicted as positive), for increasing threshold values and plots all values in the FPR-TPR plane like in the plot of Figure 5-36.

It is noted that MCC considers success and failure of prediction (for both positive and negative occurrence) in the same way, i.e., without distinguishing the consequences of misprediction. To account for this issue, Maurer et al. (2015b) propose to set the optimal decision thresholds evaluating the economic consequences of misprediction, i.e. multiplying the terms of Eqn. (4.36) with weighting factors. Despite this issue becomes relevant when risk assessment is preparatory for remediation of buildings, this logic has not been introduced in the present methodological analysis, i.e., the same weight has been given to all terms to avoid subjective consideration on the cost of repair and remediation. With the same spirit, the overall success and failure rates (OSR and OFR), defined respectively as the percentages of successful and unsuccessful prediction, have been computed to evaluate the prediction performance.

The validation method has thus been applied to the reinforced concrete buildings of Christchurch, considering separately minor, moderate and severe damage as discriminating occurrence in accordance with the post seismic survey of buildings (Figure 5-34). Observers may argue that a mismatch exists between the classification of damage used for prediction and damage survey. For prediction, Fotopoulou et al. (2018) define four classes of damage (Slight, Moderate, Extensive, and Complete) in accordance with the criterium defined by Hazus (FEMA, 2003). In the post-earthquake survey of damage at Christchurch, van Ballegooy et al. (2014) distinguished three classes (“Minor”,” Moderate”, “Severe”). An option to eliminate this mismatch would be the removal of a damage class in prediction. To avoid such a subjective choice,

prediction and validation have been performed separately, adopting MDR as a predictive variable (it accounts for all four damage classes of damage in a probabilistic way) and relating MDR with the observed damage.

For each condition, the area under the curve AUC (Figure 5-36) and the values indicating the prediction performance are reported in Table 5-9. These results indicate a variable capability of the proposed method to capture observation, being the ROC curves higher than the plane bisecting line, but with variable distances. The prediction is not particularly exciting for minor damage level (Figure 5-36.a), possibly because of a subjective, not clearly and uniquely identifiable, recognition of injuries of buildings that smooths the border between positive and negative occurrences. However, when looking at the overall success of prediction, i.e., the percentage of correctly predicted cases, an OSR value equal to 68.5% is obtained even for this class. The quality of prediction increases noticeably with the damage level, which means that a stronger relation exists between MDR and damage, as confirmed by the increasingly higher values of the decision threshold and the Overall Success Rate.

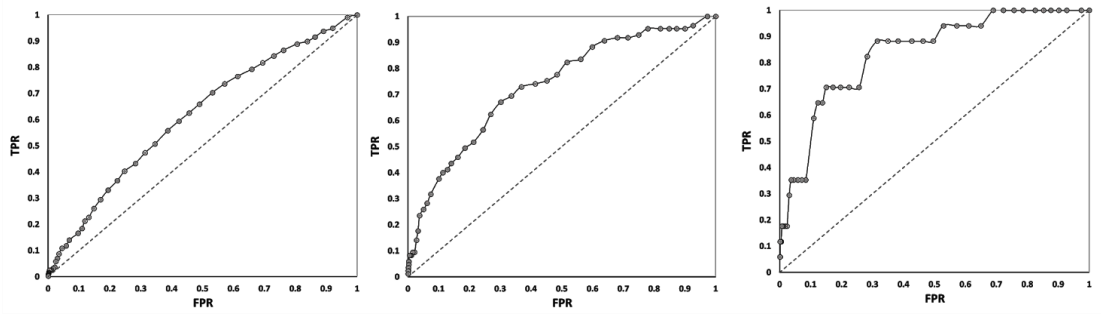

Figure 5-36 ROC curves evaluated by matching the predicted MDR to the liquefaction-induced damage on reinforced concrete buildings that underwent (a) minor, (b) moderate or (c) severe damage during the February 22nd, 2011 earthquake.

Table 5-9 Output of the Kongar et al. (2015) validation test for the prediction of damage on reinforced concrete buildings.

Damage Level	AUC	OPTIMAL MDR THRESHOLD	TPR	FNR	TNR	FPR	OSR (%)	OFR (%)
Minor	0.69	≈0.20	0.46	0.54	0.77	0.23	68.5	31.5
Moderate	0.77	≈0.30	0.75	0.25	0.84	0.16	83.4	16.6
Severe	0.89	≈0.40	0.42	0.58	0.95	0.05	94.2	5.8

As shown in Figure 5-33.a, the vulnerability of light wooden dwellings of Christchurch is not much affected by the structural characteristics but mainly depends on the subsoil response. Damage on this building category can thus be strictly associated with the phenomena, sand ejecta, and lateral spreading induced by liquefaction at the ground level. Considering this premise, the validation test of Kongar et al. (2015) has also been applied to the wooden buildings assuming the empirical indicator of land damage LSN defined by van Ballegooy et al. (2014) as engineering demand parameter and deriving the damage level for each of them from the classification of Figure 5-34. The results summarized in Figure 5-37 and Table 5-10 show a fairly good correlation between LSN and damage. The overall success rate of this prediction oscillates around 70% for all damage levels (basically two-thirds of the cases), according to the outcomes reported by other authors (Kongar et al., 2015). The reason for misprediction could be sought in other factors not captured by the considered indicator, like, for instance, the occurrence of two-dimensional conditions (e.g., local slope) that may aggravate damage (e.g. lateral spreading). However, it is important to observe that the decision thresholds, i.e., the values of LSN that maximizes MCC, increase with the damage level and for the minor damage assume a value similar to the threshold (=10) suggested by van Ballegooy et al. (2014).

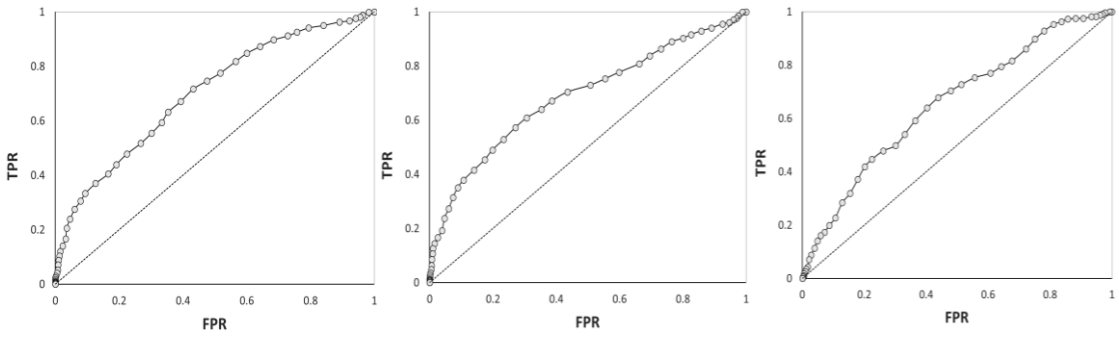

Figure 5-37 Roc curves for wooden buildings.

Table 5-10 Output of the Kongar et al. (2015) validation test for the prediction of damage on wooden buildings.

Damage Level	AUC	OPTIMAL MDR THRESHOLD	TPR	FNR	TNR	FPR	OSR (%)	OFR (%)
Minor	0.71	≈13	0.85	0.15	0.40	0.60	72.5	27.5
Moderate	0.70	≈20	0.64	0.36	0.65	0.35	64.4	35.6
Severe	0.67	≈30	0.42	0.58	0.80	0.20	72.8	27.2

5.5 Example of probabilistic liquefaction risk assessment

The procedure outlined in the previous paragraph and tested against the back analysis of the 22 February 2011 Christchurch earthquake is here developed in probabilistic terms according to the convolutional integral of the PBEE methodology. With the same approach of a probabilistic seismic risk assessment, it accounts for the seismicity of the area considering the whole range of seismic scenarios that may affect a structure or infrastructure over its lifecycle. An annual rate of exceedance is thus defined to estimate the possibility of representative intensity measures (IMs); such variable (i.e., the inverse of return period $1/T_r$) is also employed to annualize the overall outputs, the mean damage rate, and the economic loss.

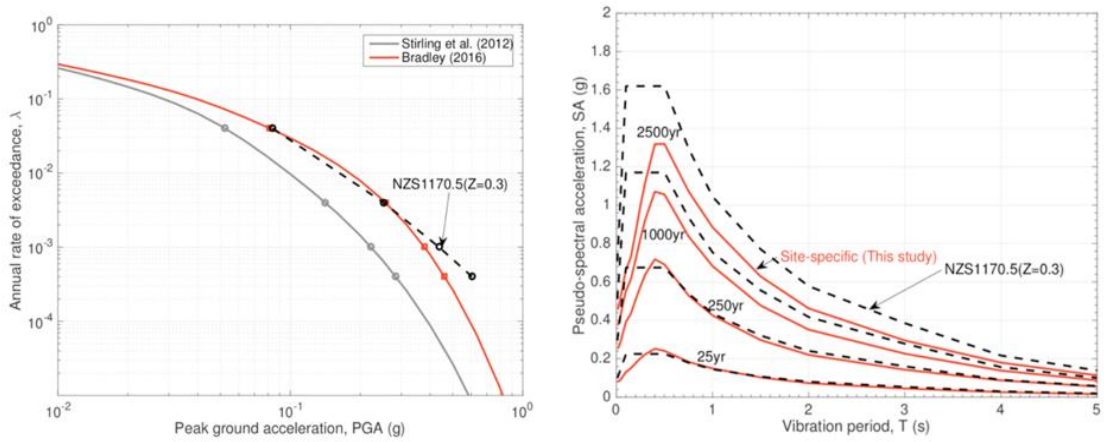

Figure 5-38 PGA hazard curves and uniform hazard spectra (UHS) defined for sites in Central Christchurch (Bradley, 2016).

For a generic site in Central Christchurch, the annual rate of exceedance (λ) of PGA and the Pseudo-spectral acceleration are shown in Figure 5-38. Four seismic scenarios (Figure 5-38), which return period ranges in 25 to 2500 years, have been considered characterizing the respective IMs through interpolation combined to the knowledge of the 'shape' of the hazard curve from the PGA and Sa(s) (Bradley, 2016). Following this approach, seismic input at each building location has been characterized by

multiplying the recorded 22 February 2011 intensity measures (CAVdp, Sa) by the rate among PGAs, to include local site amplification.

Out of the Christchurch RC-framed building stock showed in Figure 5-32, the PBEE methodology has been applied to those fitting the hypothesis of the three-layered profile defined by the ESP method. In this analysis, the subsoil characterization includes the processing of CPT profiles to evaluate the expected 1D liquefaction-induced settlements ad liquefaction severity indicators corresponding to four scenarios having return period Tr equal to 25, 250, 1000, and 2500 years. As an example, the probability density functions and maps of the Zhang et al. (2002) post-liquefaction settlement are shown in Figure 5-39 and Figure 5-40.

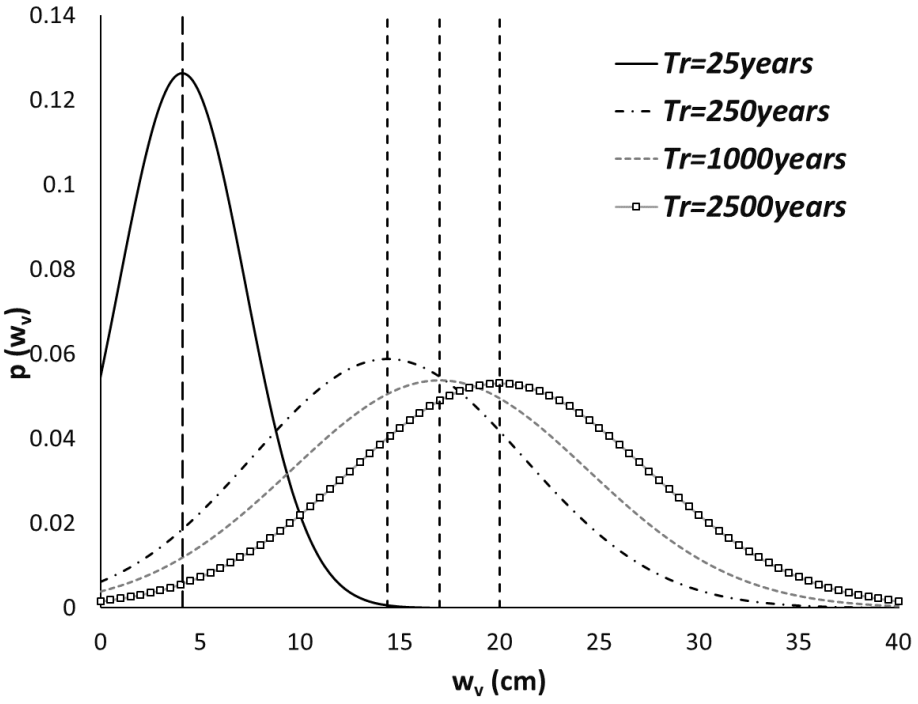

Figure 5-39 Probability density functions of post-liquefaction settlements evaluated by integrating the volumetric deformation (Zhang et al., 2002) for the selected seismic scenarios.

In the following step, geostatistical spatial interpolations allowed for evaluating the 1D settlement at each building centroids. In this phase, buildings located in areas where the estimated standard deviation error is found greater than 25% (e.g., grey areas in Figure 5-40) have been removed from the analysis due to inadequate knowledge of the subsoil.

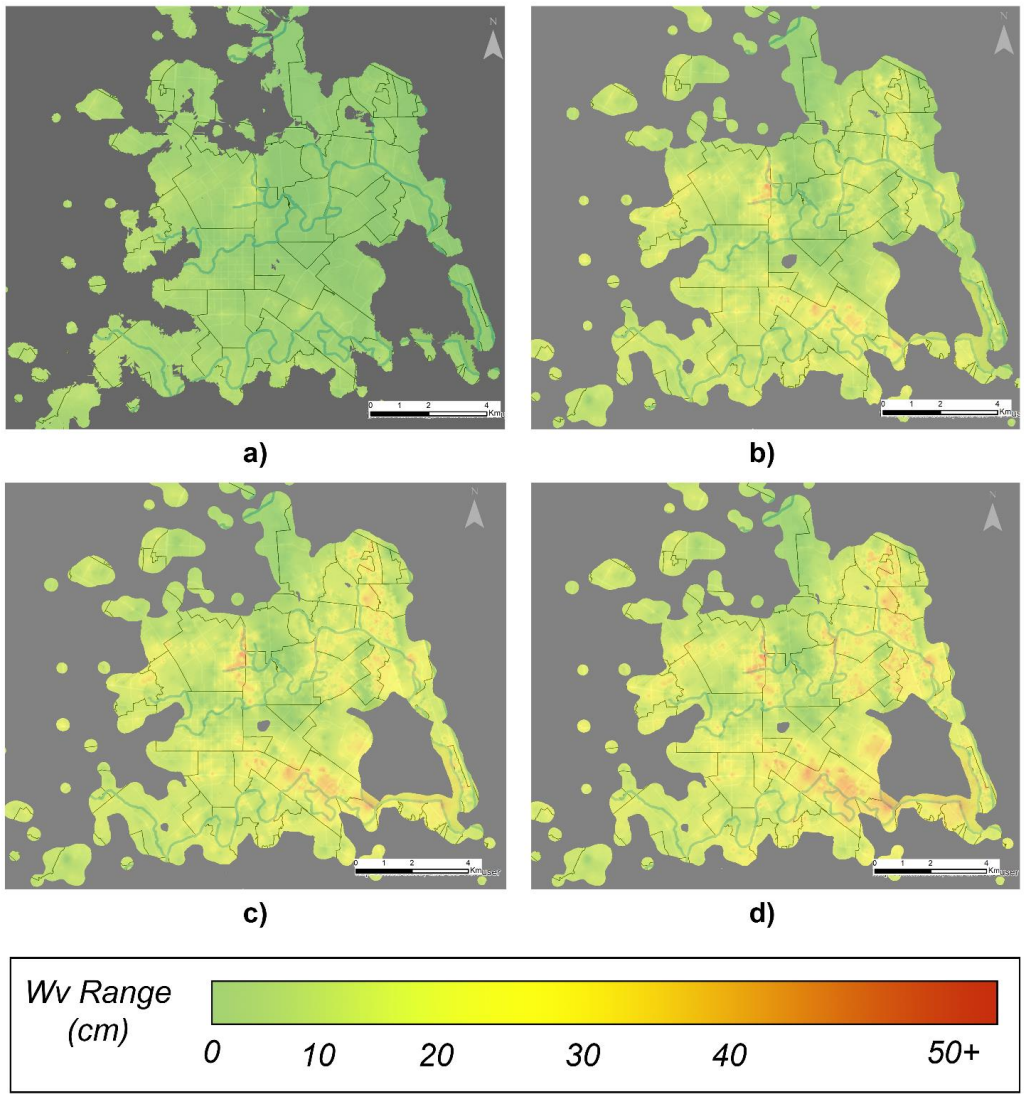

Figure 5-40 Maps of the post-liquefaction settlements (Zhang et al., 2002) for the selected seismic scenarios: a) Tr = 25 years; b) Tr = 250 years; c) Tr = 1000 years and d) Tr = 2500 years.

Once the building and subsoil databases have been created, the expected distribution of liquefaction-induced differential settlements due to the seismic hazard o the area has been evaluated on each building. In particular, for each of the seismic scenarios displayed in Figure 5-38, the mean and standard deviation of the differential settlement have been derived from the combination of the Bray and Macedo (2017) formula and the application of the error propagation theory (Eqn. 4.22, 4.28).

Consequently, the resulting mean damage rate was obtained by introducing the Fotopoulou et al. (2018) fragility model with the loss factors reported in the Hazus

(Fema, 1998) methodology, which quantifies the physical impact of liquefaction on buildings resulting from damage on structural, non-structural and drift-sensitive components.

In addition to the expected MDR evaluated joining the fragility curves only with a single value (e.g., the median) of differential settlement (Eqn.4.6), the error propagation theory enables to quantify a mean damage rate which accounts for the whole distribution of differential settlements (Eqn. 4.29). In both cases, the sum of the MDR induced by each of the considered earthquake multiplied by the annual frequency of exceedance (λ) provides the annual mean damage rate. i.e., the mean damage rate which a given RC-framed building in Central Christchurch is expected to undergo per year. Figure 5-41 and Figure 5-42 show the annual MDR evaluated on RC-framed buildings following the traditional "deterministic" approach and the annual MDR resulting from the distribution of differential settlement weighted by its probability.

Despite the fact that a preliminary observation of Figure 5-41 and Figure 5-42 may reveal that the two adopted approaches do not differ each other in estimating the annualized physical impact of liquefaction on RCF buildings, a more refined analysis has outlined that the probabilistic distribution of differential settlements will often result in a more conservative estimate of the mean damage rate. This is confirmed by the boxplot of Figure 5-43 that highlights a systematic difference of 10-20% (reaching 80% in the limit situations) among the two approaches. These evidences are mostly ascribable to the form of the Fotopoulou et al. (2018) fragility functions (Figure 4-7) and loss factors. About the former issue, the evaluated distributions of differential settlements in the study area often range in the linear section of Fotopouolou et al. (2018) fragility curves for Minor, Moderate and Extensive damage levels. This results in minimal differences in the contribution to the MDR given by such damage levels. On the contrary, more marked differences among the two approaches are emphasized by the Fotopouolou et al. (2018) curve in evaluating the probability of severe damage level. This is a consequence of the distribution of differential settlements, which mostly belong at the beginning of such a curve. Additionally, the loss factors introduced in Hazus (Table 4-4) play a non-negligible role since they assume respectively a value equal to 0.02, 0.1, and 0.45 for minor, moderate and extensive damage levels becoming 1.00 for severe damage level.

In conclusion, since it provides a more conservative result, the MDR evaluated through the probabilistic approach and displayed in Figure 5-42 will be used in the subsequent analyses.

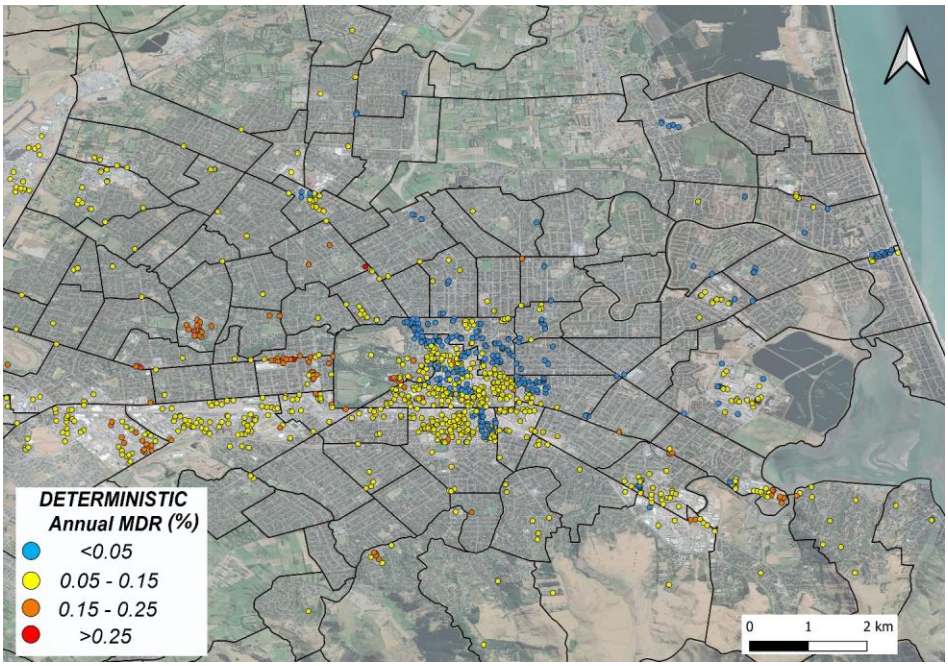

Figure 5-41 Annualized MDR evaluated through deterministic approach on RCF buildings.

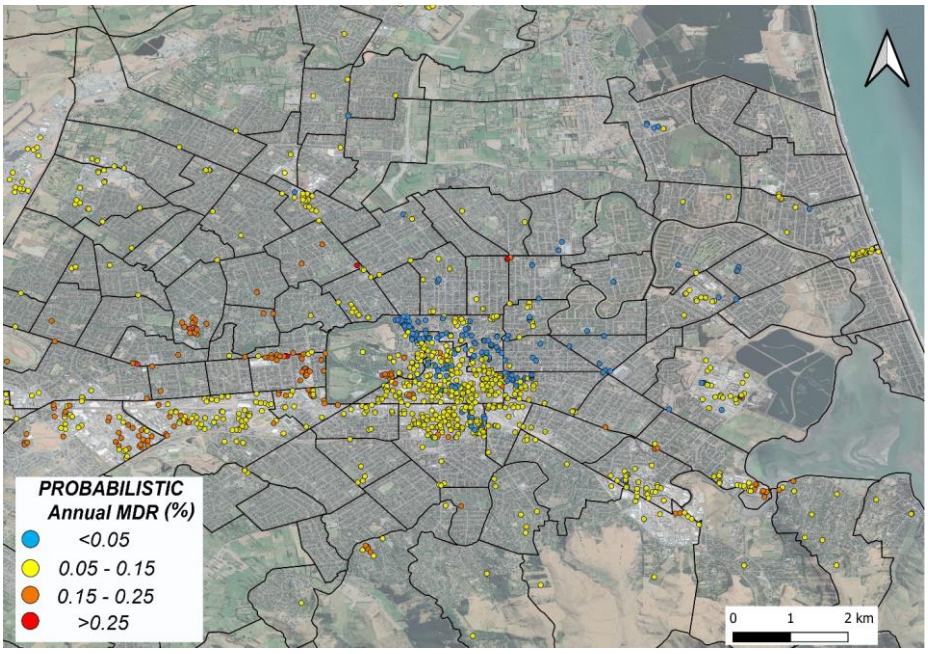

Figure 5-42 Annualized MDR evaluated through the fully probabilistic approach on RCF buildings.

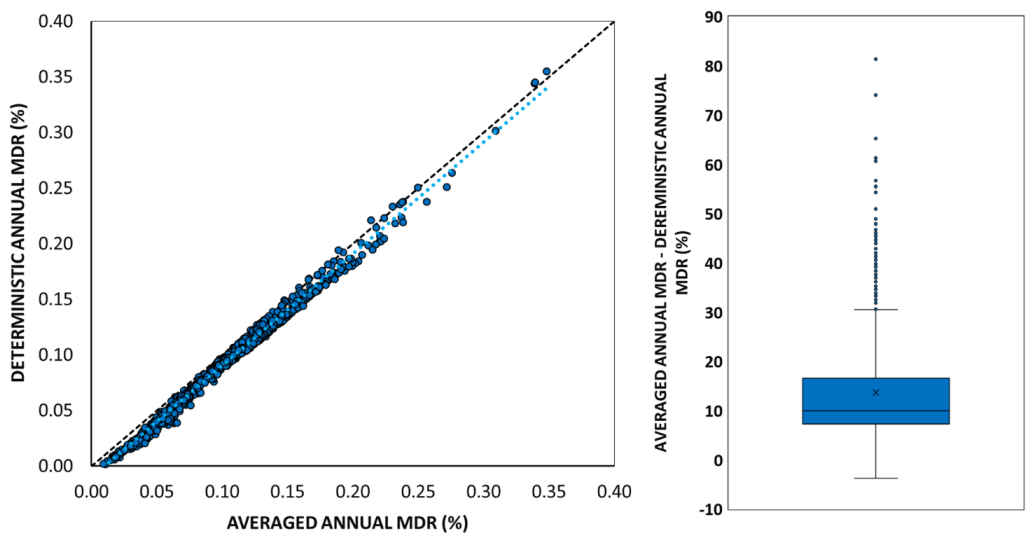

Figure 5-43 Comparison among the annualized MDR (%) evaluated through probabilistic vs deterministic approach on RCF buildings and boxplot of the probabilistic vs deterministic MDR deviation (%).

5.5.1 Estimate of the economic losses and cost/benefit analysis

The last step of the PBEE convolutive integral concerns the assessment of risk based on the introduction of decision variables: a possible objective method to establish if a given risk is acceptable or not implies to perform a cost/benefit analysis.

To this aim, the liquefaction-induced physical damage is translated into total repair costs (i.e., the costs of damage also including demolition and reconstruction costs). Additionally, restoration time must be determined and converted into monetary terms since the loss of functionality plays a focal role in both residential dwellings (where it implies to rent a new house) and economic activities (where it represents the loss of income term). This step implies the estimate of building repair cost and loss of functionality.

Thinking on Hazus residential buildings of Table 4-4. the economic total loss is computed by assuming 1000,00 €/m^2 as building unitary value; 3000,00 €/m^2 as repair/replacement cost, which is higher than the previous to account for transportation and demolition costs and a monthly cost of 10,00 €/(m^2 per month) which is an

estimate of the unitary cost for a residential dwelling rent. In this case, the sum of Eqn. 4.7 and Eqn. 4.8 can be written as showed in Eqn. 5.4, where TOT RC represents the total liquefaction-related economic loss induced by a given scenario on a residential building.

$$TOT\ RC = rc + ul\ cost\ = RC_{res1}\left(\sum_{ds} P_{i_{ds}} \cdot \left[\left(\frac{rc_{res1}}{RC_{res1}}\right)_{ds_i}\right]\right) + monthly\ rent\ cost_{res1}(\sum_{ds}(INC_{res1} \cdot FLT_{res1}) \cdot P_{i_{ds}})$$

Eq. 5.4

Thereafter, with the same logic of the annualized MDR, the total costs resulting from all the considered earthquakes can be annualized by convoluting the specific event induced loss multiplied by its Annual Frequency of Exceedance (Eqn. 4.10). Finally, the expected liquefaction-induced annual loss is assumed as a proxy of liquefaction risk on buildings, and consequently, its reduction will represent the benefit of any possible mitigating action.

The benefit/cost analysis has then been performed considering different mitigation solutions whose unitary cost ranges between 25,00 and 100,00 € /m^3. In this hypothesis, each option's economic convenience is assessed for a factor of treatment k = 1, meaning that 100% of the potentially liquefiable soil volume below a given building is treated. Additionally, it is assumed that independently from its unitary cost, each mitigation option provides an efficiency of 100% to prevent liquefaction-induced damage. For each solution, the treatment cost has been evaluated as the product of a unit cost times the volume of the potentially liquefiable sandy layer to be treated, the latter given by the thickness of the liquefiable layer and the footprint area computed below each building. The calculation has been performed considering a lifecycle of 50 years and a 30-year time horizon for all buildings; the latter information is required to calculate the annual mitigation rate to support the investment, representing the cost of mitigation.

Thus, the cost/benefit analysis has been performed on RC-F buildings of Figure 5-42, considering different unit costs of mitigation and plotting in green buildings showing benefit larger than cost. The results obtained for unit mitigation costs, respectively equal to 25, 50, 75 and 100 € per cubic meter of soil, are plotted in Figure 5-44. Obviously, once the liquefaction risk is defined in the study area, the more expensive the mitigation is and the smaller the number of buildings on which it is convenient. The different plots show that mitigation with ground improvement is

convenient for a larger number of buildings if its cost is low or very low (say 25,00 €/m^3), while it becomes less appealing when costs increase. For the larger considered cost (100,00 €/m^3) only a few buildings, most of them located in the Central Business District of the city, are worth mitigation with ground improvement. For the other residential houses of the city affected by risk, it is not convenient to undertake this kind of countermeasure. Thus, other solutions should be considered for this class of buildings, such as the stipulation of insurance policies. The implemented risk assessment procedure provides, in this case, the possibility of establishing the cost of the premium to be assigned for each building.

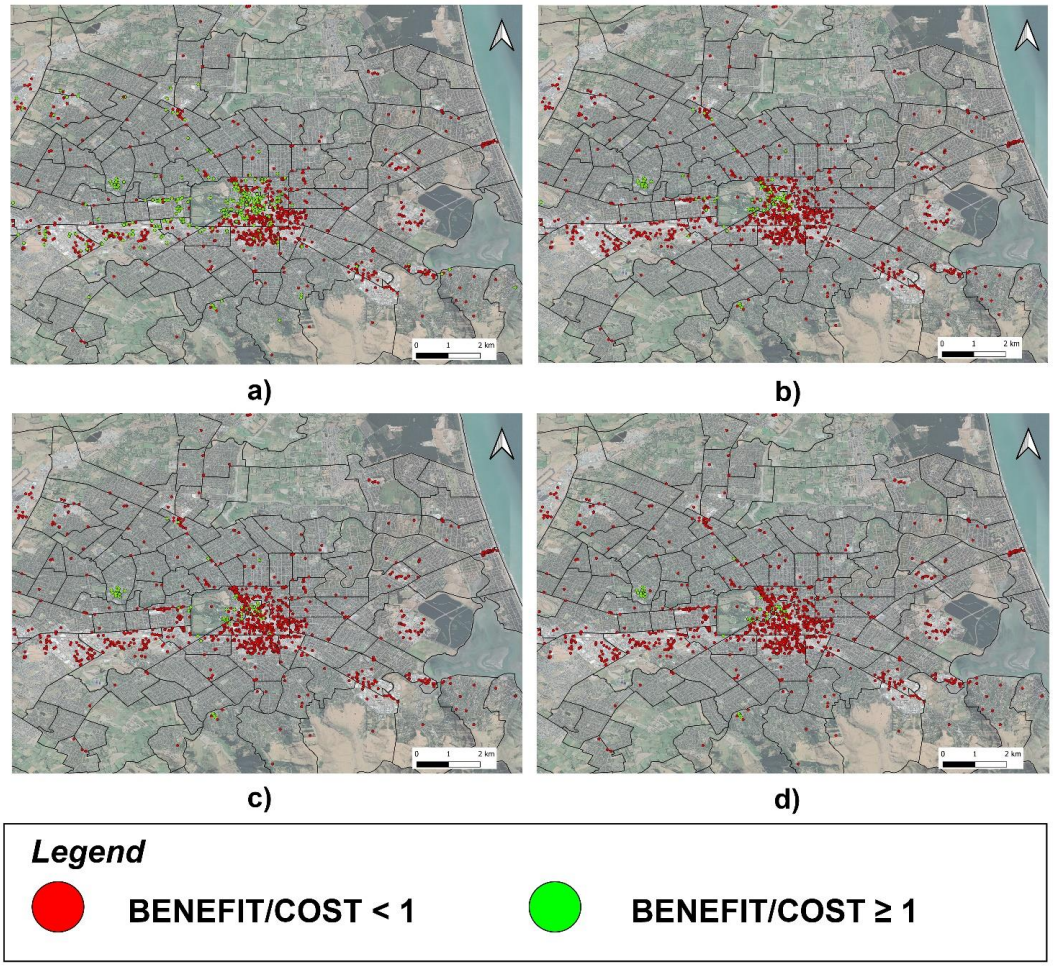

Figure 5-44 Benefit/cost analysis considering a cost of mitigation equal to 25,00 €/m^3 (a), 50,00 €/m^3 (b), 75,00 €/m^3 (c) and 100,00 €/m^3 (d).

Chapter 6. CASE STUDY 2: THE DISTRICT OF TERRE DEL RENO (ITALY)

6.1 Abstract

In May-June 2012, an intense seismic sequence hit a wide area of the southern Po Plain in Emilia Romagna (Italy). Due to the high susceptibility of some deposits in the alluvial plain, the earthquakes produced extensive liquefaction phenomena, probably the most severe in Italy's last century (Berardi et al., 1991), especially in the districts of S. Agostino and Mirabello. Ground cracks and liquefaction evidence (sand boils, settlement, and tilting of structures) were among the most relevant coseismic effects observed during the Emilia sequence. Totally, the area affected by liquefaction during the May 20th and May 29th events covered about 1200 km^2. Considering the municipalities of S. Agostino and Mirabello, the following paragraphs relate to liquefaction-induced land and buildings damage following the 20 May 2012 Earthquake. Additionally, a probabilistic liquefaction risk analysis is carried out on residential and industrial buildings. In this case, an appropriate economic model is introduced to link the expected physical impact to the annualized economic loss resulting from the considered seismic scenarios. Finally, a benefit/cost analysis is performed on an annual basis for each building to assess the convenience of any mitigation treatment.

6.2 The May – June 2012 Emilia Earthquake sequence

The 2012 seismic sequence interested the Eastern area of the Po Plain, close to the buried geological structure of the Ferrara Arc, nearly 30 km WNW of the town of Ferrara and east of the Mirandola municipality (in the Modena Province, Figure 6-1). Two mainshocks were particularly damaging: the first one, with ML 5.9, occurred on May 20th with epicentre between Finale Emilia, S. Felice sul Panaro and S. Martino Spino; the second one, with ML 5.8, occurred on May 29th about twelve km southwest of the previous mainshock.

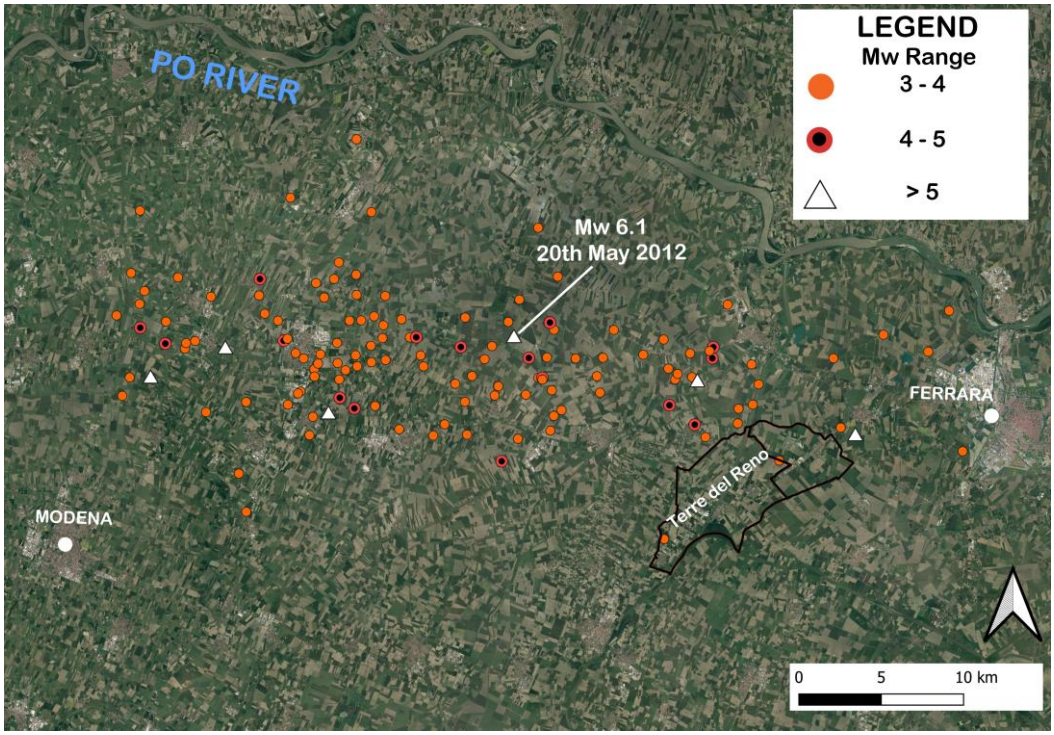

Figure 6-1 Epicenter locations of the Mw>3 shocks of the May-June 2012 Emilia Earthquake sequence.

In the past, numerous liquefaction phenomena in the study were observed after the M5 1570 Ferrara Earthquake (the magnitude has been estimated through macroseismic data), as reported by Galli (2000) and the European Catalogue (D2.4 Liquefact, 2019). In addition, the geological asset of the Po Plain (Romeo, 2012) confirmed the high properness to liquefaction for most areas of the Emilia Plain. In this context, the 20th and 29th May 2012 Earthquakes were intense enough to trigger liquefaction. These hypotheses are confirmed by post-earthquakes ground inspections made by the INGV Emergeo Working Group (2013) that performed a systematic survey of the earthquake sequence area through field, aerial and interview approaches. Data regarding 1362

observations were collected, stored in a geographical information system, and made partially available at the address http://www.esriitalia.it/emergeo/. The observations were grouped into three categories: (i) liquefaction; (ii) fracture/liquefaction; and (iii) fracture. On the whole number of 1362 sites with coseismic effects identified and surveyed over more than 1200 km^2, 768 were classified as fracture/ liquefaction, 485 as liquefaction, and 109 as fracture (Figure 6-2).

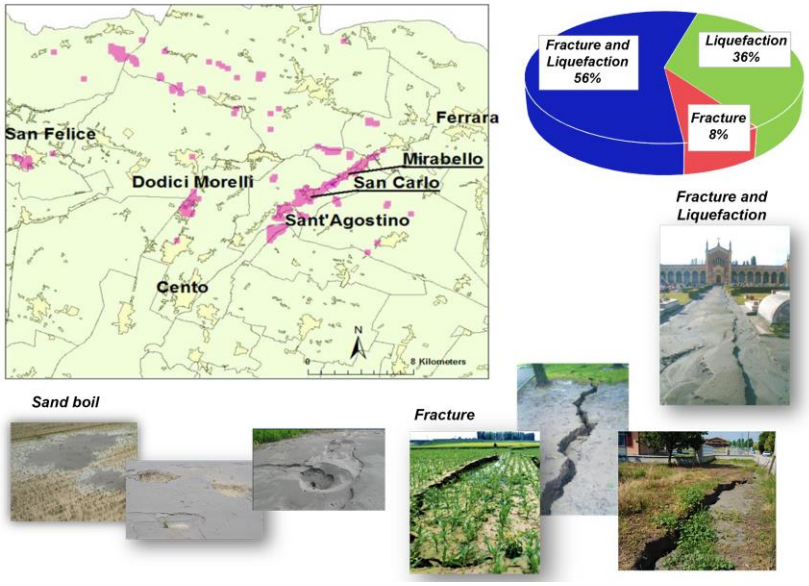

Figure 6-2 Liquefaction ground observations after the 2012 Emilia Earthquake Sequence.

Following the 20th, May 2012 event, liquefaction phenomena were observed especially in the north-eastern area of the epicenter in San Martino Spino, Burana and Scortichino, and in the south-eastern area, in S. Felice sul Panaro, Dodici Morelli di Cento, Mirabello, San Carlo and San Agostino (Figure 6-2). Soon it appeared that liquefaction evidence was not evenly distributed over the area but tended to concentrate along preferential alignments, mostly dictated by the presence of paleo-riverbeds, levees, out-flow channels and fans that are characterized by the presence of sandy layers a relatively shallow depths. The maximum distance of observed liquefaction phenomena from epicenters is about 30 km, in agreement with the regional empirical relations proposed by Galli (2000). The spatial distribution reflects the combined effects of soil susceptibility (loose cohesionless soil with shallow water table) and ground motion intensity in terms of liquefaction hazard. The area affected by liquefaction can be roughly represented as the projection to the surface of the seismogenic source (e.g., the area affected by surface deformation), and the

stratigraphic/hydro stratigraphic conditions in the upper 5–10 m become the most relevant factors in identifying areas where liquefaction was triggered.

Despite the seismic magnitudes of the May – June events were not particularly high compared to other worldwide events, the macroseismic study showed significant damage on the building stock, mainly due to the lack of building codes. Consider that this area of Emilia-Romagna was declared as seismic only with the 2003 reclassification. Therefore, the 2012 earthquakes were very impactful on that community, causing deaths and considerable destruction of the building and cultural heritage. Twentyseven people died, 13 of them due to the collapse of an industrial building; more than 12 000 structures were affected, including 147 collapsed or heavily damaged bell towers and churches (Fioravante et al., 2013).

Additionally, numerous production activities and companies located on the entire Emilia-Romagna Region (Figure 6-3) significantly increased the total economic impact caused by the 2012 earthquakes. So far, the rebuilt has cost more than 6 billion euros, excluding the indirect costs of the loss of income and the inability to operate for several months, quite huge considering the importance of the entire industrial district on the regional gross domestic product. In fact, the area affected by liquefaction hosts a high concentration of agricultural production, agri-food, industrial and handicraft units. For 2011, the Italian Institute of Statistics (ISTAT, 2018) recognized for this area a gross product of 19.6 billion euros that generated 12.2 billion euros of exports. Only in the crater of the earthquakes, including 33 municipalities, there are about 48 thousand companies and 187.000 employees (Figure 6-3).

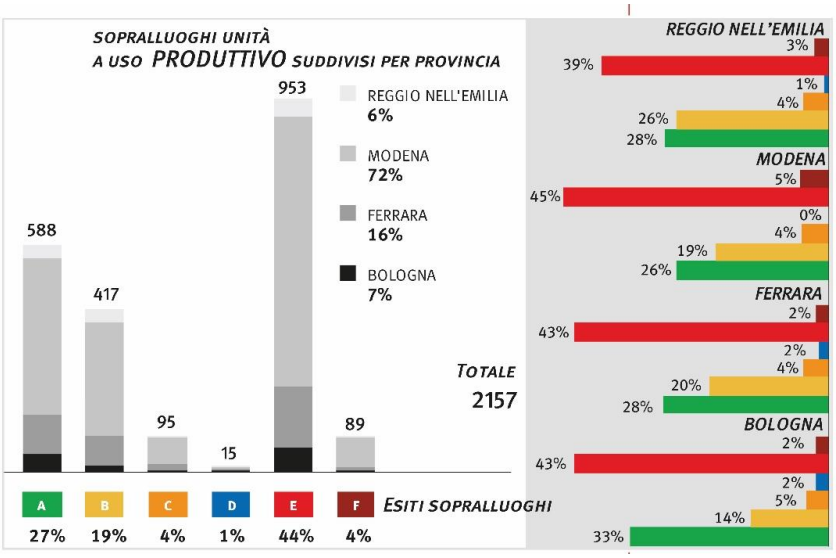

Figure 6-3 Outcome of post-earthquake damage inspections on productive activities ("Servizio Geologico, Sismico e dei Suoli, 2012").

6.3 **The Municipality of Terre del Reno**

The municipalities of Mirabello and Sant'Agostino, the latter, including the San Carlo village, were merged in 2017 to form a new municipality named Terre del Reno. Here, the Mw 6.1 earthquake of the 20th May 2012 caused extensive damages due to liquefaction: only in the village of San Carlo 186 buildings of 660 were damaged at different levels (ISTAT, 2018). In this area, Galli (2000) and Romeo et al. (2012) highlighted the presence of hidden paleochannels and paleo-levees, as seen from the Digital Elevation Model of the area. The current geomorphology of the area results from the sedimentation and erosion processes exercised by the Apennine and Alpine waterways, including the Po and the sea during the Pleistocene and partly Holocene glaciations (Romeo, 2012). The widespread presence of buried paleo-channels and paleo-embankments deriving from numerous humanmade reclamation lands carried out over the centuries is clearly recognizable on this asset. Among them, the most noticeable are the Reno and Panaro Rivers. For several centuries, the former was moving towards the west; after 1457 was placed on the current route between the municipalities of Cento and Vigarano. The latter, after having formed a wide loop downstream of Finale Emilia (Ramo della Lunga), merged with the Po of Ferrara in the territory of Bondeno. However, "the Po riverbeds were becoming hanging and often could not receive the waters of its tributaries, which favored an increase of the marshes .....". Subsequently, "the Reno had been diverted from the Po of Ferrara in 1604 and diverted to reclaim the swamps south of Ferrara to fill. … .. In 1724 the "Cavo Benedettino" channel was excavated, to also convey the waters of these marshes into the Po of Primaro, this time at Traghetto. Between 1767 and 1795, the "Cavo Passardo" was then built and the "Cavo Benedettino" dug up to connect the Reno to the Primaro with a single and straight artificial riverbed, from S.Agostino to Traghetto; then, with the construction of successive halyards in the Primaro area, the Reno River assumed the current route" (Bondesan & Bondesan, 1990). These

modifications are now widely identifiable from the geological cartography and the digital soil model (DEM) shown in Figure 6-4.

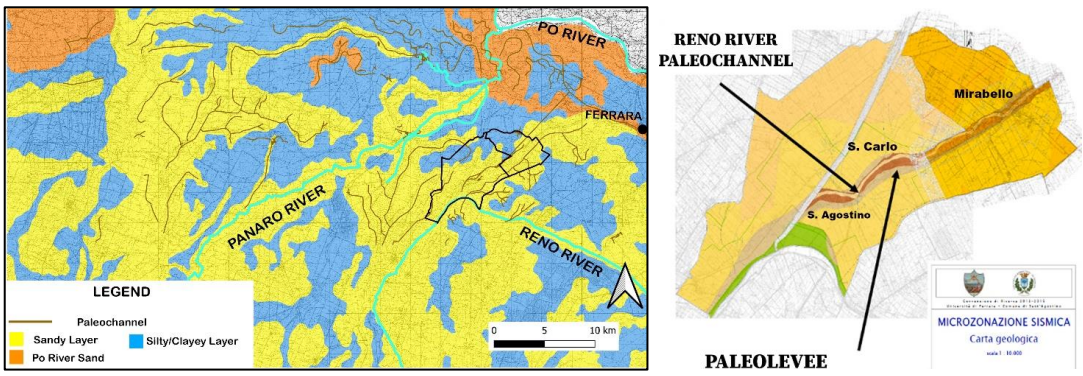

Figure 6-4 a) In the map, the paleochannels and the different types of alluvial deposits are shown; b) geomorphology of the study area.

Due to the vicinity of the epicenter (less than 20 km) and the geomorphology, the districts of San Carlo and Mirabello, were severely affected by liquefaction phenomena such as sand boils, settlements, lateral spreading and fractures. In addition to the free field ground deformation, these phenomena caused extensive damage to structures and infrastructures. Figure 6-5 shows the distribution of liquefaction induced observations in the territory of Sant'Agostino, San Carlo and Mirabello. It can be observed that most of the observed phenomena are concentrated in San Carlo and Mirabello. The maximum observed diameter of single sand ejecta was about 10 m. Many fractures, mostly in the NE–SW direction were noticed, extending for a maximum length of 50 m. Cracks were formed with gaps more than 20 cm wide and sometimes 20 cm of vertical step. Fractures without sand ejection had similar strikes but had lengths up to a few hundred meters, gaps up to 30 cm wide, and vertical steps up to 20 cm with SE and NW downthrown. In Figure 6-5, the red dots indicate liquefaction manifestations, and lines indicate fractures/liquefactions following the morphology of paleochannels. In some artificial cuts open to repair pipes, grey sand was noticed as a proof that even where sand did not reach the surface, the driving phenomenon was liquefaction. The large amount of ejected sand in San Carlo produced important cavities underground that turned into localized subsidence, sometimes accompanied by ponding. Subsidence started with the occurrence of liquefaction but, because settling and re-compaction of sediments is a slow process, it

kept increasing day by day, representing a further hazard for the involved humanmade structures (Alessio et al., 2013).

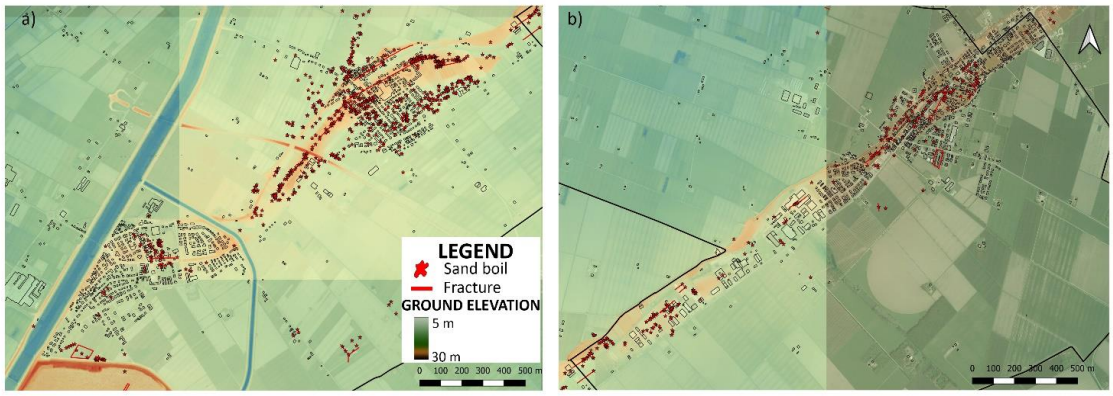

Figure 6-5 Liquefaction-induced land damage observations across S. Agostino (a) and Mirabello (b) municipalities after the May 20th 2012.

6.3.1 The industrial district of Terre del Reno

The relevance of economic activities in the area hit by the 2012 seismic sequence seriously increased the severity of the earthquake-induced economic losses leading to a decrease equal to 3.1 billion euros in the Regional Gross Domestic Product "GDP" in 2012-2013, from estimates of the Emilia-Romagna Region (Servizio geologico, sismico e dei suoli RER, 2012). In this context, the only district of S. Agostino hosts a series of factories capable of producing 2% of the Regional GDP. Here, the typical industrial building is made by single-story prefabricated reinforced concrete modules, characterized by pillars as vertical structures whit horizontal and reinforced concrete roofing tiles resting on beams. The structure is closed with masonry infills or, in more recent constructions, with reinforced concrete panels. Before 2005, when the new seismic classification established by Annex 1 of the OPCM 3274/2003 was issued, the Emilia Plain areas were not classified as seismic. Therefore, most industrial buildings were not subject to compliance with earthquake regulations. This means that the beam-column and beam-tile connections are generally made up of simple support without any mechanical connection. Furthermore, the pillars were designed to carry only the weights of the structure and the modest action of the wind. For these reasons, it was noted that most of the physical damage on industrial buildings was shaking-induced

instead of liquefaction-induced. As observed by the methods of collapse and damage, it clearly emerged that the main cause of the collapses themselves was due to the loss of the support of the structural elements main changes due to the movement caused by the shaking seismic and therefore to the lack of effective connections between the structural elements themselves. In some cases, also, the pillars collapsed (Figure 6-6).

Figure 6-6 Example of industrial buildings in the district of S. Agostino and observed collapse.

In the following paragraphs, the Hazus (Fema, 2003) procedure will be applied to the industrial district of Terre del Reno to provide an estimate of the expected liquefaction-induced annual loss. In evaluating the earthquake-induced economic losses on business activities, great emphasis is given to the loss of functionality and the damage to the inventory stock more than the physical damage. The former terms imply a loss in the business income for the period required to restore the initial conditions and a loss of market (which is often difficult to evaluate and requires tailored studies) even in the years following the earthquake. These aspects led in the worst cases, i.e., when the recovery time is estimated in several months or years, to evaluate the possibility of relocating the activity in another place.

6.4 **Hazard Analysis**

Considering the Mw 6.1 20th May 2012 Earthquake, the assessment of liquefaction hazard for the municipality of Terre del Reno has been performed following the steps described in Figure 4-14. A new probabilistic approach has been proposed in addition to the evaluation and testing of traditional liquefaction severity indicators. Taking advantage of microzonation studies' principles, it allows to account in probabilistic terms for the temporal and random variability of input variables.

Firstly, the liquefaction hazard over the study area is assessed by applying semi-empirical methods to estimate the liquefaction potential in free field conditions. It moves from three subsequent steps, which consist of: I) defining the liquefaction susceptibility based on local stratigraphic features; II) predicting the triggering of liquefaction at different depths by comparing the cyclic stress ratio and soil cyclic resistance ratio (evaluated from empirical correlation with in-situ tests) and III) estimating the liquefaction-induced ground deformation with synthetic indicators that integrate the contribution of each liquefiable layer along with a given soil profile. To accomplish this goal, geological/hydrogeological information allowing to characterize the subsoil conditions and modeling the surficial groundwater level is required. The data used in this analysis comes from the geognostic database of the Emilia-Romagna Region (https://ambiente.regione.emilia-romagna.it/it/geologia/cartografia/webgis-banchedati/banca-dati-geognostica), which contains a huge amount of geological and geotechnical information collected and merged from fragmented public and private archives. In addition to the existing ones, a series of new tests were carried out directly by the Geological, Seismic, and Soil Service after the 2012 Earthquake Sequence. To date, the database includes about 85 000 in-situ investigations.

In the district of Terre del Reno, about 200 stratigraphic profiles of boreholes and 800 CPT profiles were consulted. As shown in Figure 6-7, such in-situ tests were carried out mainly in the proximity of the inhabited centers. Many of them aimed to develop technical reports for the rebuilt of buildings after the 2012 earthquakes.

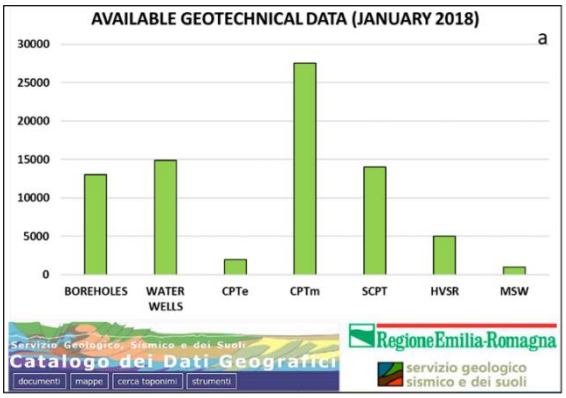

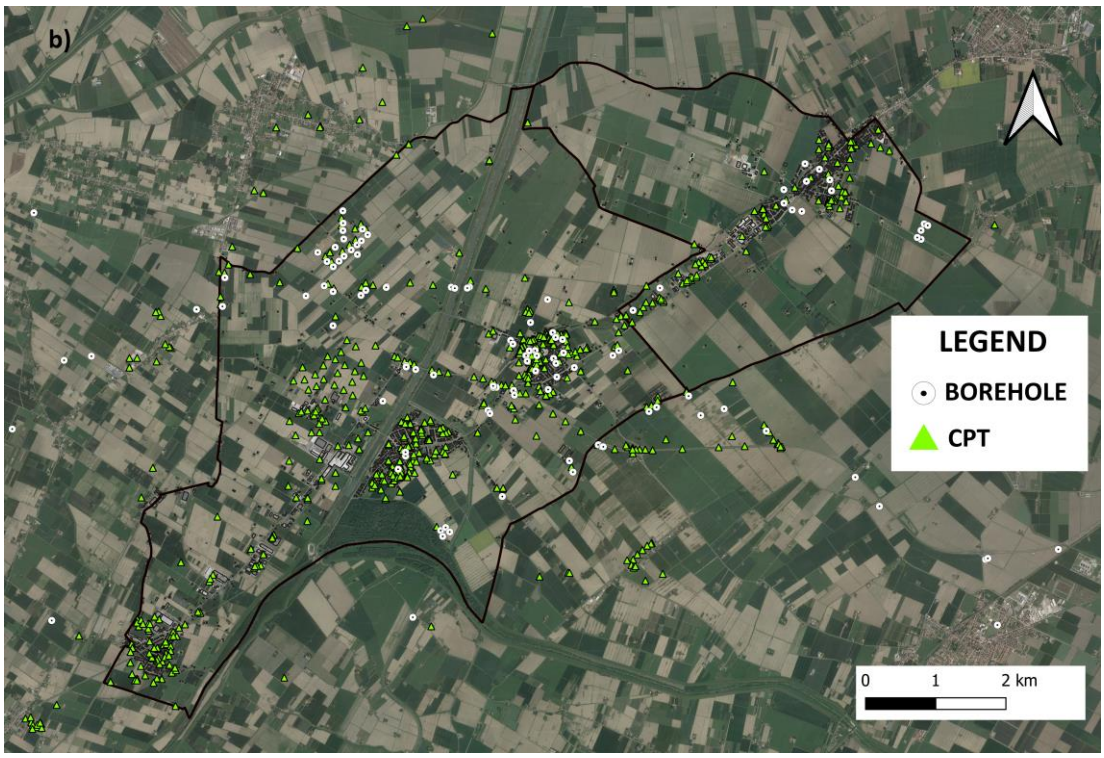

Figure 6-7 Localization of in-situ tests in the area of Terre del Reno.

Like the Christchurch case study, the CPT raw profiles were first homogenized in the same format to allow simultaneous analysis with automated algorithms. In this procedure, the difference between mechanical (CPTm) and electrical (CPTe) measures were considered applying to the CPTm tip resistance and the soil behavior factor Ic (Robertson and Wride, 1998) the empirical corrective formula proposed by Madiai et al. (2016) and plotted in Figure 4-15. The database was then enriched by collecting the available continuous core drills and correlating the soil classification with the Ic index through the empirical relationship provided by Lo Presti et al. (2016).

On the other hand, the mechanical aspect of liquefaction triggering and propagation makes the groundwater depth characterization with respect to ground level a relevant factor in any liquefaction risk analyses. For the areas of S. Carlo and Mirabello where liquefaction was extensively observed, monitoring of the hydraulic level was undertaken by the Emilia-Romagna Region from June 2012. This study, published by the Emilia-Romagna working group (Regione Emilia-Romagna, PG.2012.0134978 del 31/5/2012a; Regione Emilia-Romagna, PG.2012.0134978 del 31/5/2012b;) allowed to reconstruct the groundwater conditions in May 2012. From the obtained maps, it can be observed that the aquifer's depth follows the topography of the area, being greater (up to ≈4 meters) in the area of paleo-embankments, smaller outside it (approximately equal to 1.5 meters). In the village of S. Agostino, the water table trend was reconstructed by interpolating the measured levels in the summer period and the reported measures available from in-situ tests, namely boreholes and CPT profiles. The corresponding map (Figure 6-8) highlights an average depth greater than in the previous cases (≈5-6 meters).

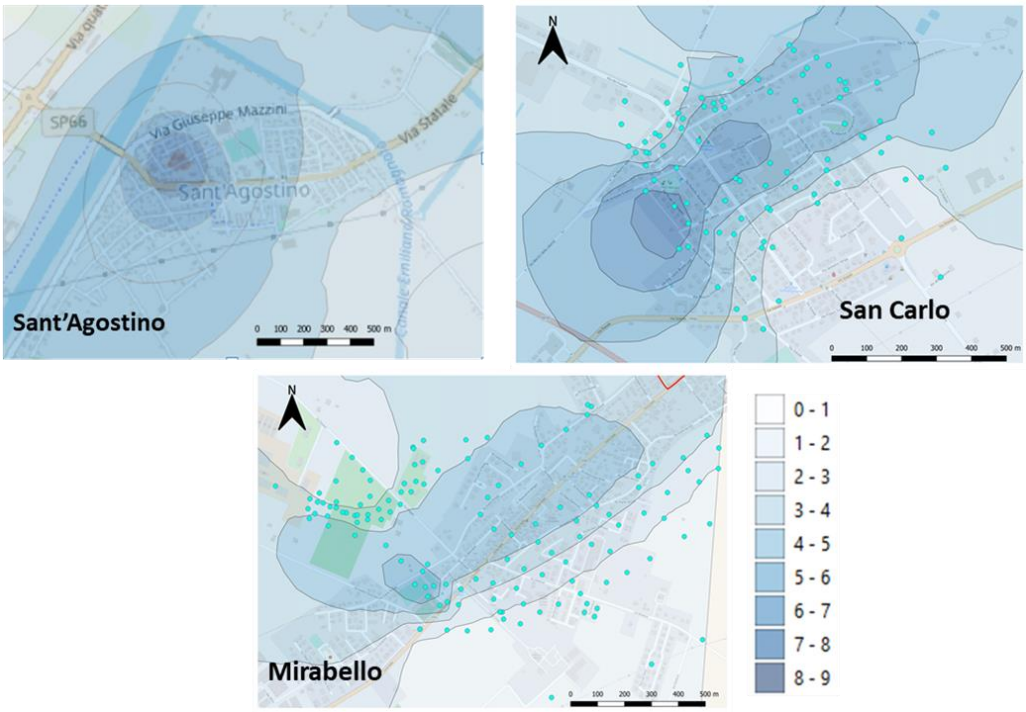

Figure 6-8 Map of groundwater depth over the districts of S. Agostino, S. Carlo and Mirabello.

After the subsoil database creation and groundwater modeling, automated processing of CPT profiles has been performed to evaluate the liquefaction susceptibility of the area. The following liquefaction hazard analysis consists of evaluating of the most used liquefaction severity indicators resulting from the May 20th (Mw 6.1) earthquake,

which Shake Map is reported in Figure 6-9. ShakeMaps provide an estimate of the spatial distribution of ground motion, obtained by interpolating data from the recording stations of the Italian Strong Motion Network (RAN) and the Strong Motion Network of Northern Italy (RAIS). The maximum peak ground acceleration (PGA) was recorded at the station of Mirandola (MRN), which was 13.4 km far from the epicenter, which reached 0.31 g (vertical component). Figure 6-9 shows a shake map computed by interpolating the recorded PGA at the RAN stations using the inverse distance weighted algorithm. The stations are located at sites classified as category C according to the soil classification system prescribed by the Italian Building Code (NTC, 2018), which is similar to that of Eurocode 8 Part 1 (EN 1998-1, CEN, 2004).

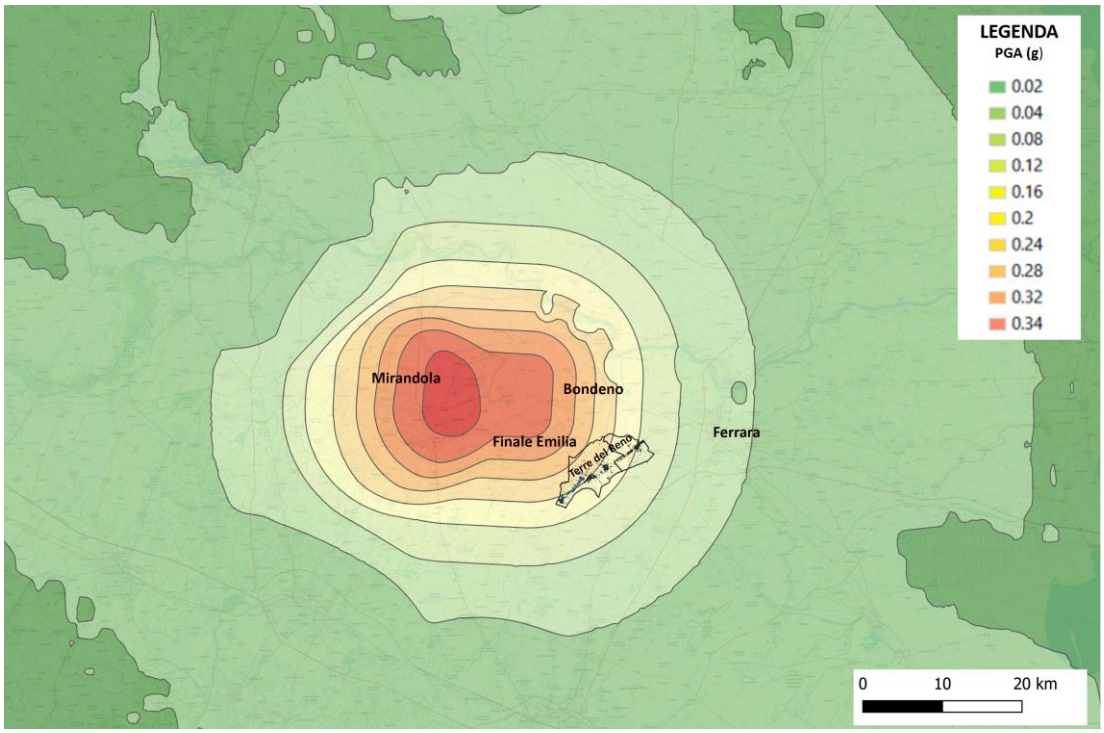

Figure 6-9 Spatial distributions of 20th May 2012 Peak Ground Acceleration from INGV Shake Map (http://shakemap.rm.ingv.it/shake/).

6.4.1 Liquefaction susceptibility of the area

The Holocene deposit of Terre del Reno is classified as moderately to highly susceptible to liquefaction based on the criteria proposed by Youd and Perkins (1978). Additionally, the existing geotechnical investigations have been interpreted for this analysis. Out of 1000 CPT profiles available for the whole area of Sant'Agostino and Mirabello, more than 800 CPT profiles have been used after data filtering with the boxplot test described in Figure 4-18 to reconstruct the geotechnical model of the area, about 170 of them located in the village of S. Carlo.

Thereafter, the liquefaction geotechnical susceptibility has been quantified through the Equivalent Soil Profile method, which assesses as liquefiable much of the territory of Terre del Reno since in almost all cases there is at least one potentially liquefiable soil layer. About 70% of the stratified subsoil can be classified as weak in terms of liquefaction resistance (red points in Figure 6-11), confirming for those profiles the presence of a medium to highly susceptible to liquefaction layer. This result stems from the geological history of the site, given by the presence of the paleo-river of Reno (Fioravante et al., 2013) that for a period of three centuries crossed the Territory of Terre del Reno (Bondesan & Bondesan, 1990); the Old Reno River paleochannel is well described by the geotechnical model which highlights the presence of liquefiable layers with variable thickness from 2 to 5 m, more variously concentrated below the districts of Sant'Agostino, San Carlo and Mirabello (Figure 6-11, Figure 6-12).

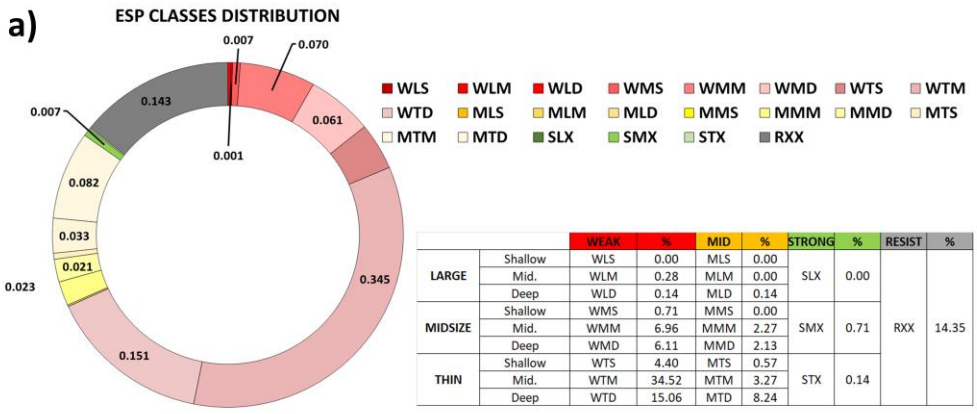

		WEAK	%	MID	%	STRONG	%	RESIST	%
LARGE	Shallow	WLS	0.00	MLS	0.00	SLX	0.00	RXX	14.35
	Mid.	WLM	0.28	MLM	0.00				
	Deep	WLD	0.14	MLD	0.14				
MIDSIZE	Shallow	WMS	0.71	MMS	0.00	SMX	0.71		
	Mid.	WMM	6.96	MMM	2.27				
	Deep	WMD	6.11	MMD	2.13				
THIN	Shallow	WTS	4.40	MTS	0.57	STX	0.14		
	Mid.	WTM	34.52	MTM	3.27				
	Deep	WTD	15.06	MTD	8.24				

Figure 6-10 Statistical distribution of the Equivalent Soil Profile in Terre del Reno.

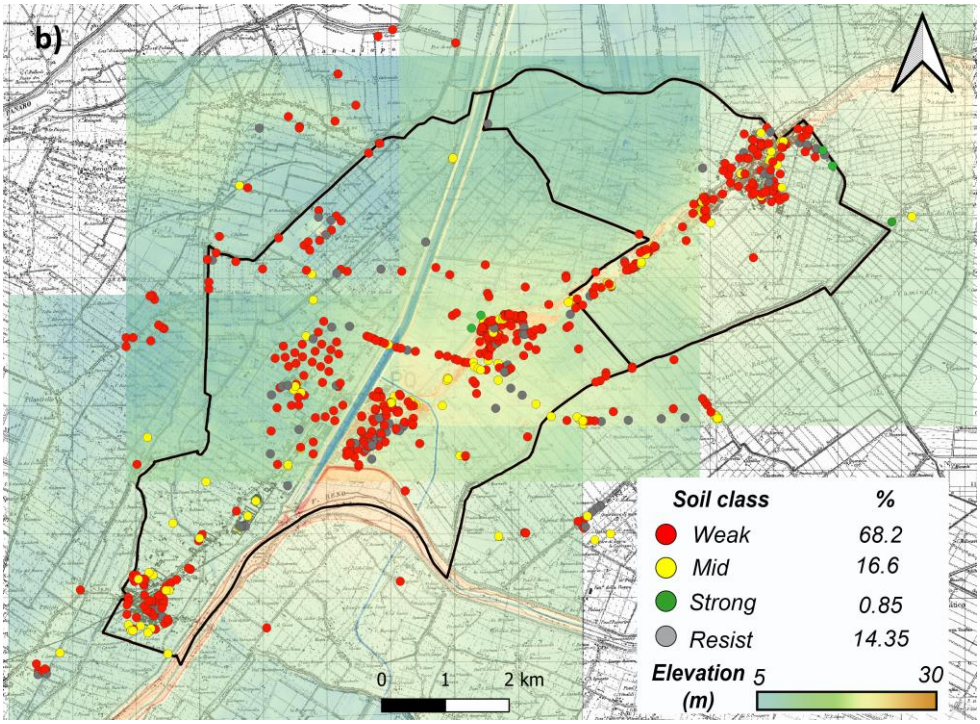

Figure 6-11 Overview of the spatial distribution of subsoil classes.

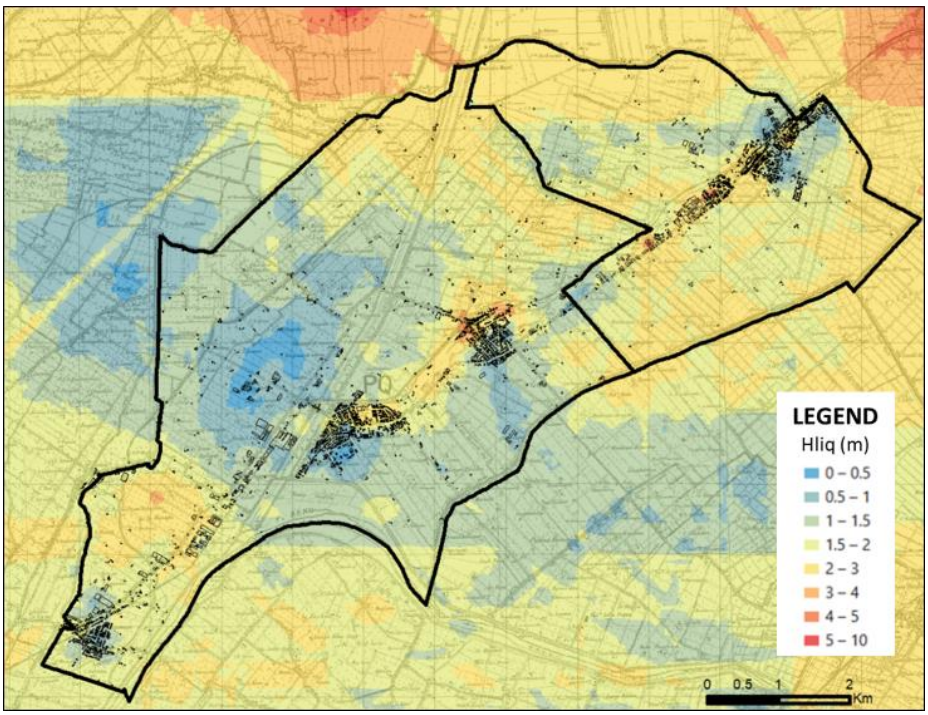

Figure 6-12 Map of the thickness of liquefiable layer evaluated through the ESP method (c)

With a classification in 22 different classes, the ESP method provides an error index (the standard normed error) that quantifies the real profile difference with an equivalent three-layer model. Histograms of Figure 6-13, show that around 90% of the subsoil profiles in Terre del Reno exhibit an ESP normed error lower than 0.05, proving that they can be largely considered three-layer models, i.e., a single liquefiable layer underlying a non-liquefiable crust layer.

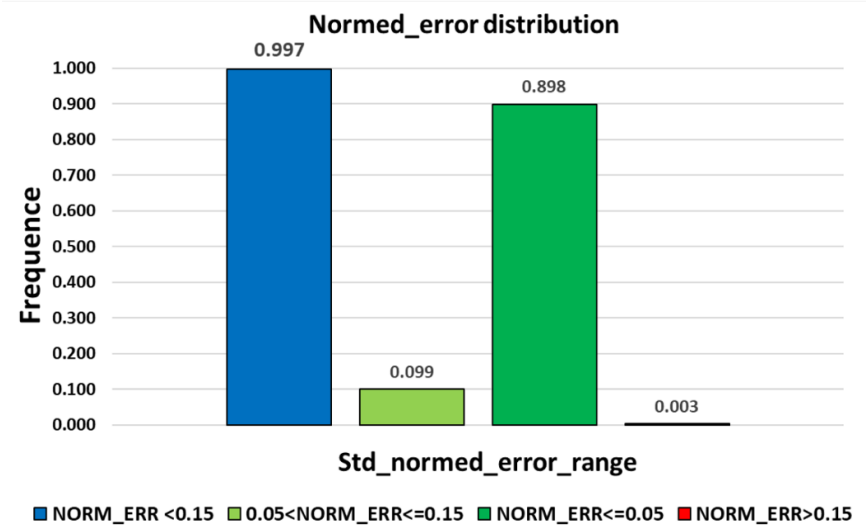

Figure 6-13 Histograms of the normed errors showing the equivalence of soil profile to the ESP model.

6.4.2 Mapping of liquefaction severity indicators

Considering the 20th May 2012 (Mw 6.1) seismic ground motion, the liquefaction hazard analysis consisted in the evaluation of some of the most widely adopted liquefaction severity indicators, namely: LPI (Iwasaki et al., 1978), w_v (Zhang et al., 2002), LSN (Van Ballegooy et al., 2014). The safety factor against liquefaction has been determined by applying the Boulanger & Idriss (2014) procedure, adopting a cutoff equal to 2.6 to the soil class indicator I_c, suggested from Robertson and Wride (1998).

During the spatial analysis, a filter was applied to the dataset of CPT profiles removing those not consistent with the spatial trend (outlier) following the procedure

described in Figure 4-18. The values of all indicators were computed correspondingly to the CPT positions and interpolated with geostatistical analyses to obtain maps covering the territory. Taking advantage of the geostatistical analysis's possible to estimate uncertainty, the standard error distribution was studied. The areas affected by errors larger than 25% have been removed from the present analysis (and represented with grey color). The obtained Maps are displayed in Figure 6-14, Figure 6-15, Figure 6-16.

Although with some differences, all maps highlight a heterogeneous distribution of values over the territory area with a stronger concentration of potentially liquefiable layers along the North-East/South-West direction. This trend reflects the geological and hydrogeological features of the territory, consisting of alluvial deposits of various composition but having major sandy components along the old Reno River channel. It is also worth noting that the spatial distribution of indicators reflects the distribution of ESP categories, proving that such criterion performs adequately in the area of Terre del Reno.

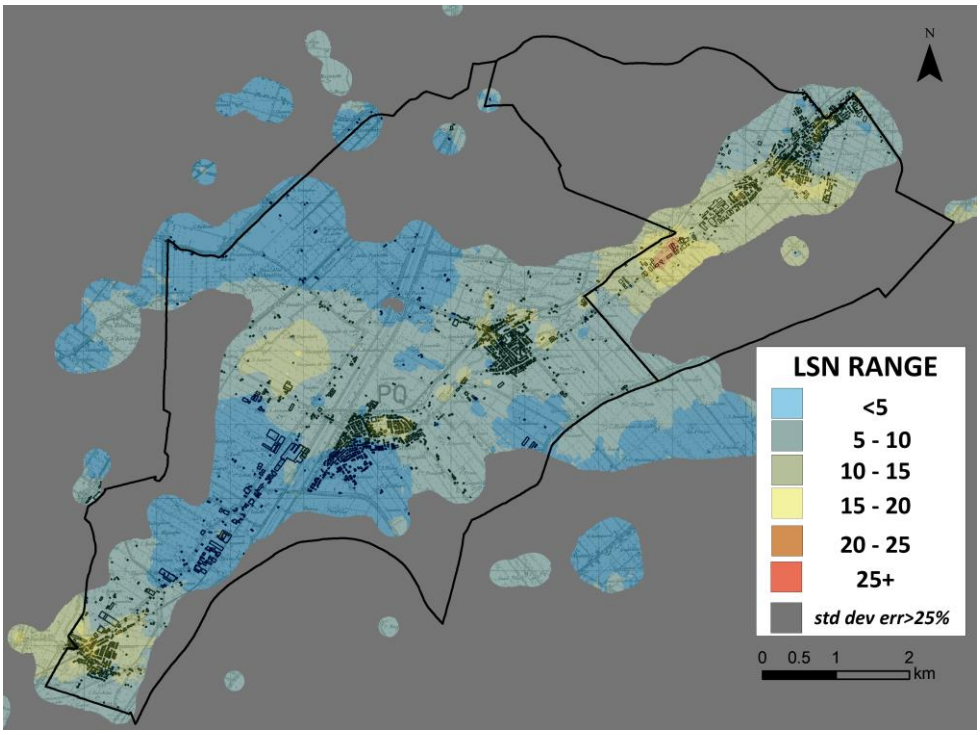

Figure 6-14 Geostatistical interpolation of "LSN" (van Ballegooy et al., 2014) on the territory of Terre del Reno; estimate error map was overlaid to the indicator Map to cut the areas where knowledge is not adequate.

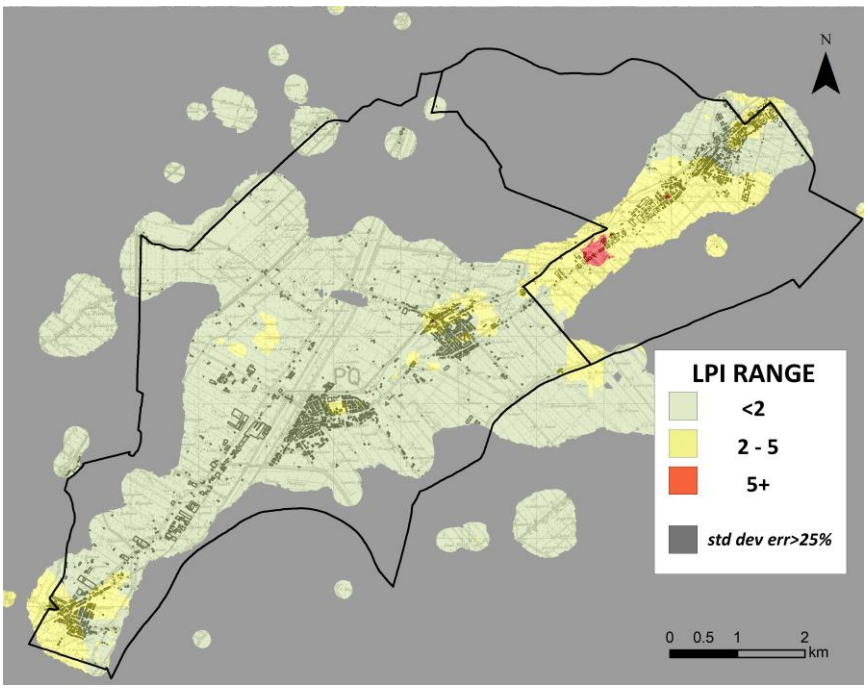

Figure 6-15 Geostatistical interpolation of "LPI"(Iwasaki et al., 1978) on the territory of Terre del Reno; estimate error map was overlaid to the indicator Map to cut the areas where knowledge is not adequate.

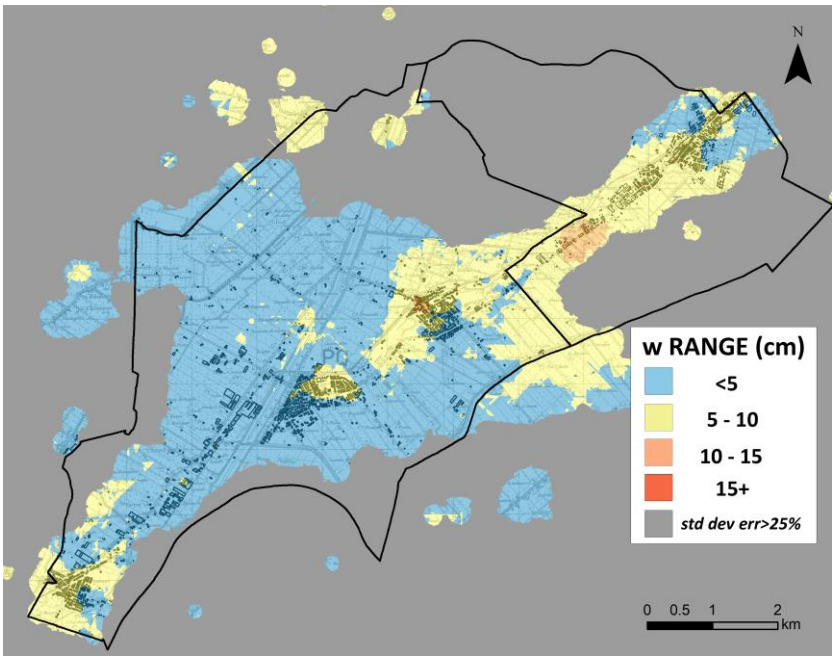

Figure 6-16 Geostatistical interpolation of liquefaction-induced 1D settlement "w" (Zhang et al., 2002) on the territory of Terre del Reno; estimate error map was overlaid to the indicator Map to cut the areas where knowledge is not adequate.

6.4.3 Lateral Spreading

The localization of liquefaction-induced damages superimposes most of the cracks on the area's morphological features, namely the old Reno River channel and its embankments. The observed building damage in S. Carlo and Mirabello arising from the analysis of technical and photographic reports available in the MUDE platform confirmed that the most recurrent and severe types of building failures were due to lateral spreading-induced differential movements and cracks.

A representative cross-section of the Southern area of San Carlo reported in Figure 6-17, shows that almost all the urban district of San Carlo is built on two human-made loose sandy embankments having different and irregular geometry. These embankments extend until Mirabello, although with a different structure.

In this context, the embankments' presence results in higher values of the factor of safety since the groundwater depth increases below them leaving the loose potentially liquefiable soils under unsaturated conditions. And therefore, because traditional liquefaction severity indicators only account for 1D conditions, weighting the liquefaction potential by the depth may lead to underestimate the effects of liquefaction in the areas of S. Carlo and Mirabello.

To avoid such occurrence, the before-defined generalized indicator "*GLD*" has been evaluated with reference to the 20th May 2012 Mw 6.1 earthquake on the entire municipality of Terre del Reno. Since it implies the punctual definition of features like the maximum slope steepness, the height of the possible free face, and distance of the considered point from the toe, it provides in this context a detailed description of the topography. Compared to the free face geometry observed in Christchurch resulting from the interaction of the Avon River and the surrounding portion of the Canterbury Plain (see Figure 5-19), the presence of two paleo embankments delineates in the municipality of Terre del Reno a complex situation since many CPT profiles are located on highly sloped ground; others are referred to a free face geometry. The analysis becomes more complex if extended to the district of Mirabello, since the height of free face and the ground slope become variable.

To accomplish this goal, the available DEM from Emilia-Romagna Region WEB-Gis was investigated together with the local and detailed analysis of significant cross-sections along the embankments, which allows characterizing the ground surface conditions and topography near the considered CPT (Figure 6-17).

Thinking on the GLD structure, all these contributions are embedded in the topographic factor "TF". Such term is quantified at each CPT location combining the contribution of the height "H" and distance from a free face "L"; additionally, great emphasis in this evaluation is given to the ground slope "S" (%) because it plays a major role in amplifying the function "TF" (Eqn. 4.3). The evaluated topographic factors, reported in Figure 6-18 zooming on the district of San Carlo, reflect the irregular geomorphology of the study area. Thinking on the municipality of S. Carlo, "H" ranges in 1.4 - 7 meters in the zone along the embankments while the ground slope "S" is generally in the range of 2-10%, reaching 15% in the worst situations. Therefore, the evaluated topographic factor in the area of San Carlo is generally greater than 1.5-2, reaching a value of 10-12 in the most critical situations (see Figure 6-18).

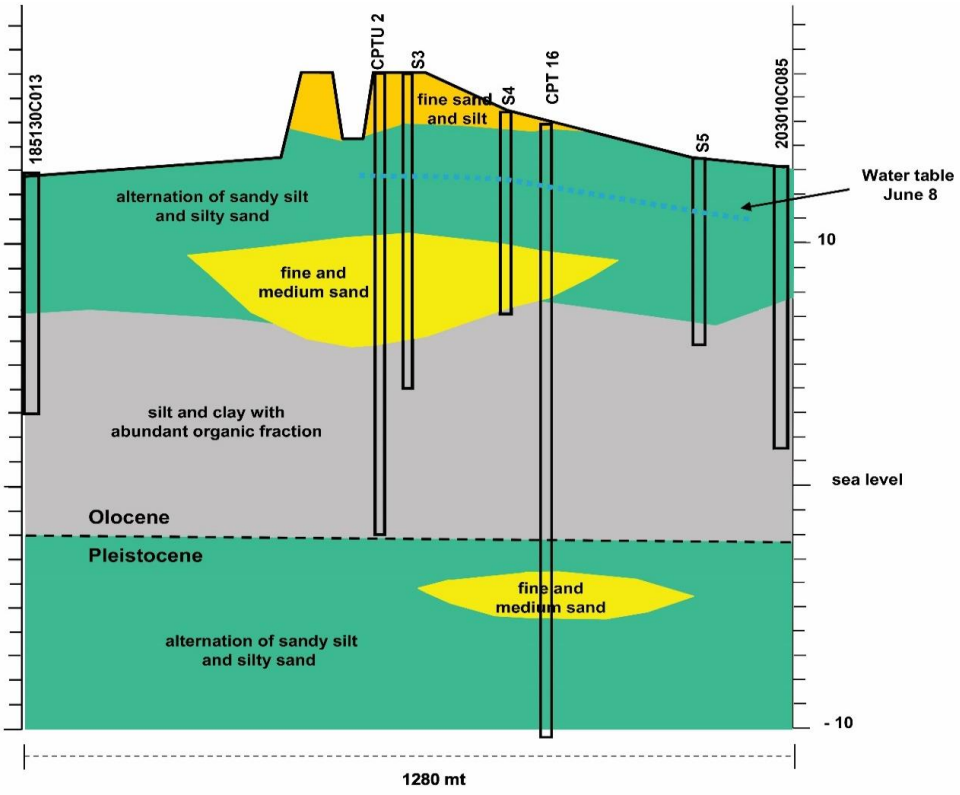

Figure 6-17 Geological cross section WNW-ESE through the San Carlo area, section AA of Figure 6-18, (Martelli, 2012)

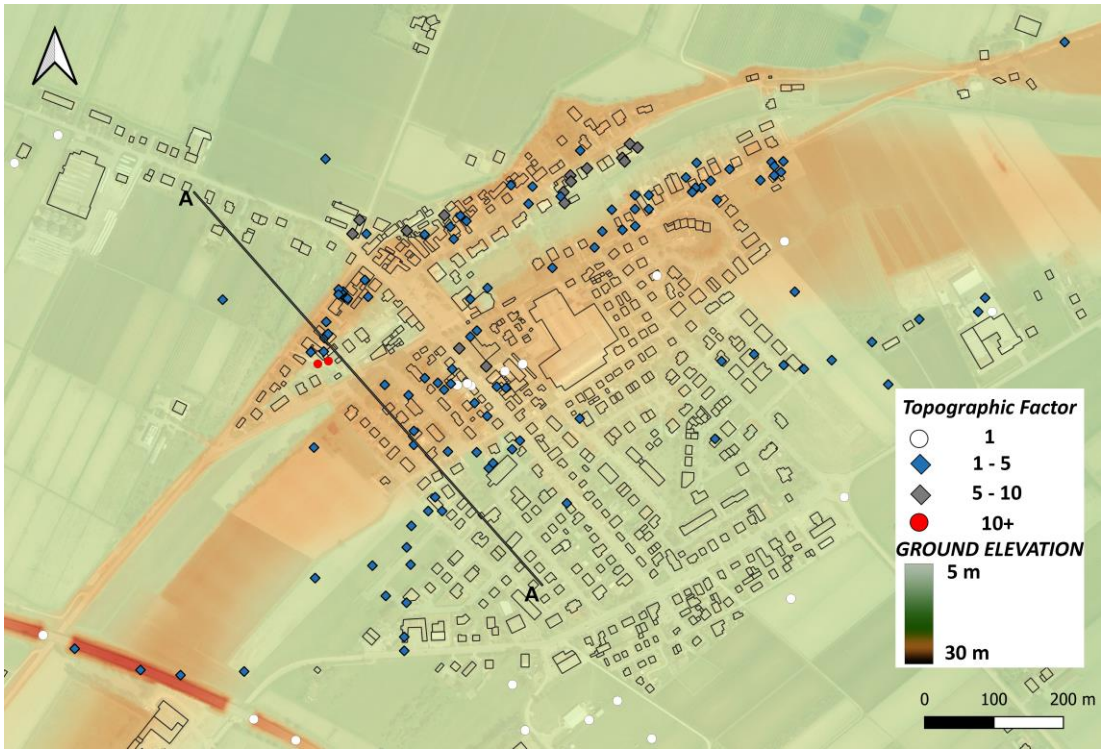

Figure 6-18 Evaluated Topographic Factors (TF) in the district of S. Carlo and trace of the section "AA" displayed in Figure 6-17.

Considering the whole municipality of Terre del Reno, the above comments result in a distribution of the generalized GLD punctual values evaluated for the 20th May 2012 earthquake, reflecting the general damage trend outlined by traditional indicators. In fact, the outlined pattern of ground deformation showed in Figure 6-19 agrees to the liquefaction susceptibility of the area (see Figure 6-11) and permanent ground deformation Maps (see Figure 6-14, Figure 6-15, Figure 6-16). In particular, Figure 6-19 highlights the highest values of the generalized *LD* indicator in almost all the zone of S. Carlo and in the South area of Mirabello, where the presence of embankments and/or slope ground determine generalized LD greater than 100 (red dots of Figure 6-19) suggesting that severe liquefaction (like extensive cracks and lateral spreading) is highly probable.

On the other hand, the GLD values are generally lower in the district of S. Agostino and in most of the surrounding alluvial plain, where an intrinsic lower liquefaction susceptibility is evaluated (Figure 6-12).

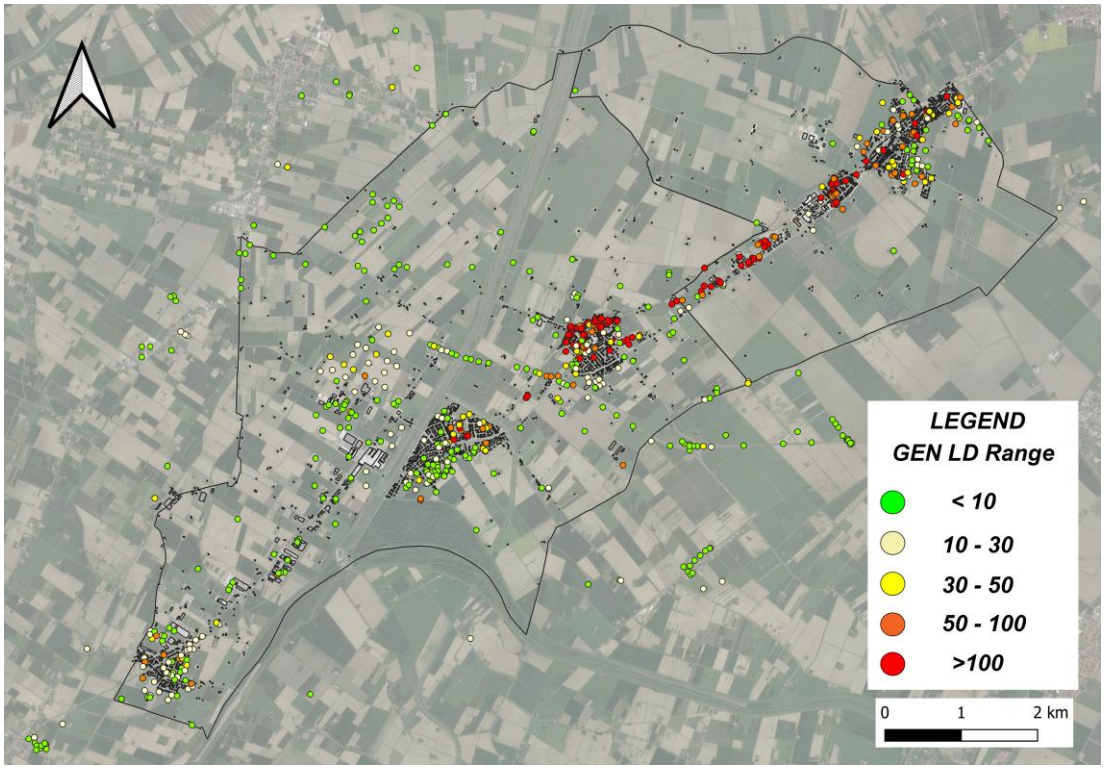

Figure 6-19 Generalized LD punctual values evaluated for the 20 May 2012 Earthquake.

A map of land damage for the 20th May 2012 event has been produced by clustering into damage levels all the observations showed in Figure 6-5. To this aim, 50x50m cells covering the entire municipality of Terre del Reno were overlapped to the liquefaction observations; reports of building damage available from the Mude Platform were also considered in this classification. According to the technical information of liquefaction evidence, it was assumed that punctual phenomena (namely sand boils) represent the less severe liquefaction-induced damage level. At the same time, fractures are assessed respectively as moderate and severe if they fall adjacent or inside a given cell. On the other hand, the ascertained presence of buildings experiencing liquefaction-induced damage was considered a proxy for severe ground deformation.

The map of liquefaction induced damage showed in Figure 6-20 classifies the areas where no liquefaction was observed with blue color, the areas characterized by minor to moderate sand ejecta and cracks with yellow, and the areas affected by severe liquefaction (cracks/lateral spreading capable of inducing building damage) with red. From the analysis of land damage, it readily emerges that the San Carlo district was

almost entirely affected by liquefaction, mostly due to the presence of the Reno River paleo-embankments. Huge liquefaction was also recorded in Mirabello, both along the SW-NE old direction and in the North area. Also in these cases, the phenomenon is strongly related to the geology and geomorphology of the area, namely the presence of Reno River embankments (which extend from San Carlo to Mirabello) and buried paleochannels (in the Northern boundary).

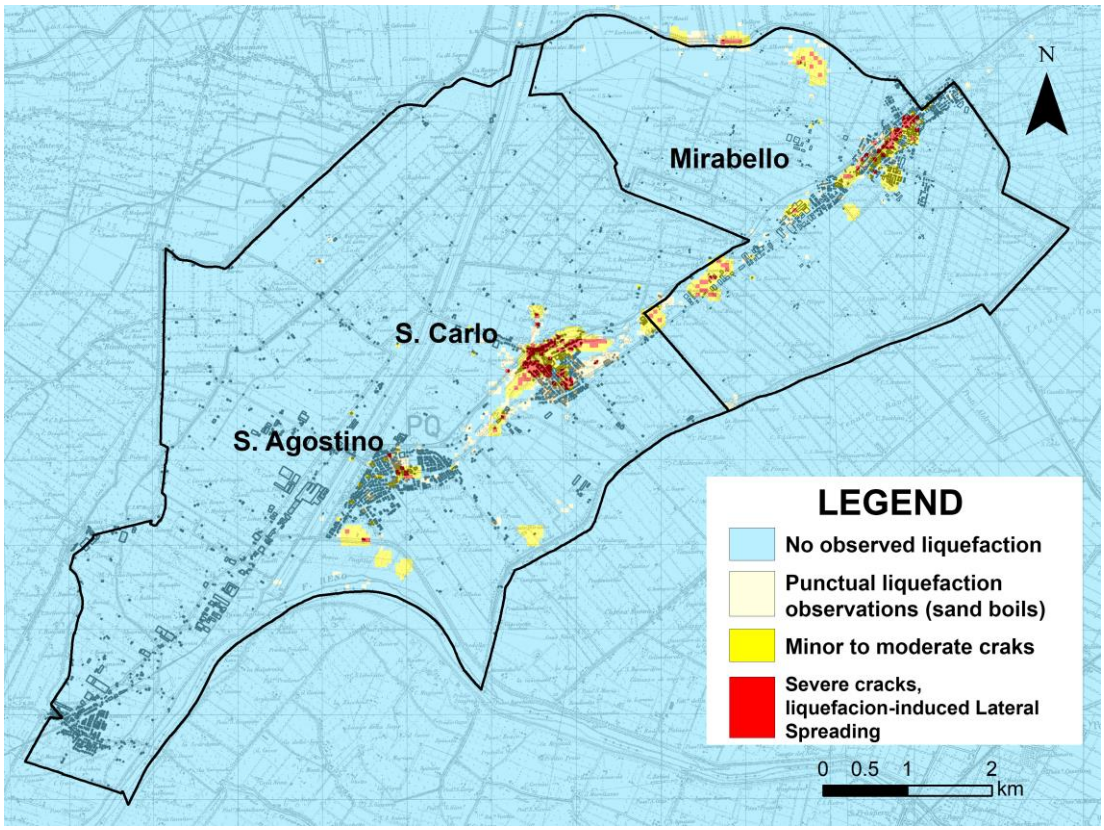

Figure 6-20 Liquefaction and Lateral Spreading Maps from "Emergeo, 2013" observations.

6.5 **Validation of Liquefaction Severity Indicators**

On the whole territory of Terre del Reno, the effectiveness of traditional indicators in predicting the liquefaction occurrence was tested by applying the criterion defined by Kongar et al. (2015) and before illustrated (Figure 4-21). The 20th May 2012 Mw 6.1 earthquake was taken as seismic input, and the calculated liquefaction severity indicators for each CPT profiles were compared with the experimental observations,

considering the liquefaction-induced damage levels on the ground outlined from Figure 6-20.

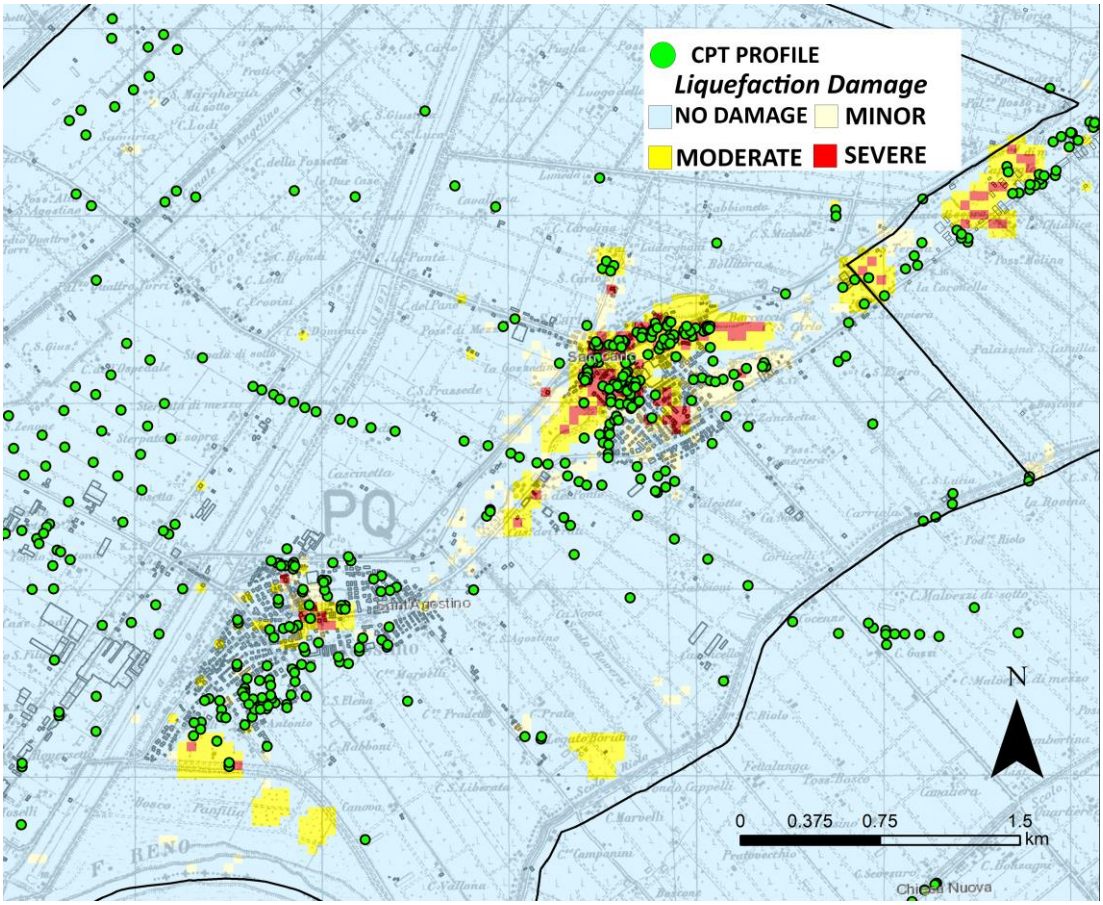

Figure 6-21 Map of liquefaction-induced ground damage superposed to the location of CPT tests, zoom on the districts of S. Agostino and S. Carlo.

The performance of traditional liquefaction severity indicators can be explained by observing their common structure which combines the effects of a weight function with the safety against liquefaction that implicitly inglobes the geology and geotechnical features of the area. Figure 6-21 shows that most of the liquefaction-induced damages in San Carlo (extensive cracking and lateral spreading) arise from the Old Reno paleochannel presence. Regarding this aspect, a first shortcoming arises from the structure of Traditional liquefaction severity indicators: referring to a 1D geometry, they do not explicitly account for the presence of a slope or free field face. In a such situation, the presence of the embankments made of unsaturated loose sands (thus classified as non-liquefiable material) is read in the calculation of each indicator as a deepening of the liquefiable layer, leading to a reduction in the weight function w

(z). Such effect is not seen in the settlement "w_v" since it integrates each points' vertical deformation along the soil profile, without considering its depth. Due to the significant differences between the indicators, it is legitimate to expect a different forecasting capacity. However, almost all the indicators depict a common general trend that recognizes the Reno River Paleochannel area as the most heavily interested by liquefaction phenomena, even if the evaluated values differ from an indicator to another.

In this context, the validation test of Kongar et al. (2015) applied to traditional indicators as back analysis of the 20th May 2012 seismic scenario demonstrates their global efficacy in predicting the occurrence of liquefaction (being the AUC in the range of 0.70 – 0.77), although with different optimal thresholds and misprediction ratios. This widely acceptable performance is also confirmed by the overall success rate, which is always found greater than 65-70%; at the same time, the overall false negative ratio is around 10%, in agreement with the results displayed by Kongar et al. (2015). The obtained results, briefly summarized in Figure 6-22 and Table 6-1, allow us to make some observations.

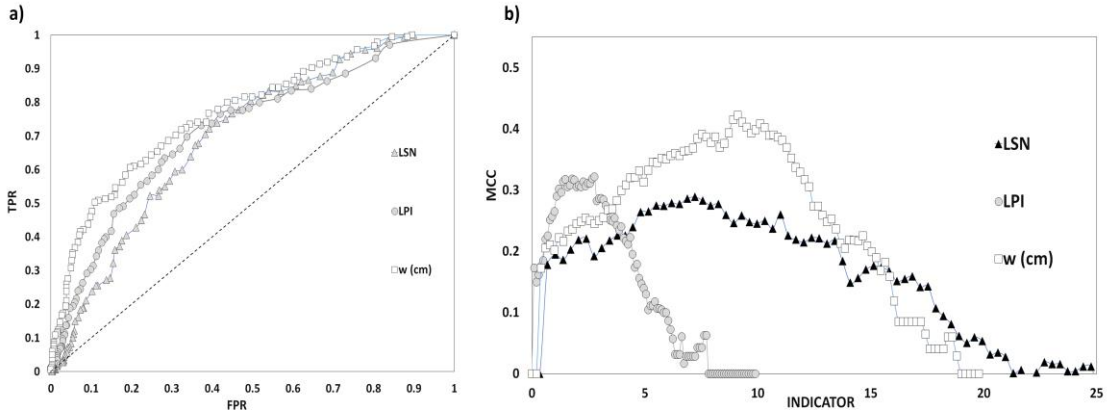

Figure 6-22 ROC curves and MCC functions after geostatistical error filtering.

Table 6-1 General performance of traditional indicators in predicting the occurrence of liquefaction, after geostatistical filtering of outliers (in the hypothesis of consistency of three layers profiles).

Liquefaction Severity Indicator	AUC	OPTIMAL THRESHOLD (MCC)	TPR	FNR	TNR	FPR	OSR (%)	OFPR (%)	OFNR (%)
LPI	0.73	≈1.5 - 2	0.64	0.36	0.72	0.28	70.0	20.9	9.1
W (cm)	0.77	≈8-9	0.55	0.45	0.84	0.16	75.9	11.6	12.5
LSN	0.70	≈7-8	0.72	0.28	0.61	0.49	63.7	29.1	7.2

Table 6-1 shows that the evaluated optimal LPI threshold capable of predicting the liquefaction/non-liquefaction (≈2) in Terre del Reno district is consistent with one of the most widely adopted classification of literature proposed by Sonmez (2003). Although in different subsoil and seismicity contexts, this value is also in agreement with the analogous value observed in the case study of Christchurch. Similar to the LPI, the LSN also shows an overall acceptable performance in terms of AUC. However, the "MCC" criterion provides, in this case, an optimal threshold approximately equal to 7-8, i.e., lower than 10, which is the value below that liquefaction is not expected to occur as reported in the New Zealand guidelines (MBIE, 2016) and van Ballegooy et al. (2014). Looking at the LSN, the overall success rate results smaller if compared to the LPI and the post-liquefaction settlement, which shows the highest AUC and overall success rate, but also the highest percentage of false negative events (12.5%).

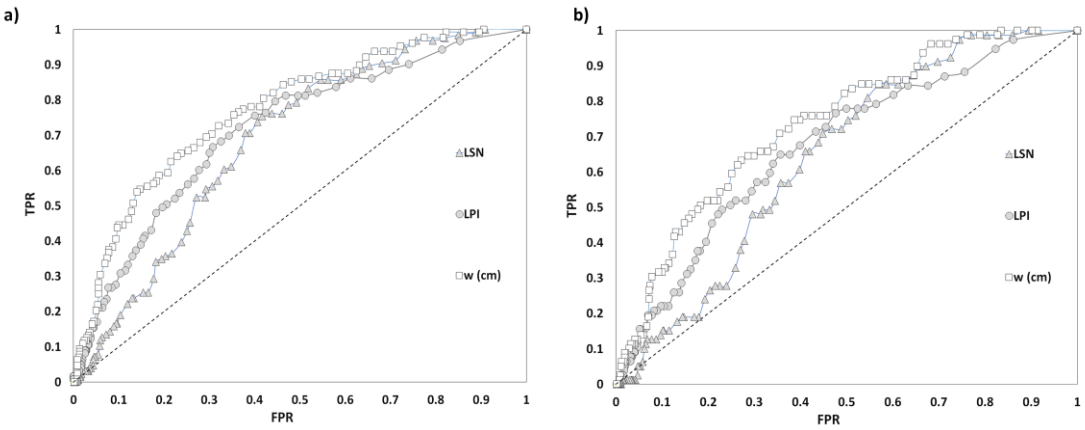

Figure 6-23 ROC curves after geostatistical error filtering for CPTs consistent with the three-layers profiles, for moderate (a) and severe (b) liquefaction-induced damage level.

In the same way, some shortcomings of traditional indicators are put in evidence from the proposed validation test. The first of them clearly appears when more severe liquefaction induced damage levels are considered. In fact, the MCC approach suggests that for each of the considered liquefaction-induced damage levels, the evaluated optimal thresholds do not change. This implies that the evaluated thresholds are independent of the severity of liquefaction or, in other words, that the adopted Matthews criterion is not completely adequate to relate the severity of damage to the calculated values. The adopted validation test results concerning the comparison between traditional indicators and higher liquefaction damage levels are reported in Figure 6-23 and Table 6-2 and Table 6-3.

Table 6-2 General performance of traditional indicators in predicting the occurrence of moderate liquefaction, after geostatistical filtering of outliers, for CPTs consistent with the three-layers profiles.

Liquefaction Severity Indicator	AUC	OPTIMAL THRESHOLD (MCC)	TPR	FNR	TNR	FPR	OSR (%)	OFPR (%)	OFNR (%)
LPI	0.73	≈2	0.67	0.33	0.69	0.31	68.8	25.2	8.0
W (cm)	0.78	≈9	0.54	0.14	0.86	0.46	80.1	11.5	8.4
LSN	0.69	≈8	0.71	0.29	0.61	0.39	62.8	31.9	5.3

Table 6-3 General performance of traditional indicators in predicting the occurrence of severe liquefaction, after geostatistical filtering of outliers, for CPTs consistent with the three-layers profiles.

Liquefaction Severity Indicator	AUC	OPTIMAL THRESHOLD (MCC)	TPR	FNR	TNR	FPR	OSR (%)	OFPR (%)	OFNR (%)
LPI	0.69	≈2.5	0.48	0.52	0.78	0.22	74.5	19.6	5.9
W (cm)	0.74	≈10	0.43	0.57	0. 87	0.13	82.1	11.5	6.4
LSN	0.65	≈8	0.71	0.29	0.55	0.45	56.9	39.7	3.4

Although its optimal thresholds are only moderately sensitive to the different liquefaction-induced phenomena, the 1D post-liquefaction settlement w_v (Zhang et al., 2002) appears to predict the moderate and severe damage levels in a quite stable way, since its AUC ranges in 0.74 – 0.78. This evidence probably results from the theoretical assumption in its definition since it integrates along the CPT profile the volumetric deformation ε_v (%), also evaluated in layers where FS_L is greater than 1, without introducing a depth weight function.

Although the Equivalent Soil Profile method demonstrated consistency with the hypothesis of three-layer profiles, the case study of Terre del Reno highlights the lack of explicit terms accounting for the soil topography as the most significant limitation in traditional indicators. In fact, looking at the distribution of liquefaction-related phenomena over the study area, it clearly appears that topography plays a non-negligible role since it represents a term of geometric irregularity, e. g. a slope capable of inducing lateral spreading, but often results in a non-conservative estimate of traditional indicators since the presence of embankments results in higher values of the factor of safety since the groundwater depth increases below them leaving the loose potentially liquefiable soils under unsaturated conditions.

Table 6-4 General performance of traditional indicators in predicting lateral spreading, after geostatistical filtering of outliers, for CPTs consistent with the three-layers profiles.

Liquefaction Severity Indicator	AUC	OPTIMAL THRESHOLD (MCC)	TPR	FNR	TNR	FPR	OSR (%)	OFPR (%)	OFNR (%)
LPI	0.75	≈1.5-2	0.67	0.33	0.71	0.29	70.4	23.3	6.3
W (cm)	0.78	≈9	0.50	0.50	0.87	0.13	80.0	10.9	9.1
LSN	0.71	≈8	0.75	0.25	0.59	0.41	62.3	34.6	3.1

In the field of empirical expeditious methods, the performance of the GLD, which primary goal consists in providing a synthetic indicator capable of predicting lateral spreading phenomena, has been herein evaluated. Similar to the traditional liquefaction severity indicators, the Kongar et al. (2015) binary test is herein applied to compare the liquefaction prediction with the 20th May 2012 Earthquake liquefaction evidence. The obtained results are displayed in Figure 6-24 ,reporting the GLD ROC curve vs. lateral spreading observations; being the AUC equal to 0.90, this plot proves a robust performance of the generalized indicator used to evaluate the lateral spreading occurrence.

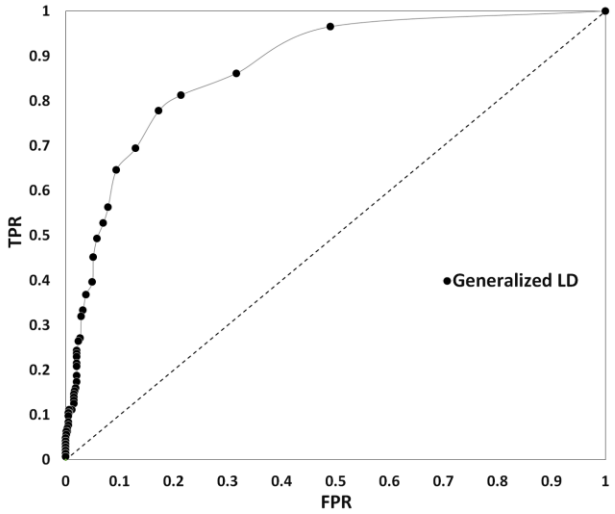

Figure 6-24 ROC curve of the generalized indicator LD vs lateral spreading observations for the municipality of Terre del Reno.

In a subsequent analysis, the spatial distribution of binary classification outputs for lateral spreading observations is determined after calculating "MCC" suggested to assume an optimal GLD threshold equal to 100: the obtained results are displayed in

Figure 6-20. Following the binary logic presented in Table 4-6, outcomes for a prediction such as whether liquefaction manifests or not are one of positive or negative depending on whether liquefaction is predicted to manifest (namely locations where genLD ≥100) or not and positive or false depending on whether the prediction is correct.

A first observation arising from Figure 6-25 is that: the introduction of the topographic factor "TF" allows to better distinguish among True and Negative events, being the latter localized far from the Reno River paleo-channel and its embankments, i.e., in areas where the "TF" is evaluated equal to 1. On the contrary, the GLD distribution outlined in Figure 6-19 results in a correct prediction of almost all the positive events localized in the area of San Carlo (azure dots of Figure 6-25.a). As expected from the spatial analysis of Figure 6-19, the validation test confirmed for the area of S. Agostino a minor/negligible impact of lateral spreading. Here, the low values of GLD well correlate with negative events, and only a few localized examples of lateral spreading are pointed out.

Looking at the district of Mirabello, despite some cases of over predictions in the South boundary represented by the yellow dots of Figure 6-25.b, the lower height of the free face embankments results in a relevant number of correctly assessed true negative events (green dots of Figure 6-25.b).

Proven the capability of GLD in correlating with lateral spreading observations, the validation method proposed by Kongar et al. (2015) has been again applied to quantify its performance in predicting all the other classes of liquefaction-induced damage. As done for traditional indicators, liquefaction surficial manifestations resulting from the main event of the 2012 Emilia Earthquake Sequence were categorized into four classes: minor (including sand boils and punctual evidence of liquefaction), minor to moderate cracking, severe cracking, and lateral spreading (Figure 6-20). For each damage level, the overall GLD performance is summarized in Table 6-5 in terms of AUC, optimal threshold values and respective variables (like TPR, FPR, TNR..).

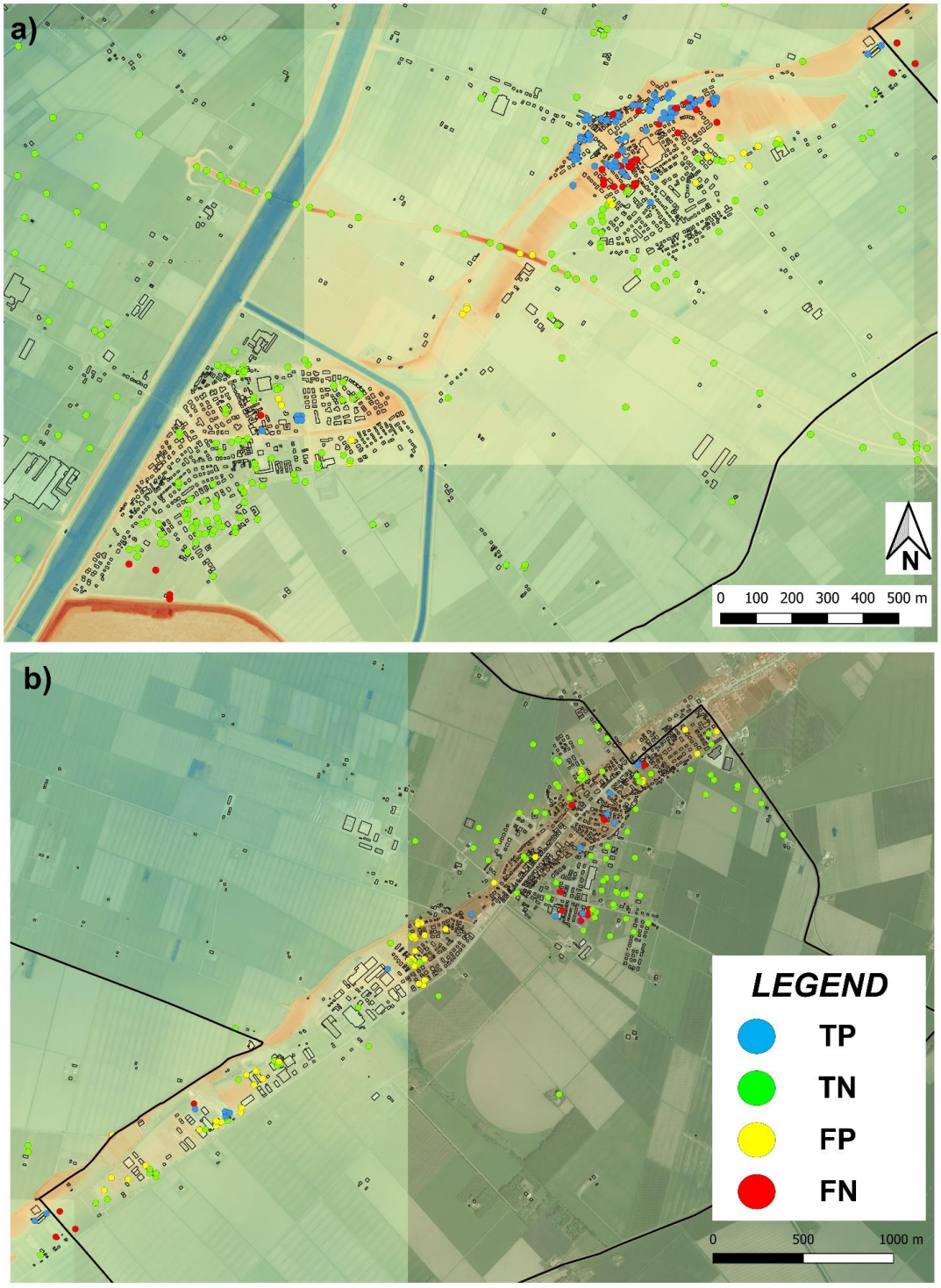

Figure 6-25 Spatial distribution of GLD results of binary test for lateral spreading (assuming an optimal gen LD threshold equal to 100), in the area of S. Agostino/S. Carlo (a) and Mirabello (b).

Table 6-5 Performance of the generalized indicator "LD" in predicting the observed liquefaction-induced damage levels after the application of the validation test.

DAMAGE LEVEL	AUC	OPTIMAL THRESHOLD	TPR	FNR	TNR	FPR	OSR (%)	OFPR (%)	OFNR (%)
Liquefaction/No Liquefaction	0.89	≈10-12	0.91	0.09	0.53	0.47	62.8	34.7	2.5
Minor to Moderate Cracking	0.88	≈25-30	0.84	0.16	0.67	0.33	69.9	27.0	3.1
Moderate to Severe Cracking	0.88	≈50	0.81	0.19	0.77	0.23	77.6	20.3	2.1
Lateral Spreading	0.90	≈100	0.56	0.44	0.92	0.08	85.0	6.3	8.7

The results summarized in Table 6-5 indicate a robust capability of the proposed indicator to foresee the different levels of liquefaction-induced phenomena, being the ROC curves higher than the plane bisecting line, with an AUC ranging in 0.88 – 0.90. This evidence suggests a more stable performance of the generalized LD if compared to the other indicators.

The optimal GLD thresholds for each damage severity level according to the MCC criterion are largely consistent with the analogous ones evaluated for the case study of Christchurch. Although further evaluations considering different case studies are required, this preliminary result proves this indicator's effectiveness in foreseeing the occurrence of liquefaction in different geological and geomorphological conditions.

Observers may argue that sometimes the evaluated Overall Success Rate (OSR) is not particularly exciting (e.g., 62.8% for minor cracks); when looking at the Overall Failure Rate (OFR), it can be observed that the most relevant contribution is represented by the Overall False Positive Ratio instead of the Overall False Negative Ratio (34.7% against the 2.5%). Since they represent the most dangerous kind of error, among the primary goals of any indicators used in risk assessment, there is the minimization of the false negative events.

On the contrary, one of the main responsible for the overprediction term in the study area may be the evaluated topographic factor TF, which significantly amplifies the shear deformation's (γ_{max}) cumulative effect.

6.6 **Probabilistic estimation of Liquefaction Potential**

Taking advantage of the huge amount of geotechnical data, an alternative probabilistic method to estimate the liquefaction potential is herein proposed following the logic approach of the microzonation.

The Italian Guidelines (ICMS, 2008; Gruppo di Lavoro MS, 2008; English version: SM Working Group, 2015) defines seismic microzonation as "the assessment of local seismic hazards by identifying the zones of a given geographic area with homogeneous seismic behaviour". The outlined strategy moves through three subsequent analysis levels, characterized by an increasing detail, and characterizes the zones in a specified context (a region, city, or district) as "stable, stable but prone to develop local amplification and prone to instability". With regard to liquefaction, the specific document entitled "LAND USE GUIDELINES FOR AREAS AFFECTED BY LIQUEFACTION (LQ), version I.0" has been published by the Technical Commission on Seismic Microzonation (ICMS LIQ, 2017) representing an integration of the "Guidelines for Seismic Microzonation" uploaded after the experience of the Emilia-Romagna earthquake that struck in 2012 the area of Po Plain and Reggio Emilia and to incorporate the studies produced in its wake. Its primary aim is the definition of general criteria and operative procedures, in coordination with State, Regional and Local Entities, to: gather accurate information about the risks induced by the presence of soils susceptible to liquefaction; manage risk in undeveloped areas (with or with no plans for development); mitigate risk in developed areas. To accomplish the expected goal, available information arising from existing databases or literature, when sufficient, represents the minimum informative elements to develop Seismically Homogeneous Map (SHM, Level 1 of detail). On the contrary, the level 3 Map of Seismic and Liquefaction Microzonation requires new ad hoc campaigns to assess Susceptibility Zones (SZ). At the same time, advanced studies accounting for soil characteristics and local site condition of seismic amplification are needed to Map Respect Zones (RZ).

The existing microzonation studies and the recent guidelines for liquefaction hazard over urban areas (Lai et al., 2020) suggest assessing the liquefaction hazard over a territory for different return periods, if possible, 475, 975, and 2475 years to account for a different level of intensity of seismic hazard. With this regard, instead of calculating a deterministic value of a given indicator, in analogy with the PGA decay curves outlined by seismic hazard studies, the developer of any liquefaction

microzonation study may provide the corresponding decay curves in terms of liquefaction severity indicators. An example of decay curves of Liquefaction Potential Index is showed in Figure 6-28, for a sample CPT located in the district of Terre del Reno i.e., the profile M306_CPT4 of Figure 6-26.

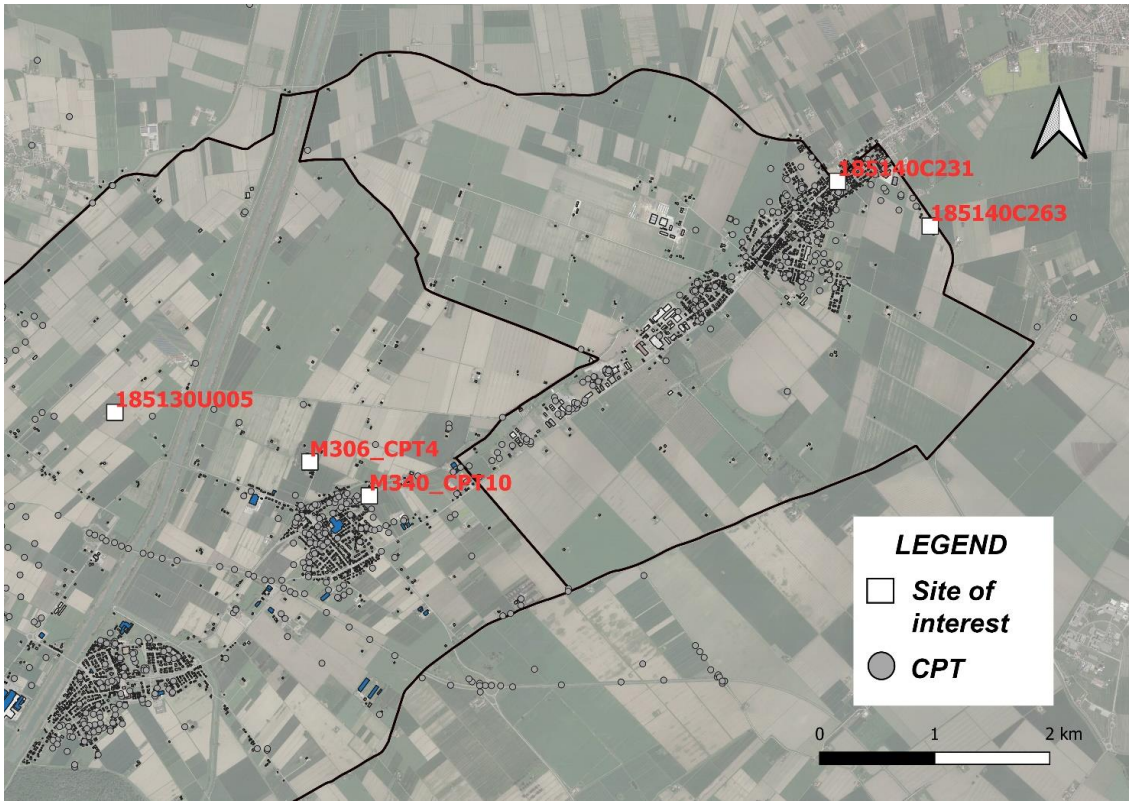

Figure 6-26 Location of the selected CPT profiles belonging to different ESP macroclasses of liquefaction susceptibility.

Following the procedure proposed by the Italian Standards (NTC, 2018), the PGA of a given scenario at the free surface has been evaluated by combining the seismic hazard of the area (http://esse1-gis.mi.ingv.it/) with the site amplification, which in turn has been modeled as a function of the Vs,30 measurements. In more detail, the 50 percentile of the acceleration at bedrock has been defined for 9 return periods, ranging from 30 to 2475 years (Figure 6-27). The stratigraphic amplification coefficient has been quantified in 1.50, as defined in the Italian Standards for a subsoil class C. On the other hand, independently from the PGA, the magnitude has been fixed equal to 6.14, i.e., the maximum expected Mw value in the area of Ferrara (http://zonesismiche.mi.ingv.it/).

The water table annual average depth ranges in 2.00 m – 3.70 m for the alluvial plain of Emilia-Romagna Region (Figure 6-27a) as reported by the ARPA monitoring surveys, three different situations are introduced. This implies processing the CPT profile by assuming a depth of the groundwater equal to 1.5, 2.0, and 2.5 m, respectively, for spring, annual and autumn conditions.

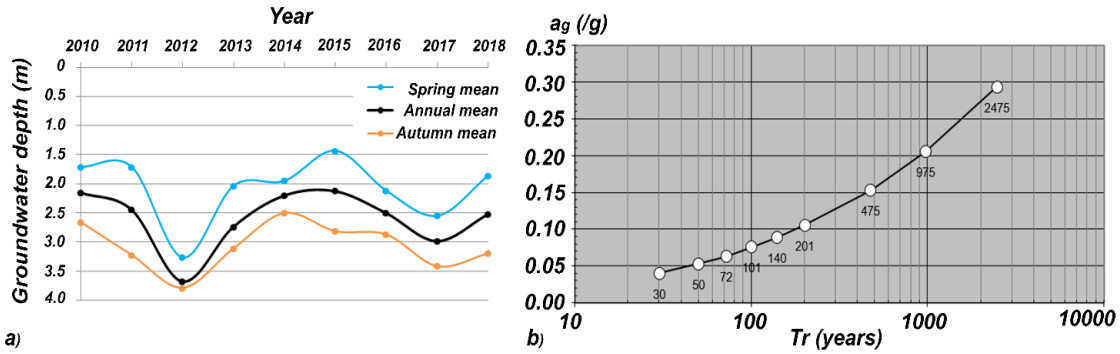

Figure 6-27 a) Mean annual groundwater depth from the Emilia Romagna ARPA monitoring system; b) seismic hazard for the district of S. Agostino, from the Italian Standards (NTC, 2018).

Considering the variability of groundwater level, for each seismic scenario, the factor of safety against liquefaction is evaluated along with each soil profile with the Boulanger and Idriss (2014), adopting an Ic cutoff equal to 2.6. As an example, Figure 6-28 shows a set of LPI decay curves for M306_CPT4 soil profile of Figure 6-26: the Iwasaki Liquefaction Potential Index is reported since it is employed in many worldwide Standards to develop microzonation studies (MBIE, 2016; ICMS-LIQ, 2017; Yasuda & Ishikawa, 2018).

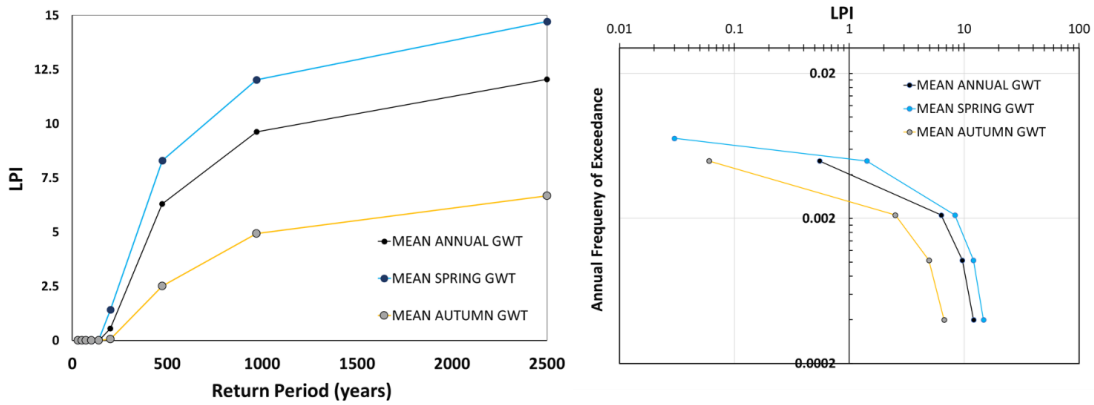

Figure 6-28 Figure Expected LPI values for the selected CPT profile as a function of the earthquake return period (a) and annual frequency of exceedance of a given value of the LPI (b) in the area of Terre del Reno.

This step represents a preliminary outcome of any microzonation study and a supporting tool in building design or urban planning. In fact, it would allow to quantitatively determine if liquefaction is likely to occur over an area, especially during the building lifecycle, considering different seismic and groundwater scenarios. This also makes it possible to save resources when liquefaction is not likely to occur (or if it is not likely to determine surficial manifestations) and evaluate the need for new ad-hoc campaigns and more detailed analysis when a critical situation is encountered.

In a more advanced step, the Monte Carlo simulation proposed by Lai et al. (2020) has been applied to evaluate the liquefaction potential on selected CPTs in Terre del Reno district. These subsoil profiles (which are listed in Table 6-6) represent different liquefaction susceptibility levels.

This analysis aim is to evaluate the influence of the different input variables, on the LPI, on each ESP crr-based class. In particular, the uncertainty of soil parameters is accounted for by treating the most representative variables as random ones, whose individual realizations feed a deterministic model. On the other hand, the seismic input accounts for the whole range of possible peak ground accelerations, as proposed by the performance-based engineering approach, with their respective return periods. Finally, the analysis is repeatedly used to assess the liquefaction hazard till the results are fully stabilized.

Table 6-6 Selected CPT profiles for liquefaction hazard assessment. For each of them, the hazard analysis has been carried out for the whole range of the random realizations and the whole range of seismic scenarios.

ID	Hcrust (m)	Hliq (m)	Mean CRR	ESP CLASS	SUSCEPTIBILITY LEVEL
M340_CPT10	10.40	7.40	0.116	WLD	HIGH
185140C231	4.15	3.60	0.171	MMM	MEDIUM
185140C263	15.40	4.00	0.259	SMX	LOW
185130U005	2.70	0.20	0.599	RXX	VERY LOW/NO

To acquire a stable result, 5000 random realizations of the input variables, including the groundwater seasonal fluctuation and soil properties variability, are introduced. About the seismic input, nine earthquake scenarios that return period ranges in 30 to 2475 years are defined as bedrock acceleration “ag” (NTC, 2018).

The core of the above-mentioned procedure is represented by the Monte Carlo simulations, in which the following parameters affecting the liquefaction hazard at the study area are considered as random variables:

water table depth, which annual average value ranges in 2.00 m – 3.70 m for the alluvial plain areas of Emilia-Romagna Region, was extracted from the ARPA monitoring surveys carried out between the 2010 and 2018 and shown in Figure 6-27;

a threshold value of the Soil Behavior Type Index IC which allows separating clay-like (i.e., non-liquefiable soil) from sand-like (i.e. liquefiable soil) response has been assumed as a discrete variable sampled from the values of the vector v = [2.4 2.5 2.6 2.7]. The first three values were defined by Boulanger and Idriss (2016), and they have the same probability of being sampled. The same authors also introduce a fitting parameters CFC which can be modelled through a random variable having 0 mean and 0.29 standard deviation (Lai et al., 2020);

the PGA value at the free surface has been evaluated for each realization by combining the seismic hazard of area (http://esse1-gis.mi.ingv.it/) with the site amplification which in turn has been modelled as a function of the Vs,30 measurements. As shown by the USGS Vs,30 global model (https://earthquake.usgs.gov/data/vs30/), the entire study area is characterized by a Vs,30 in the range of 180-240 m/s, which according to the Italian Standards (NTC, 2018) corresponds to a soil class C or D. Like in the previous step, the magnitude Mw has been fixed equal 6.14, (http://zonesismiche.mi.ingv.it/).

An example of the obtained results for the soil profiles of Table 6-6 is showed in Figure 6-29, which relates the expected mean LPI with the seismic intensity (in terms of the return period of the above-defined scenarios). As it was expected, the liquefaction potential in the study area increases proportionally to the PGA being always equal to 0 if the PGA is smaller than 0.15g. Belonging to different susceptibility classes, the selected profiles show a different response to the seismic motion. For instance, the liquefaction phenomenon is not triggered for RXX profiles even by the 2475years return period earthquake (PGA≈0.45g).

Considering that, for RXX profiles, the liquefaction potential index is not influenced by the PGA, the boxplot of Figure 6-30 display in more detail the behaviour of CPTs having low to high liquefaction susceptibility.

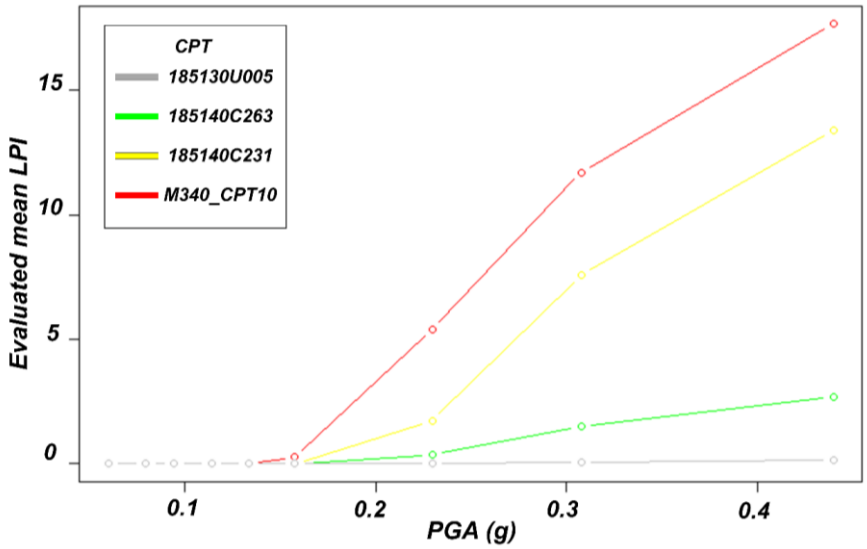

Figure 6-29 Expected mean LPI vs peak ground acceleration for the selected CPT profiles.

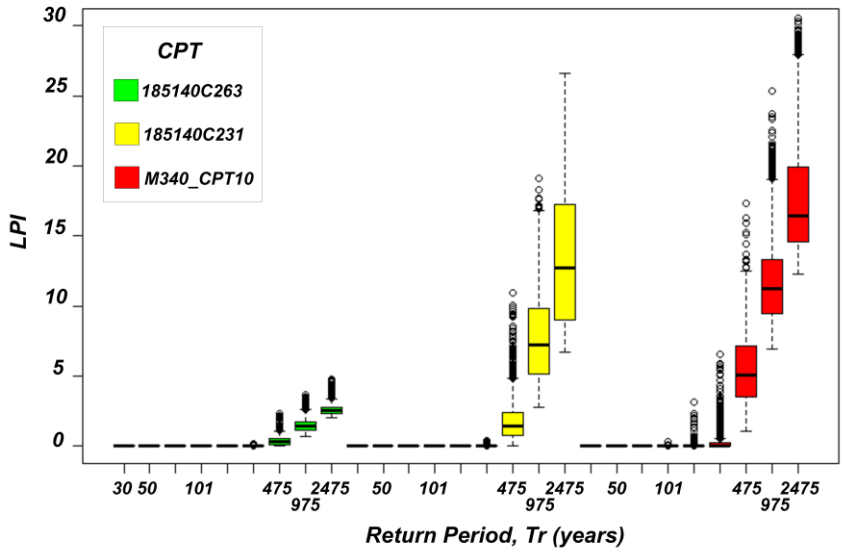

Figure 6-30 Boxplots of the evaluated LPI for each return period on CPT profiles having low (green boxes), medium (yellow boxes) and high (red boxes) liquefaction susceptibility.

Focusing on the total number of weak profiles (red points of Figure 6-11), that represent both a critical situation in terms of liquefaction susceptibility and the most common subsoil class in the study area (68.2% of the total), the before described

procedure has been applied following the steps summarized in the flowchart of Figure 6-31. In this phase, the application of Monte Carlo simulations starting from the modelling of real profile data will allow generalizing the obtained results to an entire class of soil profiles. The basic idea behind this calculation is to generate a great number of subsoil profiles belonging to any susceptibility class able to generalize the expected behaviour of similar deposits (where no CPTs have been executed) in the study area. Taking advantage from such a huge number of simulations, a technical or non-technical user may evaluate in some way the liquefaction susceptibility of a site within the study area (even from in-situ tests different from CPTs) and quantitatively have an expeditious but stable estimate of the relationship between the expected seismic motion and liquefaction potential indicators. This gives the possibility to characterize the liquefaction potential of similar soil profiles located in the study area in probabilistic terms, providing an estimate of the annual probability of reaching or exceed a value of any liquefaction severity indicator.

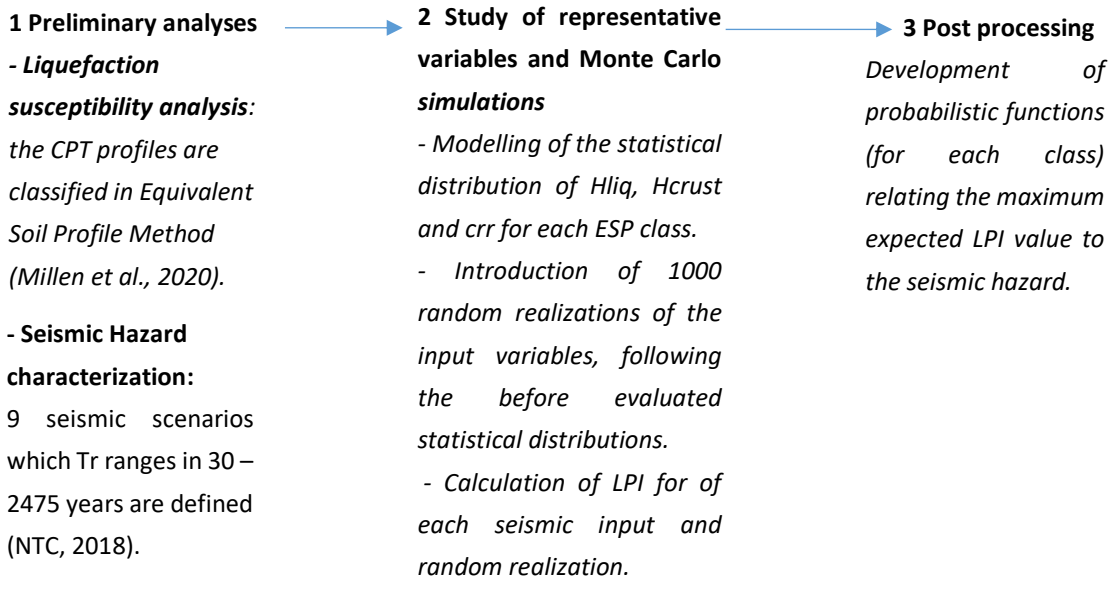

Figure 6-31 Flowchart of probabilistic LPI evaluations based on Monte Carlo analysis.

ESP CLASS	NUMBER OF CPT PROFILES	%
WLD	1	0.20
WLM	2	0.40
WMD	51	10.26
WMM	49	9.86
WMS	5	1.01
WTM	247	49.70
WTD	110	22.13
WTS	32	6.44

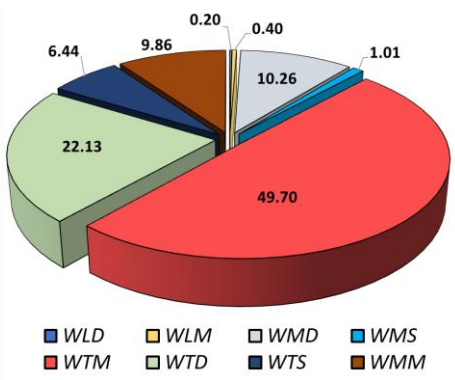

Figure 6-32 Dataset of weak soil profiles in the municipality of Terre del Reno available from the Emilia Romagna archives.

Firstly, the statistical distribution of the profiles belonging to the "Weak" crr-based class has been characterized (Figure 6-32). Due to the paucity of profiles having a "large" potentially liquefiable sandy layer, the two susceptibility classes WLD and WLM have been merged into a unique class.

The preliminary step also includes the characterization of seismic hazard in the study area. With the logic of the previous analysis, the PGA at each CPT location has been determined by combining the motion at rigid base by the site-local amplification. To this aim, a stratigraphic amplification coefficient SS = 1.50 (representative of soil class C) has been introduced, based on the Vs,30 model of the area (https://earthquake.usgs.gov/data/vs30/).

In the following step (step 2 of Figure 6-31), the statistical distribution of representative variables which define an Equivalent Soil Profile has been determined through the Easfit.exe tool (https://easyfit.informer.com/) for each of the 7 classes. In particular, the thickness and depth of potentially liquefiable layer result from the application of Millen et al. (2020) ESP method, while a unique vector storing all the punctual CRR values inside the liquefiable layers has been built for each class of susceptibility. For each variable, the application of the Kolmogorov – Smirnov "KS" and Chi-Square "χ^2" tests allowed to rank the best-fitting distributions which representative parameters are shown in Table 6-7. In addition, the performance of the more widely employed distributions (e.g. normal, gamma..) has evaluated through "KS" and "χ^2" tests to simplify the calculation when they provide an acceptable

confidence level (say $\alpha \geq 0.05$) for at least one of the two tests. Table 6-7 summarizes the obtained results and the adopted distribution for each variable.

Although the small number of CPTs belonging to this new class WLM_WLD (3) and the WMS (5) seems to suggest a lack of data to characterize the statistical distributions, it can be affirmed that in the former case a uniform random variability of the crust thickness and thickness of liquefiable layer inside the boundaries defined by Millen et al. (2020) has been assumed. In the latter situation, 5 is the smallest number of elements that the adopted fitting tool requires to give a descriptive statistic. On the contrary, the number of punctual CRR values stored in the vectors defined for the two classes allowed to make a stable estimate of their distribution. Table 6-7 shows that except for the WTD and WLM/WLD classes, all the values stored in the CRR vectors and the most of H_C and H_L values are normally distributed.

Starting from the evaluated distributions, artificial profiles trying to cover the whole range of variability of the selected variables (i.e. CRR, crust thickness and thickness of the liquefiable layer) have been generated through Monte Carlo simulations, which input parameters are listed in Table 6-7. The calculation implies the introduction of relevant parameters as follows:

- 1000 of combinations of three-layered profiles are introduced assigning a H_{liq} and H_{Crust} which reflect the obtained statistical distribution and the domain of each class defined by the authors of the ESP method have been generated;
- along with the above-defined potentially liquefiable layer, the CRR has been modelled as a random variable having its own distribution and with a step dx = 0,1 m.

Then, the liquefaction potential index "LPI" resulting from the seismic hazard of the district has been calculated on each realization by applying the Boulanger & Idriss (2014) procedure.

Table 6-7 Statistical distribution of crr, Hliq and Hcrust for each ESP class.

ESP CLASS	Variable	Best K-S ranked distribution	Best χ^2 ranked distribution	Adopted Distribution	Parameters
WTS	crr	Gen. Extreme value	Gumbel Max	Normal	$\mu = 0.109$ $\sigma=0.004$
	H_c (m)	Gen. Extreme value	Gen. Logistic	Normal	$\mu = 1.5$ $\sigma=0.4$
	H_{liq} (m)	Weibull	Gen. Gamma	Uniform	lower = 0 upper = 2.10

WTM	crr	Wakeby	Burr	Normal	μ = 0.114 σ=0.01
	H_c (m)	Johnson SB	Johnson SB	Normal	μ = 4.15 σ=1.35
	H_{liq} (m)	Weibull	Erlang	Uniform	lower = 0 upper = 2.00
WTD	crr	Wakeby	Burr	Gamma	α=20.613 β=0.006
	H_c (m)	Beta	Levy	Uniform	lower = 5.20 upper = 19.10
	H_{liq} (m)	Power Function	Wakeby	Gamma	α=2.50 β=0.5
WMS	crr	Beta	Dagum	Normal	μ = 0.1108 σ=0.005
	H_c (m)	Gen. Extreme Value	-	Normal	μ =1.40 σ=0.20
	H_{liq} (m)	Dagum	-	Normal	μ = 4.40 σ=1.05
WMM	crr	Lognormal (3P)	Lognormal (3P)	Normal	μ = 0.119 σ=0.015
	H_c (m)	Gen. Extreme Value	Gamma	Normal	μ =4.70 σ=1.20
	H_{liq} (m)	Power Function	Exponential	Normal	μ = 4.40 σ=1.00
WMD	crr	Log Logistic (3P)	Burr	Normal	μ = 0.12 σ=0.022
	H_c (m)	Weibull	Pearson (4P)	Lognormal	σ=0.291 μ = 2.279
	H_{liq} (m)	Burr	Fatigue Life	Gamma	α=22.20 β=0.1744
WLM_ WLD	crr	Pearson5 (3P)	-	Lognormal	σ=0.164 μ = -2.15
	H_c (m)	-	-	Uniform	lower = 4.1 upper = 10.4
	H_{liq} (m)	-	-	Uniform	lower = 7.00 upper = 14.00

For each ESP class, the obtained distributions of LPI values arising from the seismic hazard of Terre del Reno are listed in the following tables. As an example, the expected LPI values with for WTS profiles (summarized in Table 6-8) are displayed in Figure 6-33, which boxplots show a significative increasing in LPI for seismic return periods at least equal to 475 years, i.e. for a PGA ≥ 0.20g. Considering the most severe event

(Tr = 2475 years), liquefaction almost surely occurs in WTS subsoil since mean LPI is equal to ≈8.

Table 6-8 Expected LPI distribution in the area of Terre del Reno for the ESP class "WTS".

SUSCEPTIBILITY CLASS: WTS						
Tr (years)	**amax (g)**	**Min LPI**	**25 Quantile LPI**	**Mean LPI**	**75 Quantile LPI**	**Max LPI**
30	0.06	0	0	0	0	0
50	0.08	0	0	0	0	0
72	0.094	0	0	0	0	0
101	0.114	0	0	0	0	0
140	0.134	0	0	0	0	0.01
201	0.158	0	0	0	0	1.10
475	0.229	0	0.39	1.3	2.46	6.24
975	0.308	0.58	2.51	4.75	7.05	10.50
2475	0.44	1.47	4.65	8.02	11.30	15.70

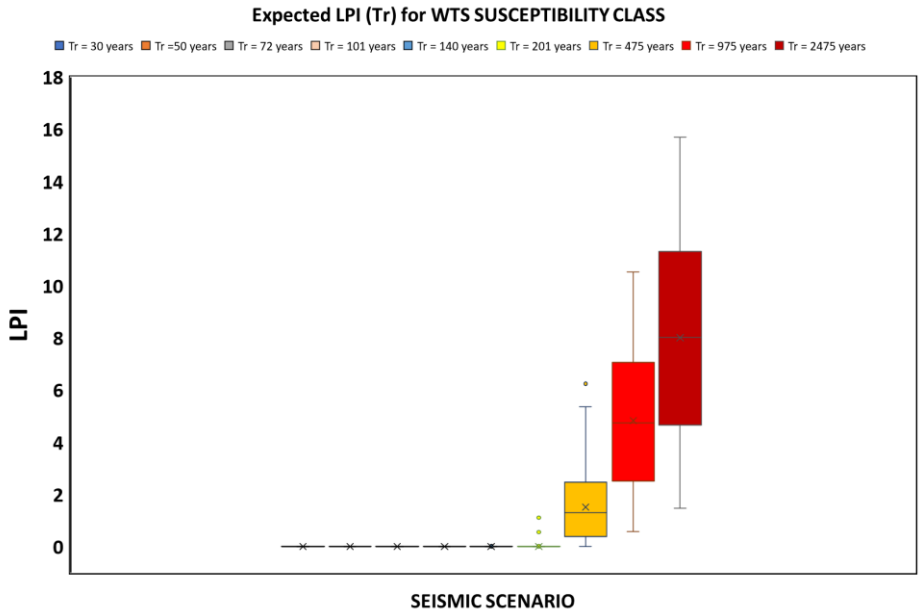

Figure 6-33 Boxplot of the LPI distribution in the area of Terre del Reno for the ESP class "WTS".

In the following Tables, the final overview of LPI distribution for each ESP class in the area of Terre del Reno is presented.

SUSCEPTIBILITY CLASS: WTM						
Tr (years)	**amax (g)**	**Min LPI**	**25 Quantile LPI**	**Mean LPI**	**75 Quantile LPI**	**Max LPI**
30	0.06	0	0	0	0	0
50	0.08	0	0	0	0	0
72	0.094	0	0	0	0	0
101	0.114	0	0	0	0	0
140	0.134	0	0	0	0	0.06
201	0.158	0	0	0.01	0.06	0.27
475	0.229	0.07	1.35	2.4	3.5	4.9
975	0.308	0.68	2.89	4.96	6.78	8.94
2475	0.44	1.12	4.29	7.25	9.76	12.99

SUSCEPTIBILITY CLASS: WTD						
Tr (years)	**amax (g)**	**Min**	**25 Quantile**	**Mean**	**75 Quantile**	**Max**
30	0.06	0	0	0	0	0
50	0.08	0	0	0	0	0
72	0.094	0	0	0	0	0
101	0.114	0	0	0	0	0
140	0.134	0	0	0	0.03	0.25
201	0.158	0	0	0.01	0.06	0.27
475	0.229	0.01	0.26	0.58	1.19	4
975	0.308	0.04	0.63	1.26	2.43	7.14
2475	0.44	0.16	1.04	1.95	3.53	10.8

SUSCEPTIBILITY CLASS: WMS						
Tr (years)	**amax (g)**	**Min LPI**	**25 Quantile LPI**	**Mean LPI**	**75 Quantile LPI**	**Max LPI**
30	0.06	0	0	0	0	0
50	0.08	0	0	0	0	0
72	0.094	0	0	0	0	0
101	0.114	0	0	0	0	0
140	0.134	0	0	0	0	0
201	0.158	0	0	0	0.02	0.43
475	0.229	2.35	4.18	5.56	7.02	13.32
975	0.308	8.02	10.70	13.1	15.41	23.35
2475	0.44	13.57	16.90	20.12	23.35	33.04

SUSCEPTIBILITY CLASS: WMM						
Tr (years)	**amax (g)**	**Min LPI**	**25 Quantile LPI**	**Mean LPI**	**75 Quantile LPI**	**Max LPI**
30	0.06	0	0	0	0	0
50	0.08	0	0	0	0	0
72	0.094	0	0	0	0	0
101	0.114	0	0	0	0	0
140	0.134	0	0	0	0.03	0.16
201	0.158	0	0.14	0.23	0.34	0.78
475	0.229	2.8	4.86	5.68	6.52	9.65
975	0.308	7.2	9.90	11.63	13.17	18.42
2475	0.44	10.49	14.34	16.99	19.19	27.88

SUSCEPTIBILITY CLASS: WMD						
Tr (years)	**amax (g)**	**Min LPI**	**25 Quantile LPI**	**Mean LPI**	**75 Quantile LPI**	**Max LPI**
30	0.06	0	0	0	0	0
50	0.08	0	0	0	0	0
72	0.094	0	0	0	0	0
101	0.114	0	0	0	0	0
140	0.134	0	0	0.03	0.08	0.27
201	0.158	0	0.14	0.28	0.45	1.23
475	0.229	0.15	1.92	2.95	4.02	6.92
975	0.308	0.58	4.27	6.15	7.85	12.34
2475	0.44	1.13	6.40	9.08	11.33	18.4

SUSCEPTIBILITY CLASS: WLM_WLD						
Tr (years)	**amax (g)**	**Min LPI**	**25 Quantile LPI**	**Mean LPI**	**75 Quantile LPI**	**Max LPI**
30	0.06	0	0	0	0	0
50	0.08	0	0	0	0	0
72	0.094	0	0	0	0	0
101	0.114	0	0	0	0	0
140	0.134	0	0.01	0.04	0.08	0.28
201	0.158	0.07	0.41	0.60	0.82	1.70
475	0.229	3.59	6.08	7.84	9.70	13.63
975	0.308	8.17	12.26	15.63	18.89	24.74
2475	0.44	12.23	17.93	22.45	27.18	36.8

The plots of Figure 6-34 and Figure 6-35 summarize the relationships between the PGA and maximum LPI for the 7 subclasses of “Weak” profiles. Despite the high/very

high liquefaction susceptibility of these subsoils, liquefaction is never triggered for PGA ≤ 0.15g. Conversely, when the seismic motion is sufficiently strong to trigger liquefaction (say PGA > 0.15), significative differences in the subsoil response exist among the susceptibility classes.

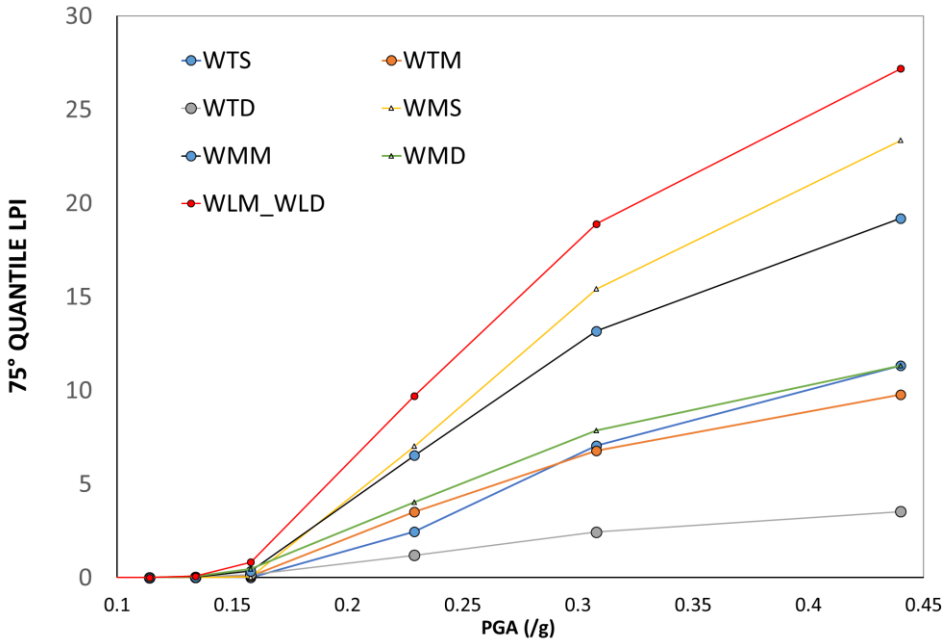

Figure 6-34 Expected 75quantile of LPI values for each susceptibility class given the seismic hazard of the area.

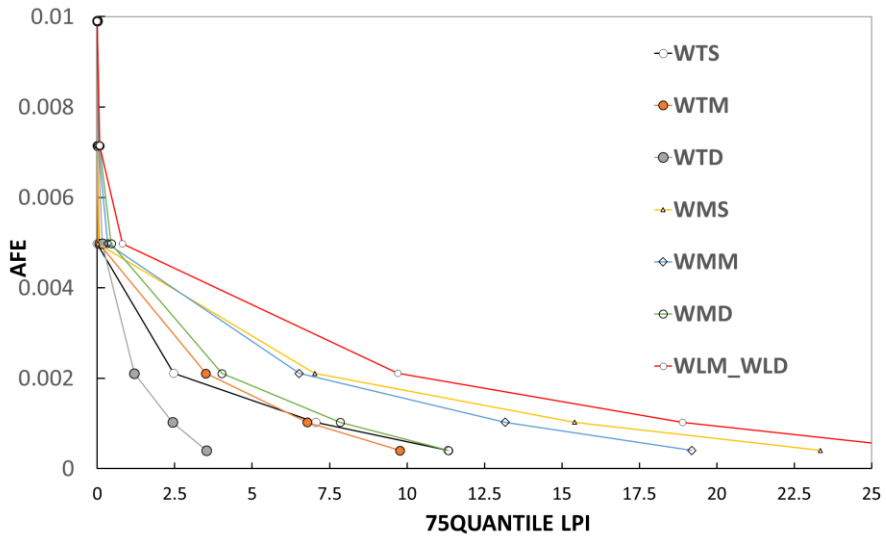

Figure 6-35 75quantile of LPI vs annual Frequency of exceedance for the analysed ESP classes.

In conclusion, the obtained results in the municipality of Terre del Reno show that: looking at the most susceptible subsoil classes i.e., WLM_WLD, the annual frequency of exceedance for LPI=5 is equal to 0.004, which approximately corresponds to 20% in 50 years (Figure 6-35). In this situation, the obtained result suggests performing for WLM_WLD subsoils more detailed geotechnical and structural investigations in any design analysis aimed at evaluating the cost/benefit analysis of a liquefaction countermeasure.

6.7 **Liquefaction Risk Assessment**

The methodology recalled in Figure 4-14 has been firstly tested on residential dwellings against the 20th May 2012 Earthquake scenario, then applied to residential and industrial buildings following the convolutive integral of the PBEE. As done for the Christchurch case study, building typology and characteristics together with subsoil composition and properties for the municipality of Terre del Reno have been managed in a GIS platform, which allowed to characterize the spatial distribution of relevant variables as well as to localize the expected damage and compare estimates with the post-earthquake surveys.

6.7.1 Typology, characteristics and damage on buildings

The study area highlighted in Figure 6-36 includes the urban districts of Sant'Agostino, San Carlo, and Mirabello, mostly constituted of poor unreinforced masonry 1-2 stories buildings representing 90% of the total building portfolio. The urban development of the villages of Sant'Agostino, San Carlo, and Mirabello has been analyzed in the present work by digitizing the information obtained from aerial photos (flights of 1954, 1994, and 2008) and crossing them with land use maps drawn up in 1976 and 2003. Buildings showed in Figure 6-36 are reported with different colors depending on their construction period. As can be seen, the three aggregates developed similarly, with a certain temporal continuity up to 1994. However, most of the buildings date back to 1976, with many buildings already present in 1954. Only a limited number of buildings, mostly located in the peripheral areas, were constructed after 1994-2003. The detailed examination of the built heritage carried out by

consulting ISTAT databases (https://www.istat.it/) National Geoportal (http: //www.pcn.minambiente.it/mattm/service-wms/) and of the Emilia-Romagna Region (http://geoportale.regione.emilia-romagna.it/it/mappe), reveals that most of them are masonry, except in more recent cases where reinforced concrete constructions prevail. Anyway, almost all buildings considered have been designed with seismic regulations not adequate for the latest standards.

To assess the consistency of the Terre del Reno building heritage, the databases of the Emilia-Romagna Region (http://servizigis.regione.emilia-romagna.it) and the aerial photography available in the National Geoportal were firstly consulted (http: // www.pcn.minambiente.it/mattm/) which respectively report general information on the geometry (area, average height), intended use (residential, industrial, cultural/educational, etc.) and the historical urban development of the three villages (Figure 6-36).

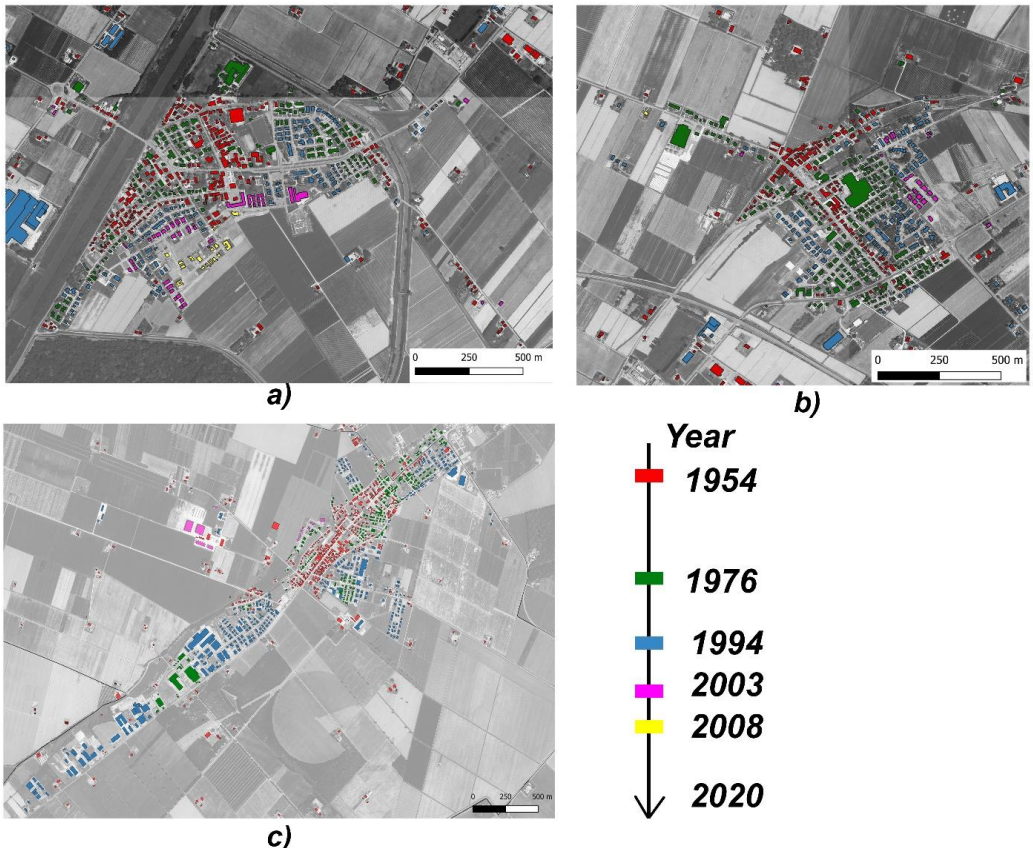

Figure 6-36 Building's constructions in the municipalities of S. Agostino (a), S. Carlo (b), and Mirabello (c) are classified according to their period of construction after the analysis of (1954, 1994, 2008) aerial photography and (1976 and 1994) land use maps.

Subsequently, the MUDE, FENICE, and SFINGE databases of the Emilia-Romagna Region (http://www.regione.emilia-romagna.it) were consulted to estimate the damage that occurred during the seismic sequence of May-June 2012. They were respectively established for civil, public, and industrial buildings. Concerning private residential buildings, the MUDE platform contains the technical report managing the reconstruction, the post-earthquake damage surveys according to the AEDES format (AEDES - Baggio et al., 2009 datasheets), and the photographic documentation of the damaged building (Figure 6-39).

6.7.2 Assessment of liquefaction-induced building damage

The interaction of liquefaction effects with human-made structures was particularly strong, especially in the village of San Carlo, where many buildings, roads, fenced walls and lifelines were severely affected, and damaged by fractures and liquefaction-induced phenomena. Notably, a high percentage of the water wells in the area were filled by the liquefied sand, often up to the top. The ejected sand (liquefaction and fracture/liquefaction category) was mainly grey medium-to-fine sand and, but in minor amounts, hazel sand, suggesting that liquefaction could come from two distinct layers. Immediately after the seismic sequence of May-June 2012, the Emilia-Romagna Region, in collaboration with technicians, engineers, and the Department of Civil Protection coordinated more than 40 000 inspections to assess the safety of buildings through the Aedes board format (Servizio Geologico, Sismico e dei Suoli 2012).

In this study, the liquefaction-induced damage on residential buildings was classified through by analyzing post-seismic surveys (Aedes format) and over 400 Mude reports relating to buildings that required contributions for reconstruction following the 2012 earthquake. In fact, the Mude platform was established by the Emilia Romagna Region (https://www.regione.emilia-romagna.it/terremoto/mude-modello-unico-digitale-per-ledilizia) to manage with the same procedure the building repair or reconstruction and the request for contributions. At the time of carrying out this study, the number of claims for damages concerning private buildings in the Municipality of Terre del Reno was 402. For each of these practices, the available documentation was examined with the scope of assessing the damage level, distinguishing the shaking-induced contribution from the effects of liquefaction. This analysis has purely scientific purposes, and its results must be framed in a statistical context and not referred to individual cases, especially considering the limited

information available. Concerning the shaking-induced building damage, the classification proposed by the European Macroseismic Scale (EMS-98) shown in Figure 6-37a was used to quantify the level of damage experienced by any building. In contrast, the criteria proposed by van Ballegooy et al. (2014) for the Christchurch Case study were herein adopted to quantify the liquefaction-induced damage typology and severity. In most cases, the observed damage was alternatively attributable to one of the two types; where the buildings showed both types of damage, the liquefaction rate was qualitatively estimated as reported in the table in Figure 6-37b.

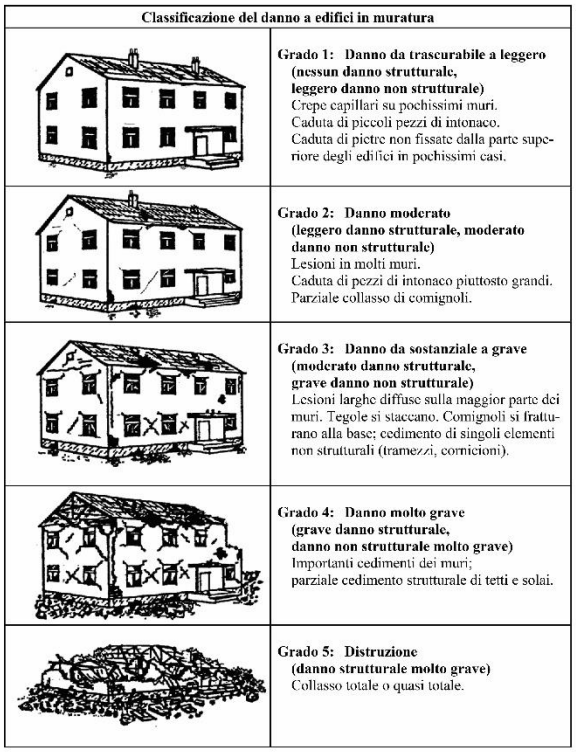

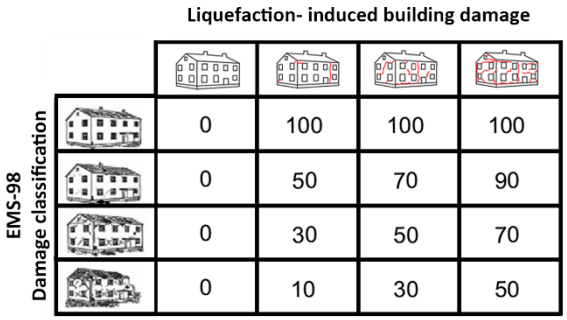

Figure 6-37 Classification of shaking-induced building damage from the European Macroseismic Scale (EMS-98) (a) and matrix showing the percentage of liquefaction-induced economic losses on buildings that have suffered resulting damage from the combination of the two phenomena (b).

One of the key points in damage database creation is distinguishing the liquefaction-induced damage from the shaking-induced and combined damage. To this aim, technical and photographic reports of surveyed buildings provided a helpful tool to support the judgment. The overall pattern of liquefaction induced damage on dwellings, obtained from detailed engineering judgment of the technical reports, is

showed in Figure 6-39. The damage classification shows that buildings in Sant'Agostino experienced slight/moderate damage. In contrast, severe and moderate/severe liquefaction-induced building damage was respectively observed in the districts of S. Carlo and Mirabello. The major evidence of liquefaction-induced damage in the municipality of Terre del Reno are the presence of sand ejecta and cracks on the basement floor, building rotation, differential and absolute settlements (Figure 6-39).

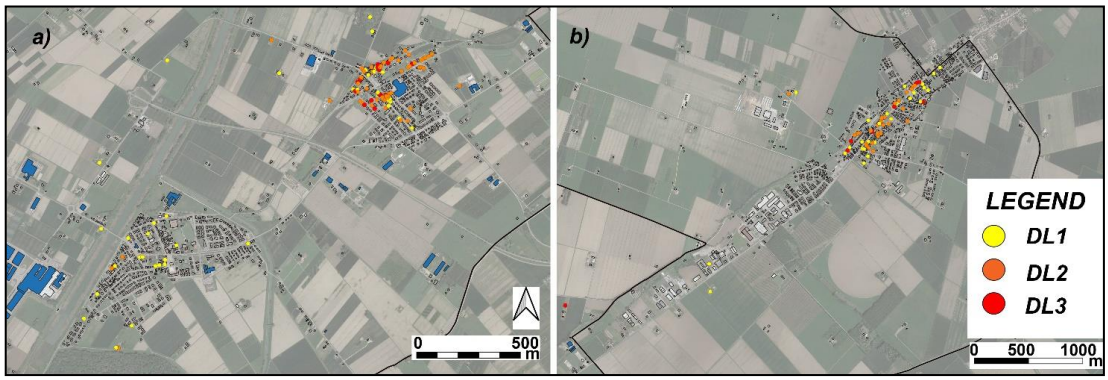

Figure 6-38 Mapping of the observed liquefaction-induced building damage assessed through the van Ballegooy et al. (2014) criterion for the districts of S. Agostino and S. Carlo (a) and Mirabello (b).

Figure 6-39 Examples of the most typical liquefaction-induced building damage in the municipality of Terre del Reno.

The adopted damage classification, aimed at distinguishing the liquefaction-induced damage from the shaking induced, allowed to quantify at the municipality scale the overall economic damage from liquefaction. This analysis results are summarized in Figure 6-40 for each of the three villages of Sant'Agostino, San Carlo, and Mirabello, accounting for the sums paid for the reconstruction as of December

2018. The pie charts of Figure 6-40 reflect the damaging trend outlined in Figure 6-38, being the liquefaction-induced damage more severe in San Carlo and Mirabello villages, respectively 89% and 56% of the total, and less huge in Sant'Agostino (24%).

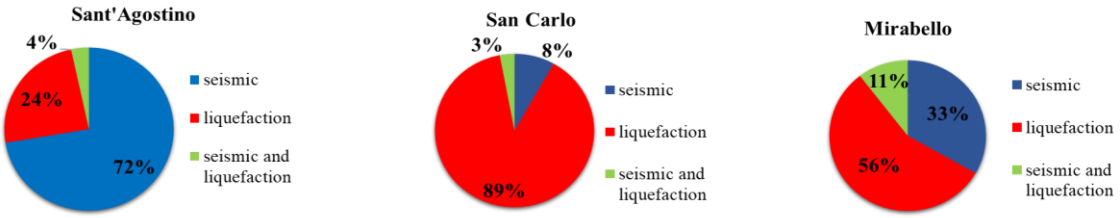

Figure 6-40 Once the data was collected, a statistical analysis of the costs was carried out, considering separately the three districts of S. Agostino, S. Carlo and Mirabello.

6.7.3 Subsoil composition and properties

In the present analysis, around 800 Cone Penetration Test (CPT) profiles extending below 8 m depth from the ground surface and uniformly distributed over the studied territory have been considered. Such a density of territory coverage with subsoil data enables reconstruction with enough accuracy in distributing the different variables over the territory. Additionally, the Equivalent Soil Profile method's application has demonstrated consistency with the three layers model hypothesis in the study area since the normed error is less than 0.15 for the 99% of the profiles.

6.7.4 Estimate of damage on residential buildings

The above considerations led to the definition of the methodology for the analysis of damage to buildings based on the steps described below.

- Characterization of building stock (geometry, number of stories, model building type based on the construction period, use);
- Subsoil modeling below each building: the three-layer model was schematized through the application of the ESP method (Millen et al., 2020), while the Liquefaction Severity Number LSN (van Ballegooy et al., 2014) and the consolidation settlement wv (Zhang et al., 2002) at the building centroids were obtained after geostatistical interpolation;
- Calculation of the shear-induced settlement "w_s" with formula proposed by Bray and Macedo, (2017) and of the total absolute settlement "w_{max}". In this

phase, the term "w_e" of Eqn. 3.23, i.e., the contribution to the settlement of the ejecta material, has been neglected since difficult determination.

- Evaluate the differential settlement as a percentage of the absolute settlement by using Eqn. (4.5), where α is assumed to be equal to the median value (0.54);
- Estimate the probabilities corresponding to each damage level with the fragility curves proposed by Fotopoulou et al. (2018). Since these curves refer to reinforced concrete buildings, while the analysis carried out also concerns masonry buildings, the median values provided by the authors were modulated, leaving them unchanged for buildings built after 1976, as presumably made of reinforced concrete, and scaling by a factor of 3 for buildings before that date, presumably masonries. This factor is assumed to equal the ratio between the Eurocode's acceptable angular distortions for reinforced concrete and masonry buildings (ENV1997, 2004).
- compute the Mean Damage Rate (*MDR*) with the loss factors for each damage level expressed in Table 4-4 (FEMA, 2003).

Regarding Terre del Reno's residential buildings, the potential of liquefaction-induced building damage provoked by the 20th May 2012 Earthquake has been assessed by applying the analytical procedure before summarized, which expected physical impact is displayed in Figure 6-41 in terms of MDR (Eqn. 4.6).

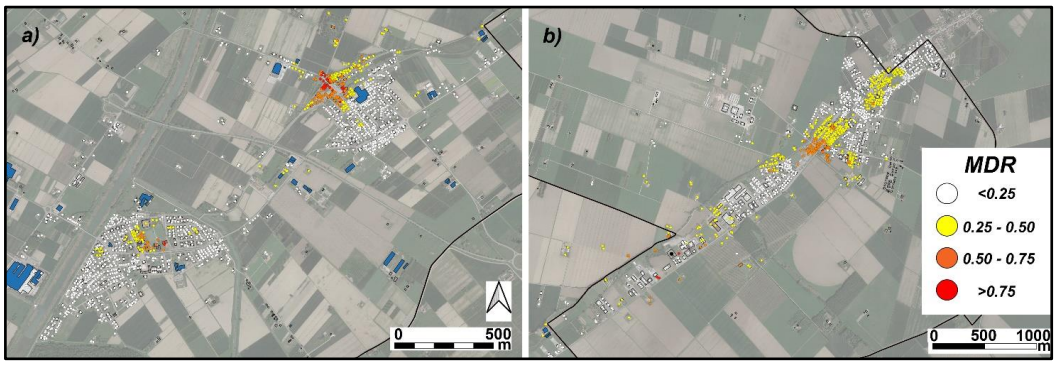

Figure 6-41 Expected Mean Damage Rate on residential buildings for the 20 may 2012 Earthquake scenario in the districts of S.Agostino/S. Carlo (a) and Mirabello (b).

It can be observed that the spatial distribution of expected liquefaction-induced physical damage on the entire municipality reflects the damage observations previously described (Figure 6-38). In the following paragraph, a quantitative assessment of such correlation is presented.

6.7.5 Validation

As for assessing liquefaction ground severity in free field conditions, the statistical test proposed by Kongar et al. (2015) has been herein implemented to validate the effectiveness of the applied methodology in forecasting the liquefaction-induced structural damage. In such a case, the test consisted of attempting a correlation among the liquefaction-induced damage and the expected mean damage rate, with a variable threshold. In fact, the mean damage rate represents a proxy of liquefaction-induced physical impact on structures and results from the evaluation of a differential settlement combined with the fragility model proposed by Fotopoulou et al. (2018). The area under the curve "AUC" has been evaluated for the building affected by minor, moderate, and major damage. Also, for each of the threshold values, the Matthew correlation coefficient *"MCC"* (Matthews, 1975) has been calculated.

Considering that the consistency of the three-layer model has been proven on the entire study area, the validation test has been applied over the entire building database: the evaluated building settlements have been related to the liquefaction-induced damage classification, which has been assessed from post-earthquake rapid inspections and detailed engineering evaluations available in the "Mude" platform. This analysis gives a reasonable distribution of the true positives, and false negatives as a function of the thresholds assumed for settlement. In fact, considering that better predictive models locate points of the ROC curve towards the top left of the plot, the AUC is a generalized measure of model quality, assuming no specific threshold. The plot's diagonal is equivalent to random guessing (AUC = 0.5), while AUC = 1 is a good prediction. In this case, for each of the considered damage levels, AUC results generally are greater than 0.50. Thus, the obtained results show a good correlation between the event and selected variables.

These results indicate a variable capability of the proposed method to capture observation, being the ROC curves higher than the plane bisecting line, but with variable distances. The prediction is not particularly exciting for minor damage level (Figure 6-42), possibly because of a subjective, not clearly and uniquely identifiable, recognition of buildings' injuries that smooths the border between positive and negative occurrences. However, when looking at the overall success of prediction, i.e., the percentage of correctly predicted cases, an OSR value equal to 65.8% is obtained even for this class. The quality of prediction increases noticeably with the damage level, which means that a stronger relation exists between MDR and damage, as

confirmed by the increasingly higher values of the decision threshold and the Overall Success Rate.

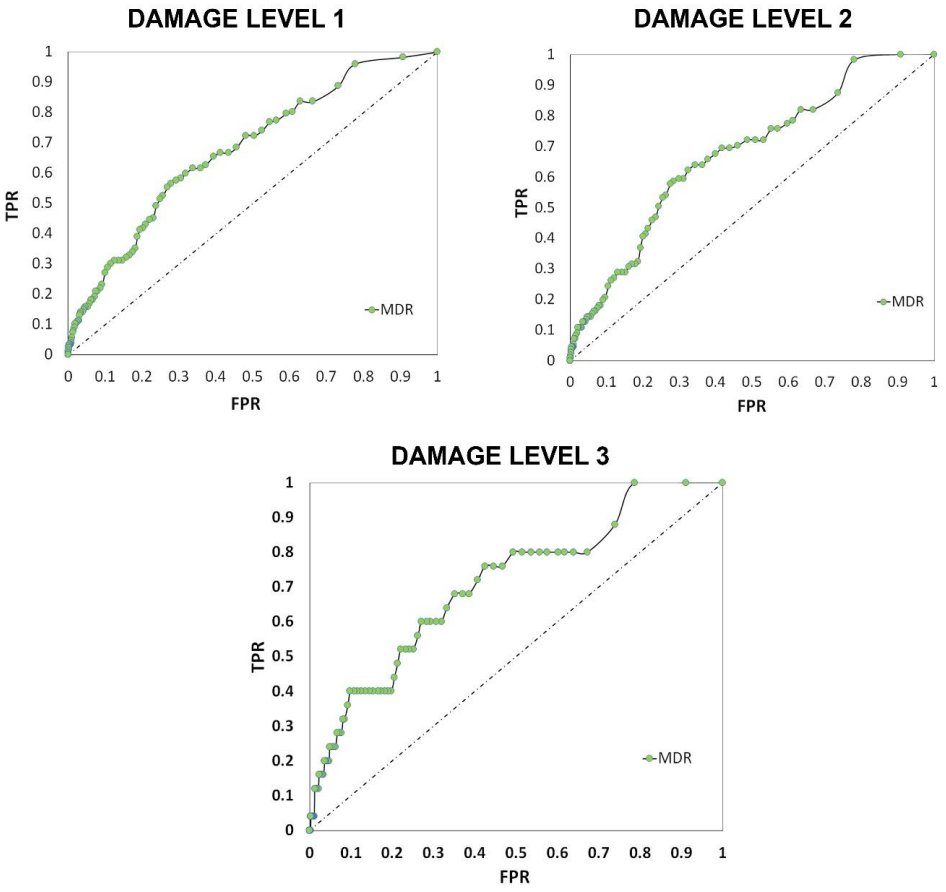

Figure 6-42 ROC curves evaluated by matching the predicted MDR to the liquefaction-induced damage on residential buildings that underwent minor (Damage Level 1), moderate (Damage Level 2) or severe (Damage Level 3) during the May 20th, 2012 earthquake.

Table 6-9 Output of the Kongar et al. (2015) validation test for the prediction of damage on residential buildings.

Damage Level	AUC	OPTIMAL MDR THRESHOLD	TPR	FNR	TNR	FPR	OSR (%)	OFPR (%)	OFNR (%)
Minor	0.69	≈0.20	0.62	0.38	0.66	0.34	65.8	31.9	2.3
Moderate	0.68	≈0.30	0.58	0.42	0.73	0.27	71.9	26.5	1.6
Severe	0.73	≈0.45-0.50	0.40	0.60	0.90	0.10	89.7	9.8	0.5

6.8 Application of the PBEE Methodology

After the procedure has been applied and tested against the 20th May 2012 Earthquake, a probabilistic risk analysis is here conducted for both civil and industrial buildings of Terre del Reno considering the area's seismic hazard. According to the PBEE Methodology described in detail in Section 4, the liquefaction risk on residential and industrial buildings has been assessed in probabilistic terms following the step summarized in the flowchart of Figure 6-43.

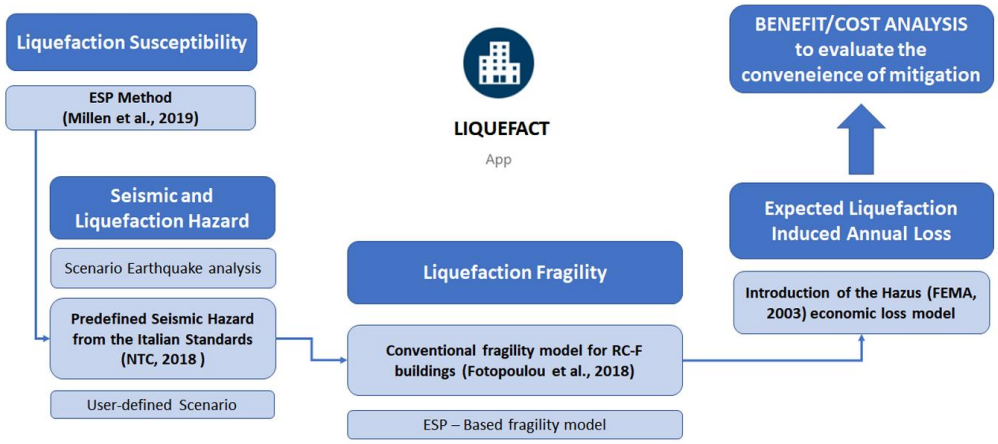

Figure 6-43 Flowchart of the procedure to evaluate the impact of liquefaction on residential and industrial buildings, modified from Liquefact Project (D7.3).

The seismic hazard is determined according to the approach defined in the Italian Standards (NTC, 2018): four different scenarios, corresponding to return periods between 30 and 975 years, which result from the definition of the limit states of construction regulations for a reference period VR of 50 years are introduced. As explained above, the seismic intensity measures used in the procedure (CAV,dp, and Sa1.0) were obtained by scaling the accelerogram of the 20th May 2012 event with respect to each considered event's PGA. For each scenario, the absolute liquefaction-induced building settlements, the differential settlements, the probabilities corresponding to each damage level were calculated with the fragility curves of Fotopoulou et al. (2018), scaling the medians based on the type of building (masonry, reinforced concrete). In this step, the error propagation theory has been introduced to

assess the physical impact on structures resulting from the whole distribution of differential settlements.

In evaluating the maximum absolute building settlement, great emphasis has been assigned to the lateral spreading in the areas of paleo-embankments since post-seismic observations outlined this phenomenon as the main responsible for structural damage. Hence the generalized LD indicator is herein introduced in the Bray & Macedo (2017) Eqn. 3.24 instead of the LSN, to emphasize the contributions of lateral displacements in areas where severe lateral spreading was experienced during the 2012 Emilia Earthquake Sequence. Since a ratio among GLD and LSN is approximately equal to 3 in the study area, from Eqn. 3.23 it is legitimate to expect a more severe liquefaction-induced building settlement when the GLD is considered. As an example, Figure 6-44 shows the location of buildings that are expected to collapse for a 475 and 975 years return period seismic scenario.

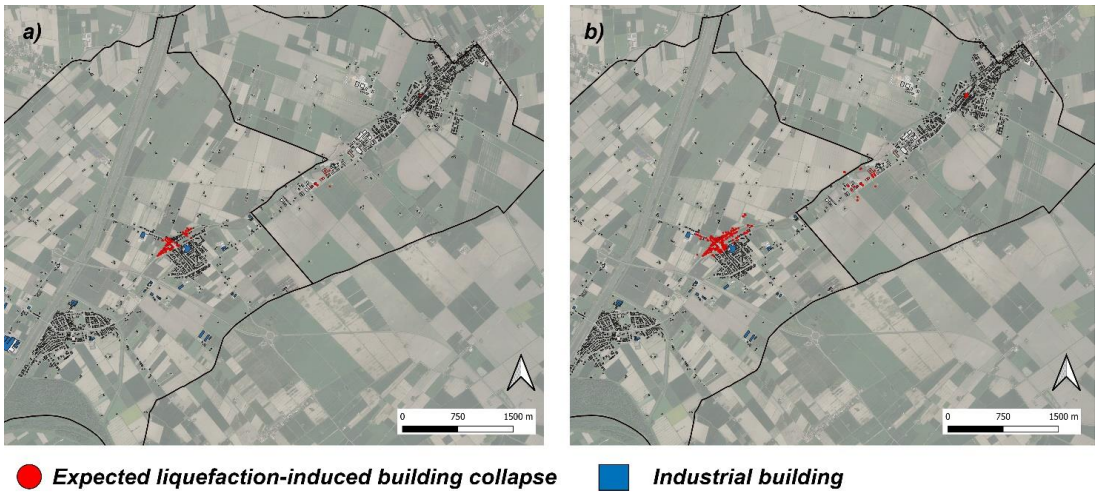

Figure 6-44 Expected liquefaction-induced building collapse for a 475 years (a) and 975 yeas (b) return period scenario.

Then, the loss factors of Table 4-4 have been associated with the Fotopoulou et al. (2018) expected damage levels to estimate the MDR on each building with the logic proposed by Hazus (Fema, 2003). The MDR evaluation on an annual basis, representing the ratio among the expected liquefaction – induced building damage and the total reconstruction cost, is carried out by convoluting the MDR resulting from all the seismic scenarios, each multiplied by the inverse of the earthquake return period.

The obtained annual MDR on Terre del Reno building stock, which provides a proxy of liquefaction risk, is shown in Figure 6-45.

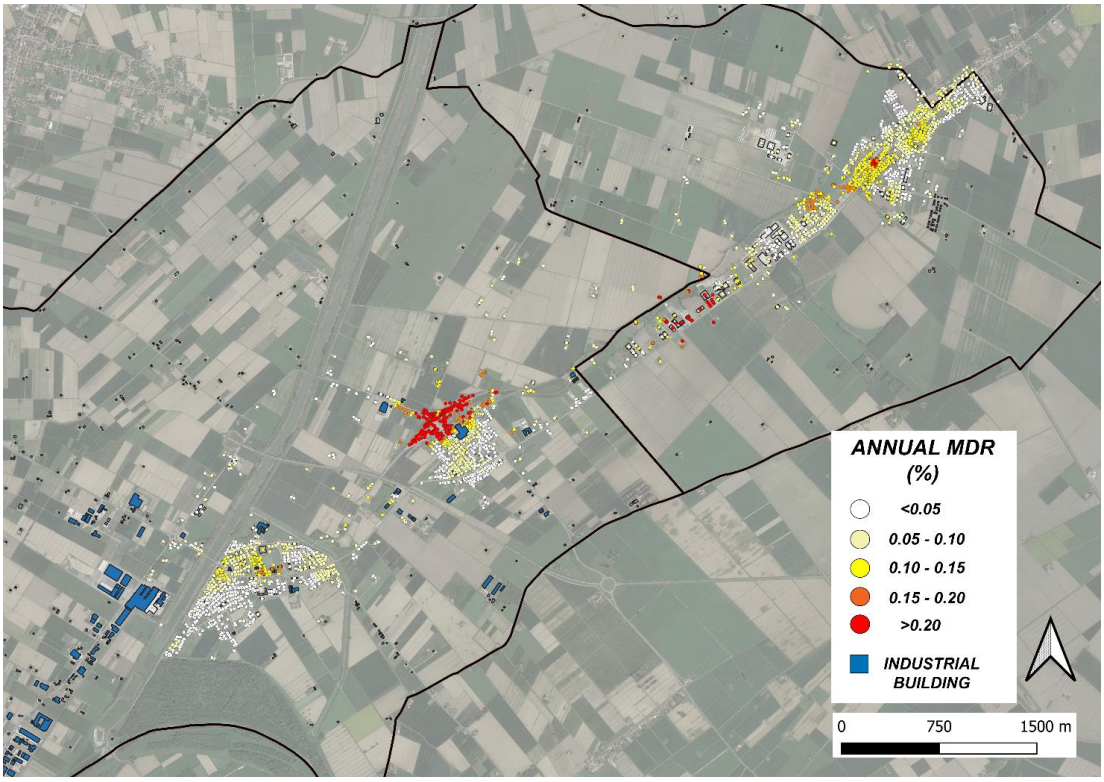

Figure 6-45 Mean Damage Ratio on residential buildings for the above defined seismic hazard.

The following benefit/cost analysis has required to explain the demolition/reconstruction and loss of income terms. Concerning the former, a cost of demolition and reconstruction (RC) equal to 2 500.00 €/m^2 was assumed for residential buildings. Such amount is obtained from the examination of Mude technical reports and corresponds to the average contribution allocated for repairing buildings damaged by liquefaction in the study area. On the other hand, the cost associated with the loss of income of the *INCi* structure, which for residential buildings means the rental of another property for the period of non-use, was estimated on a monthly basis equal to 6.00 €/m^2. For a given seismic scenario, the total liquefaction-induced economic loss and the corresponding annualized risk obtained from the product of the total economic loss and the frequency of occurrence of the earthquake (1 / Tr) were quantified. Finally, the total liquefaction risk on civil buildings resulting from the considered seismic hazard is computed by the sum of the corresponding annualized risks. Once the liquefaction risk was determined on an annual basis, the economic convenience of four

different possible mitigation interventions was assessed using the criteria of the benefit/cost analysis, assuming unitary costs of treatment ranging from 25.00 - 100.00 €/m^3. For each of them, the total amount to be invested in mitigation was assessed as the product of the intervention's unitary cost for the volume of land to be treated. The latter was quickly calculated for each building by multiplying its footprint area by the thickness of the potentially liquefiable layer evaluated in the building's centroid.

Having therefore defined the benefit on an annual basis as a risk reduction, for the purposes of the benefit/cost analysis, the expenditure related to mitigation was also annualized. Considering the unit cost of the generic land improvement technique, the depreciation of the invested capital was initially assessed over a time horizon of 30 years, considering this as the residual average life of the buildings and applying an average annual interest rate of 3%. In these hypotheses, the buildings on which it is convenient to intervene are highlighted in Figure 6-46. Assuming that, regardless of the cost, each of the techniques effectively reduces the risk of liquefaction, the number of buildings on which it is convenient to carry out the treatment is inversely proportional to the cost of the same. In fact, as can be seen from Figure 6-46, mitigation is convenient for a greater number of buildings if its cost is low or very low (let's say less than 50.00 €/m^3), while it becomes less attractive for higher costs. In particular, due to the higher costs considered (100.00 € /m^3), only the buildings for which the risk, outlined in Figure 6-45, is substantial, show an economical convenience of mitigation.

On the contrary, for dwellings not affected by such a high level of risk, it is less convenient to invest in land consolidation. For these buildings, other solutions could be considered, such as taking out insurance policies that implie the tolerance of a certain risk level. In this case, the risk analysis procedure implemented offers the possibility to establish the cost of the award to be awarded to each building. However, it should be pointed out that this outcome is purely indicative since it is based on average values introduced in the analysis and that the results could differ significantly if the considered building has other characteristics (residual useful life, reconstruction costs, etc.) or the element at risk is higher like for buildings of cultural heritage.

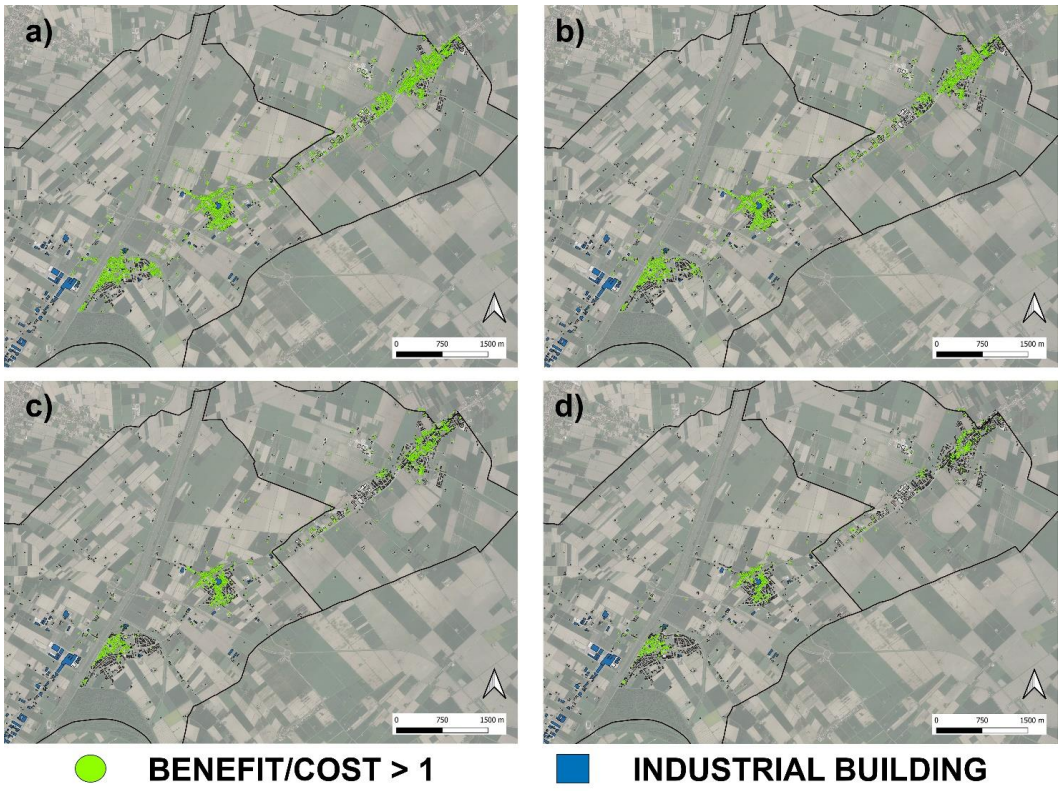

Figure 6-46 Benefit/cost analysis for different mitigation solutions: a) mitigation cost equal to 25.00 € /m^3; b) mitigation cost equal to 50.00 €/m^3; c) mitigation cost equal to 75.00 €/m^3; d) mitigation cost equal to100.00 €/m^3.

6.8.1 Liquefaction risk assessment on a small industrial district

With reference to the industrial district of S. Agostino highlighted in Figure 6-47, the liquefaction-induced economic loss resulting from the seismic hazard of the area has been evaluated. In a preliminary step, the database of industrial buildings has been created; it includes 40 structures belonging to the 12 largest companies, whose annual revenues range between 5 and 60 million euros (https://www.reportaziende.it/emilia_romagna).

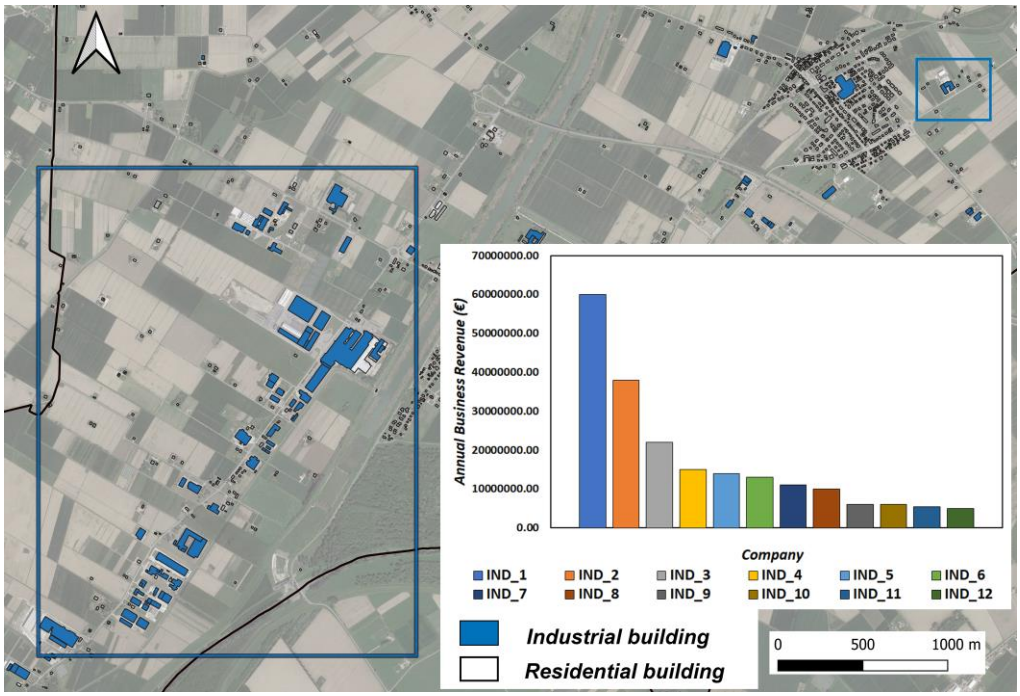

Figure 6-47 The industrial district of Sant'Agostino and annual revenue of the considered factories.

Other information required for risk assessment (i.e. ID, location, footprint area, height, MBT) is collected in addition to the annual business revenue. Conversely, in the absence of a detailed evaluation of the contents (equipment, machinery, etc.), for each company, this value has been assumed equal to half of its annual business revenue.

Given the above-mentioned subsoil modeling, for each scenario, the absolute liquefaction-induced building settlements have been evaluated through Eqn. 3.23. Following the approach of Figure 4-14, the liquefaction-induced physical impact in

terms of MDR has been estimated on each industrial building by combining the Bray and Macedo (2017) method with the fragility model defined by Fotopouolu et al. (2018). In this calculation, the error propagation theory has been employed to better account for subsoil spatial variability and their inference in the result. Finally, like residential buildings, the annual MDR has been evaluated considering the return period of the selected seismic scenarios.

The next step concerns the evaluation of the liquefaction-induced total loss on an annual basis. If compared to the application of the Hazus methodology for residential dwellings, the main difference is that for business activities, the loss of functionality (which includes the loss of income/loss of market, need of relocating the activity) and the damage on instruments are much more impacting than the cost of structural damage. For the selected buildings of Figure 6-47, the reconstruction and utility loss costs have been respectively calculated by applying Eqn. 4.7, and 4.8. As done for residential buildings, again, the reconstruction cost per square meter (RC_i) has been derived from the analysis of industrial building damage reported in dedicated regional Platforms (https://openricostruzione.regione.emilia-romagna.it/ricostruzione-attivitaproduttive). This value has been quantified approximately in ≈1'000,00 €/m^2, which corresponds to the averaged amount paid by the Emilia Romagna Region for rebuilding industrial structures in the selected district, broadly includes the costs of structural and nonstructural (i.e., instrumental) damages. On the other hand, the fraction of damaged stock and the utility loss costs (Eqn. 4.7 and 4.8) are related to the business annual revenue.

As a proxy of liquefaction risk on the industrial district of S. Agostino, the liquefaction-induced annual loss, respectively divided by the annual business revenue and by the total reconstruction cost and are showed in Figure 6-48 and Figure 6-49. These ratios reflect the susceptibility of the area, being the district of S. Carlo and Mirabello the most prone to liquefy. The results of probabilistic liquefaction risk assessment showed in Figure 6-48 and Figure 6-49 suggest a low liquefaction risk in the study area being the expected annual loss respectively lower than 1-1.5‰ of the annual business revenue and in the range of 0 – 10% of the total structural reconstruction cost.

On the other hand, past studies adopting traditional fragility models for low rise and low code RC-F buildings (Syner-G fragility function manager, http://www.vce.at/SYNER-G/) and illustrated in Liquefact D7.3 (2019) highlighted for the selected industrial area a seismic risk 10 times higher than liquefaction one.

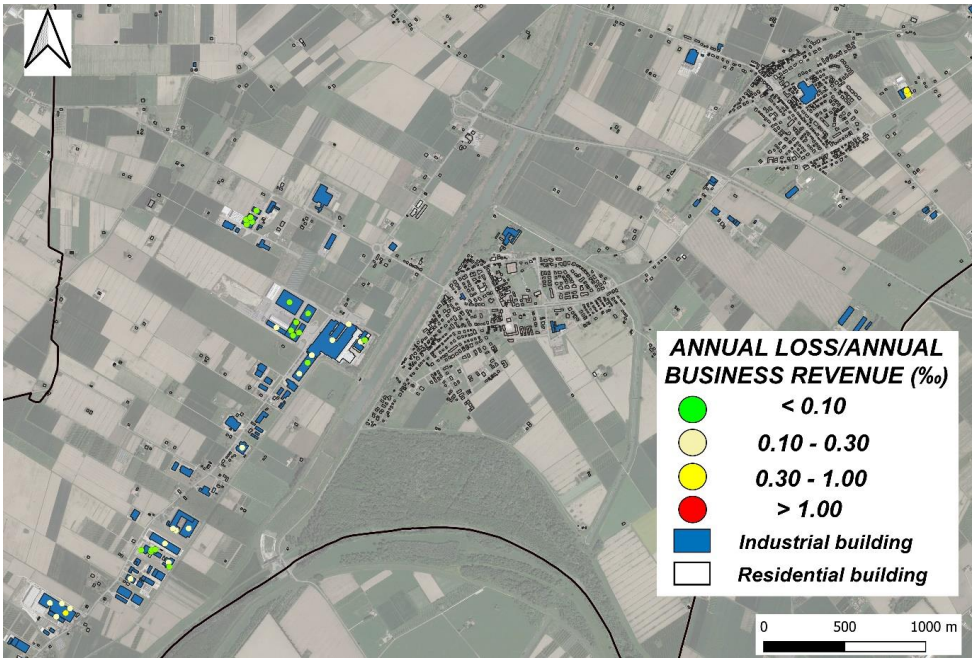

Figure 6-48 Map reporting the estimated liquefaction risk for industrial buildings in terms of annual loss/annual business revenue.

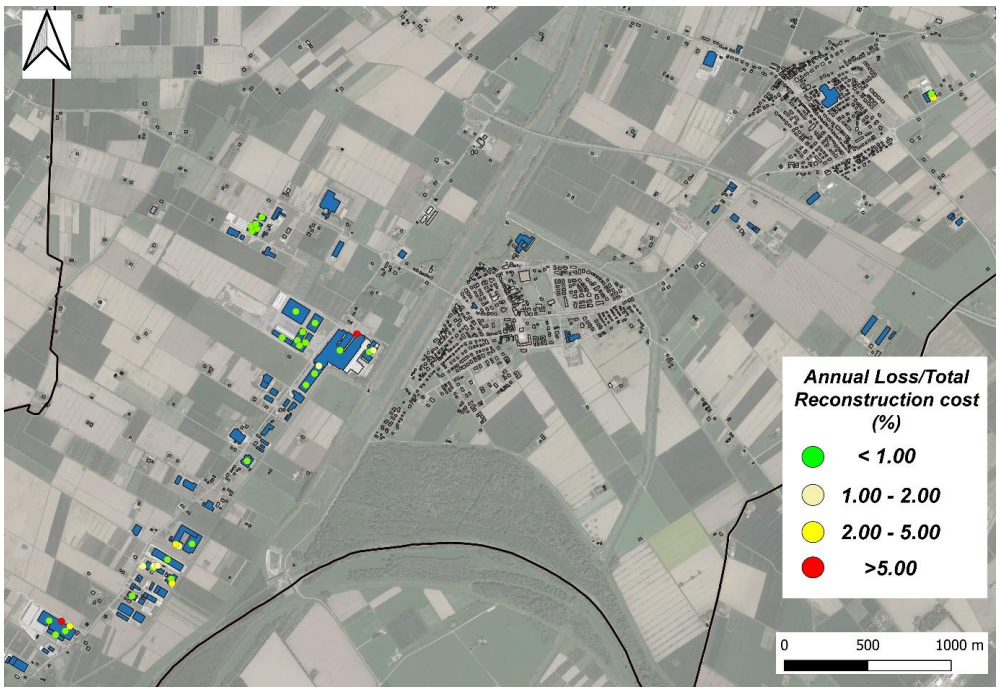

Figure 6-49 Map reporting the estimated liquefaction risk for industrial buildings in terms of annual loss/building reconstruction cost.

Despite the moderate liquefaction risk on the selected industrial district (Figure 6-48), the applicability of any mitigation option may be convenient if considering the annual revenue of the considered activities. And therefore, this opportunity has been evaluated through a benefit/cost analysis, based on the same approach adopted for residential buildings. In particular, various mitigation solutions have been considered over a 30-years' time-horizon, assuming a 3% mortgage rate for the annualized cost-benefit analysis. As observed for residential buildings, the economic convenience of mitigation decreases with increasing the unitary cost of treatment. An example of the output is plotted in Figure 6-50, assuming two mitigation solutions' costs: € 50.00 and € 100.00 per cubic meter of soil.

Due to the expected liquefaction-induced annual loss, it can be concluded that mitigation is advantageous in the following situations:

the industrial building is located on high liquefaction susceptible soil deposits, which results in the higher probabilities of liquefaction-induced physical damage;

the total volume of the potentially liquefiable layer to be treated is limited (say the building footprint area or the thickness of the sandy layer are small enough to provide a low volume of soil to be treated). This gives the chance to mitigate the risk with a sustainable cost;

the company has very high annual incomes, i.e., >50'000'000,00 €/year, which justifies the investment of a considerable amount of capital.

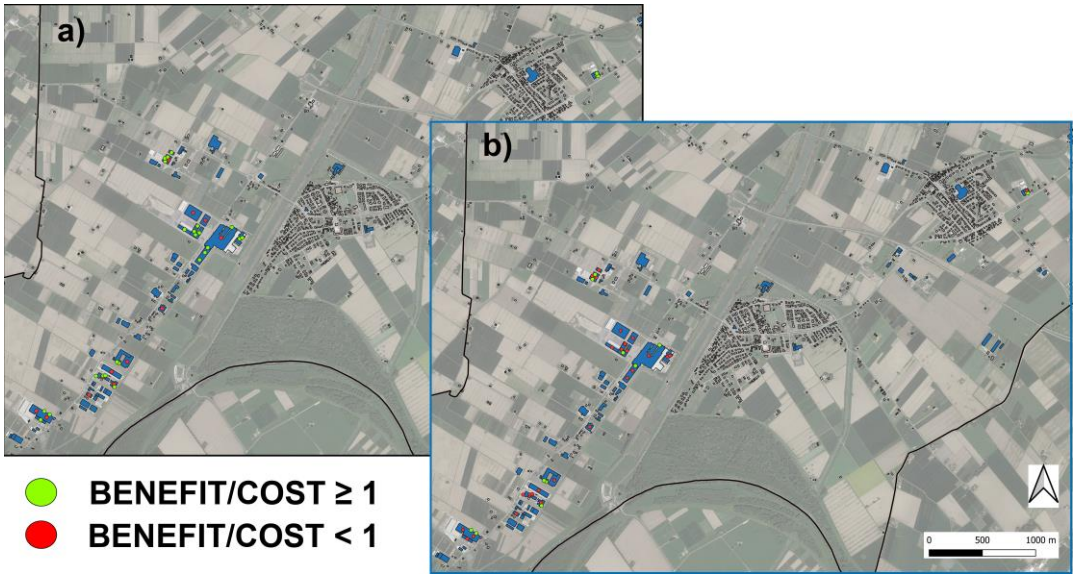

Figure 6-50 Example of benefit/cost analysis on the industrial district assuming a unitary mitigation cost respectively equal to 50.00 €/mc (a) and 100.00 €/mc (b).

Additionally, the different approaches in estimating the liquefaction-induced economic loss for residential and industrial buildings require further consideration. In the latter situation, ad-hoc studies on the elements at risk (which includes the company inventory and the availability of capital goods) are recommended for the purpose of a strategic benefit/cost analysis and the quantification of the loss of market consequent to a given hazard. Such a detailed evaluation tailored to the specific company, which obviously will address the assessment to increasing risk levels is not the objective of this work. In this study, due to the lack of specific economic expertise judgment, an expeditious alternative way to interpret the benefit/cost analysis is shown in Figure 6-51. The ratio between the annual risk and the annual mitigation rate is displayed as a continuous variable. This attempts to explain that in some cases, the possibility of undertaking a liquefaction countermeasure should be considered even if the benefit/cost rate is not strictly greater than 1.

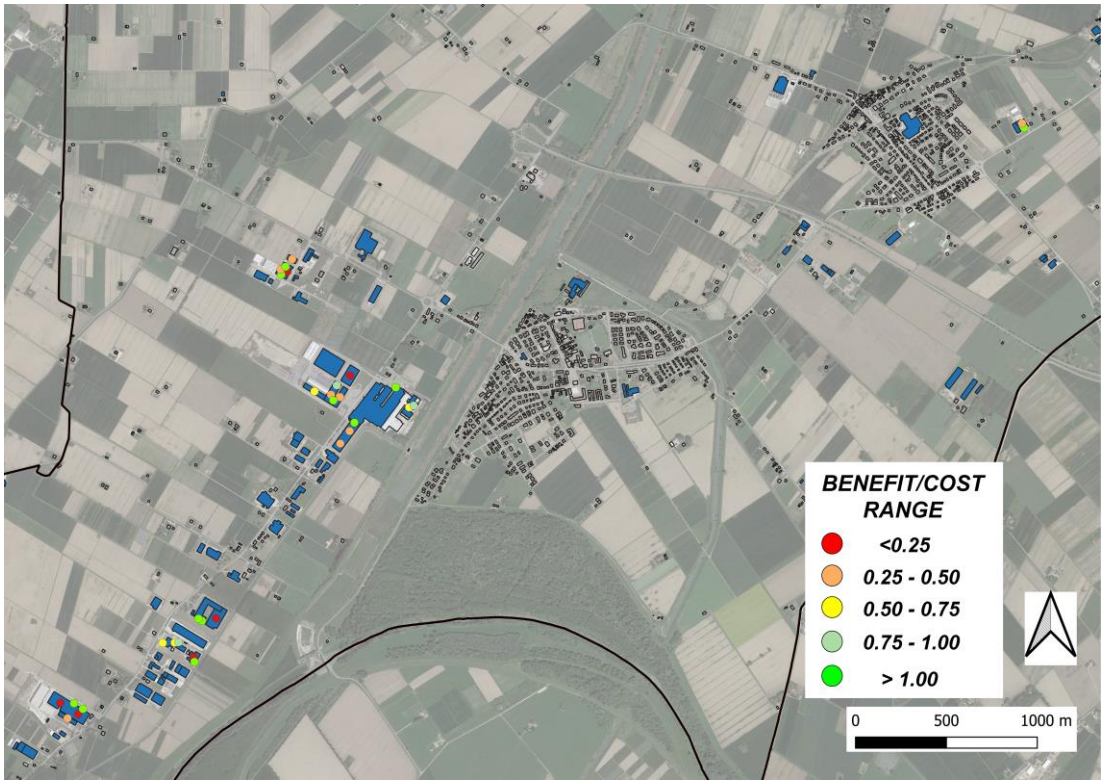

Figure 6-51 Benefit/cost rate on the industrial district assuming a unitary mitigation cost equal to 100.00 €/m^3.

CONCLUSIONS

A novel methodology to quantify liquefaction hazard, vulnerability and risk assessment over urban systems is herein presented to fulfill a gap of the up to date procedures of seismic risk assessment. The proposed procedure aims to be comprehensive as it frames in a sequential multi-level analysis issues related with seismic hazard, subsoil characteristics, structural response of buildings, estimates of damage, economic losses. Its application has been tested on two case studies, the 2010-2011 earthquake sequence of Christchurch (New Zealand) and the seismic event of May 22nd, 2012 in Terre del Reno (Italy), exploiting the detailed and rich documentation created for reconstruction.

The assessment, carried out over large areas, implies identifying on a local basis the different factors forming risk (hazard, vulnerability, and exposure) and, for each step of the analysis, characterize each factor, quantify the most representative parameters and combine all factors in a unitary predictive model. In details, seismic hazard, subsoil susceptibility, physical vulnerability, the economic and social relevance of structures have been defined on a probabilistic basis selecting the most appropriate criteria in the existing literature.

The spatial distribution of quantities regarding subsoil has been computed interpolating the data derived from investigation. Geostatistical tools have been used with this purpose as they enable to compute the statistical distribution of the estimate error. In conjunction with other statistical factors, this function is included in the convolutive integral calculation defined by PBEE, to account for the reliability of estimate in the probabilistic assessment of risk. Additionally, knowing the reliability of the estimate distributed over the studied area enables to plan additional investigation in order to optimize the use of resources.

Calculation of risk is performed considering several seismic hazard scenarios, corresponding to different annual occurrence probabilities. In a preliminary analysis

(Hazard assessment), the liquefaction-induced ground deformation (PGDf) has been evaluated combining seismic hazard with subsoil intrinsic susceptibility, the latter quantified through the ESP method defined by Millen et al. (2020). This assessment, often accomplished through more straightforward semi-empirical formulation (Eqn. 3.12), leads to categorizing the ground damage, and forms a judgment criterion to decide whether further analyses need to be performed on the superstructure.

The effectiveness of traditional liquefaction severity indicators in foreseeing liquefaction on the selected case studies has been quantitatively proved by the validation criterion proposed by Kongar et al. (2015). When the geostatistical filtering of inconsistent data is applied to the CPT dataset, liquefaction is correctly predicted by each indicator in ≈70% of the cases. However, the study of the ESP error distribution highlighted a more heterogeneous stratigraphy for the city of Christchurch compared with the case study of Terre del Reno. In the former context, the dense alternation of liquefiable and non-liquefiable layers creates the conditions for a more complex dynamic response (called system response by Cubrinovski and Van Ballegooy, 2017) of the deposit, where liquefaction does not affect all layers, as postulated by the indicators, but affects some of them selectively and propagates with time to closer layers. Based on the above consideration, the repetition of the analysis on selected subsoil profiles, i.e. those more closely referable to a simple three-layer model (only one liquefiable layer surrounded by two non-liquefiable layers) increased the effective performance of indicators up to approximately 80%.

In the following phase, the combined application of the Kongar et al. (2015) and Powers (2011) criteria demonstrated that the accuracy of traditional indicators decreases when more critical situations (like severe cracking and lateral spreading) are analyzed. In particular, the geological/geomorphological setting of Christchurch and Terre del Reno pointed out the paramount role of the topography in liquefaction-induced damage, despite traditional liquefaction indicators commonly neglect it. A proposal is made to account for this contribution by introducing the generalized indicator *"GEN LD"* for combined liquefaction and lateral spreading, which calculation on the selected case studies has shown a robust agreement between prediction and observation and between optimal thresholds for different damage levels.

The quantification of vulnerability is one of the most important yet delicate phases of the risk assessment process. For earthquakes induced liquefaction, vulnerability models imply to embrace seismic input, mechanical properties of subsoil, and structure into a unique scheme that captures their mutual interaction. Numerical tools, coupled

with advanced constitutive models, enable to simulate very accurately the role of each element concurring in the dynamic response of buildings founded on liquefiable soils. However, when dealing with territorial risk assessment, these models are hardly applicable due to the lack of information, and thus a simpler characterization of factors becomes necessary. The present work has explored the application of a vulnerability scheme to the assessment of reinforced concrete buildings at the urban scale. In the attempt to trade off simplicity and accuracy, recent solutions offered in the literature have been combined in a sequential procedure articulated in the following steps: (i) Absolute settlements of buildings are estimated with a recent formula that incorporates the paramount factors inferring their role from a large number of numerical analyses; (ii) Absolute settlements are then transformed into differential settlements, more indicative of damage, with a relation stemming from a parametric numerical calculation where the spatial variability of subsoil properties is probabilistically reproduced; and (iii) Differential settlements are finally used as the engineering demand parameters to quantify with fragility functions derived from the literature the probability of damage for reinforced concrete buildings not specifically designed to resist seismic actions.

The validity of the method has been tested on the case studies of February 22nd, 2011 M_w6.2 Christchurch (New Zealand) and 20th 2012 May M_w6.1 Emilia (Italy) Earthquakes, exploiting a rich catalogue of buildings, the post-earthquake damage surveys, and a very dense database of geotechnical investigations. In both the cases, the geostatistical data treatment has been proposed to manage the uncertainty connected with the determination of subsoil properties, filter inconsistent data and quantify the variance inherent with the estimate. The validation of the model performed with a quantitative criterion has revealed a correlation between prediction and evidence, although with a variable degree of satisfaction. The Overall Success Rate, i.e., the fraction of successful prediction (damage or undamaged), is about two thirds for the lower damage level and increases up to more than 90% or for the higher damage level.

A similar analysis has been performed for the light wooden buildings present in Christchurch city, considering damage associated with subsoil failure only, i.e., without considering the structural characteristics, and adopting the liquefaction severity number LSN (van Ballegooy et al., 2014) as engineering demand parameter. In this case, the success rate of prediction has been equal to about two-thirds for all considered damage levels.

One of the most immediate outcomes of the proposed calculation scheme is the cost-benefit analysis, that governs possible mitigation strategies. With this goal, physical damage has been transformed into economic loss, which has been compared to the cost of mitigation on an annual basis (Hazus, FEMA, 1998). The choice of the optimal solution generally depends on a series of consideration involving technical efficiency, feasibility of treatments in relation to the scope of the project, boundary conditions, environmental and subjective issues. Neglecting the physical constraints that could orient toward specific technical solutions, in the present context of risk assessment, the convenience has only been evaluated in terms of cost-effectiveness. In the different scenarios has been observed that mitigation with ground improvement is convenient for a larger number of buildings if its cost is low or very low (say less than 25.00 €/m^3), while becomes less appealing when costs increase. For the larger considered cost (100.00 €/m^3) only few buildings, most of them respectively located in the Central Business District of Christchurch and on the Old Reno River embankments in the district of Terre del Reno), are worth of mitigation with ground improvement. For the other residential houses, it is not convenient to undertake this kind of countermeasure. Other solutions should thus be considered, such as the stipulation of insurance policies. The implemented risk assessment procedure provides in this case the possibility of establishing the cost of the premium to be assigned for each building.

FUTURE DEVELOPMENTS

Being aware of the simplification and without pretending to be exhaustive, the proposed methodology introduces a robust logical framework to comprehensively account for the most relevant factors that contribute to liquefaction-induced building damage in the computation of the expected annual economic loss. Obviously, the whole methodology is susceptible to improvement. For instance, the ESP method gives a more detailed quantitative estimation of liquefaction susceptibility than the geological criteria. However, it does not say anything about more complex soil stratigraphy (e.g., 5 or more layers). At the same time, in the typical structure of traditional liquefaction severity indicators, several aspects governing liquefaction (like system response, the interaction between liquefied layers and seismic motion,

topography, etc.) are neglected. Although still susceptible to improvement, the herein proposed *"GEN LD"* indicator represents an expeditious method to account for the effect of topography. However, further evaluations on new worldwide case studies introducing different subsoil, geometry and seismic conditions are needed to confirm its complete generalization.

Thinking on structural vulnerability, the fragility curves of Figure 4-7 are derived for buildings of fixed, although typical, an array of columns and plan dimensions. At the same time, they have been applied to other building geometry. Additionally, the relation between differential and absolute settlements has been derived under simplified yet conservative assumptions, e.g., focusing on distortion and neglecting other possible causes of damage (like tilting). Finally, the Hazus (FEMA, 2003) economic model, which was primarily proposed for seismic risk assessment procedures, has been adopted for liquefaction-induced economic losses.

Therefore, refinement should consist in the introduction of more pertinent schemes, e.g., a more detailed classification and characterization of buildings, more accurate calculation schemes for absolute and differential settlements, an integrated economic-loss model, and the adoption of a global criterion to evaluate the convenience of any mitigation options accounting for the main (objective and subjective) factors governing this choice.

REFERENCES

Alessio G. et al., 2013: “Liquefaction phenomena associated with the Emilia earthquake sequence of May–June 2012 (Northern Italy)”. Nat. Hazards Earth Syst. Sci., 13, 1–13, 2013.

Ambraseyes N.N., 1988: "Engineering seismology". Earthquake Engineering and Structural Dynamics, Vol. 17, pp. 1 -105.

Andrus, R. D., and Stokoe, K. H. 1997. “Liquefaction resistance based on shear wave velocity”. NCEER Workshop on Evaluation of Liquefaction Resistance of Soils, Salt Lake City, UT, Technical Report NCEER-97-0022.

Andrus, R. D., and Stokoe, K. H. 2000. “Liquefaction resistance of soils from shear wave velocity”. J. Geotech. Geoenviron. Eng., ASCE, 126 (11), 1015 – 1025.

Ang, A. H., and Tang, W., 1984: "Probability Concepts in Enginering Planning and Design". Volume I Basic Principles. New York, USA: John Wiley and Sons.

Arias A., 1970: “A measure of earthquake intensity”. Seismic design for nuclear power plants, R. J. Hansen, ed., MIT Press, Cambridge, Mass.

ASTM International (2014a). “Standard Test Methods for Downhole Seismic Testing”. ASTM D7400-14. West Conshohocken, PA: ASTM International.

Baecher G. B. and Christian J. T., 2003: “Reliability and statistics in geotechnical engineering”. Chichester, England: Wiley, 605 pp.

Baggio C., Bernardini A., Colozza R., Corazza L., Della Bella M., Di Pasquale G., Dolce M., Goretti A., Martinelli A., Orsini G., Papa F., Zuccaro G., 2009: “Manuale per la compilazione della scheda di 1° livello di rilevamento danno, pronto intervento e agibilità per edifici ordinari nell’emergenza post-sismica (AeDES)”. Dipartimento della Protezione Civile.

Baker J.W., and Cornell C.A., 2008. “Uncertainty propagation in probabilistic seismic loss estimation”. Structural Safety, 30, 236–252.

Baker, J.W., Faber, M.H., 2008: "Liquefaction Risk Assessment Using Geostatistics to account for Soil Spatial Variability". Journal of Geotechnical and Geoenvironmental Engineering, Vol. 134, 14-23.

Bartlett S. F., and Youd, T. L., 1995: “Empirical prediction of liquefactioninduced lateral spread.” J. Geotech. Engrg., 121(4), 316–329.

Berardi R., Margottini C., Molin D. and Parisi A., 1991: “Soil liquefaction: case histories in Italy”. Tectonophysics, 193 (1991) 141-164.

Bertalot D, and Brennan AJ (2015) Influence of initial stress distribution on liquefaction-induced settlement of shallow foundations. Geotechnique, 65(5):418–428. DOI: 10.1680/geot.SIP.15.P.002.

Bird, J., Crowley, H., Pinho, R., Bommer, J.; 2005: “Assessment of building response to liquefaction induced differential ground deformation”. Bulletin of the New Zealand Society for Earthquake Engineering, 38-4, Dec. 2005, 215-234.

Bird, J., Bommer, J., Crowley, H., Pinho, R., 2006: “Modelling liquefaction-induced building damage in earthquake loss estimation”. Soil Dynamics and Earthquake Engineering 26 (2006) 15–30.

Blockley D., 2013: "Earthquake Risk Management of civil infrastructure: integrating soft and hard risks". Woodhead Publishing Limited, 2013.

Bondesan A., Bondesan M., 1990: "Breve storia idrografica del territorio ferrarese". http://www.naturalistiferraresi.org/wp-content/uploads/2017/03/Storia-Idrografica-del-Ferrarese.pdf.

Boscardin M.D., Cording E.J., 1989: "Building response to excavation-induced settlement. Journal of Geotechnical Engineering". Vol. 115, No. 1, January, 1989. ©ASCE, ISSN 0733-9410/89/0001-0001. Paper No. 23066.

Boulanger, R.W., and I.M. Idriss, 2006: "Liquefaction susceptibility criteria for silts and clays". Journal of Geotechnical and Geoenvironmental Engineering 132(11):1413–1426.

Boulanger, R.W., and I.M. Idriss, 2008: "Closure to Liquefaction Susceptibility Criteria for Silts and Clays". Journal of Geotechnical and Geoenvironmental Engineering. 134(7):1027-1028.

Boulanger R.W., Idriss, I.M., 2014. “CPT and SPT based liquefaction triggering procedures”. Department of Civil and Environmental engineering, University of California at Davis.

Boulanger R.W. and Idriss I.M., 2016: "CPT-based liquefaction triggering procedure". J Geotech Geoenviron Eng.https ://doi.org/10.1061/%28ASCE%29GT.1943-5606.00013 88.

Bradley B.A., Lee D.S., Broughton R. and Price C., 2009: “Efficient evaluation of performance-based earthquake engineering equations”. Structural Safety, 31, 65–74.

Bradley B.A., 2010: "Epistemic uncertainties in component fragility functions". Earthquake Spectra, 26(1): 41-62.

Bradley B.A., Quigley M.C., Van Dissen R.J., and Litchfield N.J., 2014: "Ground motion and seismic source aspects of the Canterbury Earthquake Sequence". Earthquake Spectra, v. 30, p. 1–15, doi: 10.1193/030113EQS060M.

Bradley B.A., 2016: "Strong ground motion characteristics observed in the 13 June Mw6.0 Christchurch, New Zealand earthquake". Soil Dynamics and Earthquake Engineering 2016, Vol. 91, pp. 23-38.

Bray J.D, R.B.Sancio, T. Durgunoglu, A. Onalp, T.L. Youd, J.P. Stewart, R.B. Seed, O.K. Cetin, E. Bol, M.B. Batuary, C. Christensen, and T. Karadayilar. 2004a. "Subsurface characterization at ground failure sites in Adapazari, Turkey". Journal of Geotechnical and Geoenvironmental Engineering 130(7):673–685.

Bray, J.D., R.B. Sancio, M.F. Riemer, and T. Durgunoglu. 2004b. "Liquefaction susceptibility of finegrained soils". Pp. 655–662 in Proceedings of 11th International Conference on Soil Dynamics and Earthquake Engineering and 3rd International Conference on Earthquake Geotechnical Engineering, edited by D. Doolin et al. Singapore: Stallion Press.

Bray J.D., and Sancio R.B., 2006. "Assessment of the liquefaction susceptibility of fine grained soils". Journal of Geotechnical and Geoenvironmental Engineering 132(9):1165–1177.

Bray JD, and Dashti S., 2014: "Liquefaction-Induced Building Movements". Bulletin of Earthquake Engineering, Springer, Vol. 12(3), 1129-1156, DOI: 10.1007/s10518-014-9619-8.

Bray, J. & Macedo, J., 2017. 6th Ishihara lecture: “Simplified procedure for estimating liquefaction-induced building settlement”. Soil Dynamics Earthquake Engng 102, 215–231.

Breitung, K., 1984: "Asymptotic approximations for multinormal integrals". ASCE Journal of Engineering Mechanics, 357-366.

Bruneau, M., Chang, S., Eguchi, R., Lee, G., O'Rourke, T., Reinhorn, A. M., Shinozuka, M., Tierney, K., Wallace, W., and Winterfeldt, D. V. 2003. "A Framework to Quantitatively Assess and Enhance the Seismic Resilience of Communities". Earthquake Spectra, 19(4), 733–752.

Brzev S., Scawthorn C., Charleson A.W.,Allen L., Greene M., Jaiswal K., Silva V., 2013: GEM Building Taxonomy 2.0". GEM Technical Report, Gem Technical Report 2013-02 V1.0".0.

Bullock Z, Karimi Z, Dashti S, Porter K, Liel AB, Franke KW (2018) A physics-informed semi-empirical probabilistic model for the settlement of shallow-founded structures on liquefiable ground. Géotechnique [https://doi.org/10.1680/jgeot.17.P.174].

Bullock Z, Dashti S, Liel A., 2019a: "Assessment Supporting the Use of Outcropping Rock Evolutionary Intensity Measures for Prediction of Liquefaction Consequences".Earthquake Spectra, Vol. 35, 4, 2019.

Bullock Z, Dashti S, Karimi Z, Liel A., Porter K, Franke KW, 2019b: "Probabilistic Models for Residual and Peak Transient Tilt of Mat-Founded Structures on Liquefiable Soils". J. Geotech. Geoenviron. Eng., 2019.

Campbell, K. W., and Bozorgnia, Y. 2011. Predictive equations for the horizontal component of standardized cumulative absolute velocity as adapted for use in the shutdown of U.S. nuclear power plants, Nucl. Eng. Des. 241, 2558–2569.

CEN (2004a). EN 1998-1, Eurocode 8—design of structures for earthquake resistance, part 1: general rules, seismic actions and rules for buildings. European Committee for Standardization, Brussels.

CEN (2004b). EN 1998-5, Eurocode 8—design of structures for earthquake resistance, part 5: Foundations, retaining structures and geotechnical aspects. European Committee for Standardization, Brussels.

CEN (2008), PrEN 1997-1. Geotechnical Design-General Rules, European Commission for Standardization.

Cetin, K. O., Seed, R. B., Der Kiureghian, A., Tokimatsu, K., Harder, L. F., Kayen, R. E., and Moss, R.E. S. 2004. "Standard penetration test-based probabilistic and deterministic assessment of seismic soil liquefaction potential". J. Geotechnical and Geoenvironmental Eng., ASCE 130(12), 1314–340.

Chiles, J., & Delfiner, P., 1999: "Geostatistics: modeling spatial uncertainty". John Wiley & Sons, New Yark, 720 p.

Chilès J. P. and Delfiner P., 2012: "Geostatistics: Modeling Spatial Uncertainty", 2nd Edition – Wiley - ISBN: 978-0-470-18315-1, p. 726.

Ching J., Porter K.A., and Beck J.L., 2009: “Propagating uncertainties for loss estimation in performance-based earthquake engineering using moment matching”. Structure and Infrastructure Engineering, 5(3), 245–262.

Comerio M.C. (editor), 2005: “PEER testbed study on a laboratory building: exercising seismic performance assessment”. PEER Report. PEER 2005/12.

Cornell, C.A., and Krawinkler, H. 2000. “Progress and Challenges in Seismic Performance Assessment”. PEER Center News, 3, 1-3.

CRED & UNISDR, 2018: Economic losses, poverty & disasters 1998-2017.

Crowley H., Bommer J.J., Pinho R. and Bird J., 2005: “The impact of epistemic uncertainty on an earthquake loss model”. Earthquake Engineering Structural Dynamics, 34(14), 1653–1685.

CSAPEISLA, 2016: "State of the Art and Practice in the Assessment of Earthquake-Induced Soil Liquefaction and Its Consequences".

Cubrinovski M, Hughes M, Bradley B, McCahon I, McDonald Y, Simpson H, Cameron R, Christison M, Henderson B, Orense R, O’Rourke (2011a) Liquefaction Impacts on pipe networks. Short Term Recovery Project No. 6 Natural Hazards Research Platform. University of Canterbury.

Cubrinovski M, Bradley B, Wotherspoon L, Green R, Bray J, Wood C, Pender M, Allen J, Bradshaw A, Rix G, Taylor M, Robinson K, Henderson D, Giorgini S, Ma K, Winkley A, Zupan J, O’Rourke T, DePascale G, Wells D (2011b) Geotechnical aspects of the 22 February 2011 Christchurch earthquake. Bullettin of the New Zealand Society for earthquake engineering. Vol. 44, N. 4, December 2011.

Cubrinovski M., Bray J., Taylor M., Giorgini S., Bradley B., Wotherspoon L., Zupan J., 2011.c: "Soil Liquefaction Effects in the Central Business District during the February 2011 Christchurch Earthquake". Seismological Research Letters. 82. 893-904. 10.1785/gssrl.82.6.893.

Cubrinovski M., Henderson D., Bradley B., 2011d: "Liquefaction impacts in residential areas in the 2010 - 2011 Christchurch Earthquakes". Proceedings of the International Symposium on Engineering Lessons Learned from the 2011 Great East Japan Earthquake, March 1-4, 2012, Tokyo, Japan.

Cubrinovski M., Robinson K., Taylor M., Hughes M. & Orense R., 2012: "Lateral spreading and its impacts in urban areas in the 2010-2011 Christchurch earthquakes". New Zealand Journal of Geology and Geophysics, 55(3), 255-269.

Cubrinovski M., 2013: “Liquefaction-Induced Damage in the 2010-2011 Christchurch (New Zealand) Earthquakes". In: Proceedings of the 7th International Conference on Case Histories in Geotechnical Engineering, 29 Apr–4 May, Chicago, Illinois.

Cubrinovski M., Hughes M., Bradley B., Noonan J., McNeill S., English G., & Hopkins R., 2014: “Performance of Horizontal Infrastructure in Christchurch City through the 2010-2011 Canterbury Earthquake Sequence”. Christchurch: Civil & Natural Resources Engineering, University of Canterbury.

Cubrinovski M. and Robinson K., 2015: "Lateral spreading: evidence and interpretation from the 2010-2011 Christchurch earthquakes". 6th International Conference on Earthquake Geoechnical Engineering.

Cubrinovski M. and van Ballegooy S., 2017: “System response of liquefiable deposits”. 3rd Int. Conf. on Performance Based Design in Earthquake Geotechnical Engineering.

Daniell J.E., Khazai B., Wenzel F., Vervaeck A., 2012:"The Worldwide Economic Impact of Earthquakes". Proceedings of the 15th World Conference of Earthquake Engineering, Lisbon, Portugal.

D’Appolonia E., 1954: "Symposium on dynamic testing of soils". ASTM International.

Dashti S., Bray J.D., Pestana J.M., Riemer M., and Wilson D., 2010a: "Mechanisms of Seismically Induced Settlement of Buildings with Shallow Foundations on Liquefiable Soil". Journal of Geotechnical and Geoenvironmental Engineering, 136(1):151–164. DOI: 10.1061/ ASCE GT.1943-5606.0000179.

Dashti S., Bray J.D., Pestana J.M., Riemer M., and Wilson D., 2010b: "Centrifuge testing to evaluate and mitigate liquefaction-induced building settlement mechanisms". Journal of Geotechnical and Geoenvironmental Engineering 136(7):918–929.

Del Gaudio C., Roati A., Rota M., Ricci P., Penna A., Verderame G. M., 2019: "Empirical fragility curves for RC Italian residential buildings". XVIII Convegno ANIDIS.

De Natale G., Troise C., Somma R., 2020: "Invited perspectives: The volcanoes of Naples: how can the highest volcanic risk in the world be effectively mitigated?". Natural Hazards and Earth Systems Science. 20, 2037–2053, 2020

Dickenson S., 2005: “Recommended guidelines for liquefaction evaluations using ground motions from probabilistic seismic hazard analyses”. Report to the Oregon Department of Transportation, June 2005, 93 pp.

Dipartimento della Protezione Civile, DPC (2017). “Linee guida per la gestione del territorio in aree interessate da liquefazioni (LQ). Versione 1.0”. Roma 2017.

Dobry R. and Liu L., 1994: "Centrifuge modeling of soil liquefaction". In 10th World Conference of Earthquake Engineering.

Ellingwood B., 2001: “Earthquake risk assessment in building structures”. Reliability Engineering and System Safety, 74, 251–262.

El Mohtar C.S., Bobet A., Santagata M.C., Drnevich V.P., Johnston C.T., 2013: "Liquefaction Mitigation Using Bentonite Suspensions", Journal of Geotechnical and Geoenvironmental Engineering, 139 (8).

Emergeo Working Group, 2012: “Technologies and new approaches used by the INGV EMERGEO Working Group for real-time data sourcing and processing during the Emilia Romagna (northern Italy) 2012 earthquake sequence”. ANNALS OF GEOPHYSICS, 55, 4, 2012; doi: 10.4401/ag-6117.

Emergeo Working Group, 2013, G. Alessio, L. Alfonsi, C. A. Brunori, P. Burrato, G. Casula, F. R. Cinti, R. Civico, L. Colini, L. Cucci, P. M. De Martini, E. Falcucci, F. Galadini, G. Gaudiosi, S. Gori, M. T. Mariucci, P. Montone, M. Moro, R. Nappi, A. Nardi, R. Nave, D. Pantosti, A. Patera, A. Pesci, G. Pezzo, M. Pignone, S. Pinzi, S. Pucci, S. Salvi, C. Tolomei, P. Vannoli, A. Venuti, and F. Villani: "Liquefaction phenomena associated with the Emilia earthquake sequence of May–June 2012 (Northern Italy)". Nat. Hazards Earth Syst. Sci., 13, 935–947, 2013.

EPANTYK, 2009. "Development of GIS software for the representation of the structural wealth of the municipalities of the country and of its structural vulnerability in buildings block level. YP.ES.A, H.D, KEDKE, TEE, pp 39.

Fardis M.N., Karantoni F.V., Kosmopoulos A., 1999. "Statistical study of damage due to Aegion earthquake of 15-6-95". Final Report to Earthquake Planning and Protection Organization, University of Patras, Department of Civil Engineering, Division of Construction Engineering, Patras, July (in Greek).

FEMA/NIBS, 1998. HAZUS - Earthquake Loss Estimation Methodology. Vol. 1, 1998.

FEMA & NIBS, 1999. “HAZUS99 user and technical manuals”, Federal Emergency Management Agency Report: HAZUS 1999, Washington D.C., USA.

FEMA/NIBS 2003. “HAZUS-Earthquake – Technical Manual”. Federal Emergency.

Fenton, G. A. 1999. "Random field modeling of CPT data". Journal of geotechnical and geoenvironmental engineering, 125(6), 486-498.

Fenton G.A. and Griffiths D.V., 2000: "Rberar2d". RFEM.

Fikri R., Dizhur D., Quinn Walsh K., Ingham J.,2018: "Seismic performance of Reinforced Concrete Frame with Masonry Infill buildings in the 2010/2011 Canterbury, New Zealand earthquakes". Bulletin of Earthquake Engineering https://doi.org/10.1007/s10518-018-0476-8.

Fioravante V., Giretti D., Abate G., Aversa S., Boldini D., 2013: 2Earthquake geotechnical engineering aspects: the 2012 Emilia Romagna earthquake (Italy)". Seventh international Conference on Case Histories in Geotechnical Engineering, April 29 th – May 4th, 2013. Chicago (US).

Fotopoulou S., Karafagka S., Pitilakis K., 2018, Vulnerability assessment of low-code reinforced concrete frame buildings subjected to liquefaction-induced differential displacements, Soil Dynamics and Earthquake Engineering 110 (2018) 173–184.

Franke K. W., and Kramer S. L., 2014: "Procedure for the Empirical Evaluation of Lateral Spread Displacement Hazard Curves". JOURNAL OF GEOTECHNICAL AND GEOENVIRONMENTAL ENGINEERING. January 2014.

Galli P., 2000: “New empirical relationships between magnitude and distance for liquefaction”. Tectonophysics 324, 169-187.

Galli P. and Meloni F., 1993: “Liquefazione Storica. Un catalogo nazionale”. Quat. Ital. J. Quat. Sci. 6. Pagg. 271–292.

Gerace A., 2018. “Equivalent simplified soil profiles for liquefaction assessment”. MSc Thesis, University of Porto (FEUP).

Giannaraki G., Kassaras I., Roumeliotti Z., Kazantzidou-Firtinidou D., Ganas A., 2018. "Deterministic seismic risk assessment in the city of Aigion (W. Corinth Gulf, Greece) and juxtaposition with real damage due to the 1995 Mw6.4 earthquake. Bulletin of Earthquake Engineering.

Giovinazzi S., Lagomarsino S., 2004: "A macroseismic method for the vulnerability assessment of buildings". Proceedings of the 13th WCEE, Vancouver, BC, Canada, August 1–6, paper No 896

Giovinazzi S., Wilson T., Davis C., Bristow D., Gallagher M., Schofield A. et al., 2011: "Lifelines performance and management following the 22 february 2011 christchurch earthquake, New Zealand". Bulletin of the New Zealand society for earthquake engineering, Vol. 44, No. 4, December 2011.

Goda K. and Hong H.P. 2008: “Estimation of seismic loss for spatially distributed buildings”. Earthquake Spectra, 24(4), 889–910.

Grant, R., Christian, J.T., and Vanmarcke, E.H. 1974. “Differential settlement of buildings”. Journal of Geotechnical Engineering Division, ASCE, 100(9), pp. 973-991.

Guha-Sapir D. and Vos F., 2011: "Earthquakes, an Epidemiological Perspective on Patterns and Trends". R. Spence et al. (eds.), Human Casualties in Earthquakes, Advances in Natural 13 and Technological Hazards Research 29, Springer Science + Business Media B.V. 2011.

Hasofer A. M. and Lind N. C., 1974: “An exact and invariant first-order reliability format”. Journal of the Engineering Mechanics Division, ASCE 100(EM1): 111–121.

Honjo Y. and Kazumba S., 2002: "Estimation of autocorrelation distance for modeling spatial variabilityof soil properties by Random Field theory". The 47th Geotechnical Engineering Symposium, JGS, (p. 279-286).

Housner G.W., 1959: “Behaviour of structures during earthquake”. Journal of the Engineering Mechanics Division, ASCE 1959: 85(4): 109–129.

Hughes M., Quigey M. C., Bradley B., Hart D. E., 2015: "The sinking city: Earthquakes increase flood hazard in Christchurch, New Zealand". GSA Today, v. 25, no. 3–4, doi: 10.1130/GSATG221A.1.

ICMS, 2008: "Indirizzi e Criteri generali per la Microzonazione Sismica", approvato da Dipartimento della Protezione Civile e Conferenza delle Regioni e Province Autonome in data 13 novembre 2008. The Enghish version is: SM Working Group, Guidelines for Seismic Microzonation, Conference of Regions and Autonomous Provinces of Italy—Civil Protection Department, Rome, 2015.

ICMS-LIQ, 2017: "Microzonazione sismica. Linee guida per la gestione del territorio in aree interessate da liquefazioni (LQ)". Versione 1.0. Commissione tecnica per la microzonazione sismica. Roma, 2017. The Enghish version is: Technical Commission on Seismic Microzonation, Land Use Guidelines for Areas Affected by Liquefaction (LQ)”, version 1.0, Rome, 2018.

Idriss I. M., 1999: “An update to the Seed-Idriss simplified procedure for evaluating liquefaction potential”. Proceedings, TRB Workshop on New Approaches to Liquefaction, Publication No. FHWARD- 99-165, Federal Highway Administration, January.

Idriss, I. M., and Boulanger, R. W. 2008. “Soil liquefaction during earthquakes”. Monograph MNO-12, Earthquake Engineering Research Institute, Oakland, CA, 261 pp.

IEC/FDIS, 31010:2009. "Risk Management - Risk Assessment Techniquess" INTERNATIONAL STANDARD (ISO).

Ishihara K., 1985: "Stability of Natural Deposits During Earthquakes". Proceedings of the 11th International Conference on Soil Mechanics and Foundation Engineering. San Francisco, 1:321-376.

Ishihara K. and Yoshimine M., 1992: "Evaluation of settlements in sand deposits following liquefaction during earthquakes". Soils Found 1992;32(1):173–188.

Itasca Consulting Group, Inc. 2016. “FLAC — Fast Lagrangian Analysis of Continua, Ver. 8.0”. Minneapolis: Itasca.

ISTAT, 2018: "Dati ISTAT" [internet] <http://dati.istat.it>>.

Iwasaki T., Tatsuoka F., Tokida K., Yasuda S., 1978: "A Practical method for assessing soil liquefaction potential based on case studies at various sites in Japan". [conference]: 2nd International conference on Microzonation. - 1978: 885-896.

JAPAN GEOTECHNICAL SOCIETY JGS, 1998: “Remedial against liquefaction from investigation and design to implementation”. Japanese Geotechnical Society, Balkema eds., 433 p.

JAPAN GEOTECHNICAL SOCIETY JGS, 2011: "Geo hazard during earthquake and mitigation measures – Lessons and recommendations from the 2011 Great East Japan Earthquake".

Joyner W.B. and Boore D.M., 1988: "Measurement, Characterization, and Prediction of Strong Ground Motion", Proceedings of Earthquake Engineering & Soil Dynamics II, pp. 43- 102. Park City, Utah, 27 June 1988. New York: Geotechnical Division of the American Society of Civil Engineers.

Juang C. H., Yang S. H. and Yuan H., 2005: “Model uncertainty of shear wave velocity-based method for liquefaction potential evaluation”. J. Geotech. Geoenviron., 131(10), 1274-1282.

Kaplan S., 1981: “On the method of discrete probability distributions in risk and reliability calculations – application to seismic risk assessment”. Risk Analysis, 1(3), 189–196.

Kayen R., Moss R. E. S., Thompson E. M., Seed R. B., Cetin K. O., Der Kiureghian A., Tanaka Y., Tokimatsu K., 2013: “Shear-Wave Velocity-Based

Probabilistic and Deterministic Assessment of Seismic Soil Liquefaction Potential". Journal of Geotechnical and Geoenvironmental Engineering.

Karamitros D.K., Bouckovalas G.D., Chaloulos Y.K., 2013: "Seismic settlements of shallow foundations on liquefiable soil with a clay crust". Soil Dynamics and Earthquake Engineering. 46. 64-76.

Karimi Z. and Dashti S., 2017: "Ground motion intensity measures to evaluate II: the performance of shallow-founded structures on liquefiable ground". Earthquake Spectra, 33(1), 277-298.

Karimi Z., Dashti S., Bullock Z., Porter K. & Liel A., 2018: "Key predictors of structure settlement on liquefiable ground: a numerical parametric study". Soil Dynamics Earthquake Engng 113, 286–308.

Kirsch K. and Kirsch F., 2016: "Ground Improvement by Deep Vibratory Methods", Second Edition, CRC press, 234 pp.

Kongar I., Rossetto T., Giovinazzi S., 2015: "Evaluating Desktop Methods for Assessing Liquefaction-Induced Damage to Infrastructure for the Insurance Sector". 12th International Conference on Applications of Statistics and Probability in Civil Engineering, ICASP12 Vancouver, Canada, July 12-15, 2015.

Kramer S.L., 1996. "Geotechnical Earthquake Engineering". Prentice Hall Publishers, 653 p.

Kramer S.L. and Mitchell R.A, 2006: "Ground Motion Intensity Measures for Liquefaction Hazard Evaluation". Earthquake Spectra, Volume 22, No. 2, pages 413–438, May 2006.

Krawinkler H. (editor), 2005: "Van Nuys Hotel building testbed report: exercising seismic performance assessment". PEER Report. PEER 2005/11.

Kwona O.-S. and Elnashai A., 2006: "The effect of material and ground motion uncertainty on the seismic vulnerability curves of RC structure". Engineering Structures, 28(2), 289–303.

Lacasse, S., and Nadim, F. 1, 999: "Risk analysis in geo-engineering". Proceedings of Rocksite 1999 – International Conference on Rock Engineering Techniques for Site Characterization. Bangalore, India.

Lai C. G., Bozzoni F., Conca D., Famà A., Ozocebe A. G., Zuccolo E., Meisina C., Bonì R., Bordoni M., Cosentini R. M., Martelli L., 2020: "Technical guidelines for the assessment of earthquake induced liquefaction hazard at urban scale". Bulletin of Earthquake Engineering. https://doi.org/10.1007/s10518-020-00951-8.

Lee T.-H. and Mosalam K.M., 2006: “Probabilistic seismic evaluation of reinforced concrete structural components and systems”. PEER Report. PEER 2006/04.

Liao S. C. and Whitman R. V., 1986: “Overburden correction factors for SPT in sand”. J. Geotechnical Eng., ASCE 112(3), 373–77.

Lin S.L., Ums S.R., Nayerloo M., Buxton R., King A., 2014: "Engineering characterisation of building performance with detailed engineering evaluation (DEE) data from the Canterbury Earthquake Sequence". ASEC 2014 Conference: structural engineering in Australasia, Auckland, New Zealand.

Lin S.L., Uma S.R., King A.B., Buxton R., Horspool N.A., 2016: "A compiled and extensible database for building damage from the 2010–2011 earthquake sequence in Canterbury, New Zealand". GNS Science Report, Lower Hutt, Wellington.

Liquefact D2.4, 2019, Deliverable 2.4: "GIS database of the historical liquefaction occurrences in Europe and European empirical correlations to predict the liquefaction occurrence starting from the main seismological information".www.liquefact.eu

Liquefact, D7.1, 2019, Deliverable 7.1: "Manual for the assessment of liquefaction risk, defining the procedures to create the database, collect, define, symbolize and store information in the Georeferenced Information System and to perform and represent the risk analysis". www.liquefact.eu.

Liquefact, D7.3, 2019, Deliverable 7.3, "Full and detailed case study report of the application of the risk/resilience assessment toolbox for the selected past EILD cases". www.liquefact.eu.

Liquefact, D7.4, 2019, Deliverable 7.4, "Guidelines for the use of ground improvement technologies to mitigate the liquefaction risk on critical infrastructures". www.liquefact.eu.

Liu L. and Dobry R., 1997: “Seismic response of shallow foundation on liquefiable sand.” J. Geotech. Geoenviron. Eng., 123(6), 557–566.

Liu M., Giovinazzi S. and Lee P., 2015: "Seismic fragility functions for sewerage pipelines". (ASCE), Pipelines Conference 2015, 23-26 August, Baltimore (MD), USA.

Lo Presti D., Giusti I., Cosanti B., Squeglia N. and Pagani E., 2016: “Interpretation of CPTu in ‘unusual’ soils”. Italian Geotechnical Journal, 4/2016.

Loayza N., et al. 2009: "Natural disasters and growth: going beyond the averages", World Bank Policy Research Paper No. 4980, World Bank, Washington, DC, http://dx.doi.org/10.1596/1813-9450-4980.

Luco N., and Cornell C. A., 2007: "Structure-specific scalar intensity measures for near-source and ordinary earthquake ground motions". Earthquake Spectra23, 357–392.

Lyman A. K. B., 1941: “Compaction of cohesionless foundation soils by explosives”. Proceedings of the American Society of Civil Engineers, 67(5), pp. 769-780.

Macaulay T., 2009: "Critical Infrastructures". Taylor & Francis, 342 pp.

Madiai C., Vannucchi G., Baglione M., Martelli L., Veronese T., 2016: "Utilizzo di prove penetrometriche statiche a punta meccanica per la stima del potenziale di liquefazione". Rivista Italiana di Geotecnica 3/16, pp.14-24.

Martelli L., 2012: "The 2012 May 20 Earthquakein the Emilia plain. The geologcal viewpoint". 7th European Congress on Regional Geoscientific Cartography and Sustainable Information System Geomanagement.

Matheron, G. 1965. “Les variables régionalisées et leur estimation: une application de la théorie des fonctions aléatoires aux sciences de la nature”. Masson, Paris, France.

Matthews B. W., 1975: “Comparison of the predicted and observed secondary structure of T4 phage Iysozyme, Biochimica et Biophysica Acta – Protein Structure”, 405(2), 442-451.

Maurer B. W., Green R. A., Oliver S., Taylor O. S., 2015a: “Moving Towards an Improved Index for Assessing Liquefaction Hazard: Lessons from Historical Data”. Soils and Foundations, 55(4): 778-787.

Maurer B. W., Green R. A., Cubrinovski M., Bradley B., 2015b: "Calibrating the Liquefaction Severity Number (LSN) for Varying Misprediction Economies: A Case Study in Christchurch, New Zealand".

Maurer B. W., van Ballegooy S., Bradley B. (2017): Fragility functions for performance-based ground failure due to soil liquefaction.

Mayne P. W., Jones Jr J. S. & Dumas J. C., 1984: “Ground response to dynamic compaction”. ASCE Journal of Geotechnical Engineering, 110(6), pp. 757-774.

Mazzoni, S., McKenna, F., Scott, M., and Fenves, G. (2006). Open system for earthquake engineering simulation user command-language, Net- work for Earthquake Engineering Simulations (NEES), Berkeley, CA.

McGuire R.K., 2004: “Seismic Hazard and Risk Analysis”. EERI Monograph Series MNO-10, Earthquake Engineering Research Institute, 221 p.

Mele L., Tan Tian J., Lirer S., Flora A., Koseki J., 2018: "Liquefaction resistance of unsaturated sands: experimental evidence and theoretical interpretation". Géotechnique.

Meyerhof G. G. and Hanna A. M., 1978: “Ultimate bearing capacity of foundations on layered soils under inclined load.” Can. Geotech. J., 15(4), 565–572

Millen M., Viana da Fonseca A., Quintero J., Ferreira C., Oztoprak S., Bozbey I., Oser C., Aysal N., Kosic M., Logar J., 2020: "Equivalent soil profiles to integrate in situ tests results and soil-structure interaction in liquefiable soils. The Adapazari case-study". Bull Earthq Eng (Special issue).

Ministry of Business, Innovation & Development-MBIE, 2016: “Recommendation after the Canterbury Earthquake sequence (2010-2011)”.

Mitrani-Reiser, J., Haselton, C.B., Goulet C., Porter, K.A., Beck, J., and Deierlein, G.G. 2006. “Evaluation of the seismic performance of a code-conforming reinforced-concrete frame building - part II: loss estimation”. 8th NCEE, San Francisco, California, April 18-22, 10 pp.

Modoni G., Spacagna R. L., Paolella L., Salvatore E., Rasulo A., Martelli L., 2019: "Liquefaction risk assessment: Lesson learned from a case study". Proceedings of the 7th International Conference on Earthquake Geotechnical Engineering ICEGE, 2019, 761-773.

Moehle J.P., 2003: “A framework for performance-based earthquake engineering”. Proc. ATC-15-9 Workshop on the Improvement of Building Structural Design and Construction Practices, Maui, HI, June.

Montgomery D.C., Runger G.C., Hubele N.F., 2012: “Statistica per ingegneria”. Seconda Edizione. Copyright 2012, EGEA S.p.A.

Moss R.E.S, Seed R.B., Kayen R.E., Stewart J.P., Der Kiureghian A. & Cetin, K. O., 2006: "CPT-based probabilistic and deterministic assessment of in situ seismic soil liquefaction potential". J. Geotechnical and Geoenvironmental Eng, 132(8), 1032-1051.

Mousavi S. A, Bastami M., and Zahrai S.M., 2016: "Large-scale seismic isolation through regulated liquefaction: a feasibility study". Earthquake Engineering and Engineering Vibration, 15(4):579–595. DOI: 10.1007/s11803-016-0350-0.

National Research Council, 1985: "Liquefaction of Soils During Earthquakes", Committee on Earthquake Engineering, Commission on Engineering and Technical Systems, National Academy Press, Washington, DC.

Nadim F., 2007: “Tools and Strategies for Dealing with Uncertainty in Geotechnics”. In Probabilistic Method in Geotechnical Engineering, CISM Course and Lectures, D.V Griffith & G.A Fenton Eds. Springer, pp.71-95.

Nguyen T.V., Rayamajhi D., Boulanger R.W., Ashford S.A., Lu J., Elgamal A., and Shao L., 2012: “Effects of DSM grids on shear stress distribution in liquefiable soil”. GeoCongress 2012, State of the Art and Practice in Geotechnical Engineering, ASCE GSP 255, Oakland, CA, PP. 1948-1957.

Nigbor R.L. and Imai T., 1994. “The suspension P-S velocity logging method”. Pp. 57-61 in Geophysical Characterization of Sites, edited by R.D. Woods. International Society for Soil Mechanics and Geotechnical Engineering Special Publication TC 10. New York: International Science Publisher.

NTC, 2018: "Norme Tecniche per le Costruzioni". Ministero delle Infrastrutture e dei Trasporti, Decreto Ministeriale del 17 gennaio 2018, Supplemento ordinario alla G.U. n. 8 del 20 febbraio 2018A.

NZGS, 2016: “New Zealand Geotechnical Society, Earthquake geotechnical engineering practice-Module 3: identification, assessment and mitigation of liquefaction hazards”.

OECD, 2018:"Financial Management of Earthquake Risk", www.oecd.org/finance/Financial-Management-of-Earthquake-Risk.htm.

Olarte J., Paramasivam B., Dashti S., Liel A., Zanin J., 2017: "Centrifuge modeling of mitigation-soil-foundation-structure interaction on liquefiable ground". Soil Dynamics and Earthquake Engineering, 97 (2017), pp. 304 - 323.

Paté-Cornell M.E., 1994: “Quantitative safety goals for risk management of industrial facilities”. Structural Safety, 13, 145–157.

Pokhrel R.M., Kiyota T. and Kajihara K., 2015: “Contribution of Geostatistical Technique to Investigate the Spatial Variation of Liquefaction Potential in Urayasu City”. Japan, Proc. of the 6th International Conference on Earthquake Geotechnical Engineering, 1-4 November 2015, Christchurch, New Zealand.

Porter K.A., 2003: “An overview of PEER’s Performance-based earthquake engineering methodology”. ICASP9, Civil Engineering Risk and Reliability Association (CERRA), San Francisco, CA, July 6-9.

Porter K., 2016: A Beginner’s Guide to Fragility, Vulnerability, and Risk. University of Colorado, 92 pp.

Poulos H.G., Carter J.P., Small J.C., 2001: “Foundations and retaining structures: research and practice”. Proc. XV ICSMGE, Istanbul, vol.4, pp.2527-2606.

Powers D.M.W., 2011: “Evaluation: from precision, recall and F-measure to ROC, informedness, markedness and correlation”. J. of Mach. Lear. Tech, 2(1), 37-63.

Ramirez J., 2019: “Performance of Inelastic Structures on Mitigated and Unmitigated Liquefiable Soils: Evaluation of Numerical Simulations with Centrifuge Tests” (Doctoral dissertation, University of Colorado at Boulder).

Ramirez J., Dashti S., Liel A., Paramasivam B., 2019: "An Experimental and Numerical Study of Prefabricated Vertical Drains as a Liquefaction Countermeasure for Mat-Founded Structures". Geo-Congress 2019: Earthquake Engineering and Soil Dynamics, 219-228.

Ranghieri F., and Ishiwatari M., 2014: "Learning from megadisasters: lessons from the Great East Japan Earthquake". World Bank, Washington, DC, http://dx.doi.org/10.1596/978-1-4648-0153-2.

Regione Emilia-Romagna (PG.2012.0134978 del 31/5/2012a). “Primo rapporto sugli effetti della liquefazione osservati a S. Carlo, frazione di S. Agostino (Provincia di Ferrara)”. A cura del gruppo di lavoro per la valutazione degli effetti di iquefazione a seguito dei terremoti del 20 e 29 maggio 2012.

Regione Emilia-Romagna, PG.2012.0134978 del 31/5/2012b. “Rapporto sugli effetti della liquefazione osservati a Mirabello (Provincia di Ferrara)”. A cura del gruppo di lavoro per la valutazione degli effetti di iquefazione a seguito dei terremoti del 20 e 29 maggio 2012.

Robertson P. ,1990: “Soil classification using the cone penetration test”. Canadian Geotechnical Journal, 27(1):151–158.

Robertson P.K. and Wride C.E., 1998: “Evaluating Cyclic Liquefaction Potential Using the Cone Penetration Test”. Canadian Geotechnical Journal 35, 442–459.

Robertson, P.K. and Cabal, K.L. 2015. “Guide to Cone Penetration Testing for Geotechnical Engineering”. Gregg Drilling & Testing, Inc.

Robinson K., 2015: “Liquefaction-Induced Lateral Spreading in the 2010-2011 Canterbury Earthquakes”. PhD Thesis, University of Canterbury (in print).

Romeo R.W., 2012: “Emilia (Italy) M5.9 earthquake on 20 May 2012: an unusual pattern of liquefaction”. Italian Journal of Engineering Geology and Environment, 2 (2012).

Sadigh K., Egan J. A. and Youngs R. R., 1986: "Specification of Ground Motion for Seismic Design of Long Period Structures". Earthquake Notes, vol. 57, no.

1, p. 13, relationships are tabulated in Joyner and Boore (1988) and Youngs and others (1987).

Sancio R., Bray J. D., Durgunoglu T. & Onalp A., 2004: “Performance of buildings over liquefiable ground in Adapazari, Turkey”. Proceedings of the 13th world conference on earthquake engineering, 13WCEE, Ottawa, ON, Canada.

Schmertmann J. H., 1991: “The mechanical aging of soils”. J. Geotech. Engng, ASCE 117, No. 9, 1288–1330.

Seed H.B. and Idriss I.M., 1971: “Simplified procedure for evaluating soil liquefaction potential”. Journal of the Soil Mechanics and Foundations Division, ASCE, 97(SM9): 1249–1273.

Seed H.B., Idriss I.M., Makdisi F., Banerjee N., 1975: "Representation of irregular stresses time histories by equivalent uniform stress series in liquefaction analyses". EERC 75-29, Earthquake Engineering Research Center, University of California Berkeley.

Seed H. B. and Idriss I. M., 1982: "Ground Motions and Soil Liquefaction During Earthquakes". Earthquake Engineering Research Institute, Oakland, California, Monograph Series, p. 13.

Seed H. B., Tokimatsu K., Harder L. F. and Chung R. M., 1985: "Influence of SPT Procedures in Soil Liquefaction Resistance Evaluations”. Journal of Geotechnical Engineering, American Society of Civil Engineers, vol. 111, no. 12, p. 1425-1445.

Seed, R.B., K.O. Cetin, R.E.S. Moss, A.M. Kammerer, J. Wu, J.M. Pestana, M.F. Riemer, R.B. Sancio, J.D. Bray, R.E. Kayen, and A. Faris. 2003: "Recent Advances in Soil Engineering: A Unified and Consistent Framework". Earthquake Engineering Research Center Report No. EERC 2003-06. University of California, Berkeley.

Servizio Geologico, Sismico e dei Suoli Regione Emilia Romagna, 2012: “Terremoto 2012 geologia, rilievi agibilità, analisi dei danni”.

Sonmez H., 2003: “Modification of the liquefaction potential index and liquefaction susceptibility mapping for a liquefaction-prone area (Inegol, Turkey)”. Environ Geol 44:862–871.

Standard & Poor’s (2015): "Storm alert: natural disasters can damage sovereign creditworthiness", Standard & Poor’s Ratings and Services, 10 September.

Stokoe K.H. and Santamarina J.C., 2000: “Seismic-wave-based testing in geotechnical engineering”. International Society for Rock Mechanics.

Document No. ISRM-IS-2000-38. In Proceedings of the ISRM International Symposium, 19–24 November, Melbourne, Australia. 47 pp.

Stuedlein A., Kramer S., Arduino P. and Holtz R., 2012: “Geotechnical characterization and random field modeling of desiccated Clay”. J. Geotech. Geoenviron. Eng., 138 (11), pp. 1301-1313.

Stewart J.P., Kramer S.L., Kwak D. et al, 2016: “PEER-NGL project: Open source global database and model development for the next-generation of liquefaction assessment procedures”. Soil Dynamics and Earthquake Engineering 91.

SYNER-G, 2013: “Systemic Seismic Vulnerability and Risk Analysis for Buildings, Lifeline Net-works and Infrastructures Safety Gain”. ISBN: 978-92-79-33135-0. DOI: 10.2788/23242. Web-site: http://www.vce.at/SYNER-G/files/project/proj-overview.html

Tesfamariam S. and Goda K., 2013: “Seismic risk analysis and management of civil infrastructure systems: an overview”. In Handbook of seismic risk analysis and management of civil infrastructure systems, S. Tesfamariam and K. Goda editors, Woodhead Publishing Limited, pp.141-174.

Tokimatsu K. and Seed H.B., 1987: “Evaluation of settlements in sands due to earthquake shaking”. ASCE J Geotech Geoenviron Eng 1987;113(8): 861–78.

Tokimatsu K., Hino K., Suzuki H., Ohno K., Tamura S. & Suzuki Y., 2019: “Liquefaction-induced settlement and tilting of buildings with shallow foundations based on field and laboratory observation”. Soil Dynamics and Earthquake Engineering, 124, 268-279.

Tonkin & Taylor, 2013: “Liquefaction Vulnerability Study”. Christchurch: Tonkin & Taylor Ltd.

Toprak S., Holzer T. L., Bennett M. J., Tinsley J. C., 1999: "CPT- and SPT-based probabilistic assessment of liquefaction potential”. Proceedings of Seventh US Japan Workshop on Earthquake Resistant Design of Lifeline Facilities and Counter-measures Against Liquefaction, T. D. O'Rourke, J. P. Bardet, and M. Hamada, eds., Report MCEER-99-0019, MCEER, NY.

Office of the United States Disaster Relief Co-ordinator, “UNDRO”, 1979: “Natural disasters and vulnerability analysis”. Report of expert group meeting, 9-12 July 1979.

UN General Assembly, 2015: “The Sendai Framework for Disaster Risk Reduction 2015–2030”. Available online at www.unisdr.org/we/inform/publications/43291.

UNISDR, 2009: 2009 UNISDR Terminology on Disaster Risk Reduction. International Strategy for Disaster Reduction (ISDR), 1–30. http://doi.org/978-600-6937-11-3.

van Ballegooy S., Malan P., Lacrosse V., Jacka M.E., Cubrinovski M., Bray J.D., O'Rourke T.D., Crawford S.A., Cowan H., 2014: "Assessment of Liquefaction-Induced Land Damage for Residential Christchurch". Earthquake Spectra (30) No. 1: pages 31–55, February 2014.

Vanmarcke E. H., and Lai S. P., 1977: "Strong motion duration of earthquakes", M.I.T., Department of Civil Engineering Publication No. R77-16.

Vick S.G., 2002: "Degrees of Belief: Subjective Probability and Engineering Judgment". ASCE press, 472p.

Viggiani C., Mandolini A., Russo G., 2012: "Pile and piled foundations". Taylor & Francis, 278 pp.

Walley P., 1991: "Statistical Reasoning with Imprecise Probabilities". Chapman and Hall, London.

Wackernagel H., 1998: "Variogram Cloud". In: Multivariate Geostatistics. Springer, Berlin, Heidelberg. https://doi.org/10.1007/978-3-662-03550-4_6.

Wang, W.S. 1979: "Some Findings in Soil Liquefaction". Beijing: Water Conservancy and Hydroelectric Power Scientific Research Institute.

Yamauchi T., Tezuka H., and Tsukamoto Y., 2017: "Development of Rational Soil Liquefaction Counter-measure Consisting of Lattice-Shaped Soil Improvement by Jet Grouting for Existing Housing Estates". In Geotechnical Hazards from Large Earthquakes and Heavy Rainfalls (pp. 49-59). Springer, Tokyo.

Yasuda S. and Ishikawa K., 2018: "Liquefaction-induced Damage to Wooden Houses in Hiroshima and Tokyo during Future Earthquakes". 16 ECEE, Thessaloniki, Greece, June 2018.

Youd, T. L. and Perkins D. M., 1978: "Mapping Liquefaction-induced Ground Failure Potential". J. Geotech. Eng. Div., ASC E, 104, 433–446pp.

Youd T.L.. and Perkins D.M., 1987: "Mapping of liquefaction severity index". ASCE J Geotech Eng 1987;113(11):1374–92.

Youd T. L., Idriss I. M., Andrus R. D., Arango I., Castro G., Christian J. T. , Dobry R. , Finn L., Harder L. F. J., Hynes M. E. , Ishihara K., Mitchell J. K., Moriwaki Y. , Power M. S., Robertson P. K., Seed R. B., & Stokoe K. H., 2001: "Liquefaction Resistance of Soils: Summary Report from the 1996 NCEER and 1998 NCEER/NSF Workshops on Evaluation of Liquefaction

Resistance of Soils". Journal of Geotechnical and Geoenvironmental Engineering, 1–17.

Youd, T. L., Hansen, C. M., and Bartlett, S. F., 2002: "Revised multilinear regression equations for prediction of lateral spread displacement." J. Geotech. Geoenviron. Eng., 128(12), 1007–1017.

Youd T.L., 2018: "Application of MLR Procedure for Prediction of Liquefaction-Induced Lateral Spread Displacement". J. Geotech. Geoenvironmental Eng. 2018, 6, 144.

Youden W. J.,1950: "Index for rating diagnostic tests". Cancer. 3: 32–35. doi:10.1002/1097-0142(1950)3:1<32::aid-cncr2820030106>3.0.c.

Zadeh L.A., 1965: "Fuzzy sets". Information and Control, 8, 338–353.

Zhang G., Robertson P.K., Brachman R.W.I., 2002: "Estimating liquefaction-induced ground settlements from CPT for level ground". Canadian Geotechnical Journal 39: 1168–80.

Zhang, G., Robertson P.K., Brachman R.W.I., 2004 "Estimating liquefaction-induced Lateral Displacements from CPT for level ground". Journal of Geotechnical and Geoenvironmental Engineering. AUGUST 2004.

Zhu J., Daley D., Baise L. G., Thompson E. M., Wald D. J. and Knudsen K. L., 2015: "A geospatial liquefaction model for rapid response and loss estimation". Earthq. Spectra, 31(3), 1813-1837.

Zhu J., Baise L. G. & Thompson E. M., 2017: "An Updated Geospatial Liquefaction Model for Global Application". Bulletin of the Seismological Society of America, 107(3), 1365-1385.

Ziotopoulou K. and Boulanger R. W., 2013: "Numerical modeling issues in predicting post-liquefaction reconsolidation strains and settlements". In Proceedings of the 10th International Conference on Urban Earthquake Engineering.